TECHNOLOGY • RESEARCH HIGHLIGHTS • VISIONS • SCIENCE

333

Thermal ageing and mechanical performance of narrow-gap dissimilar metal welds

Matias Ahonen | Sebastian Lindqvist |
Teemu Sarikka | Roman Mouginot | Esa Leskelä |
Jari Lydman | Ulla Ehrnstén | Pekka Nevasmaa |
Tommi Seppänen | Pentti Arffman |
Hannu Hänninen

VTT TECHNOLOGY 333

Thermal ageing and mechanical performance of narrow-gap dissimilar metal welds

---

Matias Ahonen, Sebastian Lindqvist, Esa Leskelä, Jari Lydman, Pekka Nevasmaa, Tommi Seppänen, Pentti Arffman and Ulla Ehrnstén

VTT Technical Research Centre of Finland Ltd

Teemu Sarikka, Roman Mouginot and Hannu Hänninen

Aalto University

ISBN 978-951-38-8656-1 (Soft back ed.)
ISBN 978-951-38-8655-4 (URL: http://www.vttresearch.com/impact/publications)

VTT Technology 333

ISSN-L 2242-1211
ISSN 2242-1211 (Print)
ISSN 2242-122X (Online)
http://urn.fi/URN:ISBN:978-951-38-8655-4

JULKAISIJA – UTGIVARE – PUBLISHER

Teknologian tutkimuskeskus VTT Oy
PL 1000 (Tekniikantie 4 A, Espoo)
02044 VTT
Puh. 020 722 111, faksi 020 722 7001

Teknologiska forskningscentralen VTT Ab
PB 1000 (Teknikvägen 4 A, Esbo)
FI-02044 VTT
Tfn +358 20 722 111, telefax +358 20 722 7001

VTT Technical Research Centre of Finland Ltd
P.O. Box 1000 (Tekniikantie 4 A, Espoo)
FI-02044 VTT, Finland
Tel. +358 20 722 111, fax +358 20 722 7001

Juvenes Print, Tampere 2018

Preface

NIWEL (Nickel-Base Alloy Welding Forum) project was primarily addressed to the needs of the nuclear energy industry, and it was the fourth consecutive cooperative project on the dissimilar metal weld (DMW) topics. Tekes (nowadays Business Finland) and Finnish and Swedish power companies (TVO, Fortum, OKG and Ringhals) funded the NIWEL project. The earlier projects, ERIPARI, PERDI and SINI, covered topics like weldability, hot cracking, environment-assisted cracking and structural integrity of Ni-base Alloy DMWs. The main focus of the NIWEL project was to assess the effect of thermal ageing on the performance of DMWs.

The long-term behaviour of the DMWs is of particular interest in Finland, because there are nuclear power plants that are at critical stages of their lifetime: either beginning their operation or reaching lifetime extensions. In both cases, understanding of the ageing phenomena is of utmost importance in order to ensure safe operation for lifetimes that can reach 60 years or even beyond that.

The narrow-gap DMW without a buttering layer in the OL3 EPR plant safe-end is a first-of-a-kind design, and thus its characteristic microstructural features as well as mechanical performance must be studied carefully. It has been shown earlier that thermal ageing may cause changes in the properties of the DMWs in elevated temperature service. Thus, the main aim of the NIWEL project is to characterize the properties, both microstructural and mechanical, of a fully representative narrow-gap DMW mock-up before and after thermal ageing that corresponds to 60 years of plant operation.

Developing and maintaining the knowledge of DMW-related issues is absolutely vital for the Nordic nuclear power industry. Taking part in the most important international forums and dissemination of the experiences to the industry has been an essential theme for the NIWEL project, as well as developing research competence in Finland. Many younger generation researchers have been introduced to the field of DMW research during the project. A final seminar on the project results was held at VTT in order to transfer the gained knowledge, not only to the nuclear industry but also to conventional industries, on DMW performance and their long-term behaviour.

Contents

Preface **3**

List of symbols **7**

1. Introduction **11**

- 1.1 Application of dissimilar metal welds (DMWs) in nuclear power systems 11
- 1.2 Mechanical mismatch of DMWs 12
- 1.3 Thermal ageing of DMWs 15

2. Materials and fabrication of the studied NG DMW mock-up **16**

3. Thermal ageing treatment of the NG DMW mock-up **20**

4. Microstructural characterization of the NG DMW mock-up **22**

- 4.1 Microstructural characterization 22
  - 4.1.1 Heat-affected zone of the LAS 22
  - 4.1.2 Alloy 52 weld metal 32
  - 4.1.3 Ferrite/austenite interface 34

5. Fracture mechanical and mechanical testing **41**

- 5.1 Materials and methods 41
  - 5.1.1 Test matrix and specimens 41
  - 5.1.2 Extraction of the specimens 44
- 5.2 J-R testing according to ASTM E1820 45
- 5.3 T_0 testing according to ASTM E1921 46
- 5.4 Charpy-V testing 47
- 5.5 Tensile testing 51
- 5.6 Results 53
  - 5.6.1 J-R curves 53
  - 5.6.2 Qualification of the data 59
- 5.7 T_0 fracture toughness testing 65
  - 5.7.1 Quality of T_0 data 65
  - 5.7.2 T_0 fracture toughness testing results 67
  - 5.7.3 Inhomogeneous Master Curve analyses 72
- 5.8 Charpy-V impact toughness testing results 73
  - 5.8.1 Transition curves and temperatures 73
  - 5.8.2 Estimation of crack arrest 78
  - 5.8.3 Data from instrumented tests 82
  - 5.8.4 Non-conformance 84
- 5.9 Strength analysis 88

6. Low Temperature Crack Propagation (LTCP) testing at 55 °C in hydrogenated water **92**

- 6.1 Methods and specimens 92
- 6.2 LTCP test results 95

7. **Fractographic examinations 98**

7.1 Characterization of J-R test specimen fracture surfaces 98
  7.1.1 Crack path examination...105
7.2 Characterization of Charpy-V impact toughness specimen fracture surfaces 111
  7.2.1 Fraction of intergranular (IG) fracture observed on the fracture surfaces of Charpy-V specimens 120
7.3 Characterisation of the T_0 test specimen crack location.......................122
7.4 Characterization of LTCP test specimen fracture surfaces..................123

8. **PARENT – Program to Assess the Reliability of Emerging Nondestructive Techniques...136**

8.1 Introduction 136
8.2 Test blocks...136
  8.2.1 Blind test blocks...136
  8.2.2 Open test blocks 137
8.3 Inspection procedures..138
  8.3.1 Blind testing procedures...138
  8.3.2 Open testing procedures 139
8.4 Data processing...140
  8.4.1 Data reporting...140
  8.4.2 Scoring procedure...140
  8.4.3 Detection performance analysis...140
  8.4.4 Sizing analysis..141
8.5 Blind testing results...142
  8.5.1 Detection performance 142
  8.5.2 Depth sizing results...144
  8.5.3 Length sizing results 147
8.6 Open testing results...150
  8.6.1 Depth sizing results...150
  8.6.2 Length sizing results 155
8.7 PARENT Atlas information tool..158
8.8 Comparison of PARENT vs. PINC...159
8.9 Conclusions from PARENT 160
8.10 Future NDE work...161

9. **Discussion...163**

9.1 Microstructural characterization and hardness measurements.............163
9.2 Effect of ageing on ductile-to-brittle transition temperature 166
  9.2.1 Fracture toughness vs. impact toughness 166
  9.2.2 T_0 and T_{28J} dependence 170
  9.2.3 Initiation sites...171
9.3 Effect of ageing on the ductile J-R curves 172
9.4 Temperature dependence of J_{1mm} and ductile fracture properties in fusion boundary region...178

9.5 Weld mechanical mismatch and crack path 180
9.6 LTCP testing 181

10. Conclusions 183

11. Future work 185

References 186

Abstract
Tiivistelmä

List of symbols

a_0	Initial crack length
a_p	Final crack length
ADVPAUT	Advanced phased array ultrasonic testing
ASME	American Society of Mechanical Engineers
B	Specimen thickness
β1 and β2	Unknown parameters determined by regression algorithm
BMI	Bottom-mounted instrumentation nozzle
CMOD	Crack mouth opening displacement
CVN	Charpy-V notch
C(T)	Compact tension
DMW	Dissimilar metal weld
Δa	Crack growth
$\Delta a_{predicted}$	Predicted crack growth
Δa_p	Crack growth
δX	Tolerance in X direction
δY	Tolerance in Y direction
E_i	The measurement error in sizing flaw *i*
EBSD	Electron backscatter diffraction
EDS	Energy dispersive X-ray spectroscopy
ECT	Eddy current testing
EDM	Electrical discharge machining
E	Energy

ENSI	Swiss Federal Nuclear Safety Inspectorate
ε	Strain
FB	Flat bar
FCP	False call probability
GUW	Guided ultrasonic waves
HAZ	Heat-affected zone
HHUT	Higher harmonic ultrasonic technique
ID	Inside diameter
ID	Interdendritic
IG	Intergranular
J	J-integral
J_{1mm}	J-integral at 1 mm of ductile crack growth
J_{3mm}	J-integral at 2 mm of ductile crack growth
J_{3mm}	J-integral at 3 mm of ductile crack growth
J_{IC}	value of J-integral near the initiation of stable crack growth, a size independent value of fracture toughness
J_Q	value of J-integral near the initiation of stable crack growth, interim fracture toughness or fracture resistance
K_{Jc}	Stress intensity factor
KINS	Korea Institute of Nuclear Safety
LASH	Large amplitude excitation subharmonic UT
LBDMW	Large bore dissimilar metal weld
logistic(X)	Logistic regression function
LTCP	Low temperature crack propagation
LUV	Laser ultrasound visualization
LW	Longitudinal wave
M_i	Measured size of flaw *i*
MFC	Mechanical fatigue crack
MM	Microwave near-field microscopy
NDE	Non-destructive examination
NLUT	Nonlinear ultrasonic testing

NOBS	Number of observations
NPP	Nuclear power plant
NRA	Nuclear Regulatory Authority of Japan
NRC	The U.S. Nuclear Regulatory Commission
OD	Outer diameter
PAATOFD	Phased array asymmetrical beam time-of-flight diffraction
PARENT	The Program to Assess the Reliability of Emerging Nondestructive Techniques
PATP	Phased array twin probe
PAUT	Phased array ultrasonic testing
PINC	Program for Inspection of Nickel Alloy Components
PIONIC	Program for Investigation of NDE by International Collaboration
PNNL	Pacific Northwest National Laboratory
POD	Probability of detection
PWHT	Post-weld heat treatment
PWSCC	Primary water stress corrosion cracking
RMSE	Root mean square error
RRT	Round robin test
RT	Radiographic testing
S	Flaw size
SEM	Scanning electron microscope
σ	Standard deviation
σ	Stress
σ_{BM}	Base material strength
σ_{TS}	Tensile strength
σ_{YS}	Yield strength
σ_{WM}	Weld metal strength
σ_{zone}	Strength of 1 mm thick zone in the interface region
SAFT	Synthetic aperture focusing technique
SBDMW	Small bore dissimilar metal weld

SC	Solidification crack
SCC	Stress corrosion crack/Stress corrosion cracking
SE(B)	Single edge-notched bend
SHPA	Subharmonic phased array
SSM	Swedish Radiation Safety Authority
SW	Shear wave
T_0	Ductile-to-brittle transition temperature based on fracture toughness
T	Temperature
T_{42J}	Ductile-to-brittle transition temperature based on impact toughness
T_i	True size of flaw *i*
TFC	Thermal fatigue crack
TOFD	Time-of-flight diffraction
TR	Transmitter-receiver
TRL	Transmitter-receiver longitudinal
UIR	Ultrasound infrared tomography
UT	(conventional) Ultrasonic testing
WOL	Weld overlay
v	Poisson’s ratio
J_{1mm}	J-integral at 1 mm of crack growth
J_c	J-integral prior to initiation of brittle fracture
L	Length
M	Parameter in the blunting line
Ms	Strength mismatch
W	Specimen width

1. Introduction

1.1 Application of dissimilar metal welds (DMWs) in nuclear power systems

The structural materials used in the components and piping of primary circuits of the pressurized water reactors (PWRs) are for the most part ferritic low-alloy steels (LAS), stainless steels (SS) and nickel-base alloys (Féron 2012). LAS alloyed with low contents of Cr, Ni, Mo and V can reach high strength levels and are used for structural components (MacDonald & Cragnolino 1989), of which the most important is the reactor pressure vessel (RPV). Austenitic SS are used for structural components (Types 304, 304L, 316 and 316L) and as a corrosion-resistant cladding of the RPV and pressurizer (Types 308 and 309). Nickel-base alloys are used for high-strength components, some critical applications and welds. A combination of all these types of materials is found in the dissimilar metal welds (DMW), in which materials of different composition and crystal structure are joined. DMWs are important from the design and performance point of view. However, they have been related to a number of incidents involving intergranular stress corrosion cracking (IGSCC) (Aaltonen & Hänninen 1997, MacDonald & Cragnolino 1989, Ehrnstén 2012, Fyfitch 2012), with sensitized microstructures found in SS and Ni-base alloy safe-ends and within weld metals (Scott 1996, Lu et al. 2015). Nickel-base weld metals such as Alloys 182 and 82, with a composition similar to wrought Alloy 600, have increased the service life of DMWs by reducing carbon migration at the interface and differential expansion strains (Payne 1969). They are, however, susceptible to IGSCC and cracking incidents, involving Alloys 600 and 182 in the RPV safe ends and head penetrations as well as steam generators, have been observed in many plants due to the presence of corrosive environment, high temperature, residual stresses/strains, and material sensitization effects (Aaltonen & Hänninen 1997, MacDonald & Cragnolino 1989, Fyfitch 2012). A particular type of IGSCC in high-temperature, high-purity pressurized water reactor (PWR) water is called Primary Water Stress Corrosion Cracking (PWSCC) (Scenini et al. 2005, Andresen et al. 2007). While crack propagation along the DMW interface is most often limited to the weld metal (Seifert et al. 2008), and the cracks typically grow in axial orientation of the pipe in safe-end weld cracking incidents (Cattant 2014), an increasing susceptibility to loss of ductility has been observed especially at the weld interface region (Chung et al. 2011).

The transition zones of the DMW interfaces are usually classified as heat-affected zone (HAZ), partially-melted zone (PMZ) and unmixed zone (UMZ), and their characterization and control is of particular concern from the joint performance point of view (Lippold et al. 2015). Residual stresses and strains are well known SCC accelerants. The extent of the residual strain at weld interface has been noted as high as 40 to 50% in the weld metal, 20% in the UMZ and PMZ, about 15% in the base material HAZ and 8 to 10% within the base material (Andresen et al. 2012).

A typical example of a DMW is the RPV nozzle to safe-end weld between the SS-cladded RPV ferritic LAS and an austenitic SS pipe, using a Ni-base filler metal. These alloys present very different compositions, especially regarding the carbon and chromium contents. Due to these differences, a composition gradient forms at the interface and a complex microstructure results from the mixing and diffusion of alloying elements, notably carbon diffusion (Sarikka et al. 2017b). The reduced chromium and nickel contents in the transition region due to the dilution effects are assumed to increase the SCC susceptibility (Toloczko et al. 2016), while the formation of hard and soft layers, driven by the composition gradients, lead to lower strength area in the carbon-depleted zone and increase the strength mismatch at the interface (Laukkanen et al. 2005, Sarikka et al. 2016, 2017). The dissimilar metal weld interface region is complex and includes different microstructural regions (Sarikka et al. 2016, 2017, Peng et al. 2005, Rajeev et al. 2001, Lundin 1982). Key microstructural features, which can be found near the weld interface, include carbon-depleted zone (CDZ) (Sudha et al. 2002), martensite (Nelson et al. 1998), carbon build-up (Alexandrov et al. 2013) and Type II boundaries (DuPont et al. 2009, Chung et al. 2011).

In order to improve the SCC resistance, Alloy 690 has replaced Alloy 600 in steam generator tubes and vessel head penetration tubes. The filler metals Alloy 52, 152 and 52M were developed based on the composition of Alloy 690 and are nowadays used in DMWs. Due to the higher chromium content, they show a better SCC resistance than Alloys 182 and 82, with marked improvement in crack initiation times and SCC crack growth rate (Sui et al. 1997).

1.2 Mechanical mismatch of DMWs

In welds, the strength of the weld metal can differ from the strength of the base metal. Strength mismatch, M_s, is defined as the ratio of the yield strength of the weld metal σ_{WM} to that of the base material σ_{BM} (Kim et al. 2000). In NPPs, the dissimilar metal welds, DMWs, connect the reactor pressure vessel and the piping. Typically, the ferritic pressure vessel has a higher strength than the austenitic piping material and the weld metal. The strength mismatch of narrow-gap Alloy 52 DMWs has been extensively investigated in (Lindqvist 2014, Ahonen 2015, Sarikka 2016a; Mouginot 2017).

In addition to the strength mismatch between the weld metal and base material, Alloy 52 narrow-gap DMWs typically consist of narrow microstructural zones with varying strength properties in the interface region between RPV steel SA 508 and the weld metal Alloy 52. The hardness starts to increase from the SA 508 base material value 3 to 2 mm from the fusion boundary, associated with the beginning of the HAZ. A peak hardness of the SA 508 is obtained ~0.5 mm from the fusion boundary. After that the hardness decreases drastically and a minimum is located at the fusion boundary in the SA 508 side. A hardness peak is located on the weld metal side adjacent to the fusion boundary, due to carbon build-up. The hardness peak is only few micrometres wide. When moving away from the fusion boundary into the weld metal, the hardness decreases to the characteristic hardness of the Alloy weld metal. The mechanical properties in the interface zone between SA 508 and Alloy 52 are affected by the local and global strength mismatch and the local microstructures (Wang et al. 2013a, Fan et al. 2016, Sarikka et al. 2017a).

A typical feature of DMWs is that the crack does not grow along the initial plane, but can deviate to adjacent locations, as illustrated in Figure 1. In SE(B) specimens of Alloy 52 narrow-gap DMWs, HAZ cracks approximately 0.5 mm from the fusion boundary can deviate from the initial crack growth plane to the fusion boundary with lower tearing resistance than the adjacent zones or bulk materials (Wang et al. 2013b, Hänninen et al. 2014, Lindqvist et al. 2018). Since the crack tends to grow towards the material region with lower strength (Sarikka 2016a), HAZ cracks further than 0.5 mm from the fusion boundary can also grow from the hard HAZ towards the softer base material (Sarikka 2016a, Sarikka et al. 2016b). The crack deviation towards the fusion boundary is controlled by the strength mismatch, but is also affected by residual stresses and the microstructure. The strength mismatch affects the local constraint which is observed as localization of the stress triaxiality and the plastic strain ahead of the crack. Plastic damage is promoted in the regions with high stress triaxiality and plastic strain.

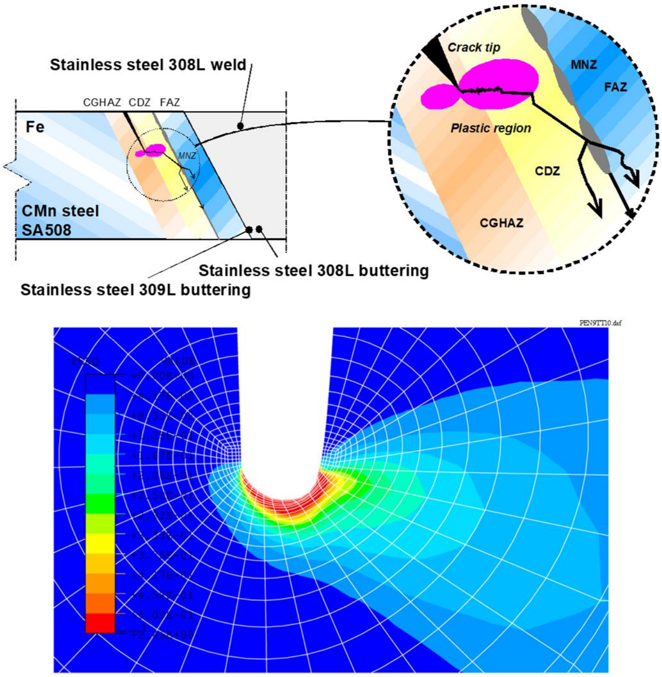

Figure 1. Irrespective of the existence of the original flaw or defect in a weld, the actual damage formation can occur and escalate in a neighbouring microstructure. This, in turn, tends to manifest itself as deviation of the crack path. (Nevasmaa et al. 2010)

Crack deviation affects the shape of the J-R curve and complicates the interpretation of the J-R curves. The J-R curve, in case of crack deviation, describes the measured crack path and not the tearing resistance along the initial crack growth plane (Wang et al. 2013b). For structural integrity analyses, it is important to obtain lower boundary J-R curves. Thus, characterisation of the effect of crack path and crack location on J-R curves in the fusion boundary region is crucial.

The strength mismatch affects also the J-integral, a parameter describing the energy required for incremental crack growth. The work done to a fracture mechanical specimen, A_{tot}, during loading is connected to the J-integral by the eta factor (η-factor), Equation (1). The η-factor solution applied in the fracture mechanical testing standards, like ASTM E1820 or ASTM E1921, is not necessary applicable for strength mismatched welds with an unsymmetrical or a discontinues plastic field. The η-factor in the standards has been obtained for materials with homogeneous mechanical properties and a symmetrical plastic field.

$$J = \frac{\eta A}{Bb} \tag{1}$$

However, based on the validation work done in SAFIR2018 project LOST (Lindqvist & Kuutti 2018) and in EU-project MULTIMETAL (Simonovski et al. 2015), the η-factor from E1921 and E1820 can be applied for cracks in the interface region between hard and soft materials, even if the strength mismatch is approaching 100 %.

1.3 Thermal ageing of DMWs

Of the materials in the studied narrow-gap dissimilar metal weld, ferritic reactor pressure vessel (RPV) steel (low-alloy steel) is considered to be the most important from thermal ageing point of view, due to its ductile-to-brittle transition behaviour and tendency to thermal embrittlement. Several different processes can lead to thermal embrittlement and degradation of the fracture mechanical properties of the RPV steel during long periods of operation in high (325 °C) temperature. Those mechanisms include precipitation hardening, such as precipitation of copper-rich phases, phosphorous segregation at the grain boundaries leading to intergranular fracture, solution of cementite and widening of the carbon-depleted zone leading to softening of the low-alloy steel in that region, and segregation of impurities to dislocations leading to strain ageing (Corwin, 1995). Of these processes, phosphorous segregation is assumed to have the most significant effect on the behaviour of the narrow-gap DMW of the current study, and other metallurgical processes are not assumed to be substantial in plant operation temperatures (Joly, 2014).

Hudson et al. (1988) showed that thermal ageing causes phosphorous segregation at the grain boundaries of low-alloy steels, which degrades the fracture toughness and impact toughness of the material. They showed that Charpy-V impact toughness test results correlate well with the phosphorous segregation. The effect of phosphorous segregation on the mechanical properties is greatest in coarse-grained materials. Thus, the effect of phosphorous segregation is assumed most significant in microstructural zones with larger grain size.

The thermal stability of Alloy 690 and its weld metals (Alloys 152 and 52) in the long-term operation of nuclear power plants, operating as long as 60-80 years, remains an important topic of research (Young et al. 2013). The susceptibility of welds to SCC depends not only on the properties of the base and weld metals, but also on the microstructural changes taking place at the interface during welding and post-weld heat treatment (EPRI 2009). Thermal ageing can also affect the SCC susceptibility of Alloy 690 and its weld metals. In particular, there is still little knowledge on the long-term behavior of these interfaces since no in-service experience is available, yet, and very few laboratory investigations have been performed on aged materials. The aim of this study is therefore to characterize the microstructural changes occurring at the RPV nozzle to safe-end ferrite/austenite interface upon thermal ageing.

2. Materials and fabrication of the studied NG DMW mock-up

The studied material in the NIWEL project was an industrially manufactured 1:1 scale DMW safe-end mock-up. The shape of the mock up is a ring, thus enabling it to be fully representative to the real component. The received piece of the mock-up with its dimensions is presented in Figure 2 a and b. The thickness of the mock-up is 94 mm, of which 12 mm from the inner diameter was excluded when cutting of the specimens for mechanical and fracture mechanical testing, as illustrated in Figure 2 a. The inner diameter of the mock-up ring is 920 mm and outer diameter 968 mm. The width of the mock-up is about 65 mm, as shown in Figure 2 b.

The mock-up consists of four different materials: SA 508 low-alloy steel base metal, Alloy 52 weld, AISI 316L stainless steel and AISI 308 cladding on top of the low-alloy steel part on the inner surface. The chemical compositions of the materials are presented in Table 1.The fusion boundary of specific interest, SA 508 - Alloy 52 weld fusion boundary, is located roughly in the middle of the mock-up, and is the fusion boundary, which is clearly recognizable in Figure 2 b.

An optical cross-section image of the mock-up showing the SA 508 low-alloy steel, AISI 308 cladding, Alloy 52 weld metal and AISI 316L stainless steel is presented in Figure 3 together with a higher magnification optical image showing the LAS HAZ and nominal pre-crack location of the test specimens. The weld is manufactured by applying the narrow-gap (NG) gas tungsten arc welding (GTAW) method without buttering and using Alloy 52 as welding consumable. The joint is welded one bead per layer. After welding, the mock-up was post-weld heat treated at 550°C for 890.4 min and at 610°C for 458.4 min. Also, the directions used for determining the orientations are seen in Figure 3.

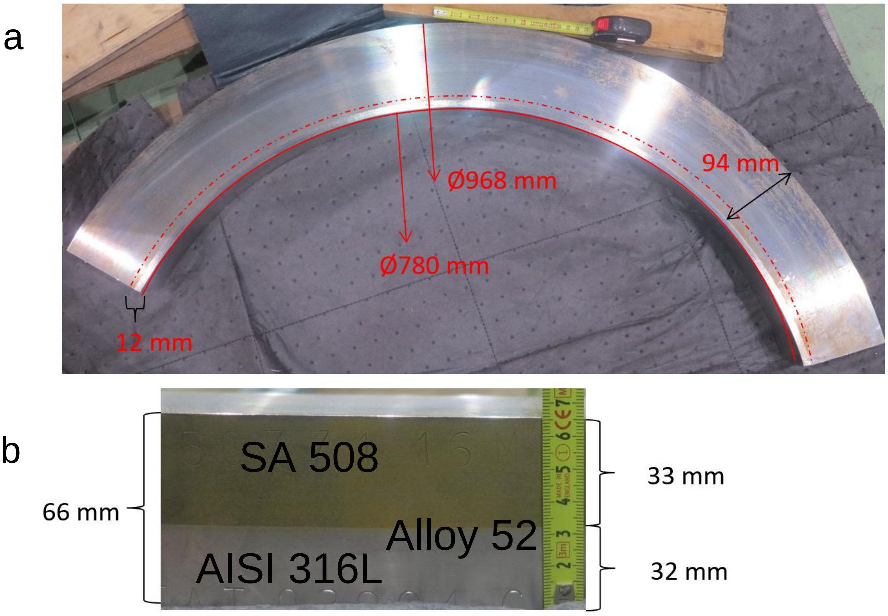

Figure 2. A photograph of the received narrow-gap dissimilar metal weld mock-up with measures shown in a. A photograph from a different angle, showing the outer surface of the mock-up ring is presented in b.

Table 1. Chemical compositions (in wt.%) of the materials used in the DMW mock-up (Areva).

	16MND5/SA 508	**AISI 316L**	**AISI 308L**	**Alloy 52**
C	0.18	0.021	0.007	0.023
Si	0.19	0.40	0.37	0.15
Mn	1.42-1.46	1.62	1.9	0.26
P	0.005	0.020	0.013	<0.005
S	0.001	0.002	0.001	0.0007
Cr	0.11-0.12	17.23	20.3	29.93
Ni	0.76-0.78	11.56	10.3	58.86
Mo	0.49-0.50	2.34	0.1	<0.01
Nb				<0.01
N		0.067	0.04	0.021
Ti				0.54
Fe	Bal.	Bal.	Bal.	10.43
Al	0.02			0.66
Co	0.01-0.02	0.022		<0.01
As	0.003-0.005			
Sn	0.003-0.004			

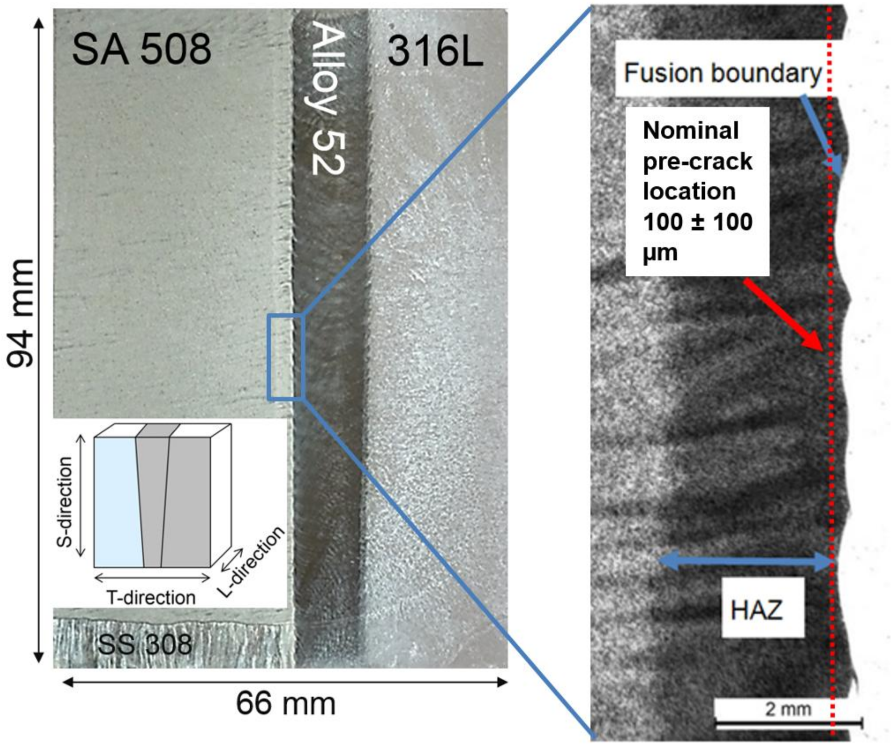

Figure 3. An optical image on the left, showing the cross-section of the NG DMW mock-up, and a larger magnification optical image on the right, where the HAZ, fusion boundary and nominal pre-crack location are shown. The directions used for determining the specimen orientations are schematically presented in a drawing on the left.

3. Thermal ageing treatment of the NG DMW mock-up

Thermal ageing was applied to two separate blocks of the test material. The ageing was conducted in a furnace at 400 °C for 5000 and 10000 h. The furnace with two blocks of the mock-up is shown in Figure 4. The mock-up block for 5000 h of ageing was outfitted with mechanical handles prior to heating the oven, in order to enable taking it out after 5000 h of ageing, and continue the thermal ageing of the other block (10000 h block) for another 5000 h. The temperature during thermal ageing was monitored using thermocouples and stayed within about ±1 °C during most of the thermal treatment. When the thermal treatment was started, the door of the furnace was not tight and thus the 5000 h block, located closer to the door, had a slightly lower temperature, measured to be 394 °C, for the first 3 days. The sealing of the door was then improved, and after that the temperature was stable and very close to 400 °C for the both blocks. The period with a slightly lower temperature for the 5000 h block was taken into account and the thermal ageing time for the 5000 h mock-up was corrected by using Larson-Miller parameter, to be exactly representative to 5000 h at 400 °C. When the 5000 h aged block was removed from the furnace, the thermal treatment was temporarily stopped due to a damaged thermocouple. The completion dates for the thermal ageing of 5000 h and 10000 h were 14.5.2016 and 12.12.2016, respectively.

The validity of the thermal ageing temperature 400 °C was evaluated based on the possible known mechanisms, which are segregation of impurities to the grain boundaries, strain ageing and carbide coarsening. The ageing times were chosen based on the assumption that P segregation is the main mechanism controlling the degradation of fracture toughness of the pressure vessel steel during ageing. Phosphorous segregation is enhanced at 400 °C without changing its mechanism, compared to the operation temperature. According to the calculations presented by Joly et al. (Joly et al., 2014), the ageing time of 10000 h at 400 °C is representative to about 60 years of operation at 325 °C from the P segregation point of view.

Thermal ageing was performed on large blocks instead of the ready specimens for fracture mechanical testing, mechanical testing, hardness testing and microstructural characterization in order to avoid surface oxidation of the actual specimens.

Figure 4. A photograph showing the furnace, feedthrough of the thermocouples and the mock-up block for 5000 h of ageing. The other block for 10000 h of ageing is behind the 5000 h block inside the oven.

4. Microstructural characterization of the NG DMW mock-up

Samples covering the LAS base material, HAZ, PMZ, UMZ and the weld metal were extracted for microstructural characterization using electrical discharge machining (EDM). Samples were ground with Struers SiC grinding papers up to 4000 grit and then polished with 3 µm, 1 µm and 0.25 µm Struers DiaPro diamond solutions. Vibratory polishing in a colloidal silica alkaline suspension was used as final polishing to remove the last deformation layers from grinding. Optical microscopy (OM) and scanning electron microscopy (SEM) were used to characterize the microstructures. Electron backscatter diffraction (EBSD) was used for grain size measurement. Energy dispersive X-ray spectroscopy (EDS) was used to characterize the composition gradients at the weld interface. Microhardness and nanoindentation measurements were carried out with an instrumented tester to study hardness profiles across the LAS HAZ and the weld interface. Microhardness measurements were done with a Vickers tip using an indentation load of 350 mN and a 50 µm step size, while nanoindentation measurements were performed with a Berkovich tip using an indentation load of 1.5 mN and a 5 µm step size.

This chapter mainly presents the results obtained for the NG DMW mock-up studied in the NIWEL project (“NIWEL mock-up”). However, some results are compared to the results obtained for the SINI NG DMW plate mock-up material (“SINI mock-up”), manufactured at Aalto University and characterized in detail in the previous DMW project, SINI (Hänninen et al. 2014).

4.1 Microstructural characterization

4.1.1 Heat-affected zone of the LAS

As seen in Figure 5, the heat-affected zone (HAZ) of the LAS extends typically about 2.5 mm from the fusion boundary to the base material (Figure 5a). The LAS base material, exhibiting a typical level of hardness for LAS (about 240 HV0.5) consists of coarse ferrite grains with a tempered upper bainite microstructure (Figure 5b). The microstructure refines progressively towards the fusion boundary due to the heat input from the welding process (Figure 5c). First, an intermediate zone is found in the HAZ with partially refined grains, followed by a grain-refined zone of higher hardness (about 280 HV0.5). Close to the fusion boundary, the higher heat input has caused grain coarsening. Adjacent to the fusion boundary is a layer of coarse grains from which carbon has diffused to the low-C/high-Cr Ni-base weld metal side of the interface (Figure 5d). This layer is called the carbon-depleted zone (CDZ) and it exhibits the lowest hardness (about 230 HV0.5).

To be noted is the presence of bands in the LAS HAZ (see Figure 5a) appearing darker or lighter. The darker bands have a smaller grain size and are harder (about 300 HV0.5) than the rest of the HAZ. Darker bands are clearly visible in the LAS side and especially in the HAZ. They are related to either smaller grain size or a higher carbon and alloying element content. They can be also the reason for the scatter in the hardness level of the LAS HAZ in the hardness profiles made across the SA 508/Alloy 52 weld metal interface. A matrix of indentations was made with 350 mN load parallel to the SA 508/Alloy 52 weld metal interface, about 750 μm from the fusion line within the SA 508 HAZ. Figures 6 and 7 show the location of the indentations and the zones where the indentations hit the darker bands. Figure 8 shows the hardness profile corresponding to the test matrix and indicates a clear correlation between the highest hardness peaks and the location of the darker bands.

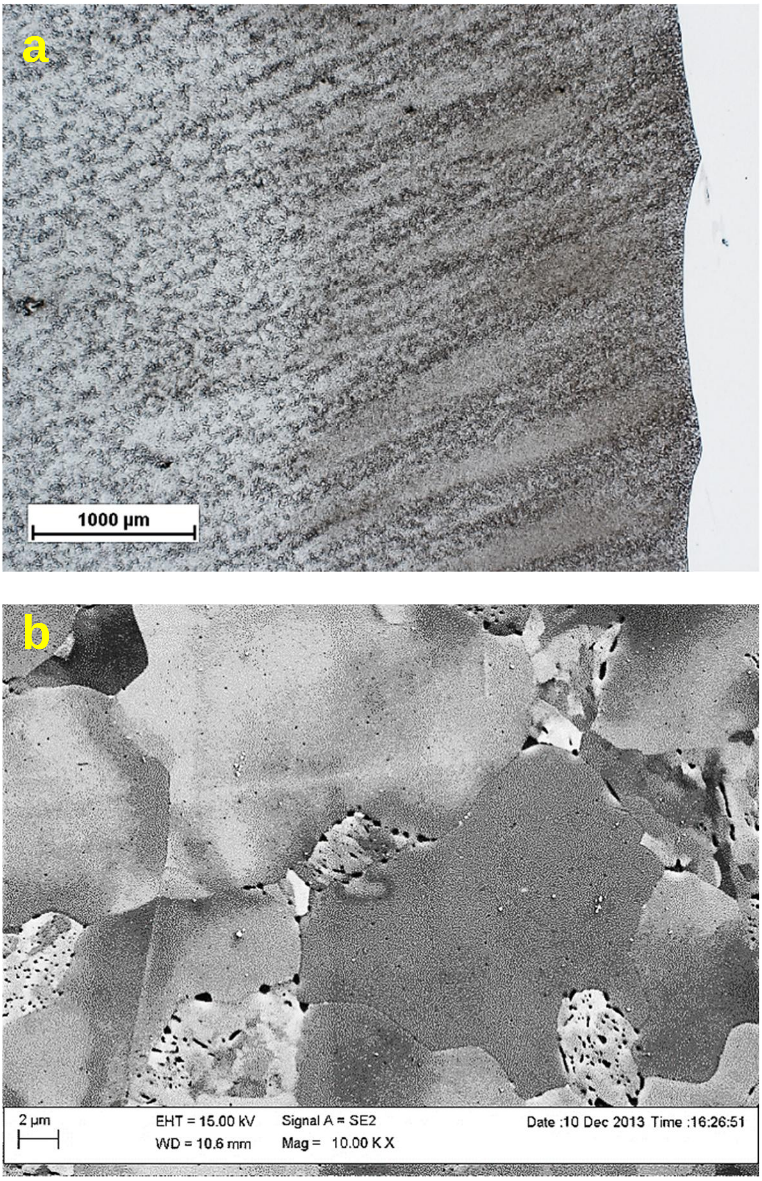
a
1000 µm
b
2 µm
EHT = 15.00 kV
WD = 10.6 mm
Signal A = SE2
Mag = 10.00 K X
Date :10 Dec 2013 Time :16:26:51

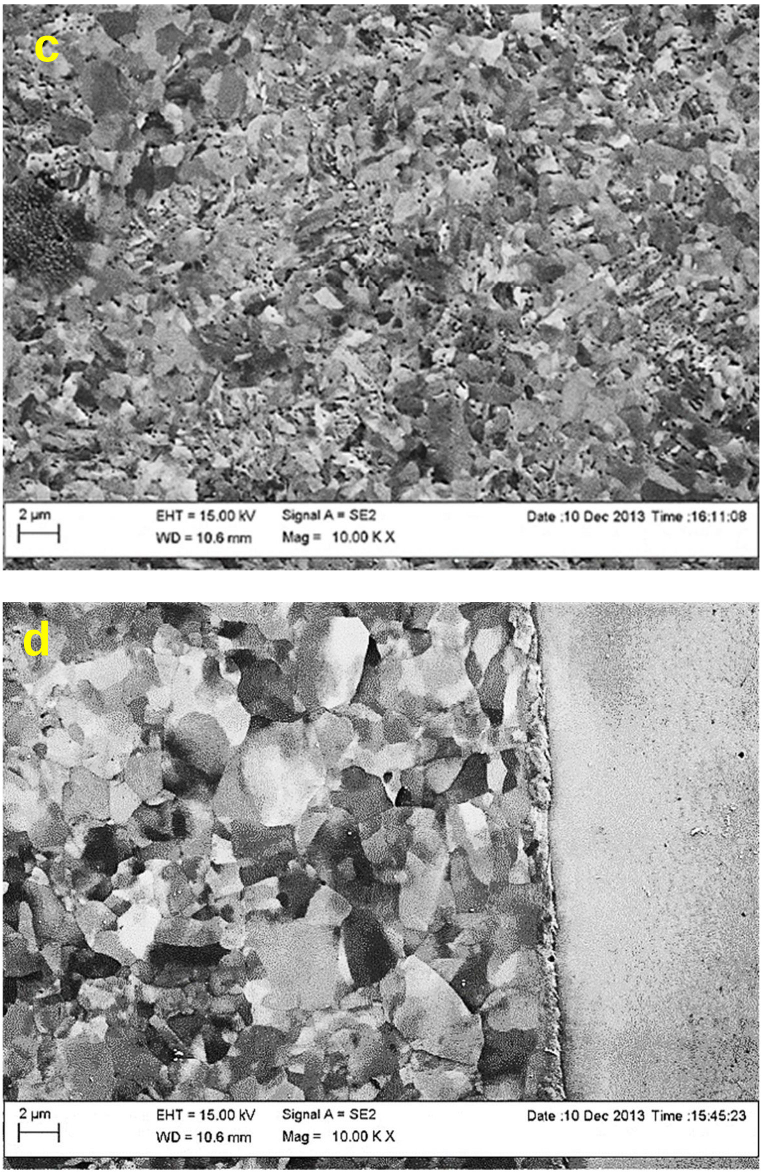

Figure 5. Typical features of the LAS HAZ of the DMW mock-ups, with a) an optical image of the LAS HAZ of NIWEL AR. Note the wavy pattern of the fusion boundary due to the weld passes and the banded structure in the LAS. SEM imageing of the LAZ HAZ in SINI mock-up shows b) the LAS base material, c) the grain-refined zone and d) the grain-coarsened zone and CDZ next to the fusion boundary.

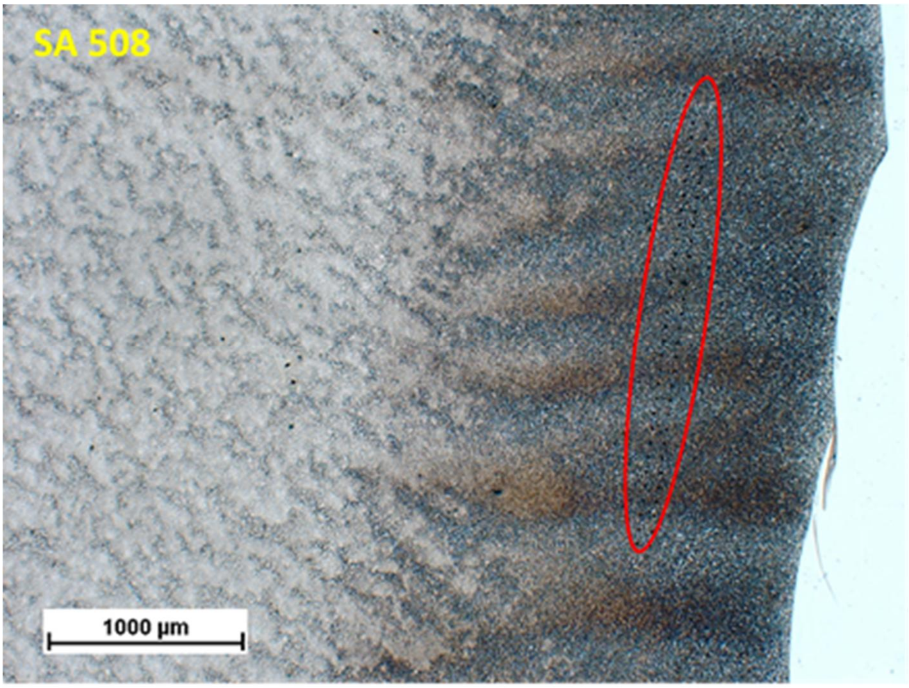

Figure 6. Location of the indentation matrix in the LAS HAZ across the banded microstructure.

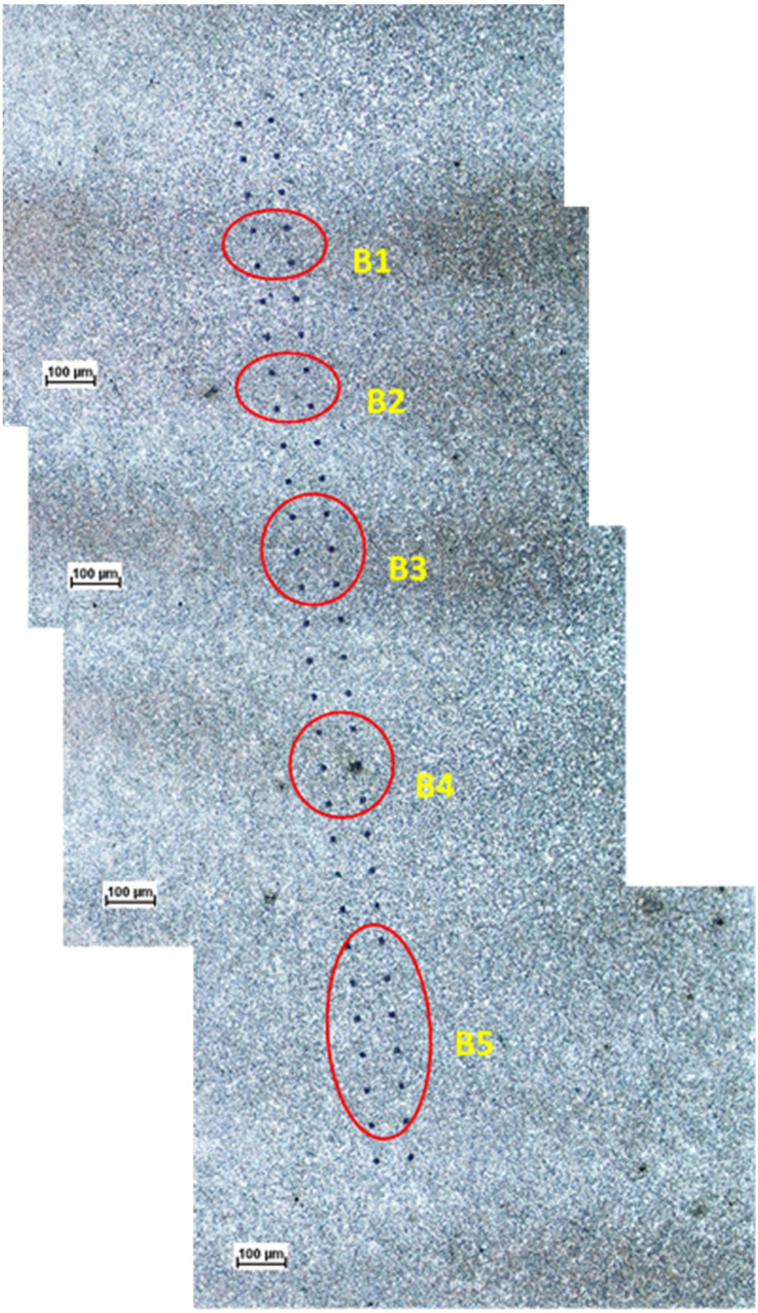

Figure 7. Identification of the zones where the indentation matrix crosses the dark bands (B1 to B5).

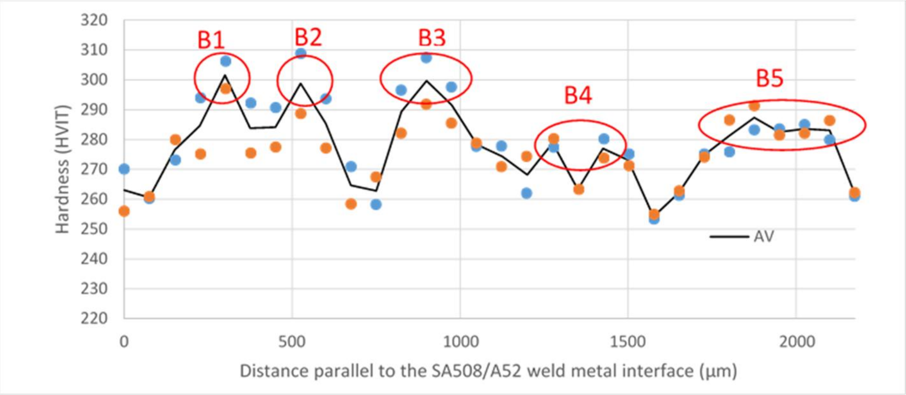

Figure 8. Hardness profile corresponding to the matrix of indentations of Fig. 7, with the zones B1 to B5 of the dark bands.

Figure 9 shows the EBSD maps which were measured in order to study the progressive grain refining in NIWEL 5000 h from 2500 to 300 µm distances from the interface, and grain coarsening near the fusion boundary. The grain size in the LAS changes from about 2.5 µm in the base material to about 1.5 µm in the grain-refined zone and back to 2.5 µm in the CDZ. No significant changes in the grain size due to thermal ageing was visible when comparing the as-received and aged NIWEL DMW mock-up samples. In addition, no changes in carbide precipitation were observed upon thermal ageing, as seen in Figure 10, showing a comparison of the precipitates in NIWEL AR and NIWEL 10000 h at increasing distances from the fusion boundary. As seen in Figure 11, the hardness profile across the LAS HAZ is clearly affected by the grain size. Since the thermal ageing at 400 °C for 10000 h does not affect the grain size or carbide precipitation, it is understandable that there are no changes in the hardness levels either.

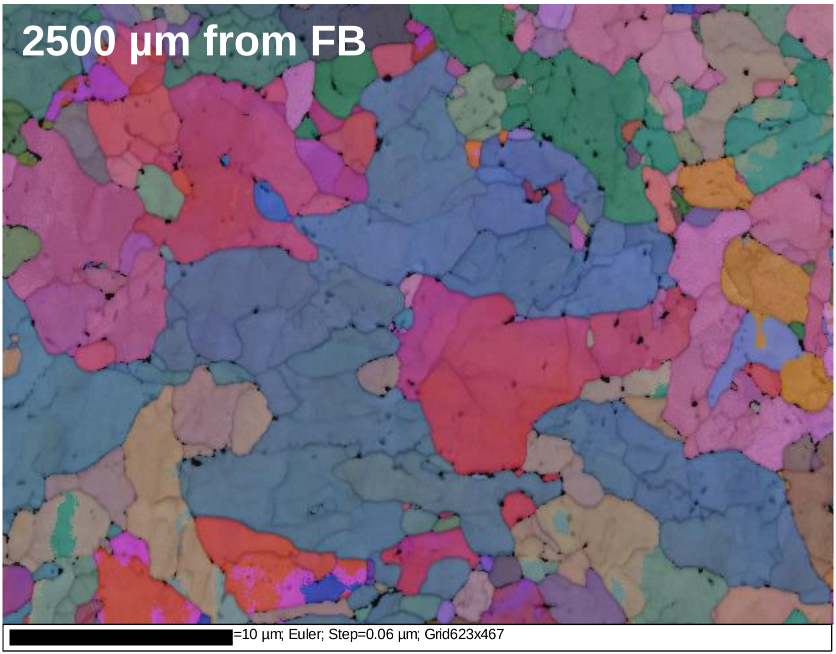
2500 µm from FB
=10 µm; Euler; Step=0.06 µm; Grid623x467

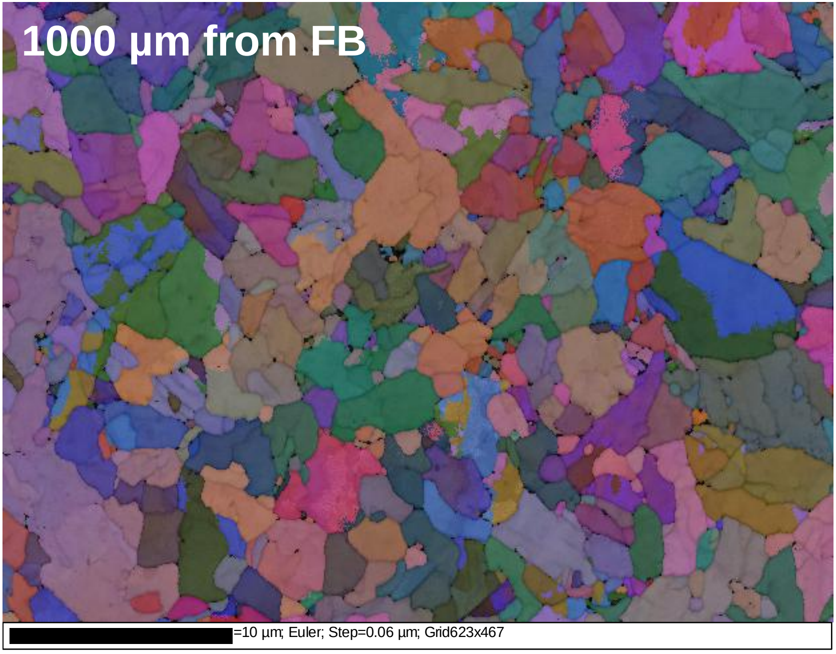
1000 µm from FB
=10 µm; Euler; Step=0.06 µm; Grid623x467

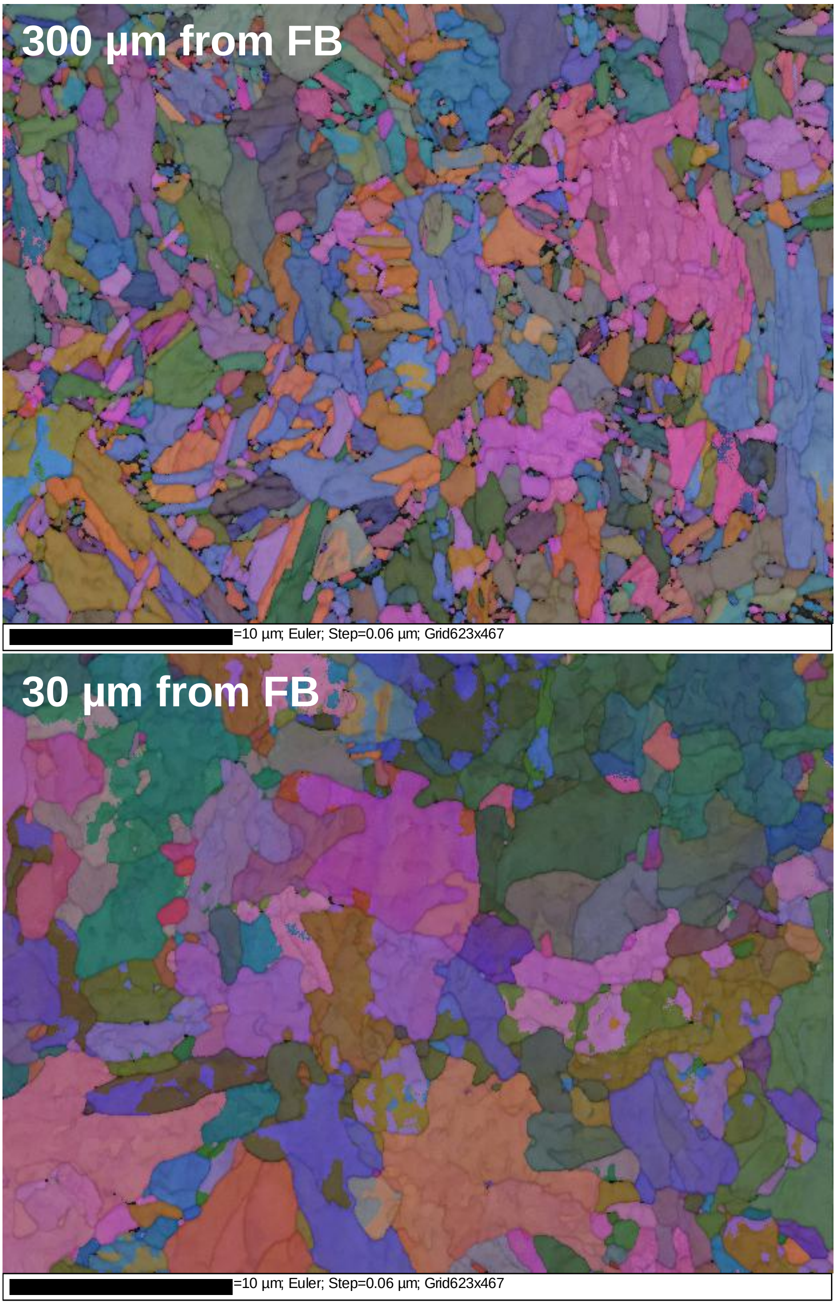

Figure 9. EBSD mapping of the microstructures in the LAS HAZ of the NIWEL 5000 h condition, at different distances from the fusion boundary (FB), images a-d. Progressive grain refining was observed from 2500 to 300 µm distances from the interface, and grain coarsening near the fusion boundary.

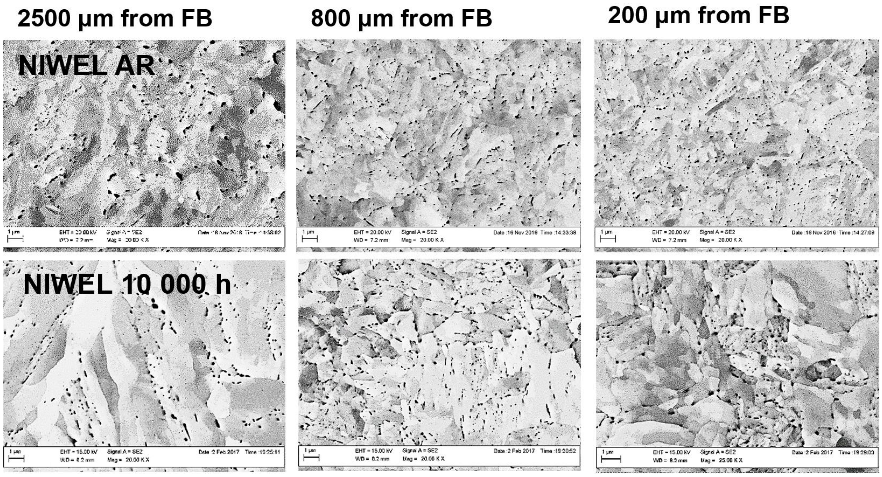

Figure 10. SEM images of the SA 508 HAZ microstructure in the NIWEL AR (above) and NIWEL 10000 h (below) conditions, showing the microstructure at 2500, 800 and 200 µm from the fusion boundary.

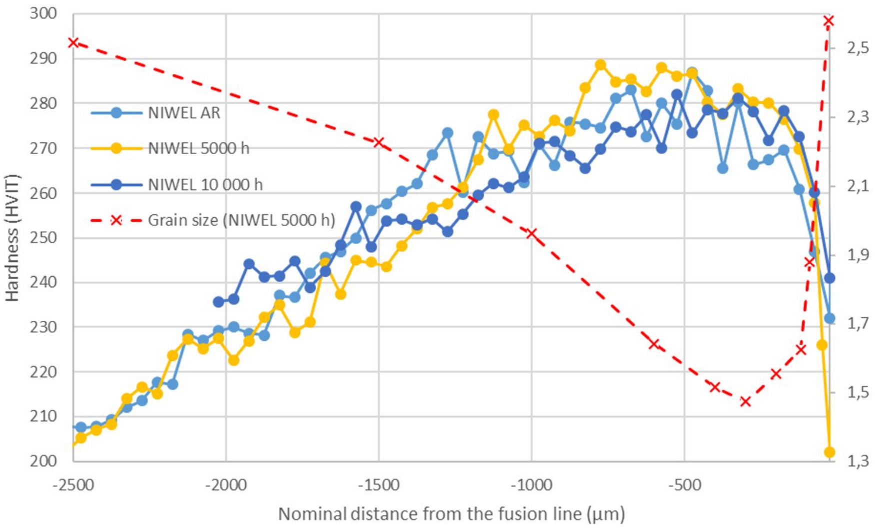

Figure 11. Comparison of the hardness profiles across the LAS HAZ in the NIWEL DMW before and after thermal ageing at 400 °C for 5000 and 10000 h, showing a clear correlation with the grain size profile.

4.1.2 Alloy 52 weld metal

As illustrated in Figure 12, showing GBs in Alloy 52 weld metal before and after thermal ageing for 10000 h at 400 °C, the thermal ageing does not have a visible effect on the microstructure of the weld metal. There is no significant influence of the thermal ageing at 400 °C for up to 10000 h on the microstructure and hardness levels of Alloy 52 weld metal (excluding the fusion boundary region) of the NIWEL DMW mock-up.

Microhardness measurements were carried out with 350 mN load in the Alloy 52 weld metal of the NIWEL DMW before and after ageing at 400 °C for 10000 h. The results are shown in Table 2. The hardness of the weld metal increases from the weld crown (about 240 HV_{IT}) to the weld root (about 270 HV_{IT}), with no observed influence of thermal ageing. Scatter in the results was attributed mostly to the heterogeneous microstructure of the weld metal and the difficulty to make measurements from exactly the same locations.

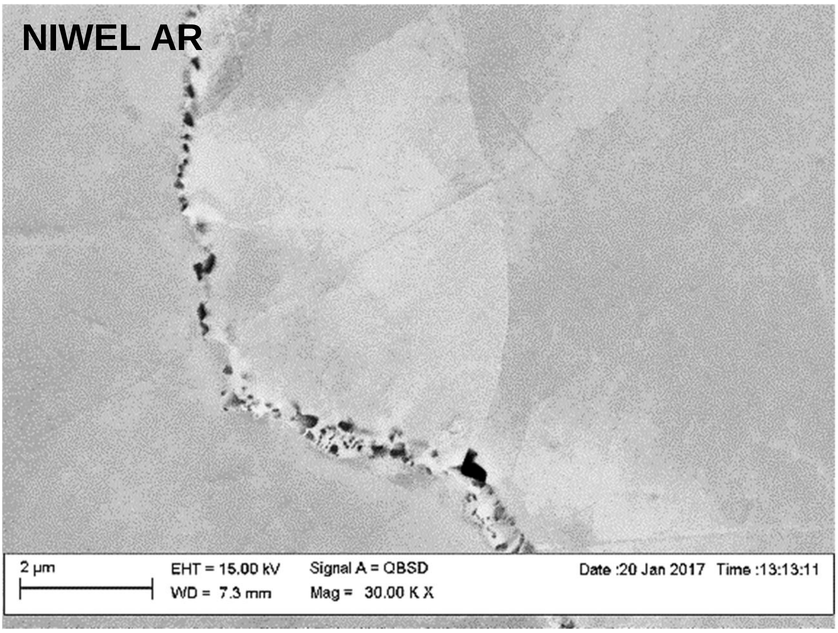

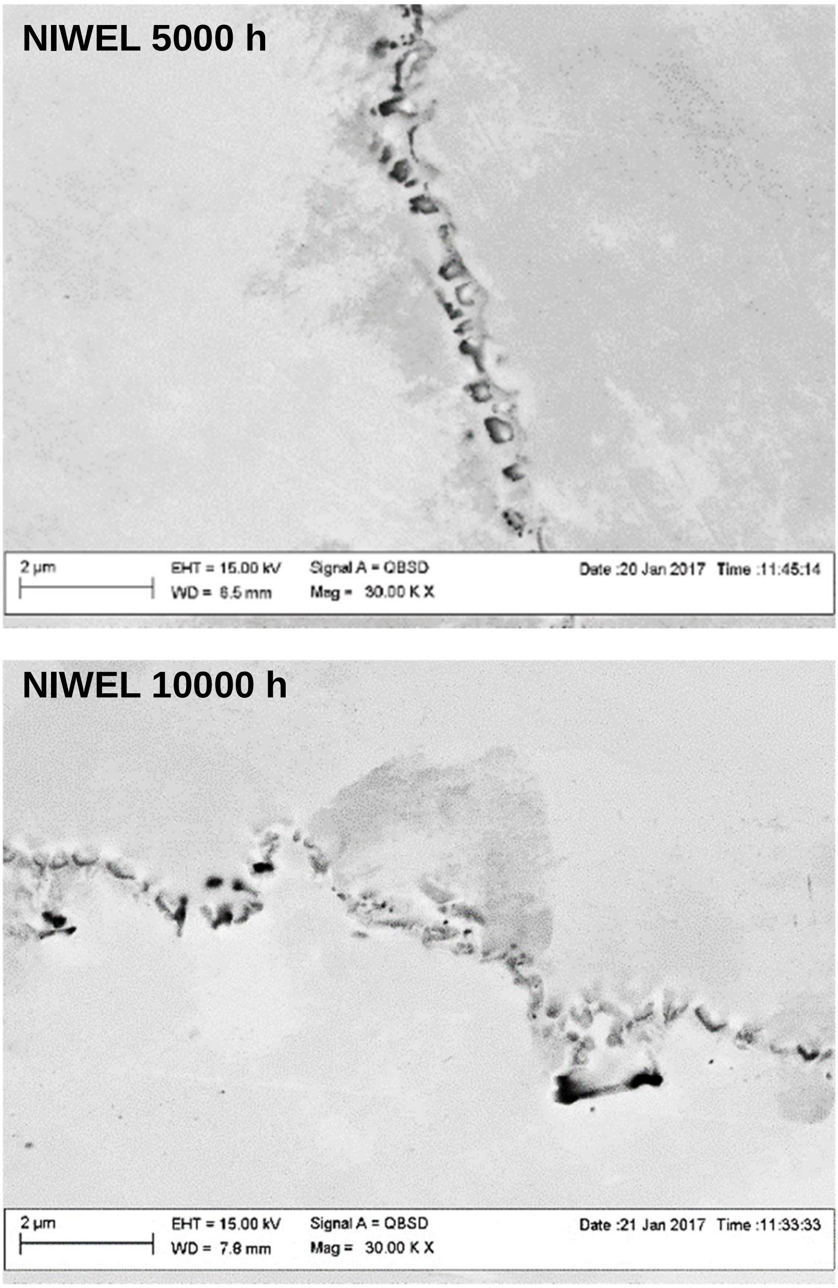

Figure 12. SEM imageing of grain boundaries in Alloy 52 weld metal from the NIWEL mock-up before and after ageing at 400 °C for 5000 and 10000 h. No clear signs of GB carbide growth were observed.

Table 2. Hardness variation in Alloy 52 weld metal in the NIWEL DMW from the weld crown to the weld root, before and after ageing at 400 °C for 5000 and 10000 h.

NIWEL	Crown		Center		Root	
	Mean HV_{IT}	SD	Mean HV_{IT}	SD	Mean HV_{IT}	SD
As-received	232	8	247	14	268	10
5000 h	243	13	249	8	270	15
10000 h	239	15	245	17	257	12

4.1.3 Ferrite/austenite interface

As seen in Figure 13, the fusion boundary changes from a rather straight line into a feathery layer of more than 10 µm wide. This layer consists of a mixture of fine bcc grains from the LAS and fcc structure from the weld metal. It is much harder (about 650 HV_{IT}) than the materials around it (less than 300 HV_{IT} for the LAS or Alloy 52). The evolution of the PMZ layer follows the structure of the weld passes. Starting from a straight fusion boundary, the PMZ grows larger as the weld pass enters the solidified weld metal and is finally swiped into the weld metal to form a swirl of hard bcc structure in the austenitic weld metal. In addition, the Fe content increases when following the weld pass, not only due to the PMZ but also due to the dilution of Fe in the transition zone between two successive weld passes. These characteristics were found in all conditions of the DMWs.

When studying the effect of thermal ageing on the transition zones, it is necessary to understand the prior effect of PWHT. PWHT is a standard procedure to temper welds after the welding process, but the clear side effect is seen in Figure 14, showing the difference in the CDZ width between SINI AW (about 10 µm wide) and SINI PWHT (more than 50 µm wide). The corresponding hardness profiles show the effect of the widening of the CDZ, as hardness decreases more and for a larger distance away from the fusion line due to PWHT. NIWEL AR exhibits the similar condition as SINI PWHT, as the same PWHT was applied for the both mock-ups. As seen in Figure 15, the CDZ about 60-70 µm wide is visible in post-weld heat treated NIWEL AR. However, subsequent thermal ageing for up to 10000 h does appear to influence neither the CDZ width nor the hardness profile (see Figure 15).

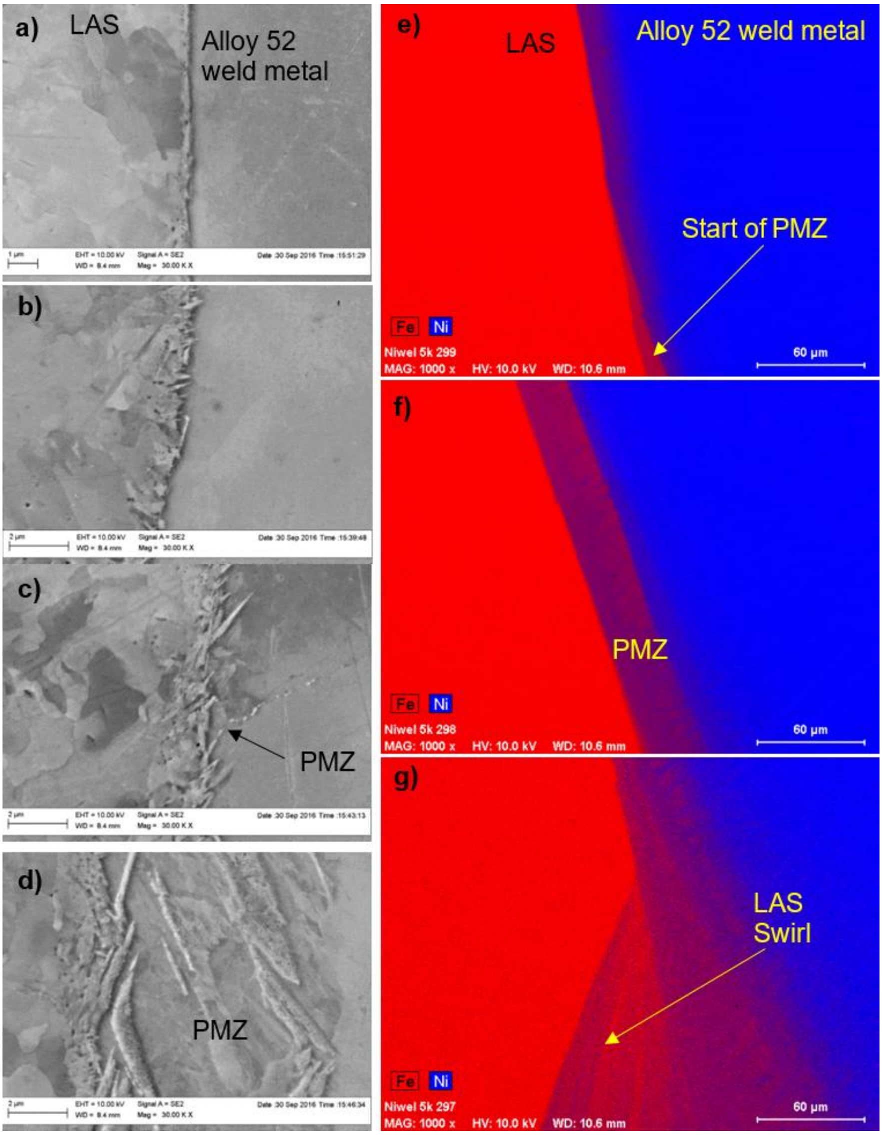

Figure 13. SEM imageing of growth of the PMZ layer from a) a straight fusion line to d) a rather large (about 10 µm) PMZ, and EDS maps showing the increase in Fe dilution into the weld metal from e) the start of PMZ to g) a LAS swirl. The beginning of the weld pass increases the width of the PMZ and the dilution of Fe (red) from the LAS to the Ni-rich (blue) weld metal.

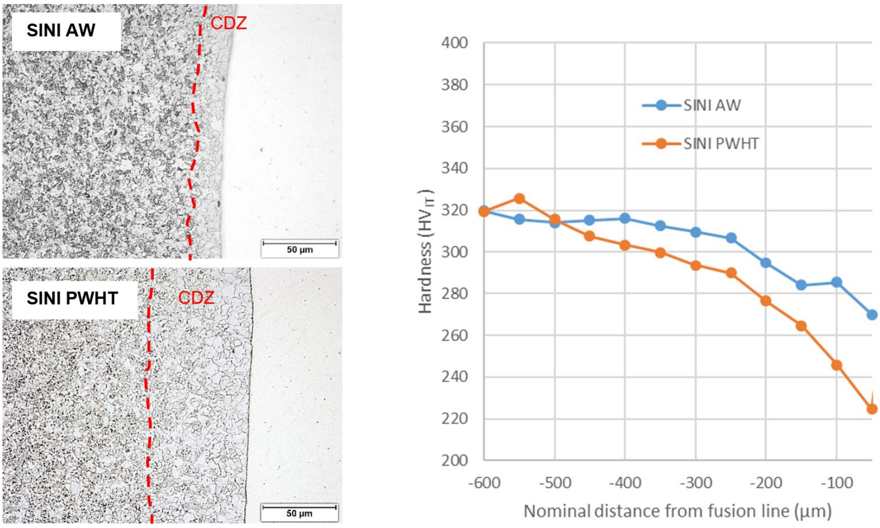

Figure 14. Optical images of the SA 508/Alloy 52 weld metal interface in SINI AW and SINI PWHT, with the corresponding hardness profiles, showing the widening of the CDZ upon PWHT.

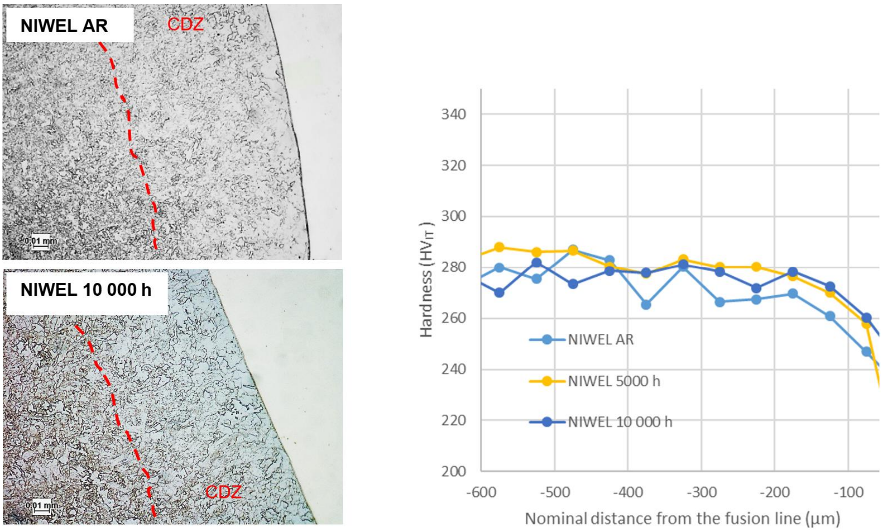

Figure 15. Optical images of the SA 508/Alloy 52 weld metal interface in NIWEL AR and NIWEL 10000 h, with the corresponding hardness profiles, showing the CDZ resulting from PWHT and no influence of thermal ageing.

As seen in Figure 16, the direct effect of the widening of the CDZ upon PWHT is visible in the weld metal side of the interface. A carbon-rich layer forms in Alloy 52 weld metal close to the fusion boundary in SINI PWHT material. As expected, the similar C-rich layer is found in NIWEL AR material. However, as seen in NIWEL 5000 h and NIWEL 10000 h samples, thermal ageing affects so that the carbon-rich layer progressively decreases in intensity and shifts away from the fusion line until it is not visible anymore. In parallel, thermal ageing clearly increases the Fe diffusion from the LAS to the weld metal.

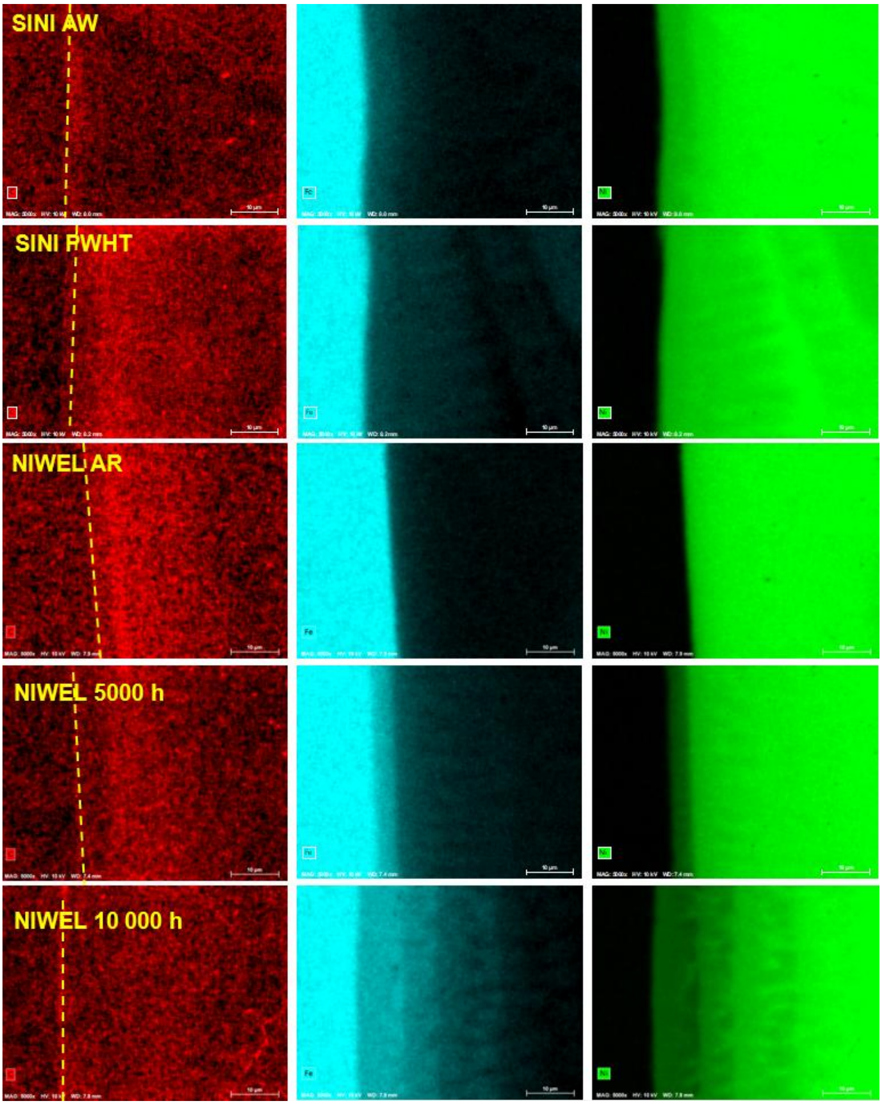

Figure 16. EDS maps over the fusion boundary (highlighted with a yellow line) in all the studied conditions, showing changes in the carbon (left), iron (center) and nickel (right) composition gradients.

Figure 17 shows the microhardness profiles of SINI AR and SINI PWHT. A clear effect of PWHT is observed, as the smooth transition from the LAS to Alloy 52 weld metal in as-welded SINI AW becomes a large hardness mismatch at the fusion boundary after the PWHT, with the lowest hardness in the LAS (220 $\mathrm{HVI_T}$) and a hardness peak in Alloy 52 weld metal adjacent to the fusion line (650 $\mathrm{HV_{IT}}$). The lowest hardness is associated with the CDZ in the LAS side. Due to the narrow width of the transition layers, nanoindentation was used to complement the microhardness results, with a step size of 5 µm, using a pattern. A smaller indentation size enables to obtain measurements with a better spatial resolution and characterize, for example, the width of the hard layers and their position as compared to the fusion boundary more precisely (Mouginot et al. 2014). Figure 18 shows the nanoindentation measurements across the LAS/Alloy 52 weld metal interface before and after PWHT in the SINI DMW. As in the microhardness measurement results, PWHT causes the formation of a hardness peak (840 $\mathrm{HV_{IT}}$) in the weld metal side of the fusion boundary, with the highest hardness levels starting at the fusion boundary and extending about 25 µm into the weld metal. The hardness profile of SINI AW does not show a similar strong mismatch: a hardness peak (667 $\mathrm{HV_{IT}}$) is present at the fusion boundary, where the indentations hit the narrow PMZ (<1 µm), but no hard layer is visible in Alloy 52 weld metal.

Figure 19 shows the microhardness profiles of NIWEL DMW before and after thermal ageing for up to 10000 h at 400 °C. The hardness profile of NIWEL AR is similar to that of SINI PWHT, with a strong hardness mismatch at the interface and a hardness peak in Alloy 52 weld metal close to the fusion boundary. The lowest hardness of NIWEL AR is found in the LAS (220-230 $\mathrm{HV_{IT}}$) and the highest hardness in Alloy 52 weld metal (536 $\mathrm{HV_{IT}}$). Thermal ageing affects the hardness profiles, as the hardness peak in Alloy 52 weld metal decreases upon ageing for 5000 h (377 $\mathrm{HV_{IT}}$) and further decreases upon ageing for 10000 h (331 $\mathrm{HV_{IT}}$). Figure 20 shows the nanoindentation hardness profiles across the interface before and after thermal ageing. In NIWEL AR, a strong hardness peak is present in the weld metal near the interface (858 $\mathrm{HV_{IT}}$) extending over 40 µm before reaching the typical hardness of Alloy 52 weld metal. After 5000 h at 400 °C, the hardness peak in Alloy 52 weld metal decreases (733 $\mathrm{HV_{IT}}$) and the hard layer is also narrower (about 5 µm). In addition, the hard layer is not adjacent to the fusion boundary anymore, but starts about 10 µm away in the weld metal. After 10000 h, the same trend is observed, with the hardness peak in Alloy 52 weld metal further decreasing (637 $\mathrm{HV_{IT}}$) and moving further into the weld metal (maximum hardness value about 20 µm from the FB). The hardness levels in the LAS and Alloy 52 weld metal further away from the fusion boundary are not affected by the thermal ageing.

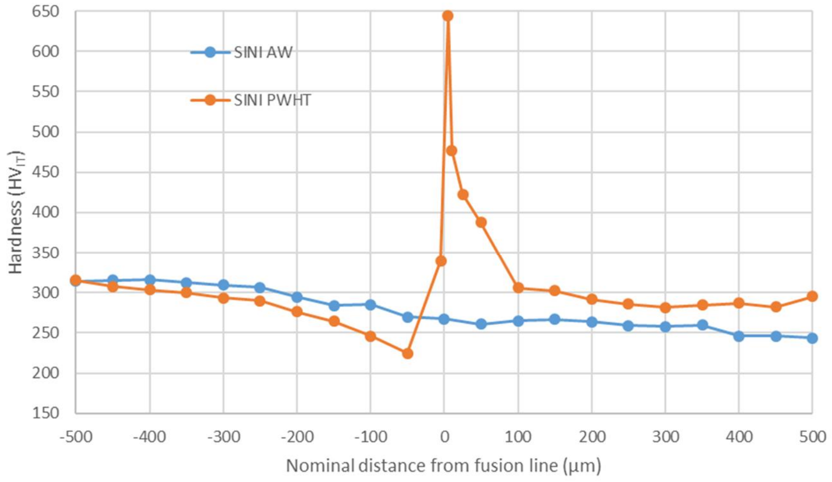

Figure 17. Comparison of the microhardness (350 mN) profiles of SINI AW and SINI PWHT at the LAS/Alloy 52 weld metal interface.

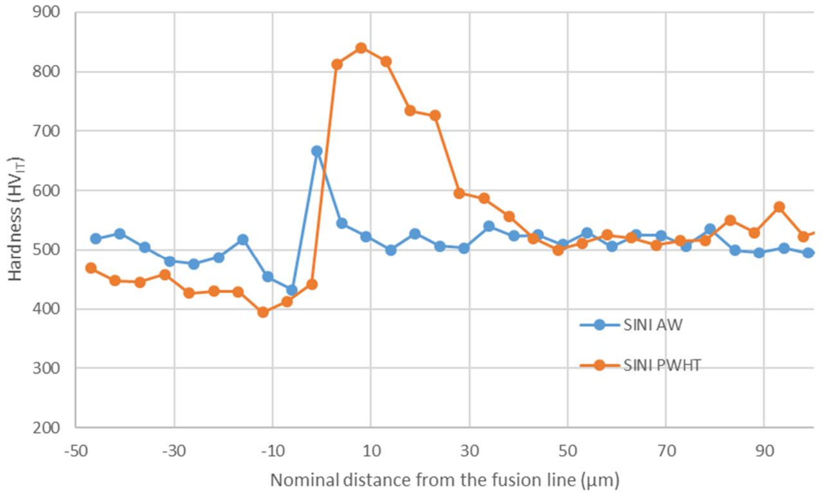

Figure 18. Comparison of the nanoindentation hardness profiles of SINI AW and SINI PWHT at the LAS/Alloy 52 weld metal interface.

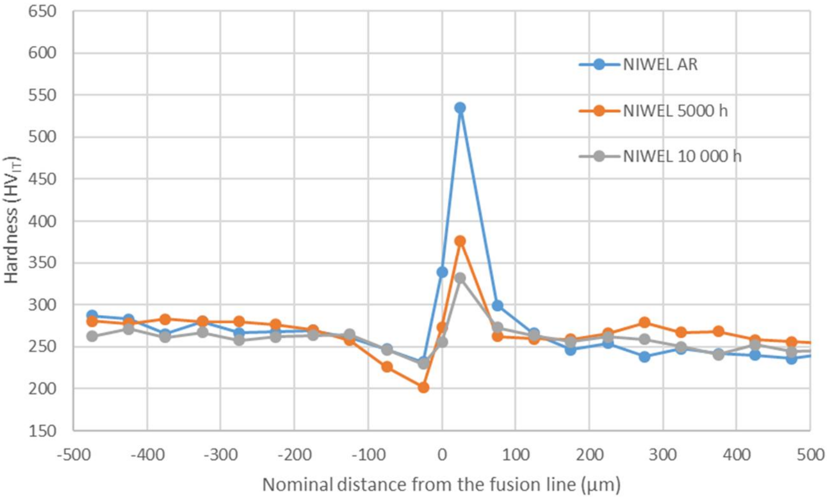

Figure 19. Comparison of the microhardness profiles of NIWEL AR, NIWEL 5000 h and NIWEL 10000 h at the LAS/Alloy 52 weld metal interface.

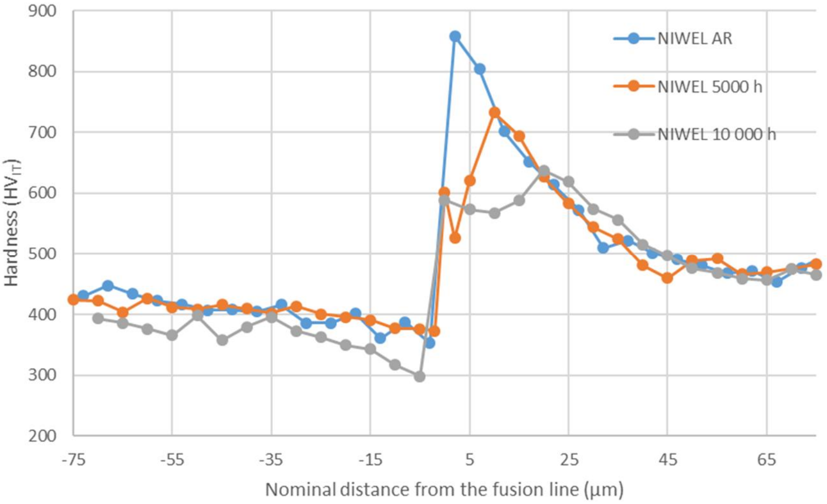

Figure 20. Comparison of the nanoindentation hardness profiles of NIWEL AR, NIWEL 5000 h and NIWEL 10000 h at the LAS/Alloy 52 weld metal interface.

5. Fracture mechanical and mechanical testing

5.1 Materials and methods

5.1.1 Test matrix and specimens

The mechanical test matrix consists of 5*10 (thickness = 5 mm, width = 10 mm, length = 50 mm) single edge-notched bend (SE(B)) specimens (Figure 21) for characterisation of T_0 ductile-to-brittle transition temperature, 1T (thickness = 25 mm, width = 62.5 mm, height = 60 mm) C(T) specimens (Figure 22) for characterisation of J-R curves, standard size 10×10 mm^2 Charpy-V specimens (thickness = 10 mm, width = 10 mm, length = 55 mm) (Figure 23) for characterisation of the ductile-to-brittle transition curve, and 1×2 mm^2 miniature tensile specimens (Figure 22) for characterisation of the strength in the fusion boundary region. The SE(B) and C(T) specimens were side grooved prior to testing.

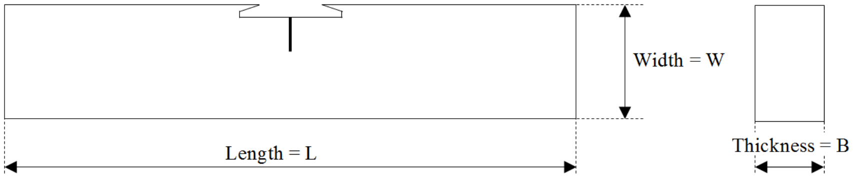

Figure 21. SE(B) specimen used for T_0 determination. W = 10 mm, B = 5 mm, L = 55 mm.

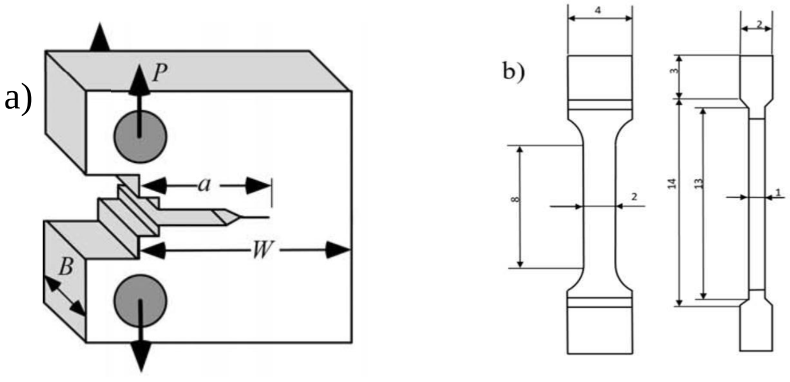

Figure 22. a) C(T) specimen, B = 25 mm, W = 50 mm, a_{notch} = 25 mm, used for obtaining the J-R curves and b) miniature flat bar tensile specimen.

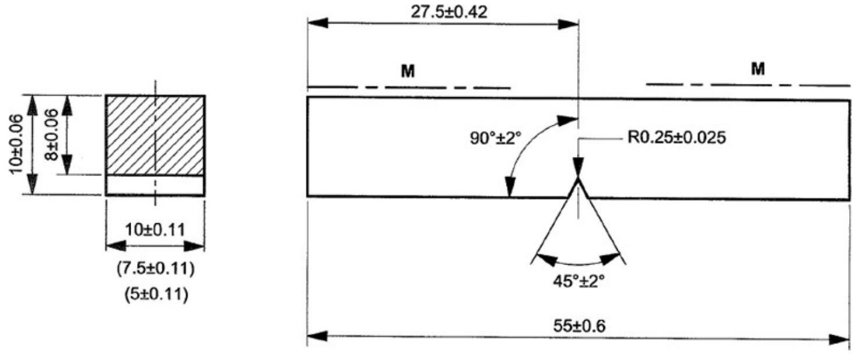

Figure 23. Charpy-V specimen.

The cracks of the C(T) and SE(B) specimens and the notch of the Charpy-V specimens are nominally located in the HAZ of the LAS, 100 µm from the fusion boundary. The cracks are parallel to the fusion boundary. The cracks of the SE(B) specimens for T_0 characterisation and the Charpy-V specimens grow in the T-L direction (transverse - longitudinal), same direction as a through-wall crack. In C(T) specimens, both T-L and T-S orientations (transverse-short, same direction as a surface crack) were used. The tensile specimens are extracted in the transverse direction, so that the gauge length of the specimen contains both weld metal, HAZ, and ferritic base material. The tensile specimens were extracted so that the fusion boundary is at the centre of the specimen.

Table 3 and Table 4 show the test matrix consisting of two parts. The upper part tells the investigated fracture mechanism and the corresponding specimen, measurement type, test temperature and specimen orientation. The lower part gives the material condition and the amount of test specimens used for characterisation of the respective fracture mechanism.

Table 3. Test matrix part 1.

Fracture mechanism	Brittle and ductile transition region	Brittle	Ductile fracture	Ductile fracture	Tensile strength
Measurement type	Impact toughness (EN ISO 148-1)	T_0 (ASTM 1920)	J-R (ASTM E1820)	J-R (ASTM E1820)	ISO 6892-1
Specimen	Charpy V-notch (CVN) 10×10 mm^2	SE(B) 5×10×55 mm^3	CT (B=25 mm)	CT (B=25 mm)	1×2×3 mm^3 flat specimens
Temperature [°C]	Ductile-to-brittle transition region	T_0	300 °C	300 °C	25 °C
Orientation	T-L (Through crack)	T-L (Through crack)	T-L (Through crack)	T-S (Surface crack)	Transverse
Crack location	Fusion boundary	Fusion boundary	Fusion boundary	Fusion boundary	x
Material condition	pc.	pc.	pc.	pc.	pc.
As-received	18	15	6	2	5
5000 h/400 °C	18	15	3	2	5
10000 h/400 °C	18	15	3	2	5

Table 4. Test matrix part 2.

Fracture mechanism	Ductile fracture	Ductile fracture	Ductile fracture
Measurement type	J-R (ASTM E1820)	J-R (ASTM E1820)	J-R (ASTM E1820)
Specimen	CT (B=25 mm)	CT (B=25 mm)	CT (B=25 mm)
Temperature [°C]	300 °C	300 °C	25 °C
Orientation	T-L (Through crack)	T-L (Through crack)	T-L (Through crack)
Crack location	Alloy 52	SA 508	Fusion boundary
Material condition	pc.	pc.	pc.
As-received	1	1	1

5.1.2 Extraction of the specimens

The specimens were manufactured by cutting several thinner slices from the DMW pipe mock-up (Figure 24) with an electro-discharge wire cutter (EDWC). The thickness of the slice depends on the thickness of the specimen. The location of the notch relative to the fusion boundary was marked on the slice through a magnifying glass. The marked location was the starting point for the EDWC. Figure 25 shows the extraction locations of the specimens. The dashed areas describe the area that is covered by the starter notch and fatigue pre-crack.

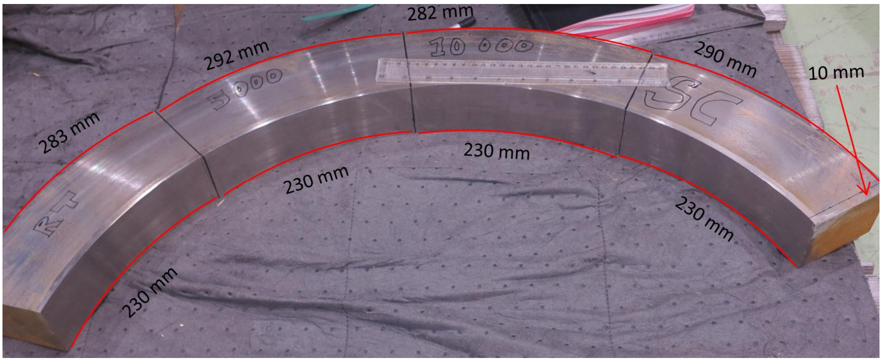

Figure 24. The mock-up was cut into four sections for characterisation of the as-received, 5000 h and 10000 h aged conditions. The ageing was performed at 400 °C.

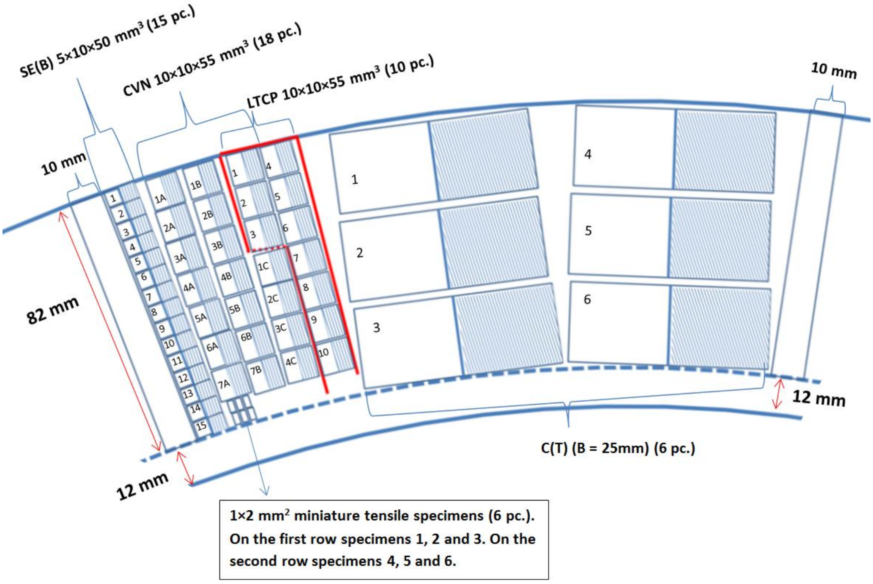

Figure 25. Extraction of the test specimens from the mock-up. No specimens were extracted from the inner surface including the cladding.

5.2 J-R testing according to ASTM E1820

The C(T) specimens extracted from the narrow-gap DMW mock-up were prepared and analysed according to ASTM E1820–13 (ASTM E1820-15 2015). The specimens were fatigue pre-cracked using a resonant testing machine with load ratio R = 0.1 and the maximum stress intensity factor was less than 21 MPa√m. The target ratio between the initial crack length and specimen width (a_0/W ratio) was 0.55-0.60.

In the tearing resistance measurements of the pre-cracked C(T) specimens unloading compliance method was applied. During the measurements the applied load and the crack mouth opening displacement (CMOD) were measured. The specimens were loaded in a 100 kN universal servo-hydraulic testing machine and CMOD was measured with a displacement gauge, with a measurement range of 12 mm. The CMOD increment for consecutive unloading compliance measurements was 0.13 mm. The dwell time before the unloading was 20 s, and no hysteresis during the unloading sequence was observed. The loading rate was 1.3 kN/s.

After the testing, the specimens were heat tinted and broken in liquid nitrogen into two halves to measure the initial and final crack length. The initial and final crack length were measured by using a measuring microscope. The initial and final crack lengths were determined according to the measurement technique from ASTM E1820. The measured crack length was used to validate the calculated crack size derived from the unloading compliance.

The J-R curves were calculated based on the load and CMOD, and compliance data according to Annex A1 of ASTM E1820–13. In compliance calculations, all points belonging to the linear load decrease and increase were used. The J-R curves were analysed according to Annex A8 and A9, with two exceptions. Firstly, the blunting line was determined by fitting a linear equation to the data in the blunting stage. Secondly, the J-R curves were shifted, so that the curves align with the blunting line going through the origin. After these modifications, the tearing resistance data between 0.15 and 1.5 mm offset lines was used to fit a power law relationship Equation (2):

$$J = J_{1mm} \times \Delta a^{m} \tag{2}$$

where J_{1mm} is the J-integral at 1 mm of crack extension, Δa is crack extension. In the J-R curve calculations the elastic modulus and Poisson's ratio were assumed to be 205 GPa and 0.3, respectively.

5.3 T_0 testing according to ASTM E1921

Fracture toughness testing was performed according to ASTM E1921-15 "Standard Test Method for Determination of Reference Temperature, T_0, for Ferritic Steels in the Transition Range" (ASTM E1921-15 2015). Before testing, the specimens were fatigue pre-cracked to the initial crack length over specimen width ratio, a_0/W, of 0.5, using RUMUL resonant testing machine. In the end of fatigue pre-cracking, the maximum value of applied stress intensity factor, K_{max}, was kept below 15 MPa√m. The fracture toughness tests were performed using MTS universal servo-hydraulic testing machine equipped with a 10 kN load cell. The maximum force varied between 1.7 - 2.9 kN. The crack mouth opening displacement (CMOD) was measured using Epsilon 3541-003M-040M-LHT clip cage, with a measurement range of -1/+4 mm.

During testing, the load, CMOD and temperature were recorded. The loading rate was in the quasi-static range, 0.3-0.6 MPa√m/s. The CMOD-load curve was used to calculate the fracture toughness, J_C or K_{Jc}, as described in the ASTM E1921.

After the measurements, the specimens were broken in liquid nitrogen into two halves to measure the crack lengths corresponding to the load instability moment and the possible ductile crack growth. The crack length was determined according to ASTM E1921. The quality of the K_{Jc} data was checked before calculation of T_0.

Since the fusion boundary region is inhomogeneous, the SINTAP and random inhomogeneity Master Curve analyses (Wallin et al. 2004) were performed. These advanced methods account for randomly distributed macroscopic inhomogeneities in the material.

5.4 Charpy-V testing

5.4.1 Specimen preparation and measurement

The notch location was checked for each Charpy-V specimen before testing. One side of each specimen was grinded with 1200 grit emery paper. After that the specimens were polished with DiaPro Mol 3 diamond suspension and MD-Mol polishing surface. The grinding and polishing machine was Struers LaboPol-21. Etax Ba technical ethanol was used to wet the polishing surface at first and to clean the specimens after polishing. The specimens were etched with 10% nital which includes 10% HNO_3 and 90% Etax Ba technical ethanol. Etching time was 5 s per specimen. Oxide layers were removed with hydrochloric acid which included 50% HCl, 50% H_2O and $C_6H_{12}N_4$. V-notches were photographed with Leica MZ12 stereo microscope and Leica DFC420 camera. Overview reprography images were taken with Olympus E-30 camera.

The specimens were also inspected visually before testing. The following specimen dimensions were measured: transverse dimensions (b and w) and specimen length (l), ligament size, radius of curvature of the notch base (from photographs) and the angle of V-notch (from photographs). The transverse dimensions were used for scaling the photographs of the fracture surfaces when measuring the percentage of ductile fracture area. The ligament size was measured from the notch bottom to the back face with a dial gauge. The notch base radius and angle of each specimen were measured optically with a mock-up, Figure 26. According to the measurements all dimensions are within the tolerances specified in EN ISO 148-3:2009 standard. No defects were observed in the specimens. Dimensions were measured with Mahr MarCal 16EW caliper, Heidenhain VRZ 404 and Leica MZ12 stereo microscope and Leica DFC420 camera.

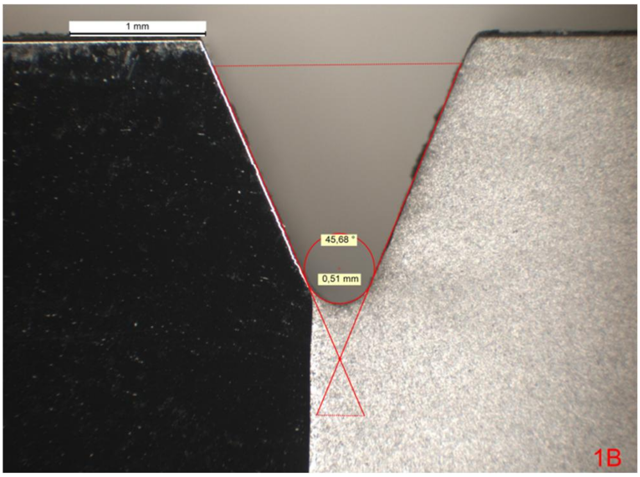

Figure 26. Measurement of notch root radius and angle.

5.4.2 Test and analysis methods

The testing was performed with an instrumented impact pendulum, PSW300, with the nominal impact energy of 300 J and the impact velocity of 5.4 m/s according to EN ISO 148-1. The pendulum is equipped with a digital angle encoder having the angle counting resolution of 160 000 pulses / 360 degrees. An ISO/DIN geometry impact striker (2 mm striker) was used in the pendulum and a static load calibration of the striker was performed before testing, following the yearly calibration programme of the striker. The loss of free swing is 0.7 J and it remains stable. This value is not subtracted from the measured pendulum energy values. The software is Charpy test program, Version 1.0.17, 27.09.2012. The pictures of fracture surfaces were taken with Nikon Digital Sight DS-Fi1 camera. Fracture appearances were measured with Crack front measurement software, Version 2.1.19, 1.10.2008. Lateral expansions were measured with Heidenhain VRZ 404.

The specimens were cooled or heated in a well-agitated liquid bath using the normal installation for instrumented Charpy testing. Depending on the test temperature either petrol ether (T < -80 °C), ethanol (-80 °C < T < +70 °C) or silicon oil (T > +70°C) was used as the heating or cooling medium. The bath temperature was measured with a calibrated thermocouple and adjusted with a PDI-controller. The bath was heated electrically or cooled by circulating liquid nitrogen through a coil installed in the bath. The bath temperature was continuously monitored and recorded during the cooling and heating phases. The hold time of a specimen at stable temperature was minimum 5 min in liquid bath. Temperatures were measured with Fluke 52 II thermometer and K-type SAB thermocouple.

The specimen was transferred from the tempering bath into the pendulum anvil with pneumatic equipment, which grips the specimen from the V-groove and which was guided to the correct position from the anvil support. The proper location of the impact was checked after each test from the specimen halves by setting the V-groove surfaces side by side and by checking the equality of the anvil marks on specimen front surfaces.

5.4.3 Determination of KV_2, LE and FA

Absorbed energy (KV_2) was calculated from the initial and final pendulum angles measured by the angle encoder and from the pendulum parameters. Lateral expansion (LE) was measured in a stand, where the broken specimen halves are pressed against a common support surface on a position outside the lateral expansion area of the specimen. Care was taken that no specimen damage (collision marks etc.) disturbe the measurement. The percentage of fracture appearance (FA) was measured from the photograph of fracture surface. Specimen transverse dimensions (b and w) were used for scaling the fracture appearance measurements. The difference between the shear (ductile) and brittle type fracture could not always be differentiated clearly by visual observation. In such cases the measured load-deflection curves may be used for guidance.

5.4.4 Analysis of data for transition temperatures

Impact toughness is characterised in terms of the mean KV_2, LE and FA vs. temperature curves estimated from the test data. The curves, X = f(T), were determined by fitting the least squares function of the form:

$$X = 0.5 * [1 + \tanh\left(\frac{T-T_{50}}{C}\right)] \qquad (3)$$

where X_{US} is the upper shelf value for X (KV_2, LE or FA), T is temperature and T_{50} and C are fitting parameters.

The upper shelf value (Equation (3)) used in data analyses (X vs. T -curves) is normally fixed to the average of values showing fully ductile fracture appearance (FA=100%). For the test series analysed here the upper shelf energy (USE) is fixed based only on one or an evaluated upper shelf value. The lower shelf value is assumed to be zero. Load as a function of time is measured by the instrumented striker and the load as a function of deflection is calculated from this data.

The characteristic load points, i.e. the general yield load F_{gy}, the maximum load F_m, the onset of unstable crack propagation F_u and the crack arrest load F_a, were determined from the load-deflection curves. The load signal consists of a quasi-static load signal and a signal due to combined vibration of the striker and the specimen.

5.4.5 Analysis of data for temperature T_{Fa4kN}

The transition criteria based on absorbed energy characterise both crack initiation and propagation, their relative proportion depends on temperature, i.e. the position in the transition range. In the instrumented Charpy test, the load vs. time response is recorded during the test, which produces information not only on the general yielding and initiation of brittle fracture but also on crack arrest after the brittle fracture initiation. The portion of the load vs. time (or deflection) record indicating brittle fracture initiation and arrest can easily be located in the graph from a rapid load drop occurring in the test before the final (ductile) fracture, Figure 27. Utilising this information from tests made at various temperatures it is often possible to construct the mean crack arrest load vs. temperature curve for the material.

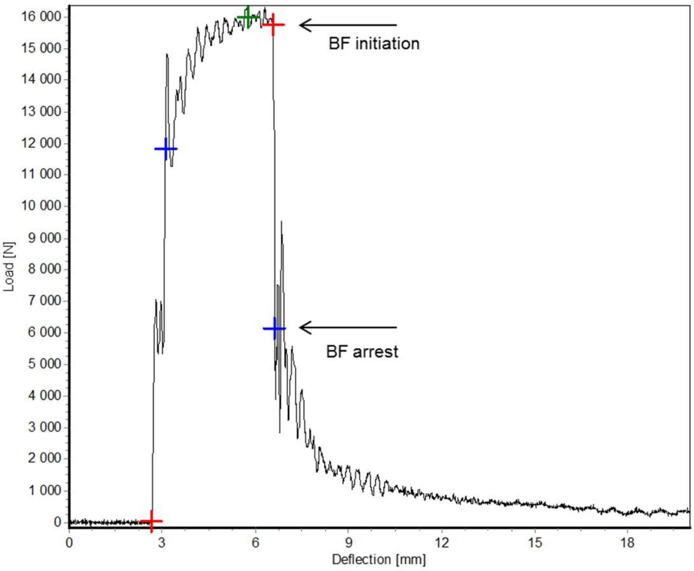

Figure 27. Example of load-deflection graph showing loads of brittle crack initiation and arrest.

For comparing the crack initiation and arrest properties in terms of the fracture toughness transition temperature, T_0, the Charpy transition temperature based on a suitable criterion shall first be converted to the consistent value of T_0 using a correlation, which for the 28 J Charpy -transition temperature, T_{28J}, is as follows (ASTM E1921-13a):

$$T_0 = T_{28J} - 18℃ \tag{4}$$

where T$_0$ (°C) is the temperature corresponding to K$_{Jc}$ (MPa√m) equal to 100 MPa√m.

The comparable crack arrest transition temperature T$_{KIa}$ (100 MPa√m) can be estimated from a correlation found to exist between this temperature and that corresponding to the 4 kN crack arrest load determined by instrumented Charpy tests [Wallin 2011]. The original data base, including irradiated and un-irradiated steels, shows the following correspondence:

$$T_{KIa} = T_{Fa4kN} + 11℃ \tag{5}$$

where T$_{Fa4kN}$ is the temperature corresponding to the mean crack arrest load of 4 kN. Transition temperature T$_{Fa4kN}$ is determined from the least squares fit by Equation (6).

$$F_a = 4\,kN * \exp(\frac{T - T_{Fa4kN}}{A}) \tag{6}$$

where F$_a$ (kN) is crack arrest load, T is temperature and T$_{Fa4kN}$ and A are fitting parameters.

If the specimen has deformed significantly between the load maximum and the onset of unstable crack extension, the load-deflection data may not be valid for crack arrest characterisation. Hence, relevant data points for this purpose were limited to those where

$$\frac{F_u}{F_m} \geq 0.75 \tag{7}$$

where F$_u$ is the load at the onset of unstable crack extension and F$_m$ is the maximum load.

5.5 Tensile testing

The tensile testing was done according to ISO 6892-1 standard ”Metallic Materials. Tensile testing. Part 1: method of test at room temperature”. The tensile testing was performed with MTS universal servo-hydraulic testing machine. The elongation of the tensile specimen during loading was measured with LaVision, an optical strain gauge relying on 3D digital image correlation (DIC). The displacement rate during testing was 0.12 mm/min up to 1 mm of displacement. After that, the displacement rate was 0.8 mm/min.

The specimens were spray painted before tensile testing. First a light layer of white base paint was sprayed. Secondly, drops of black paint were sprayed on the specimen surface to create a distinguishable speckle pattern. The test set-up consisted of two cameras placed at a 20 mm distance from the sample surface, and of two LEDs that provide constant illumination. The used aperture of the camera lenses was 2.5, and the focal length was 50 mm. The imageing frequency was 1 Hz.

Based on the images taken during testing, the DIC software calculates the movements of the speckle patterns. The post-processing software relies on an image-correlation algorithm. The algorithm searches for the maximum correlation in the reference image and deformed image by calculating the average gray-scale intensity over a subset. Based on the pattern movements the displacement of adjacent subsets can be calculated.

The post processing of the images and calculation of strains was performed with the LaVision software. The strains were calculated in the whole gauge section, Figure 28. Virtual strain gauges were placed on the gauge section, Figure 29; one in ferritic base material, one in HAZ, and one in the weld metal. The size of the strain gauge in the ferritic base material was 0.8×0.8 cm^2, the size of the strain gauge in the HAZ was 0.8×0.4 cm^2, and the size of the strain gage in the weld metal was 1.3×1.3 cm^2. The HAZ gauge is the smallest since the variation in strength is largest in the HAZ. The HAZ strain gauge was placed 0.5 mm from the fusion boundary. The weld metal strain gauge is the largest, since the strain can vary locally in the weld metal.

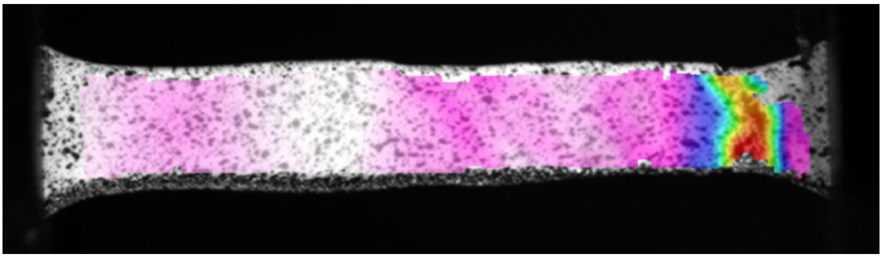

Figure 28. LaVision enables measurement of the strains in the different regions (HAZ, weld metal and base material) of tensile specimens extracted in the transverse direction.

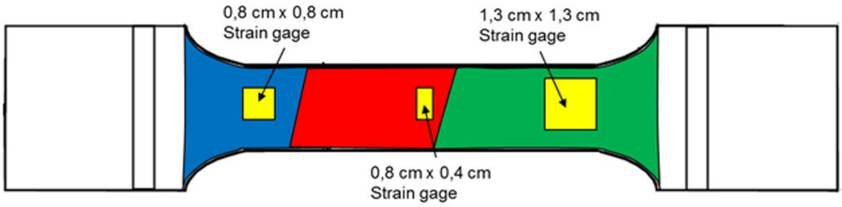

Figure 29. Virtual strain gauges were placed on the specimen to obtain the stress-strain curves for the HAZ, SA 508, and Alloy 52.

From the obtained engineering strains of the different regions, the true stress and LN strain was calculated based on Equations (8) and (11).

$$\varepsilon_{eng} = \frac{\Delta l}{l_0} \tag{8}$$

$$\sigma_{eng} = \frac{F}{A_0} \tag{9}$$

$$\varepsilon_{True} = \ln(1 + \varepsilon_{eng}) \tag{10}$$

$$\sigma_{True} = \sigma_{eng} \cdot (1 + \varepsilon_{eng}) \tag{11}$$

Equations (10) and (11) are only valid until the onset of necking, because the equations are based on constant volume and homogeneous distribution of strain along the gauge length. This simplification is adequate for the analysis done here, since only the yield strengths of the different regions are analyzed.

5.6 Results

5.6.1 J-R curves

The fracture mechanism in the J-R tests at 300 °C is ductile fracture. The J-R curves are increasing, the tearing resistance increases as the crack grows. The length of the crack growth is 5 to 8 mm. The J-R curves presented in Figure 30 to 29 show that the SA 508/Alloy 52 fusion boundary of the DMW is tough. The obtained J_Q values for the different conditions range between 220-530 kJ/m^2, and the obtained J_{1mm} values range between 398-652 kJ/m^2. The J_Q and J_{1mm} values were determined from a power line fit done to the J-R curve data between 0.15 and 1.5 mm exclusion lines. Tables 5 to 7 show the J_Q/J_{Ic}, J_{1mm}, m, M and a_0/W for each specimen and material condition.

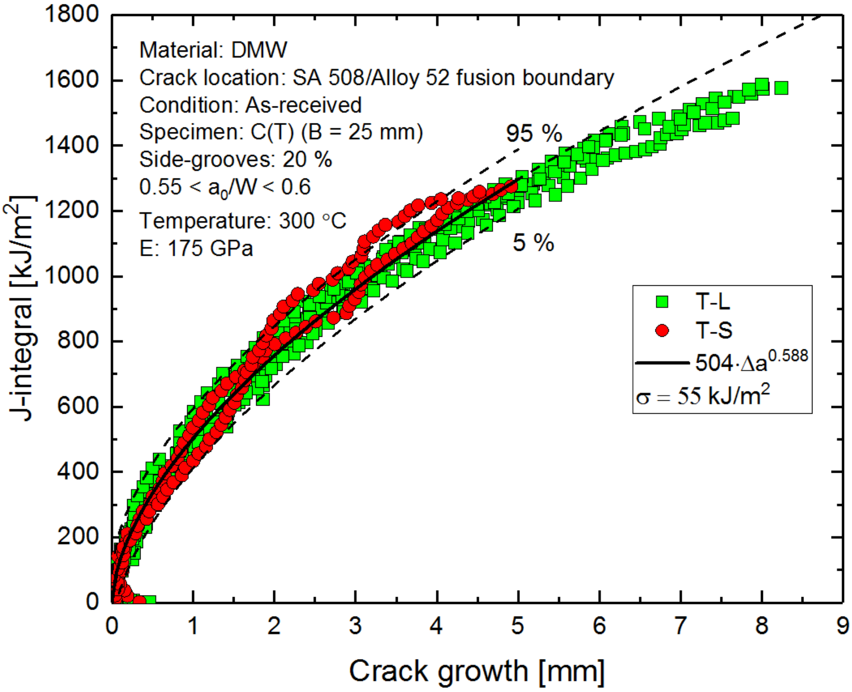

Figure 30. The J-R curves for the as-received condition.

A common J-R curve fit was determined for each condition based on the data between the 0.15 mm and 1.5 mm exclusion lines, Table 8. The 90 % confidence interval was determined for each condition. The standard deviation is largest for the material aged for 5000 h, 77 kJ/m^2. For the as-received condition and the 10000 h aged condition the standard deviation is 55 and 37 kJ/m^2, respectively.

Table 5. The parameters obtained from the J-R curve analyses for the as-received condition.

Crack location	Specimen ID	Temperature (crack orientation)	$J = J_{1mm} \times \Delta a^m$			$J = M \times \sigma_Y \times \Delta a$	a_0/W
		°C	J_{1mm} [kJ/m^2]	m	J_Q/J_{Ic} [kJ/m^2]	M	
Fusion boundary	AS 1	300 (T-L)	479	0.609	297	2	0.56
Fusion boundary	AS 2	300 (T-L)	520	0.653	321	2	0.56
Fusion boundary	AS 3	300 (T-L)	515	0.612	330	2	0.55
Fusion boundary	AS 4	300 (T-L)	484	0.544	325	2	0.56
Fusion boundary	AS 5	300 (T-L)	469	0.648	274	2	0.56
Fusion boundary	AS 6	300 (T-L)	574	0.542	420	2	0.55
In HAZ of SA 508, 0.577 mm from fusion boundary	AS 7	300 (T-S)	518	0.660	315	2	0.59
In HAZ of SA 508, 0.391 mm from fusion boundary	AS 8	300 (T-S)	463	0.802	216	2	0.59
In Alloy 52, 1.14 mm from fusion boundary	AS 9	300 (T-L)	891	0.767	836	2	0.56
In HAZ of SA 508, 1.658 mm from fusion boundary	AS 10	300 (T-L)	809	0.461	851	1.6	0.58
Fusion boundary	AS 11	25 (T-L)	602	0.653	408	2	0.60

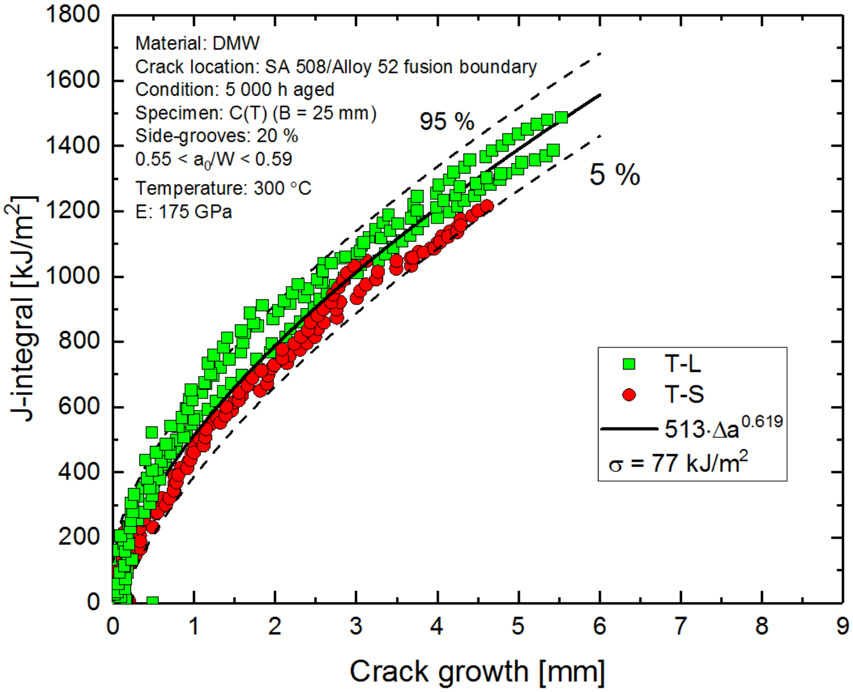

Figure 31. The J-R curves for the 5000 h aged condition.

Table 6. The parameters obtained from the J-R curve analyses for the 5000 h aged condition.

Crack location	Specimen ID	Temperature (crack orientation)	$J = J_{1mm} \times \Delta a^m$			$J = M \times \sigma_Y \times \Delta a$	a_0/W
		°C	J_{1mm} [kJ/m^2]	m	J_Q [kJ/m^2]	M	
In HAZ of SA 508, 0.14 mm from fusion boundary	5000 1	300 (T-S)	452	0.676	249	2	0.58
In HAZ of SA 508, 0.27 mm from fusion boundary	5000 2	300 (T-S)	444	0.685	239	2	0.59
In HAZ of SA 508, 0.47 mm from fusion boundary	5000 3	300 (T-L)	541	0.534	386	2	0.56
In HAZ of SA 508, 0.78 mm from fusion boundary	5000 4	300 (T-L)	583	0.646	389	2	0.56
In HAZ of SA 508, 0.72 mm from fusion boundary	5000 5	300 (T-L)	652	0.492	530	2	0.55

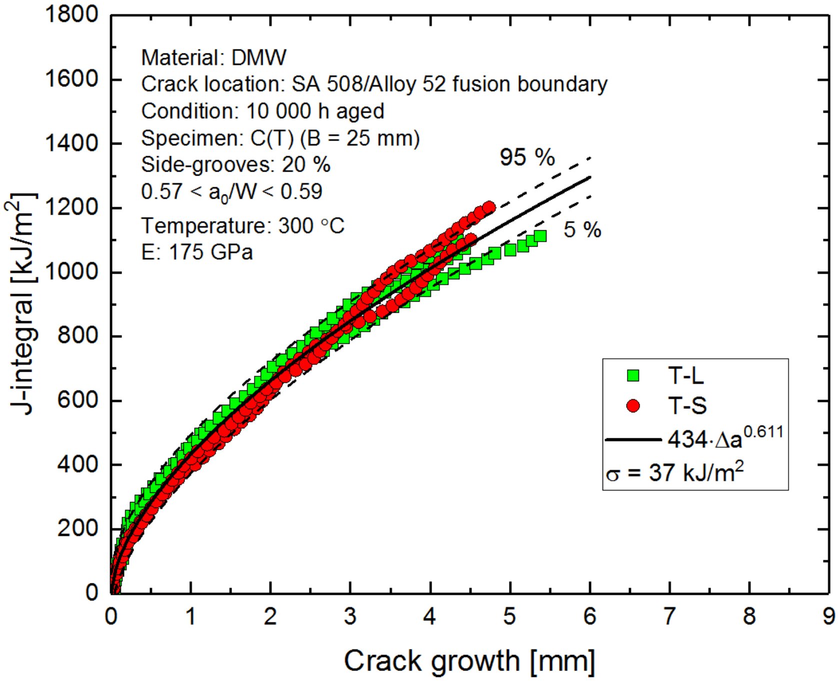

Figure 32. The J-R curves for the 10000 h aged condition.

Table 7. The parameters obtained from the J-R curve analyses for the 10000 h aged condition.

Crack location	Specimen ID	Temperature (crack orientation)	$J = J_{1mm} \times \Delta a^m$			$J = M \times \sigma_Y \times \Delta a$	a_0/W
		°C	J_{1mm} [kJ/m^2]	m	J_Q [kJ/m^2]	M	
In HAZ of SA 508, 0.12 mm from fusion boundary	10000 1	300 (T-S)	398	0.602	227	2	0.59
In HAZ of SA 508, 0.15 mm from fusion boundary	10000 2	300 (T-S)	409	0.656	220	2	0.59
In HAZ of SA 508, 0.34 mm from fusion boundary	10000 3	300 (T-L)	466	0.530	312	2	0.57
In HAZ of SA 508, 0.17 mm from fusion boundary	10000 4	300 (T-L)	439	0.557	278	2	0.57
In HAZ of SA 508, 0.39 mm from fusion boundary	10000 5	300 (T-L)	462	0.564	297	2	0.57

The J-R curves of the different conditions were obtained with specimens with cracks less than 0.8 mm from the fusion boundary. Figure 33 shows that the lowest J-R curves are obtained close to the fusion boundary. Significantly higher J-R curves are obtained with specimens with a crack over 1 mm from the fusion boundary, either in SA 508 or Alloy 52.

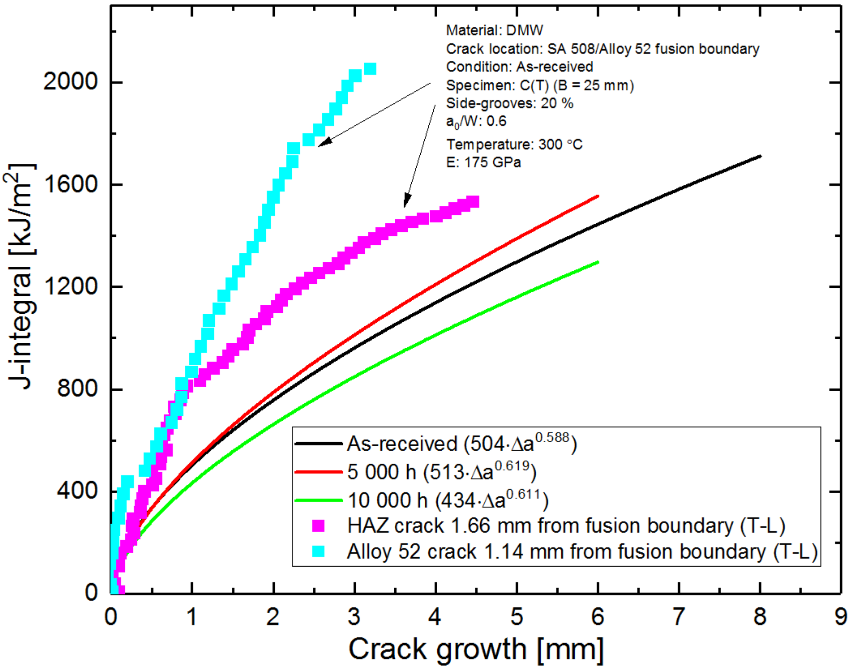

Figure 33. The tearing resistance of the as-received, 5000 h and 10000 h aged condition at the fusion boundary is compared to the tearing resistance over 1 mm from the fusion boundary.

Table 8. The parameters obtained from the common fit to the J-R curve data of the as-received, 5000 h and 10000 h aged condition.

Condition	Crack location	Tempera-ture	$J = J_{1mm} \times \Delta a^m$			$J = M \times \sigma_Y \times \Delta a$
		°C	J_{1mm} [kJ/m^2]	m	J_Q [kJ/m^2]	M
As-received	Fusion boundary	300	504	0.588	328	2
5000 h	In HAZ of SA 508, 0.14 to 0.72 mm from fusion boundary	300	513	0.619	326	2
10000 h	In HAZ of SA 508, 0.12 to 0.38 mm from fusion boundary	300	434	0.611	255	2

5.6.2 Qualification of the data

The quality of the J-R curves was analysed according to the criteria given in ASTM E1820 including criteria for crack straightness, difference between measured and calculated crack length, and the J-R data. The requirement for the straightness of the initial crack front is a_0-a_i < 0.05 B. Figure 34 shows that this requirement is fulfilled for almost all specimens. For two specimens, only one edge point is slightly outside the tolerance bounds.

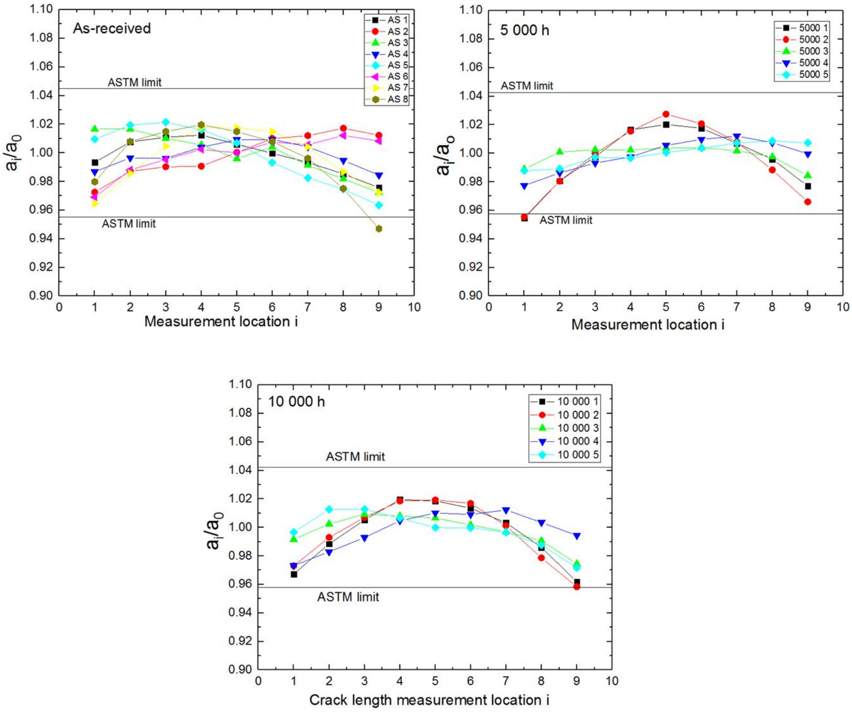

Figure 34. The initial crack front shape of the as-received, 5000 h, 10000 h aged specimens.

The requirement for the straightness of the final crack front is $a_{p(i)}$-a_p < 0.05B. Figure 35 shows that this requirement is not fulfilled for 8 specimens; the edge points are outside the tolerance bounds. The purpose of the criteria is to ensure that the crack does not grow extensively at the center and tunnel through the specimen. The results show that the crack has grown evenly at the center of the specimen.

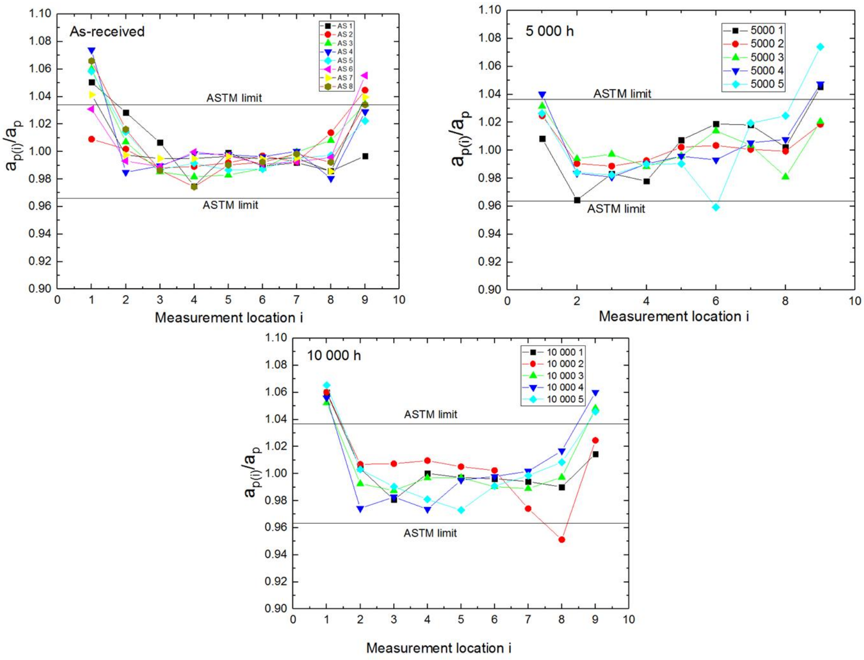

Figure 35. The final crack front shape of the as-received, 5000 h, 10000 h aged specimens.

Figure 36 shows that the differences between measured and predicted initial crack length is within the limits given in ASTM E1820, and a_0-a_{0q} is smaller than 0.5 mm.

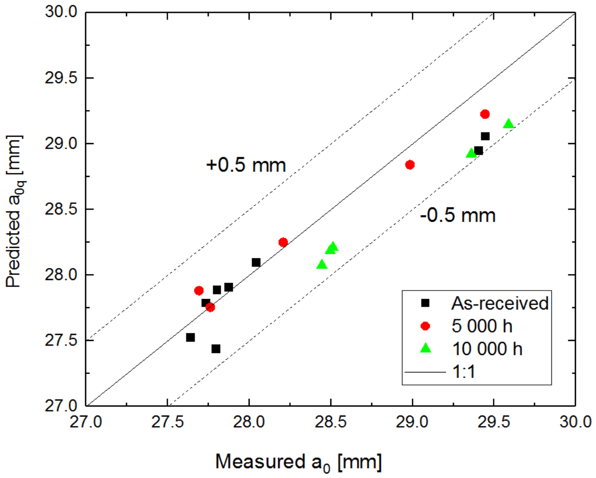

Figure 36. The difference between the initial and the predicted crack length is within the limits given in ASTM E1820.

Figure 37 shows that the difference between measured and predicted crack length is slightly outside the limits given in ASTM E1820 for 6 specimens. In all cases each of the nine crack growth measures, $\Delta a_{p(i)}$, were longer than $0.5{\cdot}\Delta a_p$.

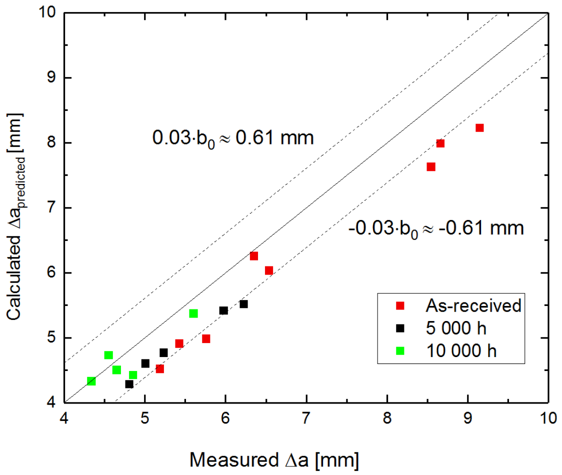

Figure 37. The difference between measured Δa_p and calculated $\Delta a_{predicted}$ shall be smaller than $0.03{\cdot}b_0$ (~ 0.61 mm).

The largest J-integral values of the J-R curves are below the maximum J-integral capacity (~1650 kJ/m^2) for all of the specimens. The maximum crack extension capacity is ~ 5 mm. The crack extension in the J-R curves of the as-received material is longer than the maximum crack extension capacity. The J-R curves extending beyond 5 mm can be affected by the specimen dimensions. The maximum crack extension for the J-R curves of the 5000 h and 10000 h aged material is within the limits of the maximum crack extension capacity.

Tables 10 to 11 show some additional requirements given in E1820. Failure of the requirement is marked in red. In the as-received condition, the difference between the predicted and measured crack length is outside the bounds defined in ASTM E1820 for 6 specimens. For the 5000 h aged material, the correlation coefficient for calculation of calculated a_{0q} is below the limit given in ASTM E1820. However, the measured and calculated initial crack length does not differ significantly from each other, Figure 36. If the criteria in the table and the criteria described above are fulfilled, then the initiation toughness can be determined as J_{Ic}, as is the case for the results of 10000 h aged material.

Table 9. J-R test quality of the as-received specimens.

Specimen ID	AS 1	AS 2	AS 3	AS 4	AS 5	AS 6	AS 7	AS 8	AS 10	AS 11	AS 9
Qualification of data	Measured value	Measured value	Measured value	Measured value	Measured value	Measured value	Measured value	Measured value	Measured value	Measured value	Measured value
The power coefficient is less than 1	0.61	0.65	0.61	0.54	0.65	0.54	0.66	0.80	0.46	0.77	0.65
Difference between a_{oq} and a_0 is smaller than the larger of 0.01W or 0.5 mm	-0.35	0.06	-0.11	0.09	0.04	0.06	-0.45	-0.38	-0.27	-0.34	0.13
The difference between $\Delta a_{predicted}$ and Δa_p is smaller than $0.15\Delta a_p$ for crack extension less than $0.2b_0$ and thereafter smaller than $0.03b_0$	**-0.91**	**-0.91**	**-0.67**	**-0.09**	**-0.50**	**-0.77**	-0.51	**-0.66**	**-0.73**	-0.23	-0.06
The number of data available to calculate a_{0q} is larger than 7	15	17	17	17	18	25	23	19	28	24	20
Number of data between $0.4J_Q$ and J_Q is larger than 2	TRUE	TRUE	TRUE	TRUE	TRUE	TRUE	TRUE	TRUE	TRUE	TRUE	TRUE
The correlation coefficient of the least square fit is greater than 0.96	**0.76**	0.98	0.96	0.98	0.97	**0.93**	**0.93**	0.96	0.98	0.99	1.00
The number of data between exclusion lines 0.15 and 0.5 is larger than zero	TRUE	TRUE	TRUE	TRUE	TRUE	TRUE	4	4	4	4	9
The number of data between exclusion lines 0.5 and 1.5 is larger than zero	TRUE	TRUE	TRUE	TRUE	TRUE	TRUE	4	4	6	4	20
The number of data between Δa_{min} /Δa_{limit} /J_{limit} is larger than 4	TRUE	TRUE	TRUE	TRUE	TRUE	TRUE	8	8	6	4	29
Qualification of J_Q as J_{Ic}											
$B>10*J_Q/\sigma_Y$	5.1	5.5	5.7	5.6	4.7	7.3	5.4	3.7	14.7	14.4	7.0
$b_0>10*J_Q/\sigma_Y$	5.1	5.5	5.7	5.6	4.7	7.3	5.4	3.7	14.7	14.4	7.0
Fulfilment of the above criteria and the crack straightness criteria	J_Q	J_Q	J_Q	J_{Ic}	J_{Ic}	J_Q	J_{Ic}	J_Q	J_Q	J_{Ic}	J_{Ic}

Table 10. J-R test quality of the 5000 h aged specimens.

Specimen ID	5000 1	5000 2	5000 3	5000 4	5000 5
Qualification of data	Measured value	Measured value	Measured value	Measured value	Measured value
The power coefficient is less than 1	0.68	0.69	0.53	0.65	0.49
Difference between a_{oq} and a_0 is smaller than the larger of 0.01W or 0.5 mm	-0.14	-0.22	0.04	0.00	0.19
The difference between $\Delta a_{predicted}$ and Δa_p is smaller than $0.15\Delta a_p$ for crack extension less than $0.2b_0$ and thereafter smaller than $0.03b_0$	-0.39	-0.51	-0.55	**-0.70**	-0.46
The number of data available to calculate a_{0q} is larger than 7	24	25	23	25	24
Number of data between $0.4J_Q$ and J_Q is larger than 2	TRUE	TRUE	TRUE	TRUE	TRUE
The correlation coefficient of the least square fit is greater than 0.96	**0.87**	**0.95**	**0.84**	**0.91**	**0.60**
The number of data between exclusion lines 0.15 and 0.5 is larger than zero	TRUE	TRUE	TRUE	TRUE	TRUE
The number of data between exclusion lines 0.5 and 1.5 is larger than zero	TRUE	TRUE	TRUE	TRUE	TRUE
The number of data between Δa_{min} /Δa_{limit} /J_{limit} is larger than 4	TRUE	TRUE	TRUE	TRUE	TRUE
Qualification of J_Q as J_{Ic}					
$B>10*J_Q/\sigma_Y$	4.3	4.1	6.7	6.7	9.2
$b_0>10*J_Q/\sigma_Y$	4.3	4.1	6.7	6.7	9.2
Fulfilment of the above criteria and the crack straightness criteria	J_Q	J_Q	J_Q	J_Q	J_Q

Table 11. J-R test quality of the 10000 h aged specimens.

Specimen ID	10 000 1	10 000 2	10 000 3	10 000 4	10 000 5
Qualification of data	Measured value	Measured value	Measured value	Measured value	Measured value
The power coefficient is less than 1	0.60	0.66	0.53	0.56	0.56
Difference between a_{oq} and a_0 is smaller than the larger of 0.01W or 0.5 mm	-0.44	-0.44	-0.31	-0.37	-0.30
The difference between $\Delta a_{predicted}$ and Δa_p is smaller than $0.15\Delta a_p$ for crack extension less than $0.2b_0$ and thereafter smaller than $0.03b_0$	-0.14	0.19	-0.42	-0.22	0.00
The number of data available to calculate a_{0q} is larger than 7	23	26	26	21	26
Number of data between $0.4J_Q$ and J_Q is larger than 2	TRUE	TRUE	TRUE	TRUE	TRUE
The correlation coefficient of the least square fit is greater than 0.96	0.998	0.999	0.995	0.998	0.998
The number of data between exclusion lines 0.15 and 0.5 is larger than zero	TRUE	TRUE	TRUE	TRUE	TRUE
The number of data between exclusion lines 0.5 and 1.5 is larger than zero	TRUE	TRUE	TRUE	TRUE	TRUE
The number of data between Δa_{min} /Δa_{limit} /J_{limit} is larger than 4	TRUE	TRUE	TRUE	TRUE	TRUE
Qualification of J_Q as J_{Ic}					
$B>10^*J_Q/\sigma_Y$	3.9	3.8	5.4	4.8	5.1
$b_0>10^*J_Q/\sigma_Y$	3.9	3.8	5.4	4.8	5.1
Fulfilment of the above criteria and the crack straightness criteria	J_{Ic}	J_{Ic}	J_{Ic}	J_{Ic}	J_{Ic}

5.7 T_0 fracture toughness testing

5.7.1 Quality of T_0 data

The criteria in ASTM E1921 determine the K_{Jc} data that can be used for T_0 analyses. The validity criteria include the allowable amount of crack growth, straightness of the fatigue pre-crack front, difference between the calculated and measured initial crack length.

The allowable limit of crack growth before cleavage is for a 5 mm wide ligament 0.25 mm. No significant crack growth was observed on the fracture surfaces of the T_0 specimens. For couple of the specimens, few plastic segments, less than 0.1 mm long, were found along the crack front. The specimens fractured by the brittle fracture mechanism.

For three specimens, the $a_0/W = 0.5$ +/- 0.05 is not fulfilled, but the specimens are included to the T_0 analyses. The largest a_0/W-ratio is 0.56, Figure 38. The calculated and measured initial crack lengths differ less than 5 %, Figure 39.

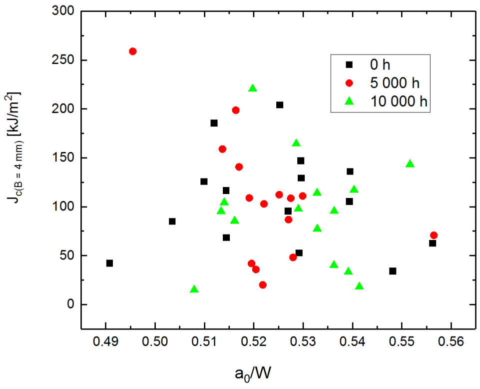

Figure 38. The crack length a_0/W between 0.49 and 0.56 has no remarkable effect on J_C.

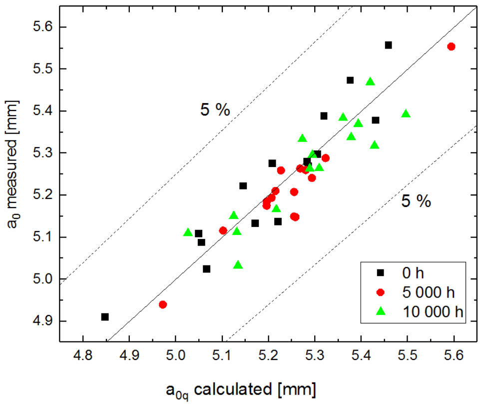

Figure 39. The calculated a_{0q} values differ less than 5 % from the measured a_0.

For 8 specimens the crack straightness criteria, $\max|a_i - a_0| < 0.5$ mm, was not fulfilled. In these cases, the crack grew partially on the weld metal side causing a skewed crack front (Figure 40 and 38). In the T_0 analyses, the specimens that do not fulfil the crack front straightness criteria are discarded. In Figure 41, all the crack fronts with red dots have at least one measurement point (out of 9) that differs more than 0.5 mm from the average crack length a_0.

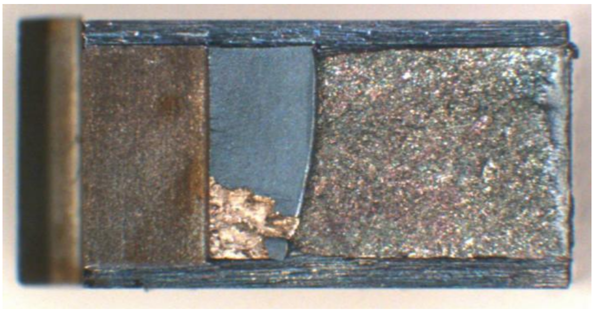

Figure 40. The growth of the fatigue pre-crack is suppressed by the weld metal, thus, the crack front can be skewed.

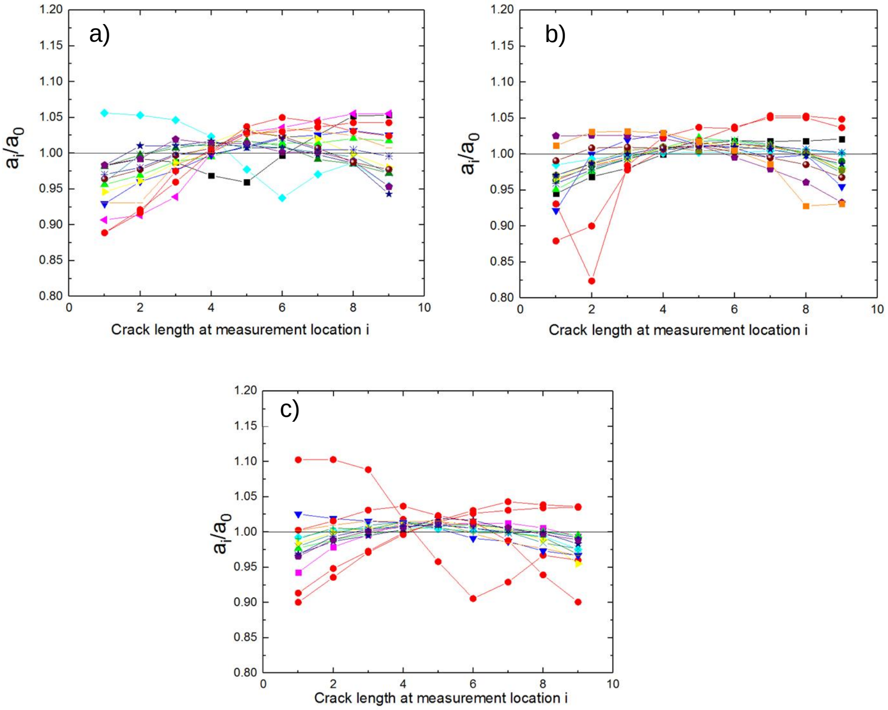

Figure 41. The crack front shape of the T_0 specimens. a) As-received, b) 5000 h aged, and c) 10000 h aged.

5.7.2 T_0 fracture toughness testing results

Figure 42 shows the T_0 results for the three different conditions. In all cases, the specimens fracture by the brittle fracture mechanism. The T_0 is -118 °C for the as-received material, -111 °C for the 5000 h aged material, and -129 °C for the 10000 h aged material. The standard deviation of the T_0 ranges between 6.6 and 7.5 °C. Since the T_0 for the different conditions is within 2σ (~ 95 % confidence interval) and ageing does not appear to have an effect on T_0, a common T_0 value was determined for all K_{Jc} values. The T_0 is then -122 °C.

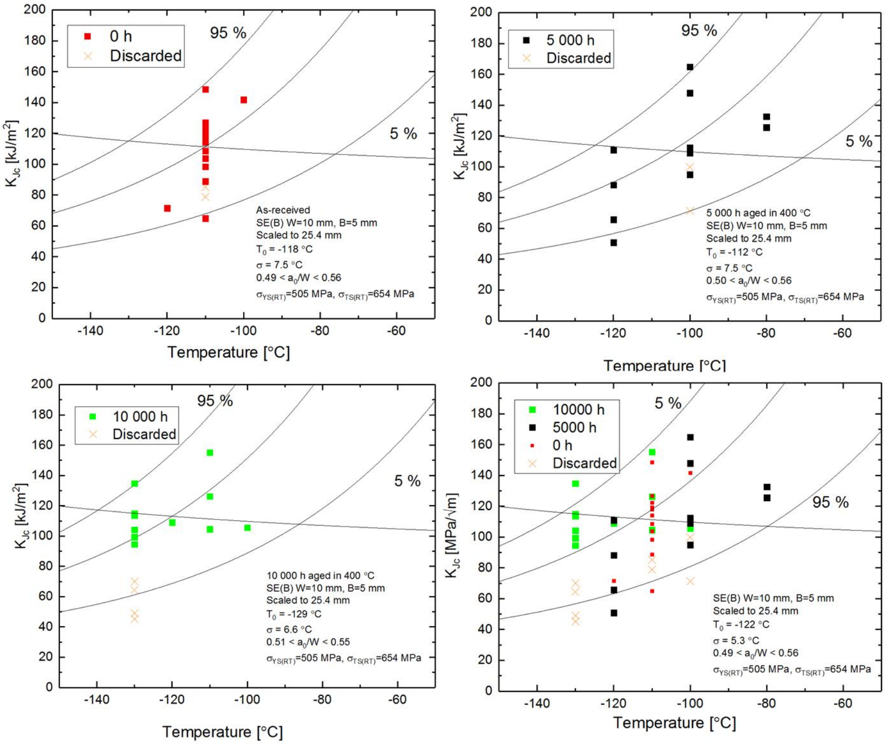

Figure 42. T_0 analyses for as-received, 5000 h and 10000 h aged conditions.

The T_0 values were determined according to the procedure described in ASTM E1921. In the T_0 analysis, the K_{Jc} values above the measuring capacity of the specimen, $K_{Jc(limit)}$, were censored to the $K_{Jc(limit)}$ value and δ was set to 0. The specimens violating the crack front straightness criteria were discarded completely. Table 12 shows the calculated T_0 values. Tables 13-14 show the different K_{Jc} values. The K_{Jc} values were scaled to correspond 25.4 mm thick specimens.

Table 12. The ductile-to-brittle transition temperature T_0 close to the fusion boundary of the Alloy 52 narrow-gap DMW.

Crack location	Average crack location from fusion boundary	Aged at 400 °C for	$K_{Jc(med)}$	The required number of valid K_{Jc} values for a valid T_0	Number of valid specimens	T_0	$T_{0(Sintap)}$
	[mm]		[kJ/m^2]			[°C]	[°C]
HAZ of SA 508	0.02	0 h	110	6	6	-118	-118
HAZ of SA 508	0.03	5000 h	106	6	6	-112	-112
HAZ of SA 508	0.09	10000 h	111	6	8	-129	-129

Table 13. The data for T_0 analyses of the as-received condition.

Tempera-ture	**Measured fracture toughness**	**Fracture toughness limit**	**Thickness corrected fracture toughness**	**Knocker delta**	**a_0/W**
[°C]	**K_{Jc} (5 mm) [MPa√m]**	**$K_{Jc(limit)}$ (5 mm) [MPa√m]**	**K_{Jc} (25mm) [MPa√m]**		
-120	98	160	72	1	0,49
-100	205	155	142	0	0,51
-110	139	157	98	1	0,50
-110	171	157	119	0	0,53
-110	215	157	149	0	0,53
-110	175	157	122	0	0,54
-110	124	157	89	1	0,51
-110	182	157	127	0	0,53
-110	162	157	114	0	0,51
-110	119	157	Crack is not straight	1	0,56
-110	154	157	109	1	0,54
-110	168	157	118	0	0,51
-110	147	157	104	1	0,53
-110	88	157	65	1	0,55
-110	109	157	Crack is not straight	1	0,53

Table 14. The data for T_0 analyses of the 5000 h aged condition.

Tempera-ture	**Measured fracture toughness**	**Fracture toughness**	**Thickness corrected fracture toughness**	**Knocker delta**	**a_0/W**
[°C]	**K_{Jc} (5 mm) [MPa√m]**	**$K_{Jc(limit)}$ (5 mm) [MPa√m]**	**K_{Jc} (25mm) [MPa√m]**		
-120	122	160	88	1	0,53
-80	189	151	133	0	0,51
-80	179	151	125	0	0,52
-100	133	155	95	1	0,56
-100	238	155	165	0	0,50
-100	142	155	Crack is not straight	1	0,53
-100	158	155	112	0	0,52
-100	154	155	109	1	0,52
-100	212	155	148	0	0,52
-120	156	160	111	1	0,53
-100	159	155	112	0	0,53
-100	96	155	Crack is not straight	1	0,52
-120	89	160	66	1	0,52
-100	159	155	112	0	0,53
-120	66	160	51	1	0,52

Table 15. The data for T_0 analyses of the 10000 h aged condition.

Tempera-ture	**Measured fracture toughness**	**Fracture toughness**	**Thickness corrected fracture toughness**	**Knocker delta**	**a_0/W**
[°C]	**K_{Jc} (5 mm) [MPa√m]**	**$K_{Jc(limit)}$ (5 mm) [MPa√m]**	**K_{Jc} (25mm) [MPa√m]**		
-100	148	155	106	1	0,53
-110	223	157	155	0	0,52
-120	153	160	109	1	0,51
-130	146	163	104	1	0,51
-110	147	157	105	1	0,54
-130	160	163	114	1	0,53
-130	192	163	135	0	0,53
-130	87	163	Crack is not straight	1	0,54
-110	180	157	126	0	0,55
-130	58	163	Crack is not straight	1	0,51
-130	95	163	Crack is not straight	1	0,54
-130	64	163	Crack is not straight	1	0,54
-130	163	163	115	1	0,54
-130	132	163	95	1	0,53
-130	139	163	99	1	0,52

5.7.3 Inhomogeneous Master Curve analyses

Table 16 shows the results of the Master Curve analyses accounting for inhomogeneities. Since the analyses result into the same T_0, the analyses indicate that the data set behaves like a typical macroscopically homogeneous material, even though the crack location relative to the fusion boundary varies between 0 and 0.150 mm. (Wallin et al. 2004)

Table 16. Analyses on the effect of possible inhomogeneities in the material on T_0.

Method	T_0	σ
Standard Master Curve method	-122	5.7
SINTAP	-122	-
Random inhomogeneity analyses	-122	< 1

5.8 Charpy-V impact toughness testing results

5.8.1 Transition curves and temperatures

The specimens with the notch in the HAZ were tested in random order. The derived energy, lateral expansion and fracture appearance based transition curves of as-received, 5000 h and 10000 h aged condition are shown in Figures 43 to 45. The black dots in the figures indicate 100 % ductile fracture. For the as-received condition, specimens 1A, 2A, 4A and 5A were excluded from the analyses. For the 5000 h aged condition, specimens 1, 2, 3, 4, 9, 10 and 16 were excluded from the analyses. The upper shelf of the 5000 h aged condition includes only one fully ductile result. However, the specimen tested at +60 °C has almost 90 % ductility and the absorbed energy is nearly the same as the upper shelf energy. Therefore, it can be concluded that the upper shelf starts at some temperature between these two specimens.

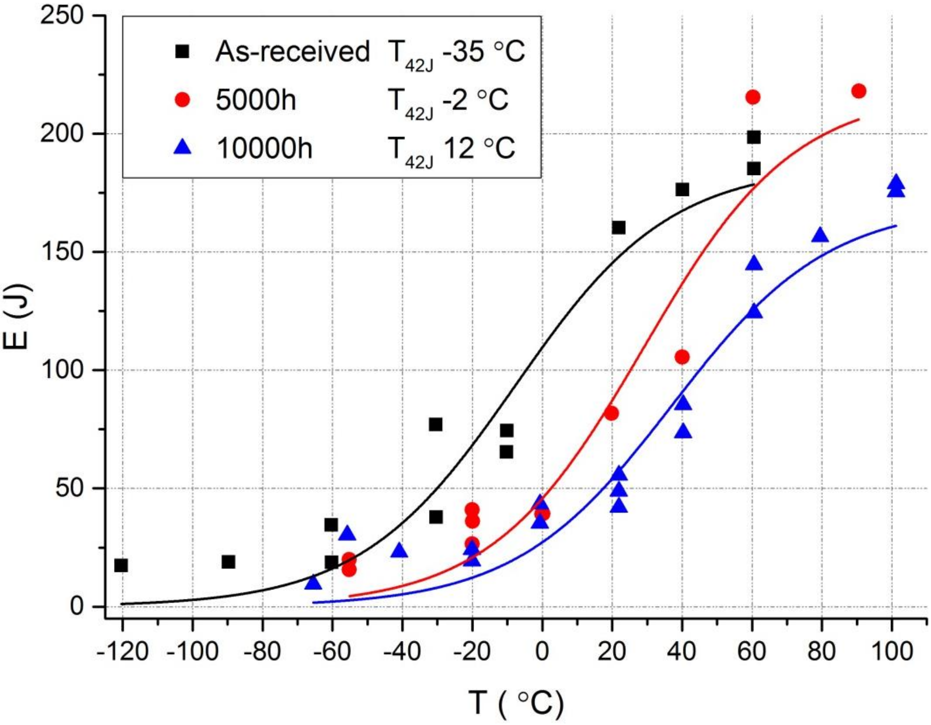

Figure 43. Transition curves of impact energy for as-received, 5000 and 10000 h aged conditions.

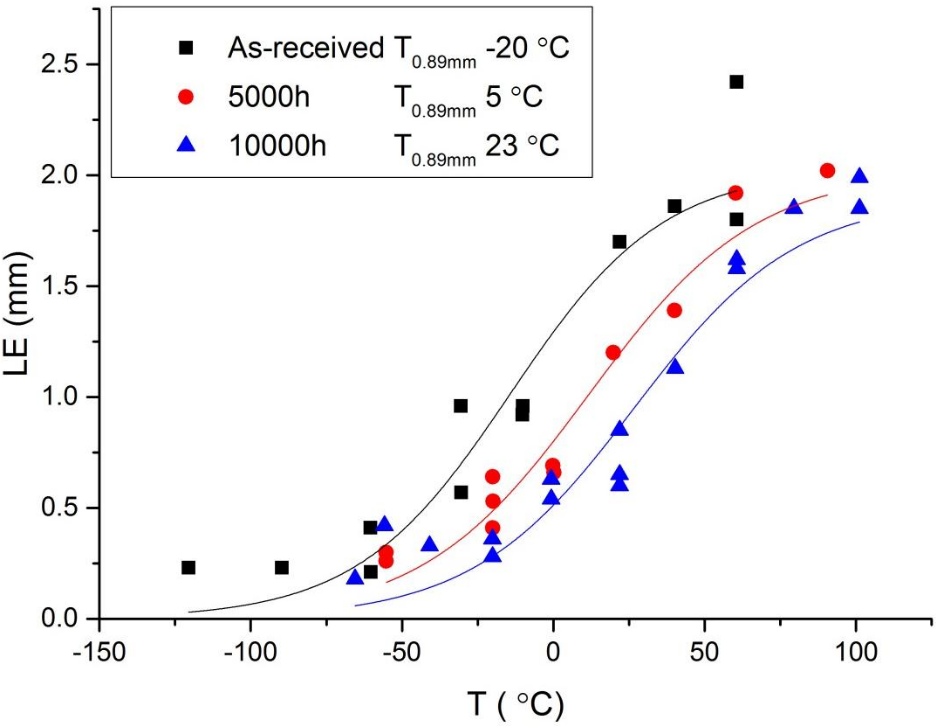

Figure 44. Transition curves of lateral expansion, as-received, 5000 and 10000 h aged conditions.

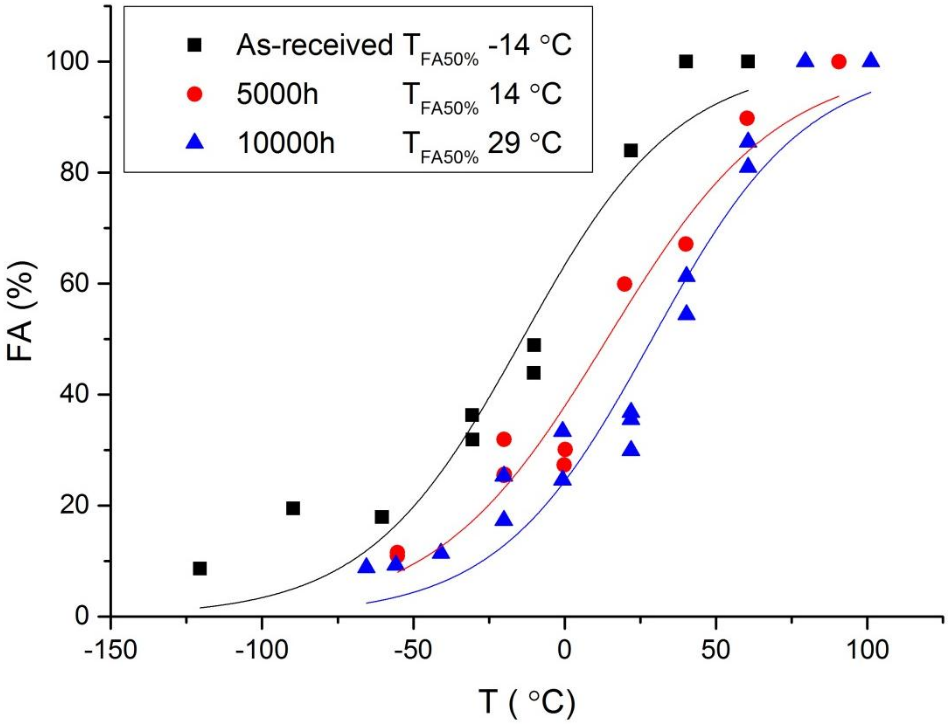

Figure 45. Transition curves of fracture appearance; as-received, 5000 and 10000 h aged conditions.

Scatter of the KV_2, LE and FA is given in Table 17. Standard deviations are quite reasonable and not much scatter is seen in load-deflection curves. Typically scatter increases when material properties are weakened, i.e. irradiation promotes material inhomogeneity. Base material (BM) has always less scatter than inhomogeneous weld metal (WM) or heat-affected zone (HAZ).

Table 17. Scatter of KV_2, LE and FA values.

Material	SD_{KV2}	SD_{LE}	SD_{FA}
	(J)	(mm)	(%)
As-received	16.2	0.20	7.2
Ageing, 5000 hours	18.7	0.12	6.1
Ageing, 10000 hours	14.2	0.16	7.7

The transition temperatures are summarized in Table 18. Fracture surfaces show a wavy appearance that follows the weld bead boundaries. Some fracture appearances were difficult to determine because of several crack growth and arrest areas. The FA values are still more exact when the area is drawn by hand than by using the traditional method.

Table 18. Summary of transition temperatures and upper shelf values measured for the as-received, 5000 h and 10000 h aged materials.

Material	T_{42J}	US_{KV}	$T_{0.89mm}$	US_{LE}	$T_{FA50\%}$	US_{FA}
	(°C)	(J)	(°C)	(mm)	(°C)	(%)
As-received	-35.22	186.8	-20.38	2.03	-14.01	100
Ageing, 5000 hours	-2.32	218.1	5.07	2.02	13.98	100
Ageing, 10000 hours	12.14	170.3	23.39	1.90	28.85	100

As a quality check of the data some correlations are presented. Energy vs. lateral expansion and energy vs. fracture appearance charts are very linear for as-received, 5000 h aged and 10000 h aged conditions, Figures 46 and 47. If a data point is further away from the trend line the result may not be correct and lateral expansion or fracture appearance need to be measured again. These charts show if the results are in order or has some data to be re-measured. All the correlations are good and they confirm good quality of the measured data.

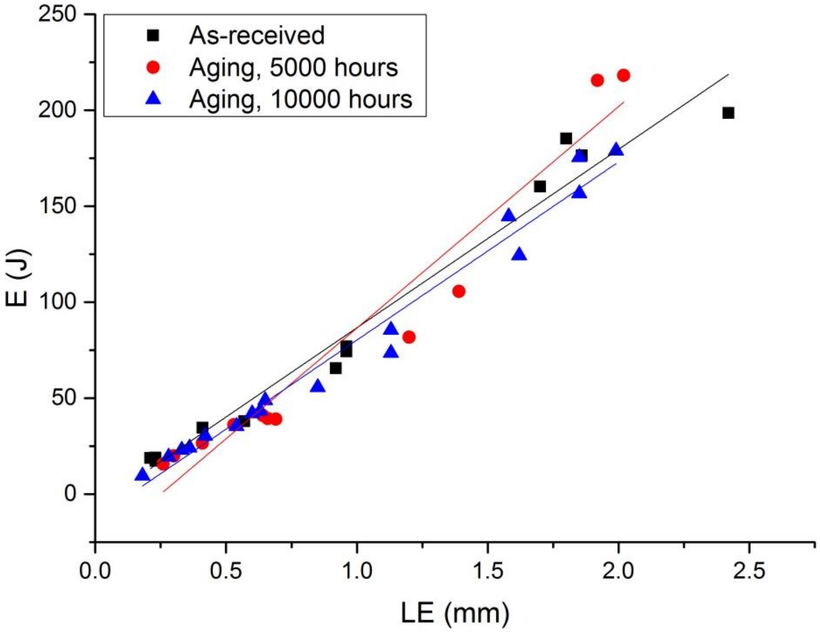

Figure 46. Absorbed energy vs. lateral expansion chart; as-received, 5000 h aged and 10000 h aged conditions.

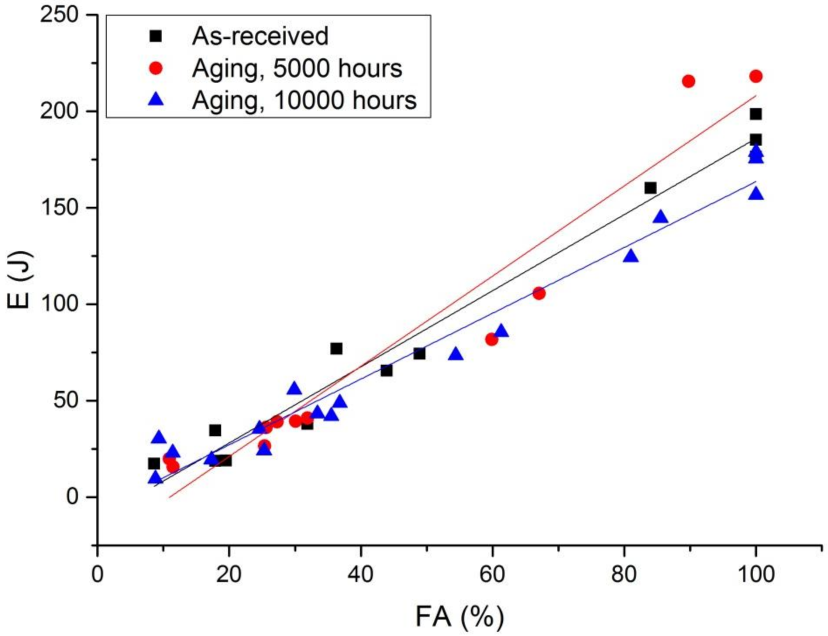

Figure 47. Absorbed energy vs. fracture appearance chart; as-received, 5000 h aged and 10000 h aged conditions.

5.8.2 Estimation of crack arrest

The crack arrest load vs. temperature data measured for the as-received, 5000 and 10000 h aged conditions are shown in Figures 48-50. The scatter of data is small for the as-received condition and the data set of valid values is large enough to enable determination of the 4 kN crack arrest load transition temperature. The data of 5000 h aged condition is little more scattered, but also here the data set of valid values is enough for estimating the 4 kN crack arrest load transition temperature. The crack arrest load vs. ageing time is presented in Figure 51.

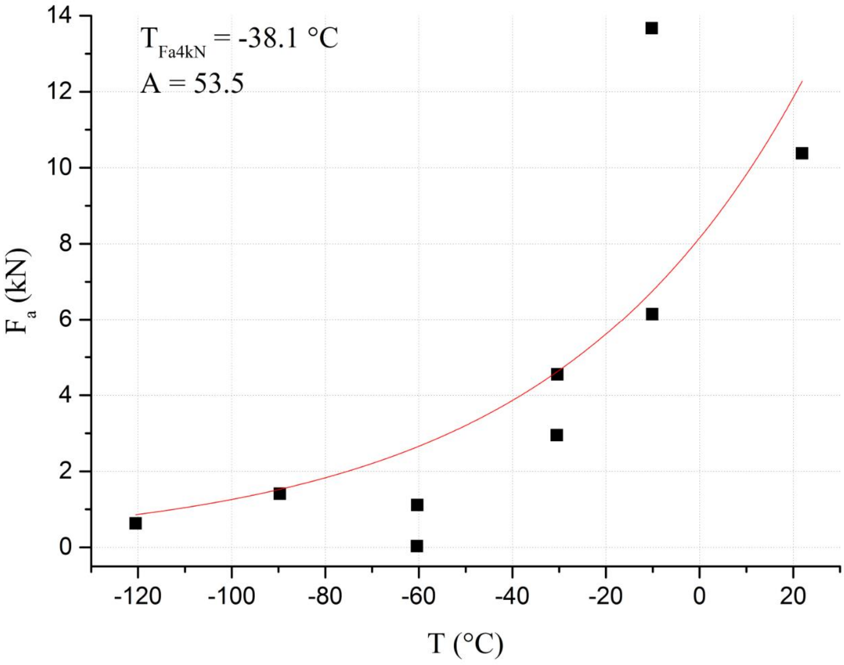

Figure 48. Crack arrest force vs. temperature for as-received condition. The fitting parameters T_{Fa}=4 kN is -38.1 °C and A is 53.5.

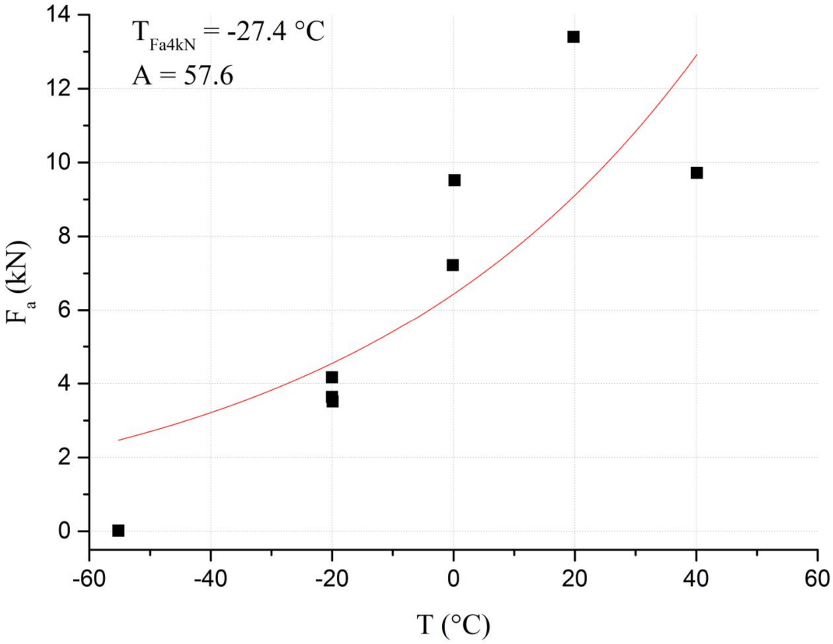

Figure 49. Crack arrest force vs. temperature for 5000 h aged condition. The fitting parameters T_{Fa}=4 kN is -27.4 °C and A is 57.6.

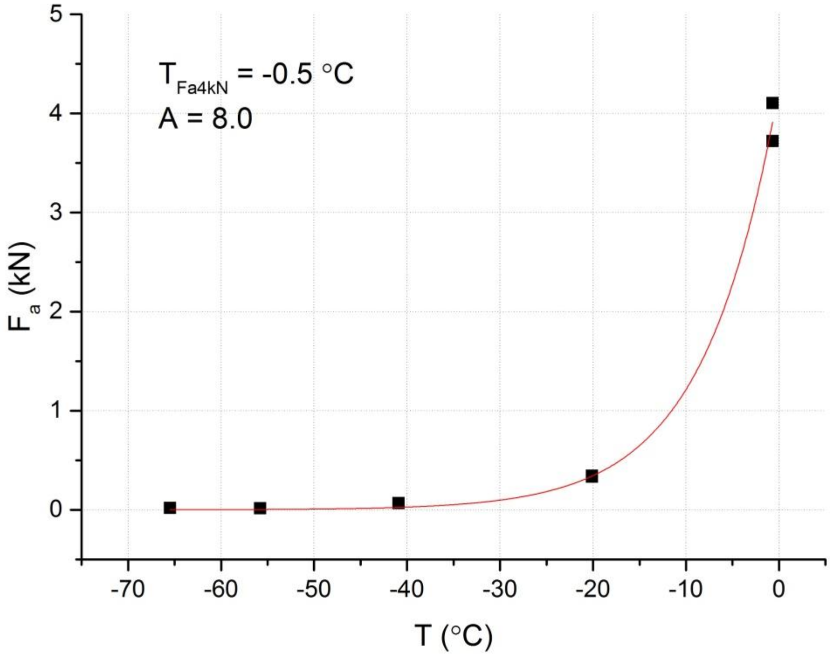

Figure 50. Crack arrest force vs. temperature for 10000 h aged condition. The fitting parameters T_{Fa}=4 kN is -0.5 °C and A is 8.0.

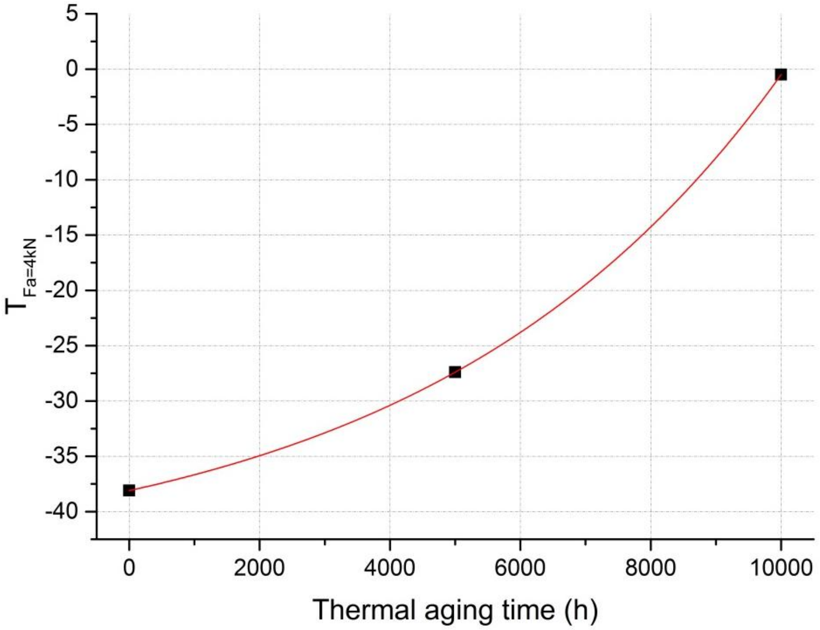

Figure 51. Crack arrest load vs. thermal ageing time at 400 °C.

The transition temperatures of the 4 kN crack arrest load (T_{Fa4kN}) and the consequent estimations of T_{KIa} are summarised in Table 19 together with the estimated T_0 data which are given for comparison.

Table 19. Estimates of crack arrest and initiation temperatures based on Charpy-V data.

Material	$T_{FA=4kN}$	T_{KIa}	T_0
	(°C)	(°C)	(°C)
As-received	-38.1	-26.7	-64.3
Ageing, 5000 h	-27.4	-16.0	-30.8
Ageing, 10000 h	-0.5	10.9	-17.2

5.8.3 Data from instrumented tests

The characteristic load values, determined from the load-deflection graphs, depend on thermal ageing and test temperature. F_{gy}, which corresponds to general yielding of the specimen, is shown in Figure 52. The maximum load parameter F_m behaves the same way as parameter F_{gy}. Behaviour of test material is shown in Figure 53. Crack arrest load was utilized for determining the crack arrest fracture toughness transition temperature T_{KIa} through its correlation with crack arrest load F_a = 4kN. Crack initiation and crack arrest loads F_u and F_a measured from the instrumented curves are shown for test material in Figure 54.

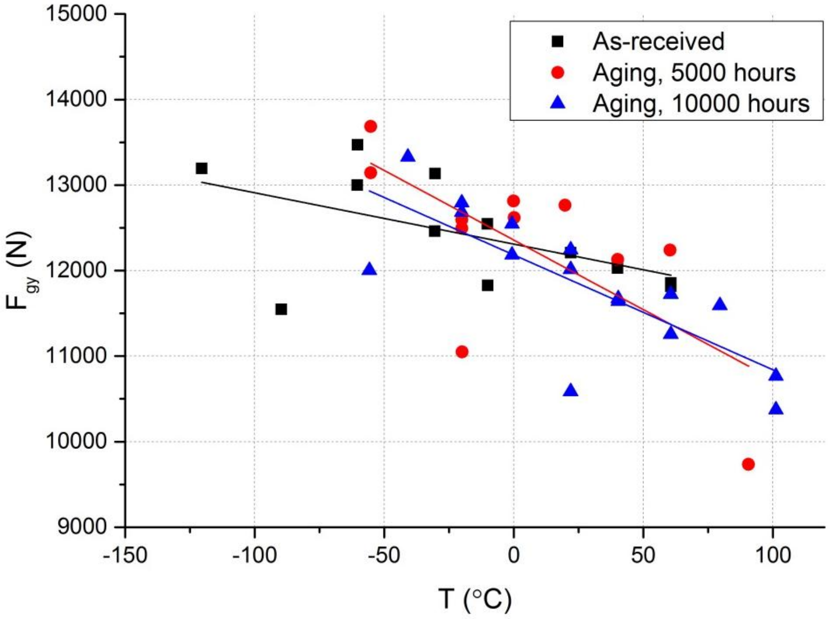

Figure 52. General yield load F_{gy} as function of temperature for test materials.

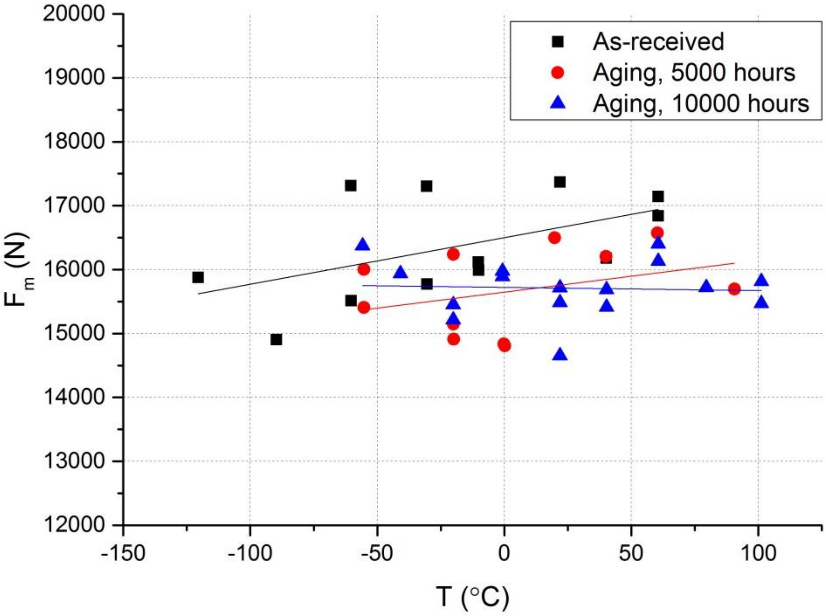

Figure 53. Maximum load F_m as a function of temperature for test materials.

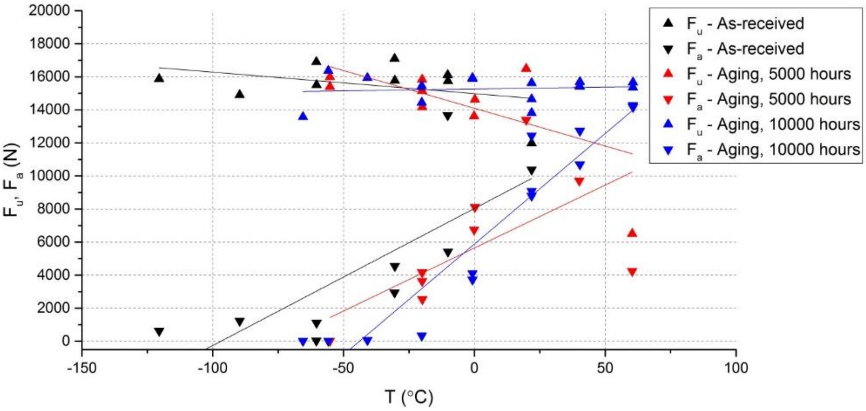

Figure 54. The onset of unstable crack propagation F_u and the crack arrest load F_a for the test materials.

5.8.4 Non-conformance

Four specimens were excluded from the test data (1A, 2A, 4A and 5A). These specimens were problematic because notches were machined either on nickel-base alloy side of the specimen or at the fusion line of nickel-base alloy and pressure vessel steel. Behaviour of specimens is different if the notch is on the nickel-base side or the pressure vessel steel side (BCC vs. FCC). Figure 55 shows that V-notch is in the middle of fusion line on the specimen 5A and not on the low-alloy pressure vessel steel side.

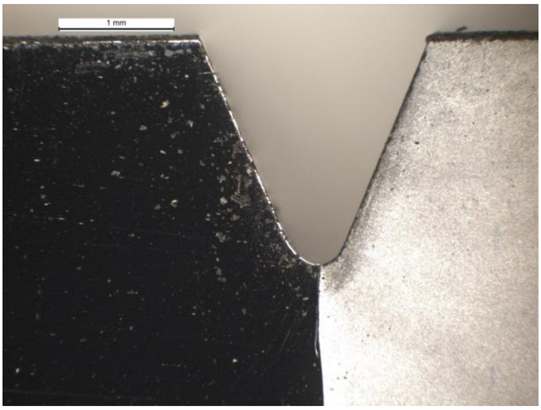

Figure 55. The V notch of the specimen 5A.

In the case of specimen 5A the fracture has begun on the nickel-base alloy side and continued to pressure vessel steel side where the need of energy for crack propagation is lower. This is clearly seen in the fracture surface and elemental analysis, Figure 56 and 54. V-notch is on the bottom of the figure. Nickel-base alloy side is ductile and pressure vessel steel side is brittle in the testing temperature of -90 ˚C.

Scanning electron microscope (SEM) was used to analyse chemical composition by an energy dispersive X-ray spectrometer (EDS) method. In Figure 56 EDS analysis location 1 is V-notch. Locations 2 and 3 near V-notch are nickel-base alloy and locations 4 and 5 are pressure vessel steel. The EDS spectra of locations 2, 3, 4 and 5 are presented in Figure 57.

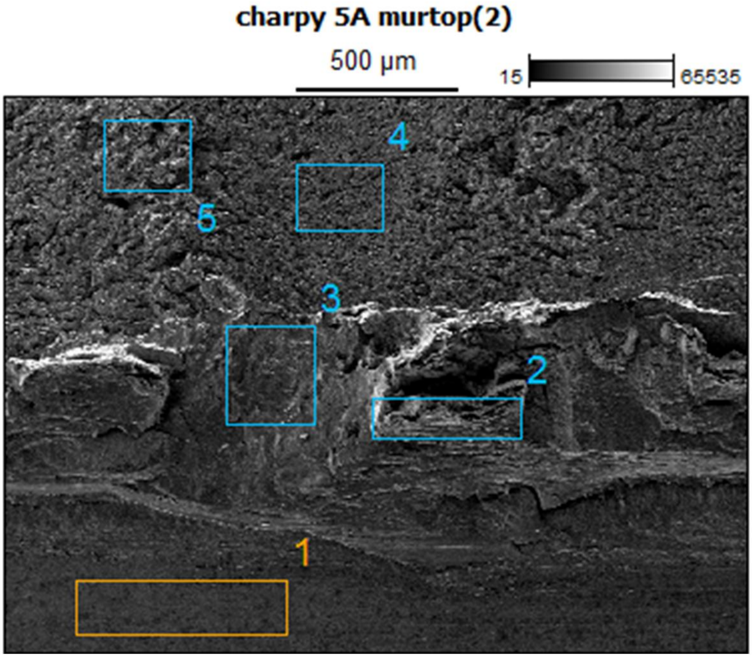

Figure 56. SEM image of specimen 5A fracture surface, secondary-electron image, 19x. Different locations for EDS-analyses are numbered in the image.

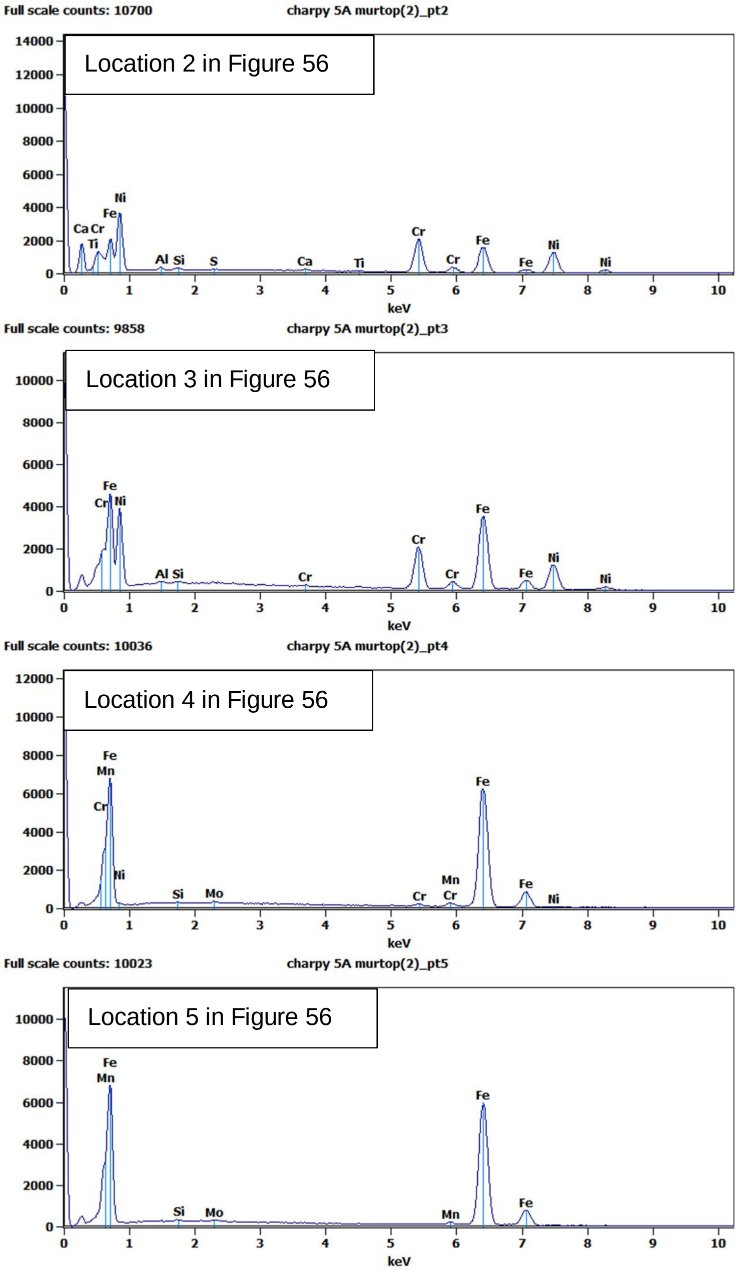

Figure 57. The EDS spectra of different locations of the specimen 5A fracture surface (see previous Figure 56).

18 specimens of 5000 h aged condition were machined. This condition had also machining problems. One specimen had the V-notch fully on the Ni-base alloy side, 8 specimens had the other side of the V-notch on the Ni-base alloy side and the other on the HAZ and 9 specimens had the V-notch fully on the HAZ. The correct location for the V-notch was the HAZ. This means that only 9 specimens were available for the testing. However, the other 9 specimens were also tested parallel at the same temperatures. SEM examination of 5000 h aged specimens showed that fracture surfaces of specimens 5 and 6 with incorrect V-notch position did not include nickel-base alloy. Therefore, the results of these specimens were added to the transition curves.

According to standard ASTM E2298-13a (2013), for each test in which the entire force signal has been recorded, the difference between absorbed energy given by the dial and/or optical encoder KV and the total impact energy W_t shall be within 15 % or 1 J, whichever is larger. If this requirement is not met but the difference does not exceed 25 % or 2 J, whichever is larger, force values shall be adjusted until KV = W_t within 0.01 J. If the difference exceeds 25 % or 2 J, whichever is larger, the test shall be discarded (ASTM E2298-13a 2013). If the measured energy is very high, such as 5000 h aged specimens 1, 2, 8, 10 and 18 have, it may happen that the strain gauge does not have enough capacity and, therefore, the calculated energy value is much lower. Also, if the specimen is very tough it does not bend enough so that the strain gauge could read the actual energy value. Based on the standard all these specimens exceed 25 %. However, this is not a matter to discard these results. Functionality of the strain gauge was checked by testing practice specimens which showed that the strain gauge works fine. In this kind of situation the measured energy is always correct because it is measured from the beginning and the end test angles, and that energy matters the most.

5.9 Strength analysis

A true stress-LN strain curve was determined for HAZ, base material and weld metal from the tensile specimens extracted in the transverse direction of the weld, Figure 58. The HAZ is the hardest zone, Figures 59 to 61. The weld metal is slightly softer than the ferritic base material, SA 508. The yield strength of the base material is 420 MPa, whereas the yield strength of the weld metal is 400 MPa. The yield strength of the HAZ is 590 MPa. No significant change in strength properties is observed in the different material regions due to ageing of the specimen, Figure 62.

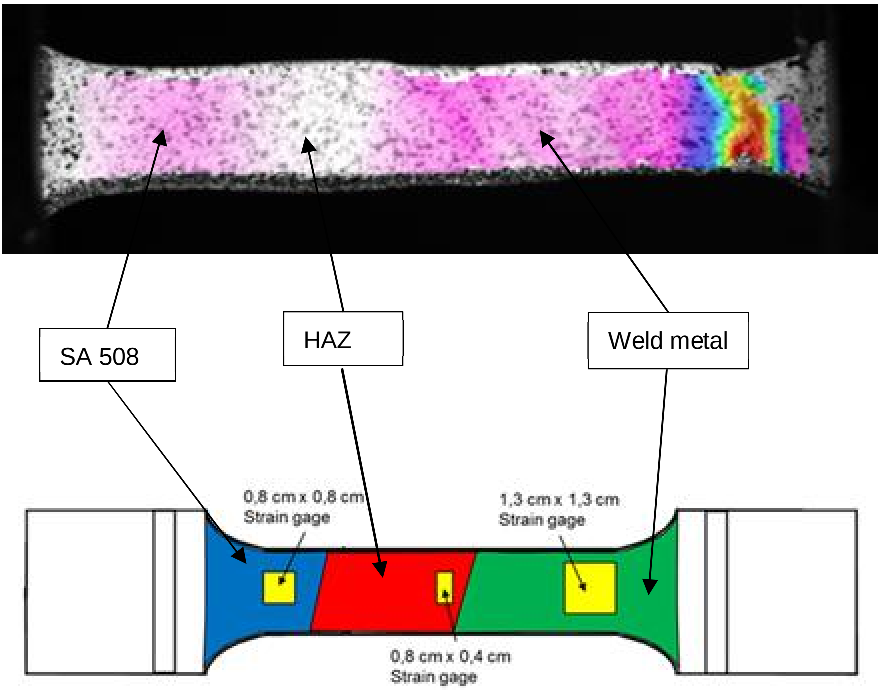

Figure 58. Location of the virtual gages placed on the transverse tensile specimen.

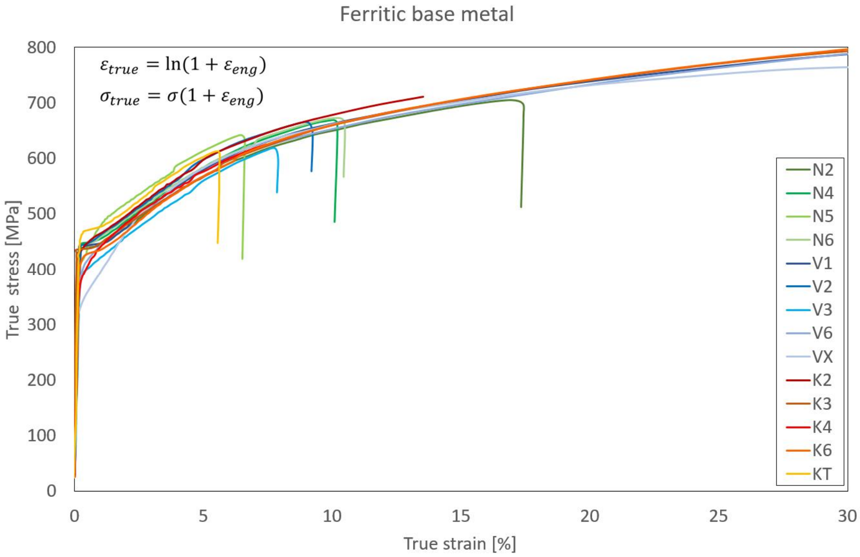

Figure 59. True stress-LN strain of the SA 508 base material.

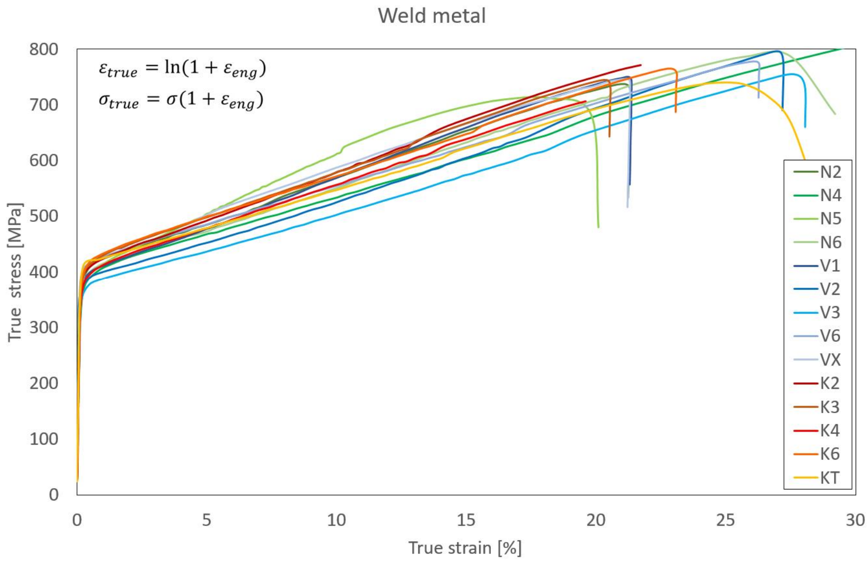

Figure 60. True stress-LN strain of the weld metal.

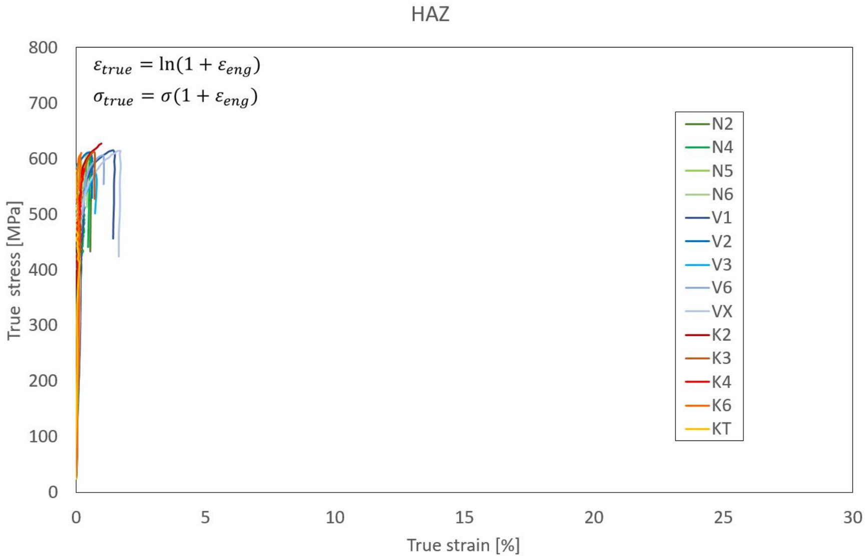

Figure 61. True stress-LN strain of the HAZ.

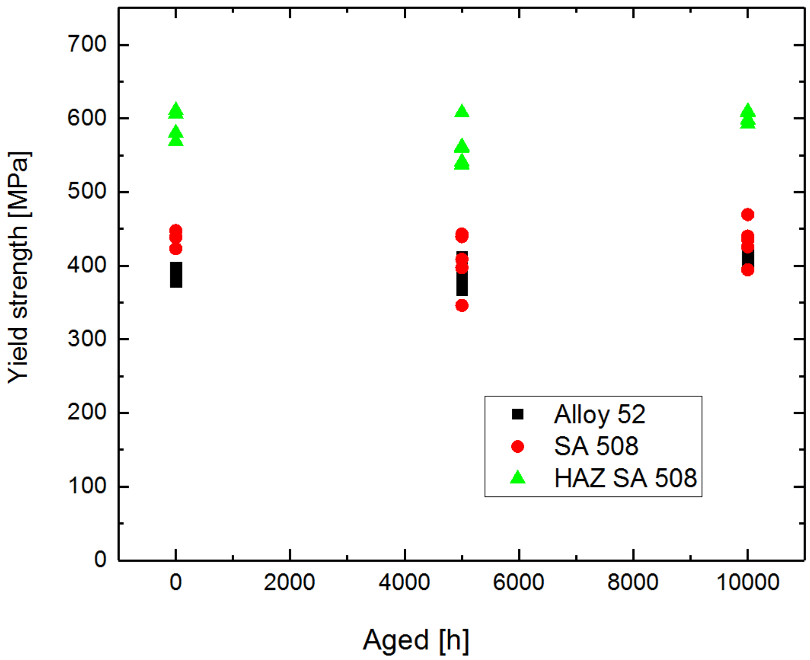

Figure 62. Yield strength of HAZ, Alloy 52, and SA 508 as a function of thermal ageing time at 400 °C.

6. Low Temperature Crack Propagation (LTCP) testing at 55 °C in hydrogenated water

Low temperature crack propagation (LTCP) is widely considered as a hydrogen-induced embrittlement phenomenon that has been observed in laboratory conditions for various nickel-based alloys at the temperature range of about 50 to 150 °C in hydrogenated water (Mills & Brown 2001, Brown & Mills 2002, Young et al. 2005, McIlree et al. 2006, Herms et al. 2009, Sakima et al. 2011, Peng et al. 2012, Ahonen et al. 2013, 2014, Ahonen 2016). No LTCP incidents in nuclear power plants have been reported in open literature to date.

Earlier work suggests, that Alloy 52 maintains its high fracture resistance with 30 cm^3 H_2/kg H_2O, whereas some specimens of Alloy 52 show a substantial reduction of fracture resistance with a higher hydrogen content, 100 cm^3 H_2/kg H_2O (Ahonen et al. 2013, Ahonen 2015). The aim of this work is to study the effect of thermal ageing on fracture mechanical behaviour of the narrow-gap Alloy 52 DMW in low temperature (55 °C) hydrogenated PWR water, representative of a possible plant shut-down environment. The studied hydrogen contents are 30 cm^3 H_2/kg H_2O, which is the content relevant for the plant operation, and 100 cm^3 H_2/kg H_2O, which is applied in order to study the effect of hydrogen and increase understanding of the LTCP phenomenon.

6.1 Methods and specimens

The fracture resistance tests in low temperature hydrogenated water were performed using pneumatic servo-controlled loading device in an autoclave and the crack growth was measured using potential drop (DCPD) method. The equipment construction is shown in Figure 63. The specimens were assembled to a specimen holder, and the clearance between the specimen and the bellows was originally set to be approximately 0.01 mm. The PD wires of the specimens were welded to the wires of the PD measurement equipment.

Charpy-sized (10x10x55 mm) SE(B) specimens were used for the J-R testing. The pre-crack of the specimens was located at mid-thickness of the weld. A schematic image showing the orientation and location of the specimens is presented in Figure 64. The orientation of the specimens is T-S, which means that the crack propagation is parallel to the dendrite growth direction and, thus, it is a susceptible orientation for LTCP.

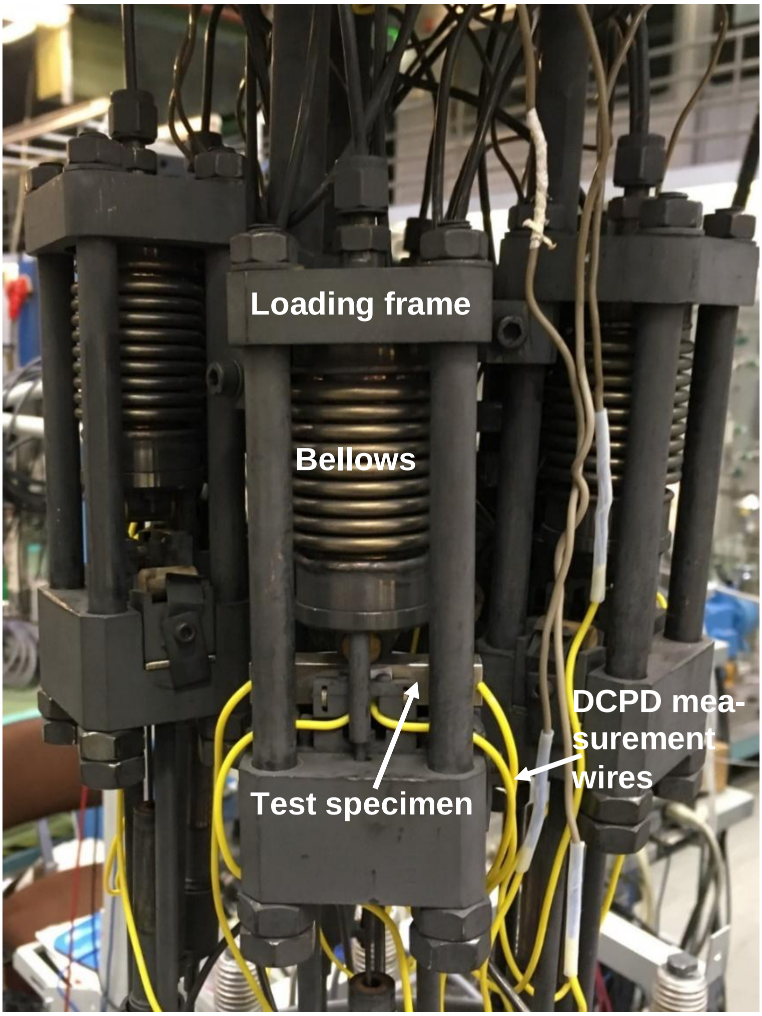

Figure 63. A photograph showing the test equipment before putting it into the autoclave.

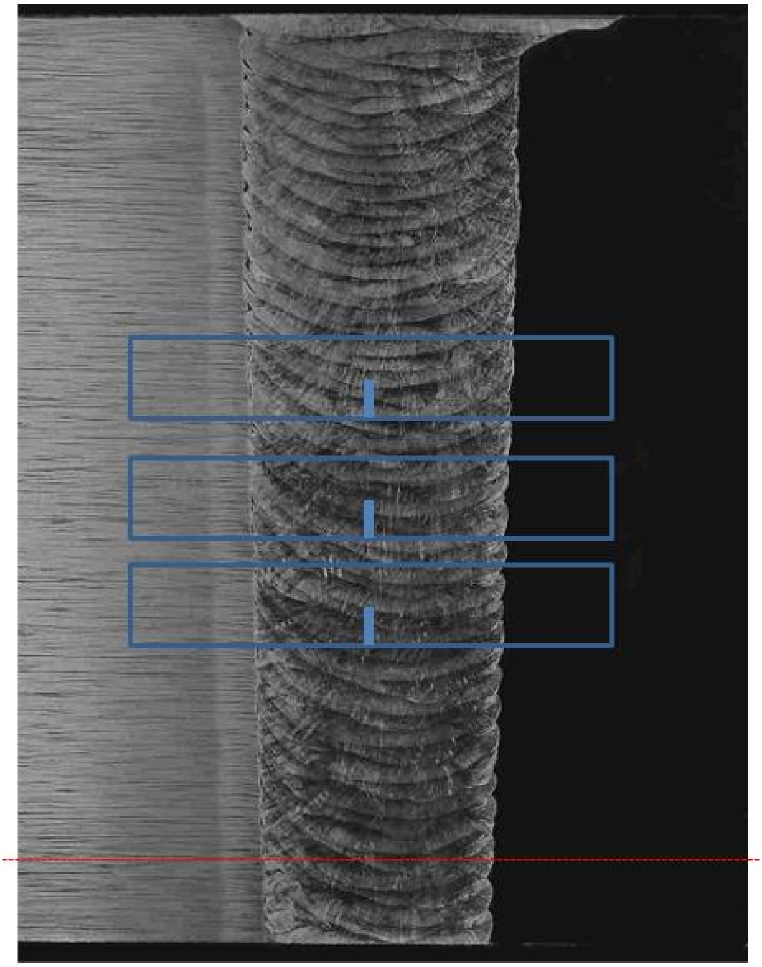

Figure 64. A schematic image showing the orientation and location of the LTCP specimens. The orientation of the specimens is T-S.

About 15 l of pure water containing boric acid (200 ppm) and lithium hydroxide (2.1 ppm) additions (pH 7.4) was put into the autoclave and heated to the temperature of 55 °C. This boric acid concentration was chosen because it corresponds to a typical PWR shut-down water chemistry. Two target levels of hydrogen concentration were chosen, 100 and 30 cm^3 H_2/kg H_2O, and the hydrogen content was measured during the test for tests with 30 cm^3 H_2/kg H_2O. For tests with 100 cm^3 H_2/kg H_2O, the hydrogen content of the water was evaluated from the hydrogen partial pressure by applying Henry's law. The actual hydrogen contents during the tests were estimated to be within ± 2-3 cm^3 H_2/kg H_2O from the target levels for the tests with 30 cm^3 H_2/kg H_2O and within ± 10 cm^3 H_2/kg H_2O for the tests with 100 cm^3

cm^3 H_2/kg H_2O. All the hydrogenated water tests were performed at the temperature of 55 °C, which was chosen because literature data is mostly attained at this temperature and the LTCP effect is the most severe below about 65 °C (Young et al. 2012).

The J-R curves were calculated according to the standard test method for measurement of fracture toughness, ASTM E 1820 – 01. There are several criteria that the test has to meet in order to be a valid J-R test according to the ASTM 1820 - 01 standard. In the case of inhomogeneous materials, the requirements of crack front evenness are not always met in practise. In addition, the acceptable specimen size is dependent on the toughness and flow stress of the material. The size criteria for these specimens of Alloy 52, are typically met for the specimens where fracture resistance is measured to be below about 200 kJ/m^2. However, it is assumed that qualitative comparison of the studied material conditions is valuable, even though the criteria of the standard are not met in most of the obtained results. The chosen loading rate was also slower than the ASTM standard requires. The slower loading rate was chosen based on literature, where a slower loading rate is suggested in order to study the environmental effect (Mills & Brown 2001). Since the specimens do not always meet all the requirements of the standard, the results obtained from the fracture toughness testing are reported as fracture resistance J_Q instead of fracture resistance J_{IC}, which is, according to the ASTM 1820-01 standard, a size-independent value of fracture toughness.

6.2 LTCP test results

The J-R curves obtained with 30 cm^3 H_2/kg H_2O are presented in Figure 65. Based on the J-R curves, substantial crack initiation does not occur during the tests, and only blunting of the pre-crack occurs. The fracture resistance J_Q of all conditions, i.e. as-received, 5000 h aged and 10000 h aged is considered to be above 400 kJ/m^2. The exact J_Q value cannot be measured because the curves do not intersect with the 0.2 mm blunting line.

When tested with a high hydrogen content, 100 cm^3 H_2/kg H_2O, the effect of hydrogen is clear in some specimens, while some others maintain J_Q values over 400 kJ/m^2, i.e. the J-R curve does not intersect with the 0.2 mm blunting line. In general, the as-received material condition exhibits the lowest fracture resistance, showing the lowest obtained J_Q value of 107 kJ/m^2. All the obtained J_Q results are presented in Table 20.

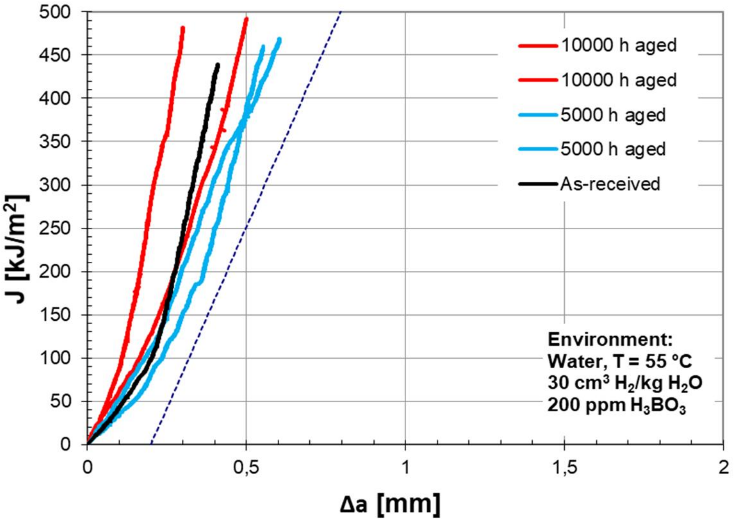

Figure 65. J-R curves of the Alloy 52 NG DMW specimens in different conditions, tested in hydrogenated low temperature water with moderate hydrogen content (30 cm^3 H_2/kg H_2O).

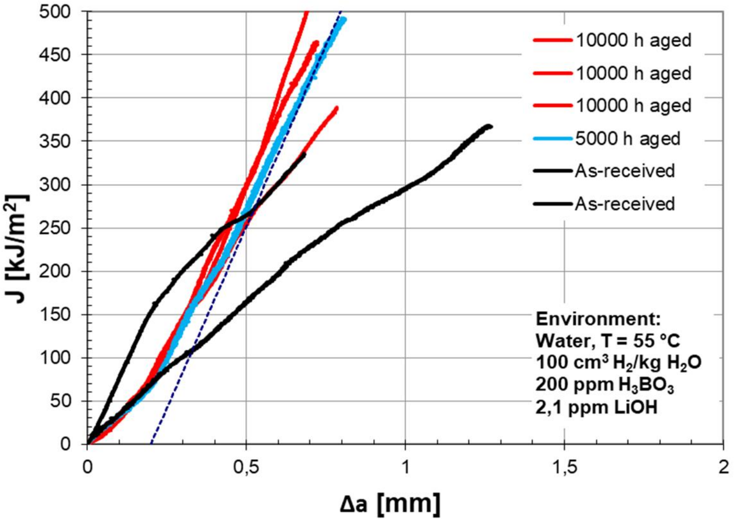

Figure 66. J-R curves of the Alloy 52 NG DMW specimens in different conditions, tested in hydrogenated low temperature water with high hydrogen content (100 cm^3 H_2/kg H_2O).

Table 20. Results of the J-R tests conducted in low-temperature (55 °C) hydrogenated water.

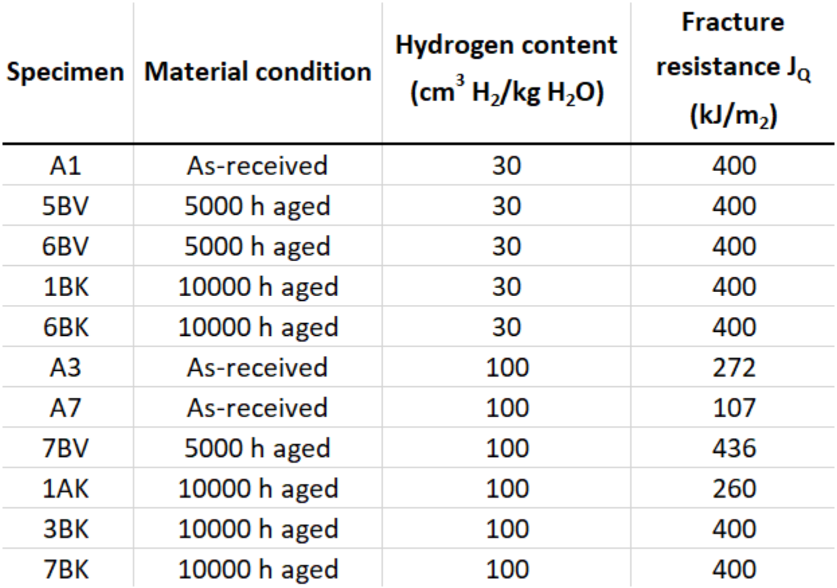

Specimen	Material condition	Hydrogen content (cm^3 H_2/kg H_2O)	Fracture resistance J_Q (kJ/m_2)
A1	As-received	30	400
5BV	5000 h aged	30	400
6BV	5000 h aged	30	400
1BK	10000 h aged	30	400
6BK	10000 h aged	30	400
A3	As-received	100	272
A7	As-received	100	107
7BV	5000 h aged	100	436
1AK	10000 h aged	100	260
3BK	10000 h aged	100	400
7BK	10000 h aged	100	400

7. Fractographic examinations

Fracture surfaces of fracture mechanical test specimens were examined in order to get more information on crack growth behaviour and the factors affecting crack propagation at the fusion boundary region. The applied methods were optical microscopy of cross-sections and SEM microscopy of both cross-sections and fracture surfaces. In addition, 3D topography measurements were applied for some specimen fracture surfaces.

7.1 Characterization of J-R test specimen fracture surfaces

The photographs of the fracture surfaces of the T-L oriented J-R test specimens tested in as-received condition are presented in Figure 67. The fracture morphology follows the wavy shape of the fusion boundary illustrated in the cross-section image (Figure 3). The bead size corresponds well with the frequency of the wavy fracture surface morphology, and the fracture surface appearance is similar in all the studied samples. Based on the photographs it was observed that the location of the fatigue pre-crack was very close to the fusion boundary because in all cases both materials of the joint, i.e. Alloy 52 weld metal (lighter in photographs) and SA 508 low-alloy steel (darker in photographs), are present on the fatigue pre-crack fracture surface. The wavy appearance of the onset of the J-R test part of the specimen fracture surface is different from the fatigue pre-crack fracture surface where the morphology is smoother typical of a fatigue pre-crack. The wavy topography is illustrated in optical 3D topography image shown in Figure 68. It was observed from the sides of the specimen halves that the Alloy 52 weld metal side of the specimens, shown on the left in images (a) – (f) in Figure 67, were more deformed during the J-R test than the SA 508 low-alloy steel side, which is in accordance with the mechanical properties.

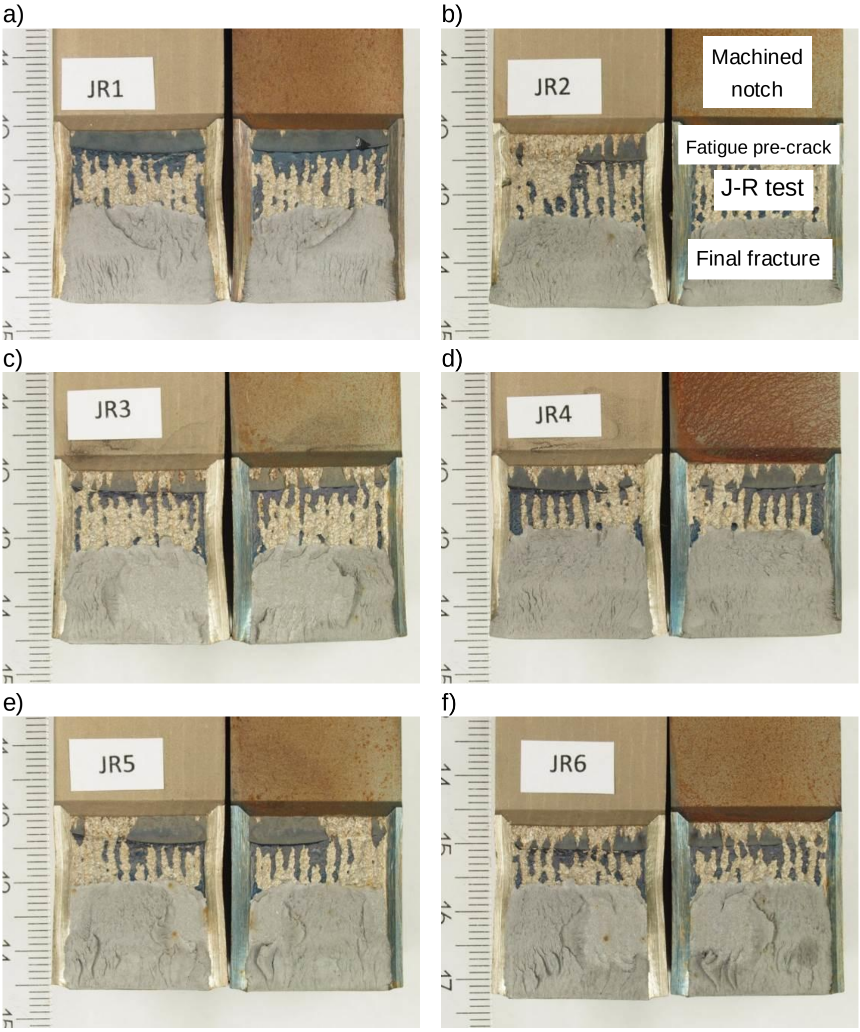

Figure 67. Photographs of fracture surfaces of the J-R test specimens JR1-JR6, as-received condition and T-L orientation, from a) to f), respectively. The different regions of the fracture surface are marked in b), illustrating the specimen JR2, and they exhibit the same pattern for each specimen.

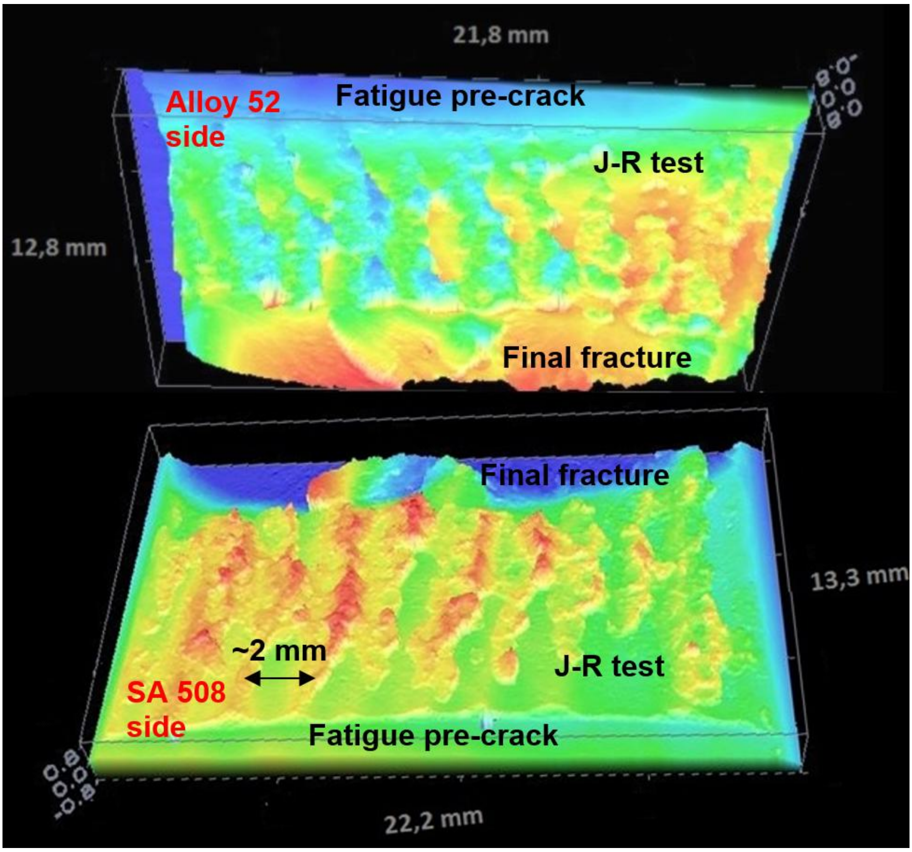

Figure 68. 3D topography images of both sides of the fracture surface of specimen JR1. The wavy fracture surface topography exhibits a period of roughly 2 mm.

The fracture surfaces of as-received condition J-R specimens, tested in T-S orientation, are shown in Figure 69. The wavy surface morphology is not as clear in the T-S orientation specimens as in the case of T-L specimens. However, crack propagation still occurs close to the fusion boundary and in both SA 508 and Alloy 52. In the case of these specimens in T-S orientation, the pre-crack location is slightly deeper in SA 508 than in the T-L specimens, but crack deflects quickly to the fusion boundary region after the onset of crack propagation.

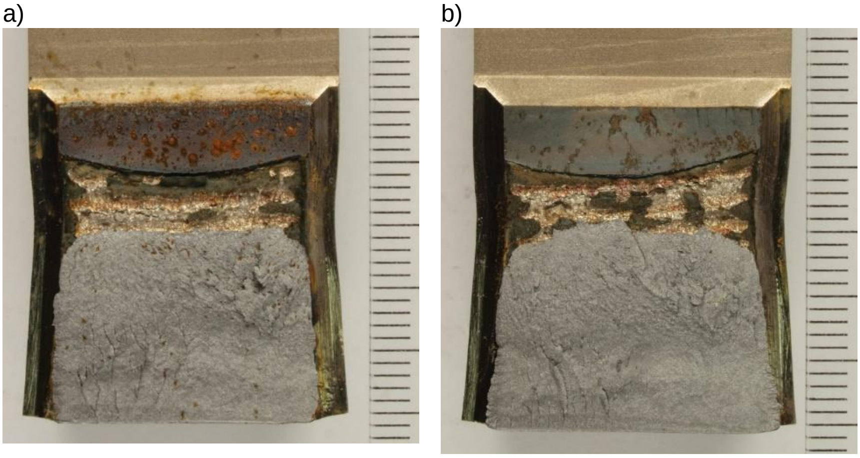

Figure 69. Photographs of fracture surfaces of the J-R test specimens, tested in as-received condition and in T-S orientation, a and b. Crack initiates in LAS, after which it deflects to the weld metal side and occasionally back to LAS side.

Photographs of the fracture surfaces of the J-R test specimens in thermally aged conditions, 5000 h and 10000 h aged, are presented in Figures 70-71, respectively.

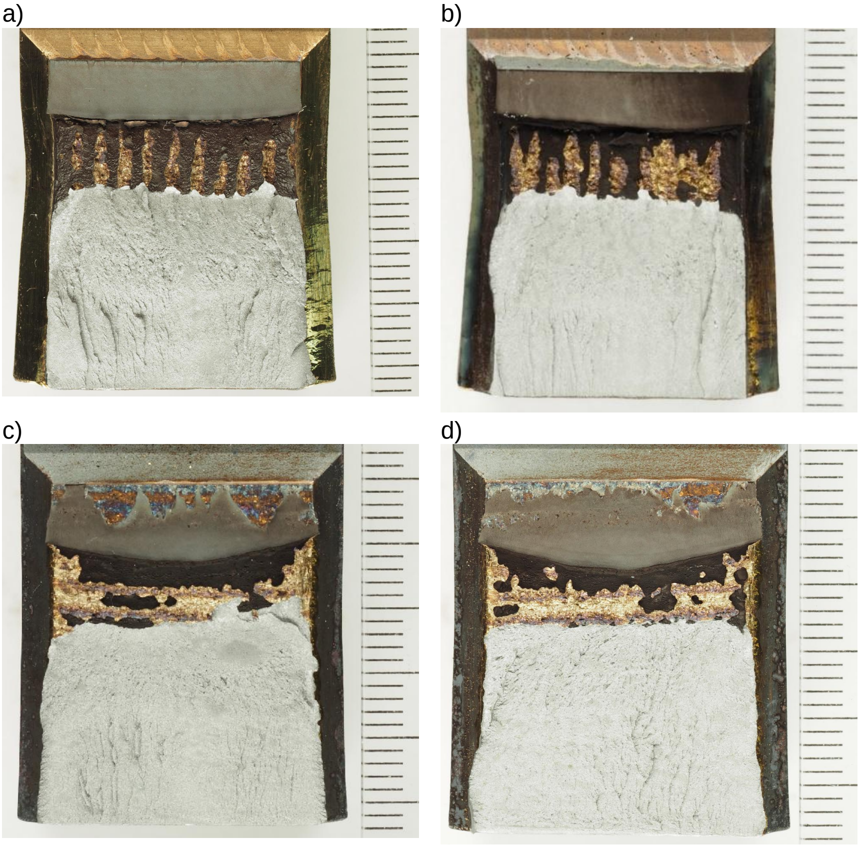

Figure 70. Photographs of fracture surfaces of the J-R test specimens, tested in 5000 h aged condition in T-L orientation, a and b, and T-S orientation, in c and d. Crack initiates in LAS, after which it deflects to the weld metal side and occasionally back to LAS side

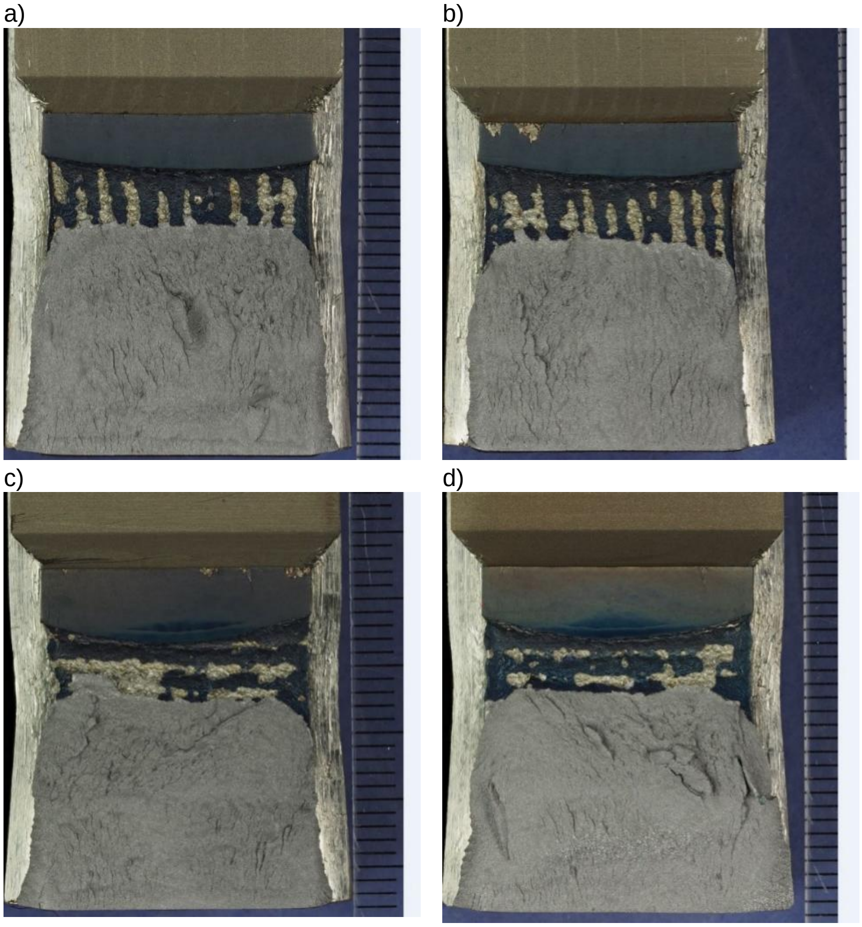

Figure 71. Photographs of fracture surfaces of the J-R test specimens, tested in 10000 h aged condition in T-L orientation, a and b, and T-S orientation, in c and d. Crack initiates in LAS, after which it deflects to the weld metal side and occasionally back to LAS side.

The appearance of a fracture surface consisting of alternating areas of SA 508 and Alloy 52 is illustrated in the SEM image in Figure 72. When the J-R test is started, the crack clearly initiates in the SA 508, but later deflects locally over the fusion boundary to the Alloy 52 side (Figure 73). It is also notable, that the fracture surface in SA 508 has a planar appearance, indicating that the crack propagation occurs in a certain zone, i.e. in the carbon-depleted zone, very close to the fusion boundary.

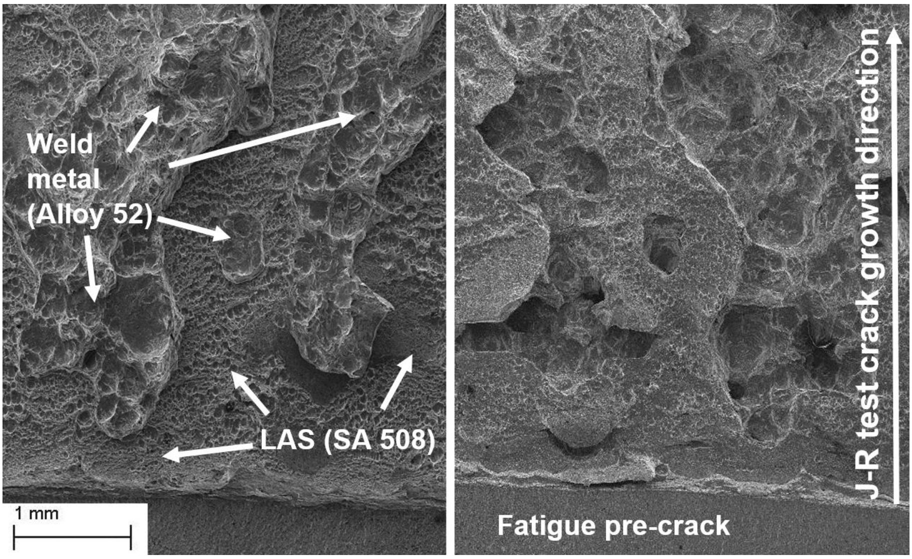

Figure 72. SEM images from the both sides of the fractured specimen at the same location showing alternating areas of Alloy 52 weld metal and SA 508 low-alloy steel. Larger dimples are seen in the areas where crack propagates in Alloy 52.

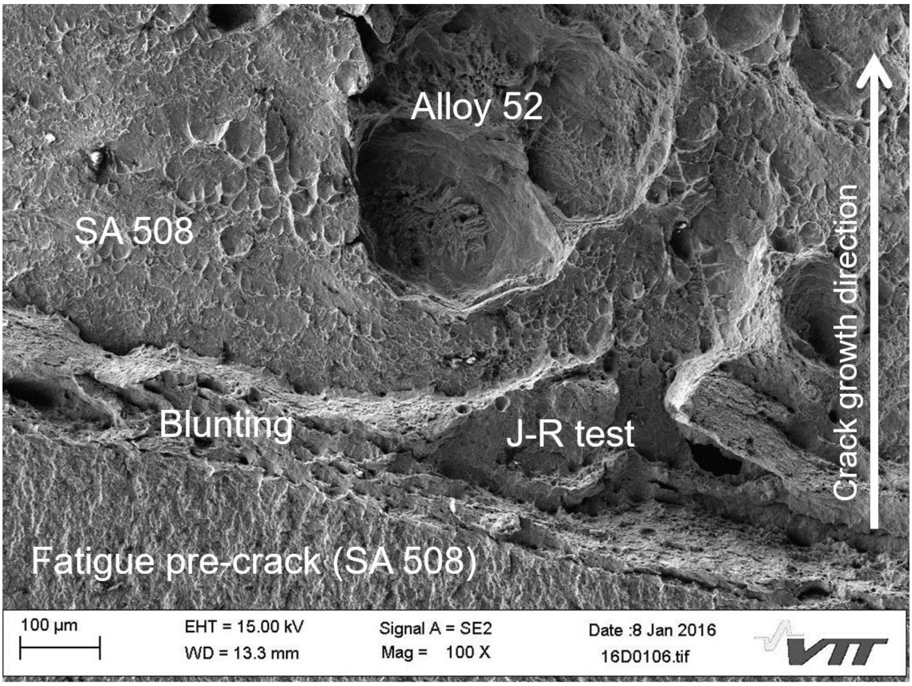

Figure 73. A SEM image showing the fracture surface of the J-R test specimen JR1 at the early part of the test. Fatigue pre-crack tip blunting occurs in the SA 508 side of the joint. After blunting, crack propagation onsets in the SA 508 side of the joint and occasionally crack deflects to Alloy 52 weld metal side (larger dimples).

7.1.1 Crack path examination

Further SEM examination reveals that at each location, where the crack deflects from SA 508 to Alloy 52, there is a small weld defect, as illustrated in Figure 74. Those weld defects are typically smaller than 100 µm, and they have a solidification structure appearance (Figure 75). They were not observed in SEM examinations of the polished cross-section samples, thus indicating that they have been tight before J-R testing. Furthermore, the weld defects show plastically deformed areas, which have been attached to the mating fracture surface by small ductile ligaments during the formation of the fracture surfaces.

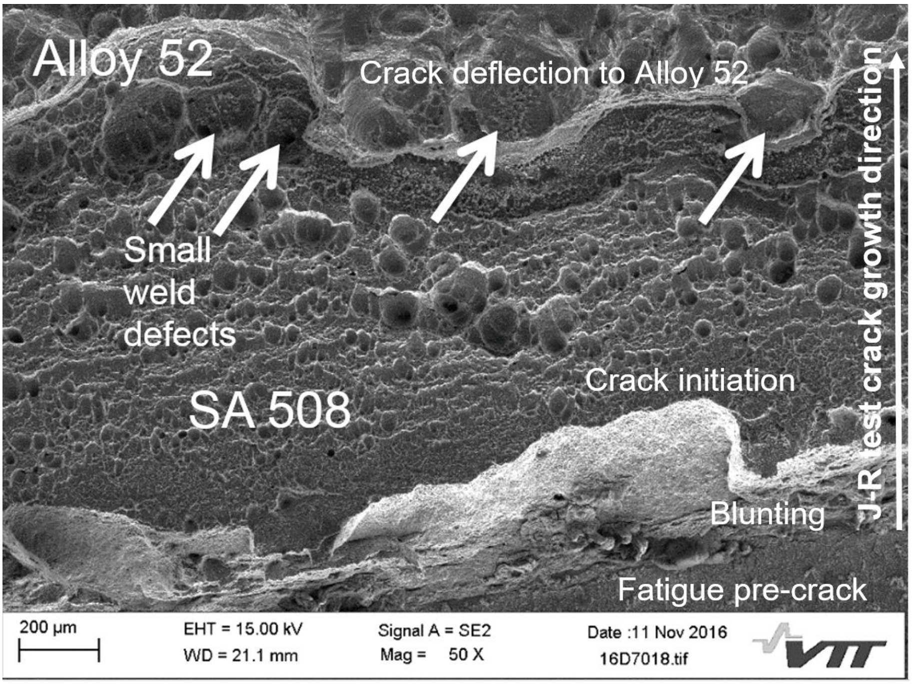

Figure 74. SEM image of the fracture surface of a J-R test specimen, T-S orientation, showing a location at the end of the fatigue pre-crack and the onset of the J-R test crack growth. There are numerous small weld defects at the location of crack deflection to Alloy 52.

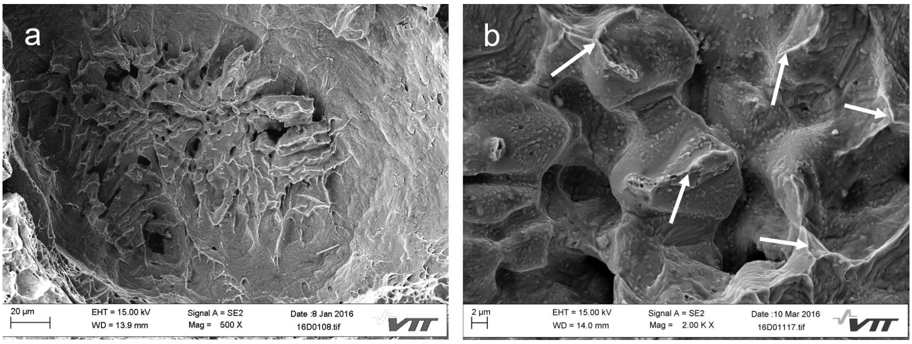

Figure 75. SEM images of weld defects observed on the fracture surface of J-R test specimens. The morphology of a small (~100 µm) weld defect, located on the bottom of a dimple in Alloy 52, is typical of a solidification structure, as shown in a. A larger magnification image of another weld defect is shown in b. Carbides are present on the surface and the weld defect has a dendritic and porous appearance. Some parts of the surface show plastic deformation (arrows) and have thus been originally attached to the mating fracture surface.

Cross-sections of J-R test specimen fracture surfaces were manufactured in order to examine the cracking path relative to the fusion boundary. A photograph showing the location of the cross-section cut of a specimen in T-L orientation is presented in Figure 76. The cut was made at the location where the wavy fracture surface structure can be seen in the cross-section. Optical microscope images of the cross-sections are shown in Figures 77-78. The optical images show that the Alloy 52 side of the specimen shows a more tortuous fracture surface with large dimples, whereas the SA 508 side shows a rather smooth fracture surface, excluding the locations where the crack has deflected over the fusion boundary to Alloy 52 side (blue arrows in Figure 78). The cracking in Alloy 52 seems to propagate often close to the weld pass boundaries (red dashed curves in Figure 78). Deflection to Alloy 52 is typically max. 0.1-0.5 mm from the fusion boundary. Crack deflections seem deeper in the Alloy 52 half of the specimen due to larger amount of plastic deformation (Figure 77). Some formation of voids is also observed beneath the fracture surface in the Alloy 52 side.

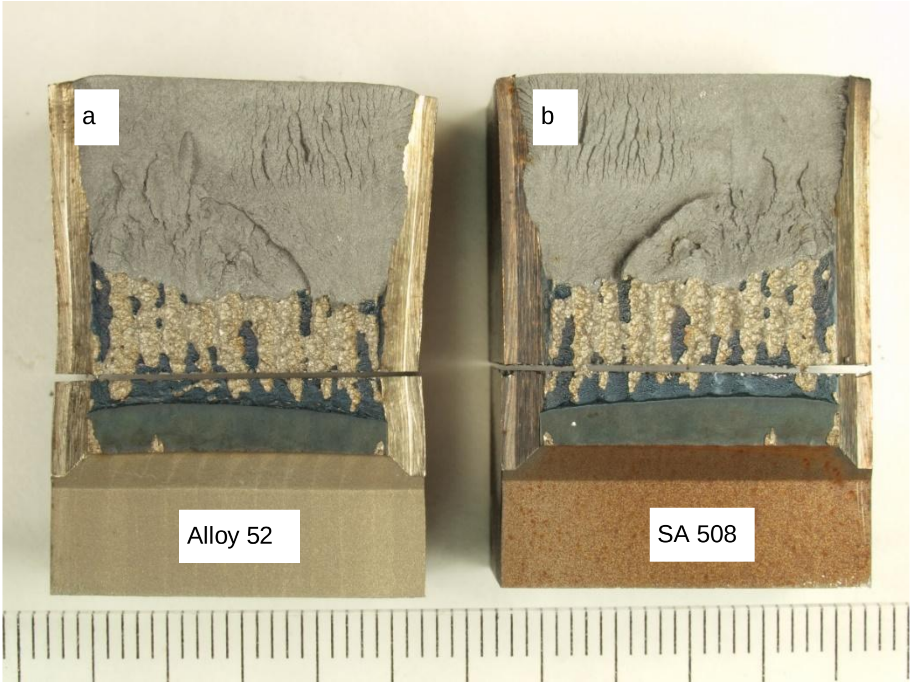

Figure 76. A photograph of the both sides of specimen JR1, a and b. Cross-section cuts were made perpendicular to the crack growth direction which is upwards in the image.

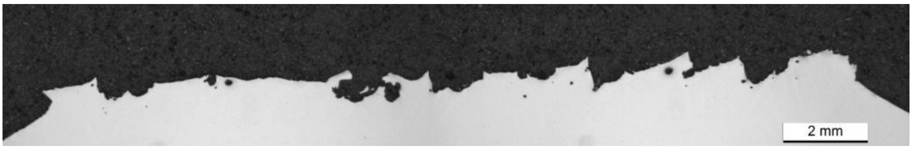

Figure 77. An optical microscope image showing the fracture surface cross-section, depicted in Figure 76 a, Alloy 52 half of the specimen.

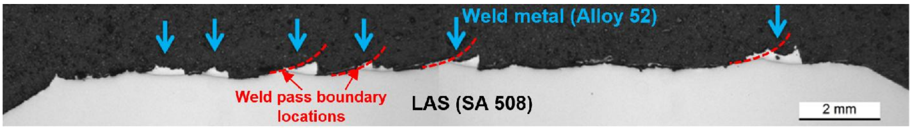

Figure 78. An optical microscope image showing the fracture surface cross-section, depicted in Figure 76 b, SA 508 half of the specimen. Cracking in Alloy 52 follows often the weld pass boundaries.

The cross-section cuts were also done parallel to the crack growth direction, Figure 79. Optical microscope images of the cuts, made for Alloy 52 side and SA 508 side of the J-R test specimen are presented in Figures 80-81, respectively. Alloy 52 appears slightly lighter in the images. In both cross-sections, cut was made in the location where crack deflects into Alloy 52 after initiating in SA 508. Optical microscope image in Figure 80 illustrates clearly how the smooth crack propagation in SA 508 turns into tortuous crack propagation in Alloy 52. In Figure 81, crack propagation is also tortuous in Alloy 52 side, but the peaks and valleys are not as pronounced as in the case of Figure 80, which implies that the Alloy 52 side of the specimen deforms more than the SA 508 side. That can also be seen when looking at Figure 79: the Alloy 52 side of the specimen shows a change in thickness in the middle, whereas the thickness of the SA 508 side has not changed much.

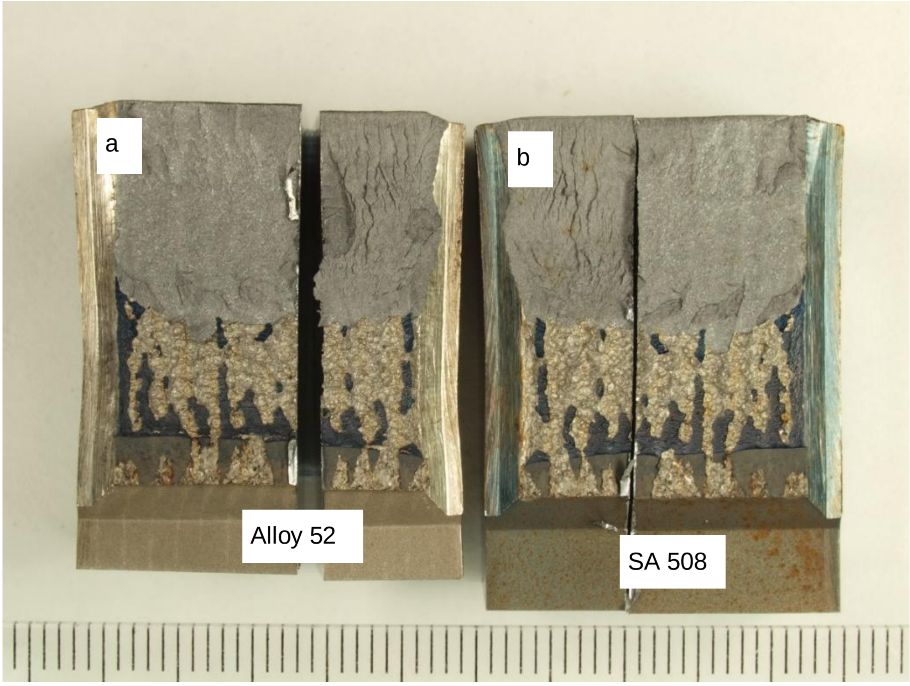

Figure 79. Photograph of the both sides of specimen JR3, a and b. Cross-section cuts were made parallel to the crack growth direction such that cut shown in a was made of the Alloy 52 (and AISI 316L) half and b of the SA 508 half of the specimen.

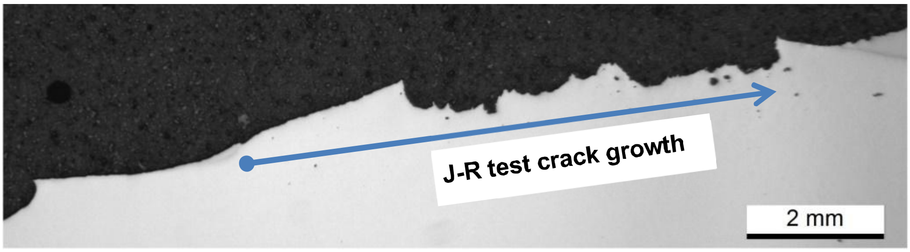

Figure 80. Optical microscope image showing the fracture surface cross-section, depicted in Figure 79 a. The crack initiates at this location in SA 508, propagates for about 2,5 mm until it deflects into the Alloy 52 side of the joint in which part the fracture surface shows a tortuous appearance. Voids, appearing dark in the image, have also formed beneath the fracture surface in Alloy 52.

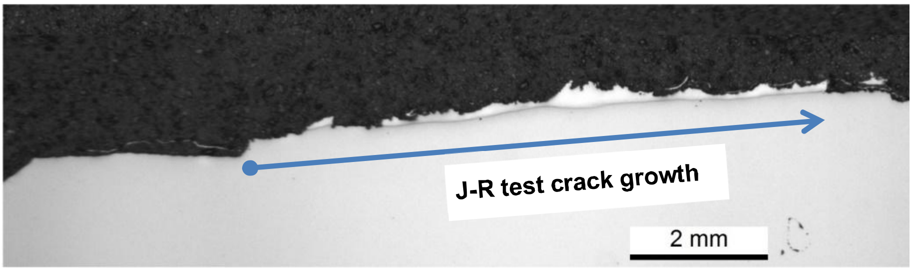

Figure 81. Optical microscope image showing the fracture surface cross-section, depicted in Figure 79 b. Crack initiates at this location in SA 508, apparently very close to the fusion boundary, but mostly grows in the Alloy 52 side that has a lighter appearance in the image.

The fraction of RPV steel on the fracture surface, Table 21, was determined from the fracture surface with image-J an image-processing programme. The distance between the fatigue pre-crack tip and the fusion boundary was determined from the cross-sections.

Table 21. Fracture surface and crack location data.

Crack location	Specimen ID	Temperature & (crack orientation)	% of RPV steel on fracture surface	% of RPV steel on the fatigue pre-crack tip	Distance between fatigue pre-crack tip and fusion boundary
		°C	[%]	[%]	[mm]
Fusion boundary	AS 1	300 (T-L)	37	100	0
Fusion boundary	AS 2	300 (T-L)	28	56	0
Fusion boundary	AS 3	300 (T-L)	27	81	0
Fusion boundary	AS 4	300 (T-L)	41	80	0
Fusion boundary	AS 5	300 (T-L)	32	74	0
Fusion boundary	AS 6	300 (T-L)	37	77	0
In HAZ of SA 508, 0.577 mm from fusion boundary	AS 7	300 (T-S)	38	100	0.58
In HAZ of SA 508, 0.391 mm from fusion boundary	AS 8	300 (T-S)	57	100	0.39

In HAZ of SA 508, 0,14 mm from fusion boundary	5000 1	300 (T-S)	45	100	0.14
In HAZ of SA 508, 0,27 mm from fusion boundary	5000 2	300 (T-S)	37	100	0.27
In HAZ of SA 508, 0,47 mm from fusion boundary	5000 3	300 (T-L)	67	100	0.47
In HAZ of SA 508, 0,78 mm from fusion boundary	5000 4	300 (T-L)	51	100	0.78
In HAZ of SA 508, 0,72 mm from fusion boundary	5000 5	300 (T-L)	70	100	0.72
In HAZ of SA 508, x mm from fusion boundary	10000 1	300 (T-S)	83	100	0.12
In HAZ of SA 508, x mm from fusion boundary	10000 2	300 (T-S)	68	100	0.15
In HAZ of SA 508, x mm from fusion boundary	10000 3	300 (T-L)	77	100	0.34
In HAZ of SA 508, x mm from fusion boundary	10000 4	300 (T-L)	72	100	0.17
In HAZ of SA 508, x mm from fusion boundary	10000 5	300 (T-L)	71	100	0.39

7.2 Characterization of Charpy-V impact toughness specimen fracture surfaces

The following presents features and observations from selected Charpy-V impact toughness test specimen fracture surfaces. A more comprehensive presentation of the Charpy-V specimen fracture surfaces is presented in Jari Lydman's Master's thesis (Lydman 2016).

Representative images of cleavage fracture appearance in transition range specimens are presented in Figures 82-83. Initiation sites were not easily detected on the fracture surfaces, and the overall appearance is often serrated and vague.

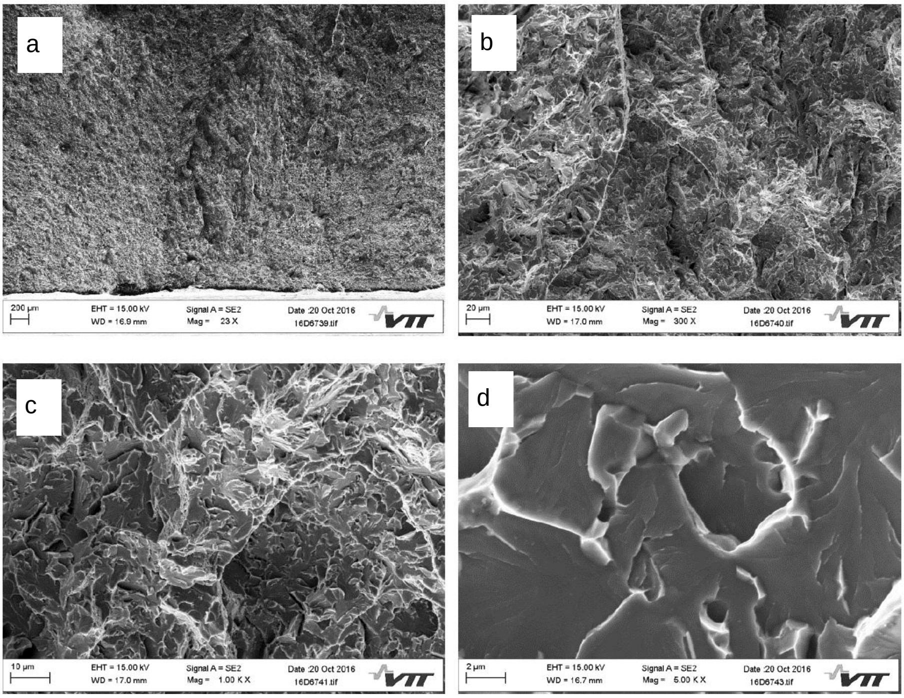

Figure 82. SEM images with different magnifications of a typical cleavage fracture from a transition range specimen, images a-d.

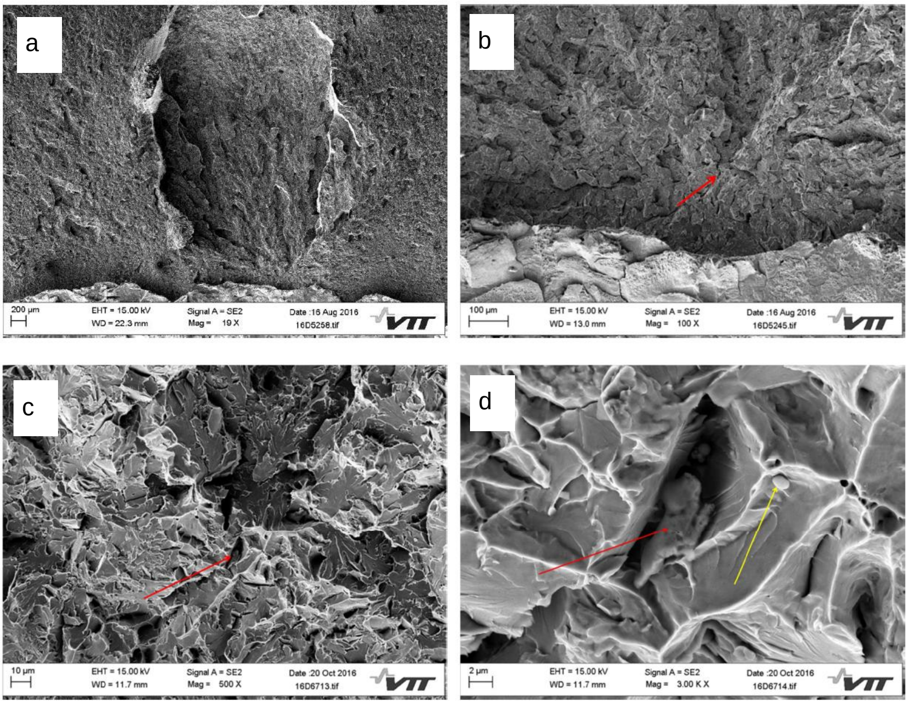

Figure 83. SEM images with different magnifications of a typical cleavage fracture from a transition range specimen, showing a facet about in the middle of the specimen fracture surface, presented in a. The initiation site for the brittle fracture is presented in b and with larger magnification in c. A specific particle initiating the brittle fracture was not found, but one somewhat large Cu-rich inclusion was observed close to the initiation site (red arrow), as well as some smaller round particles (yellow arrow), shown in d.

Cleavage fracture is the predominant fracture mode of brittle fracture. However, intergranular (IG) fracture was observed in all studied conditions (as-received, 5000 h aged and 10000 h aged) in brittle specimens. Areas of IG fracture were mainly observed in 10000 h aged specimens (Figure 84), but some IG fracture was also present in the as-received specimens (Figure 85).

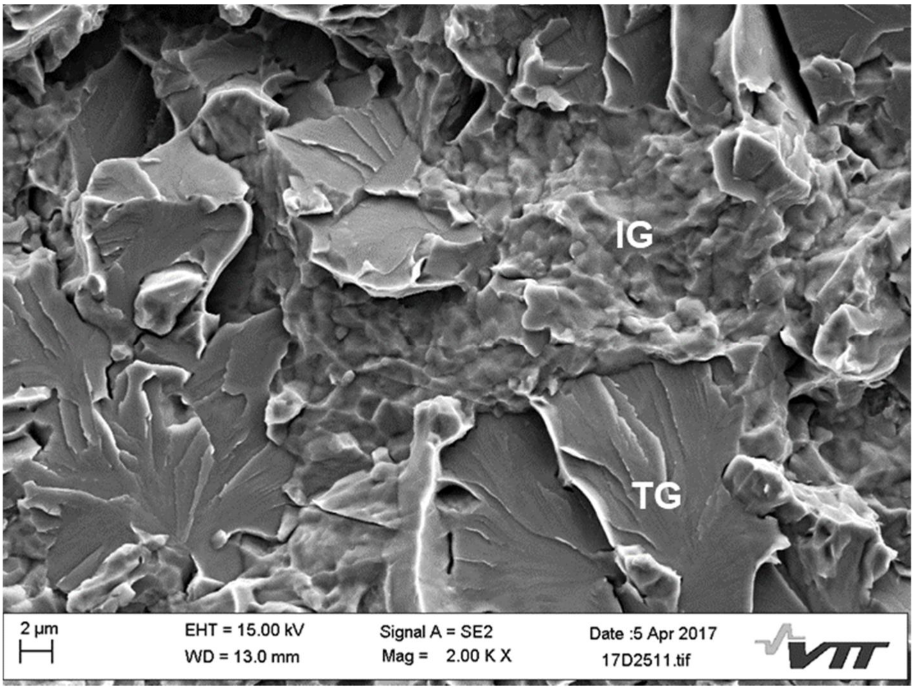

Figure 84. A SEM image showing alternating areas of IG (intergranular) and TG (transgranular) fracture on the fracture surface of a Charpy-V specimen, tested after 10000 h of ageing.

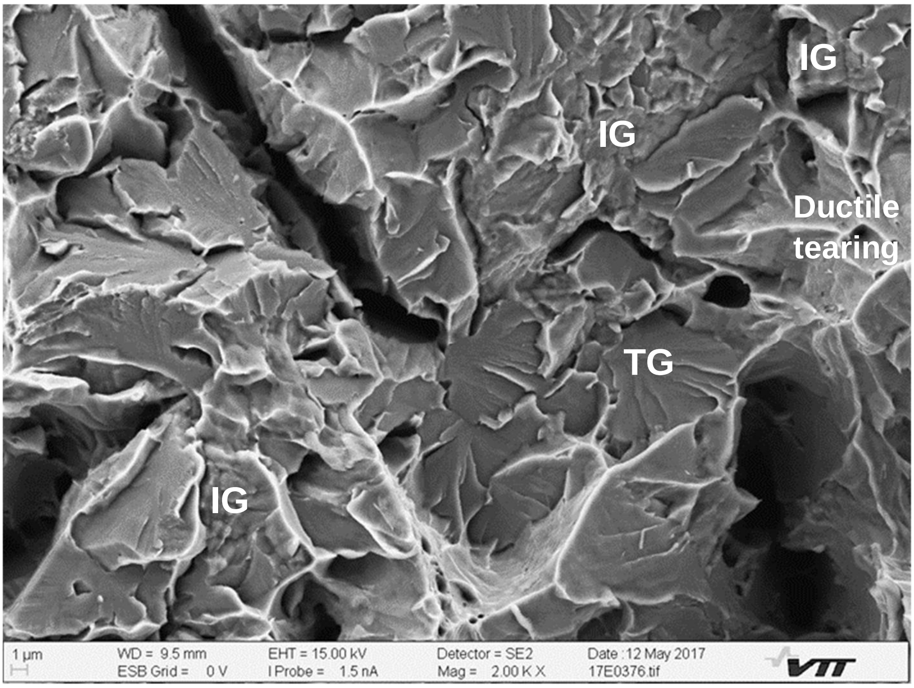

Figure 85. A SEM image showing alternating areas of IG (intergranular) and TG (transgranular) fracture on the fracture surface of a Charpy-V specimen, tested in as-received condition. Also, some ductile areas are seen in this specimen, especially on the right, at this location.

Small weld defects, that were observed on the fracture surfaces of the J-R test specimes, were observed occasionally also in ductile Charpy-V specimens. The small weld defects show the same appearance as in the J-R test specimens. Weld defects cause deflections to Alloy 52 side also in Charpy-V impact tests. A collation of SEM images with different magnifications, illustrating the appearance of the weld defects, is presented in Figure 86.

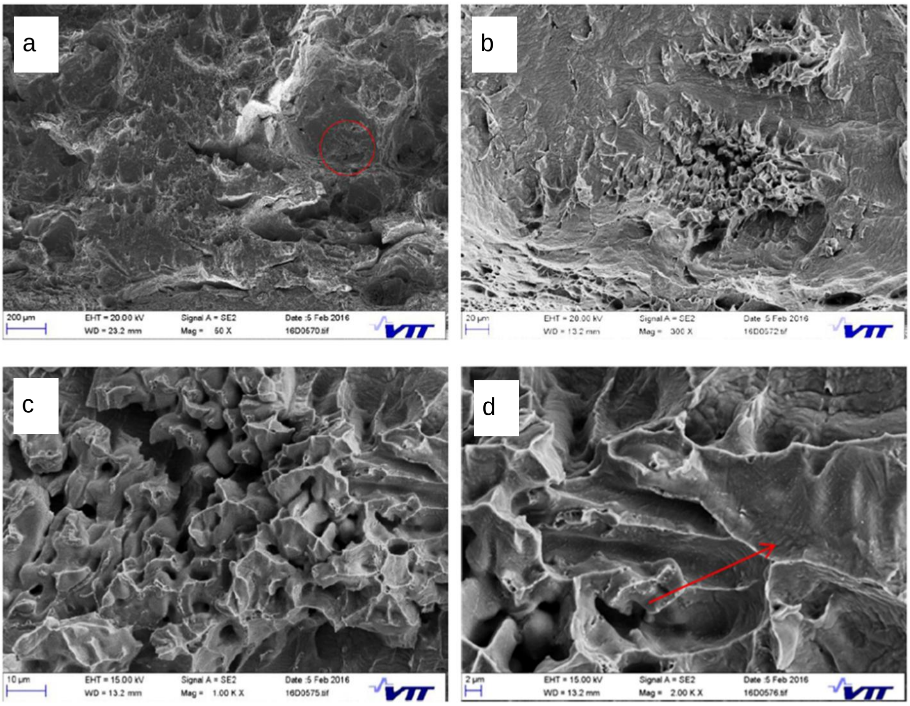

Figure 86. SEM images illustrating the appearance of the weld defects observed on the fracture surfaces of the ductile Charpy-V specimens. The location of a weld defect is circled in red in a. Details of the weld defect in different magnifications are presented in b-d. Some carbides are visible in d, highlighted with the red arrow.

Crack deflection from SA 508 to Alloy 52 side occurs in ductile Charpy-V specimens, as shown in optical microscope images of the polished and etched cross-section images, Figures 87-88. Consistently with the observations on the fracture surfaces, the weld defects have an undulating appearance, typical of a solidification structure, but the highest peaks often have sharp edges due to partial detachment to the mating surfaces and plastic deformation during the test at those locations.

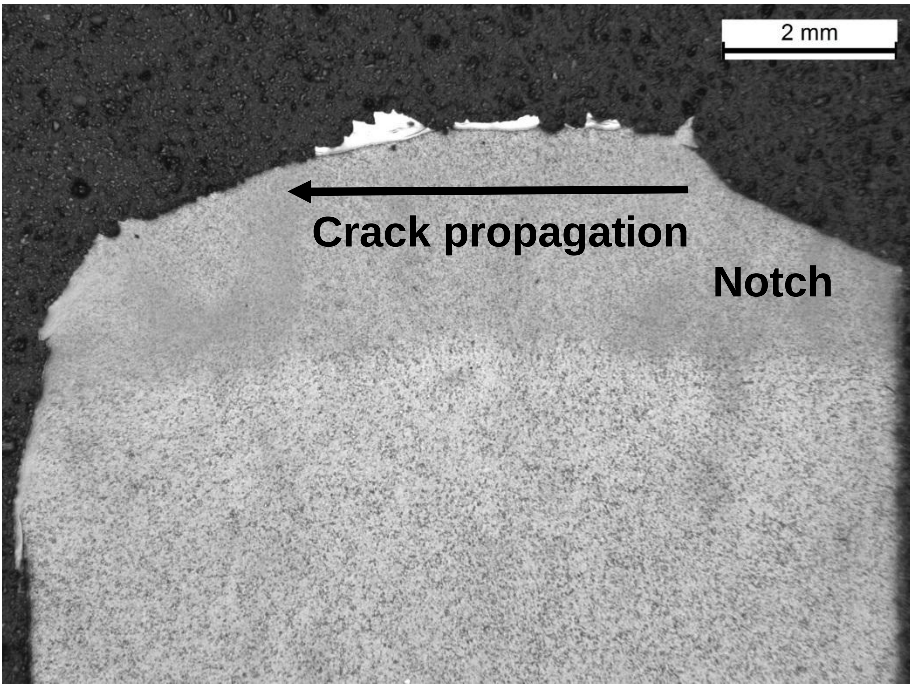

Figure 87. An optical microscope image of a polished and etched cross-section of mostly ductile Charpy-V specimen, showing crack deflections from SA 508 (appearing darker) into Alloy 52 (appearing lighter) and back to SA 508.

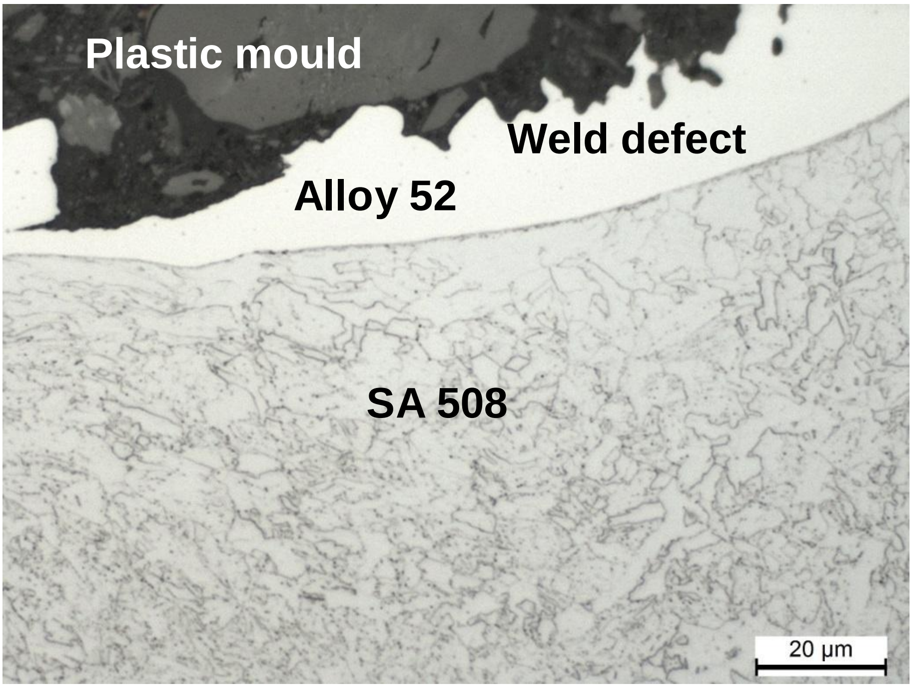

Figure 88. An optical microscope image of a polished and etched cross-section of mostly ductile Charpy-V specimen, showing the appearance of a weld defect.

In Charpy-V specimens behaving in a brittle manner, the fracture surface shows a wavy appearance, which seems to follow the shape of the weld fusion boundary, as illustrated in Figure 89, where a small magnification SEM image from a Charpy-V specimen fracture surface is shown. A SEM cross-section image of the same specimen is shown in Figure 90. The cross-section image displays how after about 150 µm wide plastic deformation zone at the specimen notch, brittle fracture initiates and propagates very close, about 0-50 µm, to the fusion boundary in SA 508.

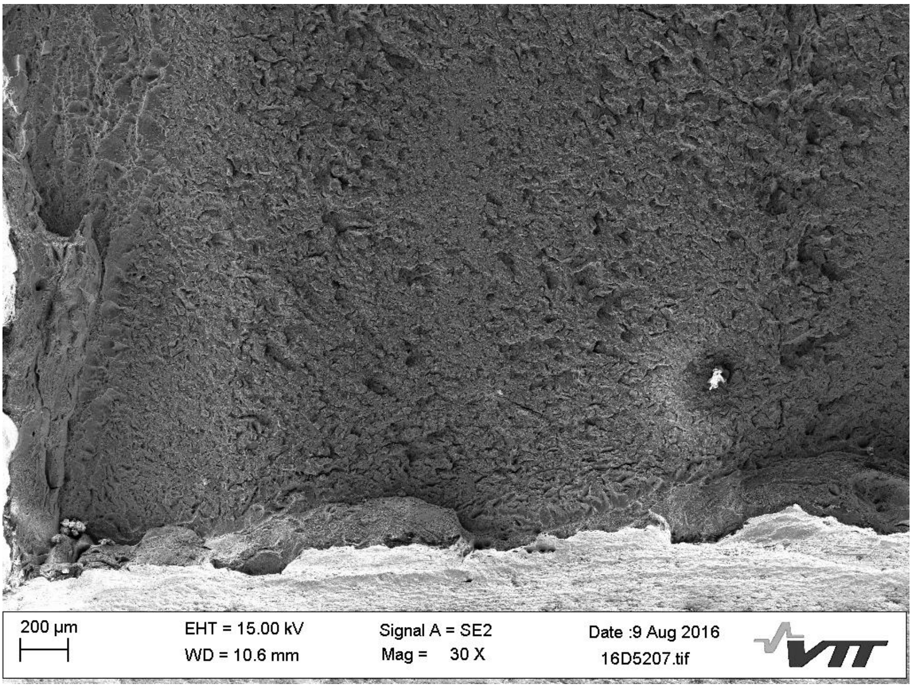

Figure 89. A SEM image of the fracture surface of a brittle Charpy-V specimen, showing the wavy fracture surface appearance, which follows the weld fusion boundary.

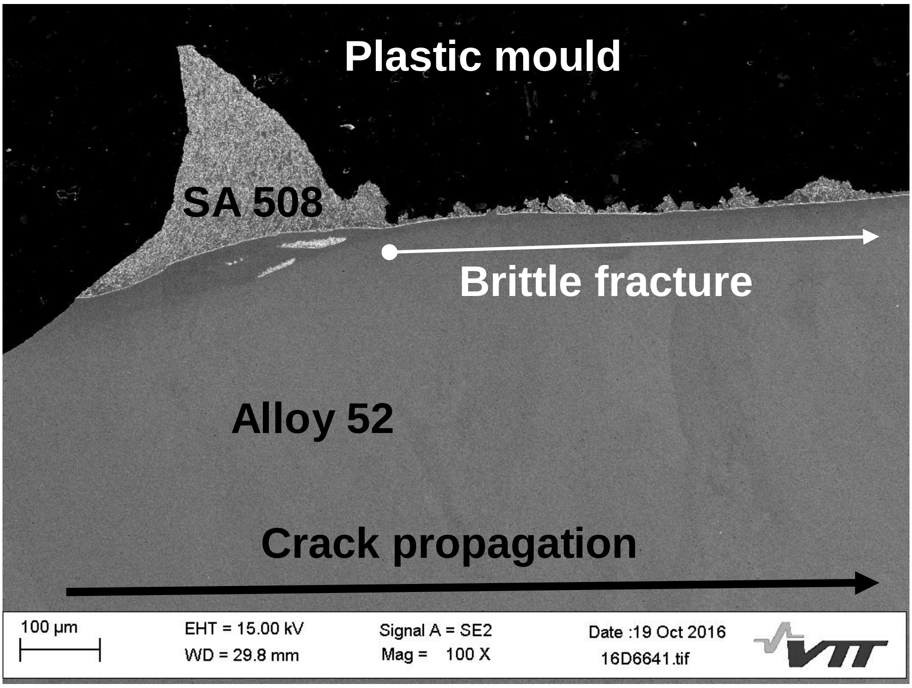

Figure 90. A SEM image of the cross-section of a brittle Charpy-V specimen.

7.2.1 Fraction of intergranular (IG) fracture observed on the fracture surfaces of Charpy-V specimens

Areas showing significant amount of IG cracking were detected in fracture surfaces of some 10000 h aged specimens, as shown earlier in this report. IG cracking was observed also in as-received material specimens, but in a smaller extent.

The effect of thermal ageing on the amount of IG fracture formed in Charpy-V tests was quantitatively measured by using the following method. Measurements were performed for two as-received and two 10000 h aged specimens, which were the ones showing low impact toughness values and a small amount of ductility on the fracture surfaces. Eight SEM images per sample were taken, all 1 mm from the V-notch and having a 1 mm spacing, and starting 1 mm from the edge of the specimen (Figure 91). The locations were chosen solely based on the distance from the notch and the edge of the specimen, and not based on their appearance, in order to avoid bias in selection of the locations. Thus, they are assumed to be representative for the fracture surface at 1 mm distance from the notch. SEM (SE) images with working distance of 15 mm and 1000x magnification (in Polaroid image size) were used in the measurements. It was observed that 1000x is the smallest magnification where it is possible to detect the areas of IG cracking from the image with a good certainty. IG fractions were determined manually from the image shown on a large computer screen by using ImageJ image processing program. An example of the IG fraction determination is presented in Figure 92. The IG fracture areas are marked with a yellow line. The software gives both the whole area of the image and the area of the marked areas, where the fraction of the IG fracture areas was determined for each specimen. The measurement results for the four specimens are presented in Table 22. The two as-received Charpy-V specimens gave similar results (about 6 and 8 % IG fracture), as did the two 10000 h aged specimens (19 and 20 %).

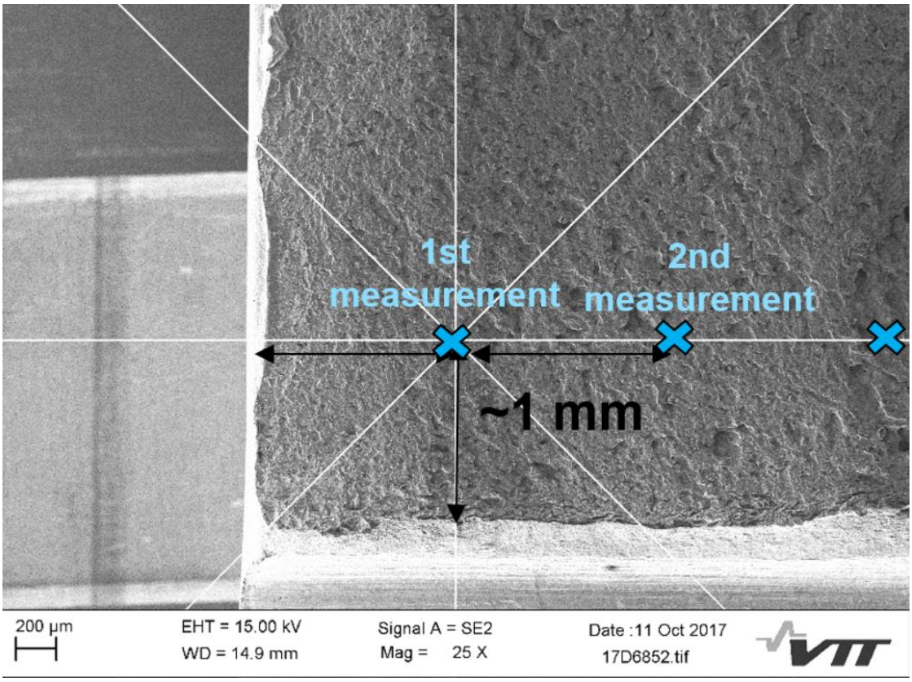

Figure 91. A SEM image of a Charpy-V specimen fracture surface showing the first two locations of the IG fraction determination. All the eight measurement points were located 1 mm from the notch and had a 1 mm spacing with each other.

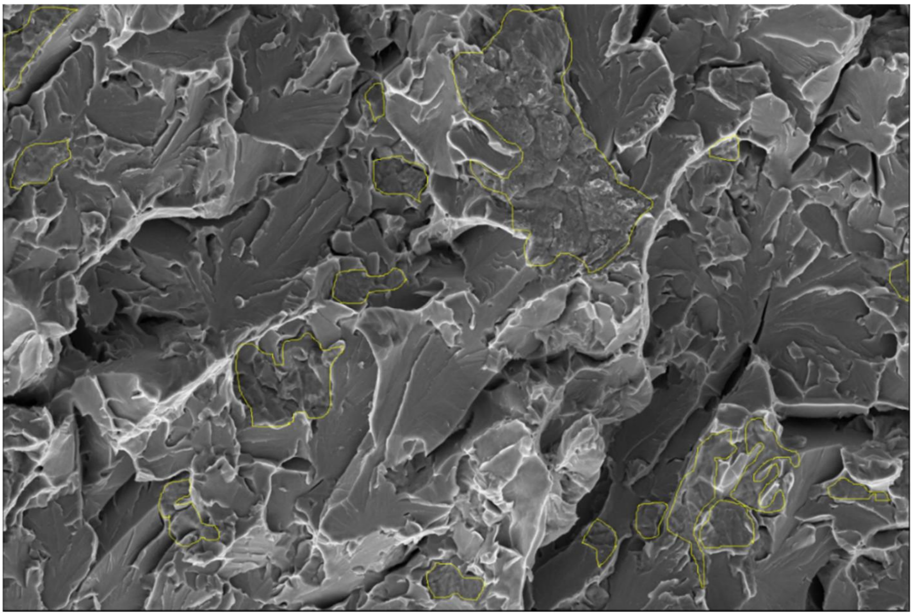

Figure 92. A SEM image of the Charpy-V specimen fracture surface, showing an example how the determination of IG cracking areas was made (yellow lines).

Table 22. Measurement results for IG fraction determination for four brittle Charpy-V specimens.

SPECIMEN									
as-rec (2B)	**IG%**	meas.1	meas.2	meas.3	meas.4	meas.5	meas.6	meas.7	meas.8
	8,1	0,10	0,15	0,12	0,02	0,05	0,14	0,03	0,05
as-rec (6B)	**IG%**	meas.1	meas.2	meas.3	meas.4	meas.5	meas.6	meas.7	meas.8
	5,6	0,08	0,06	0,07	0,00	0,02	0,05	0,06	0,10
10000 h (41)	**IG%**	meas.1	meas.2	meas.3	meas.4	meas.5	meas.6	meas.7	meas.8
	19,6	0,13	0,08	0,10	0,37	0,23	0,15	0,35	0,16
10000 h (66)	**IG%**	meas.1	meas.2	meas.3	meas.4	meas.5	meas.6	meas.7	meas.8
	18,9	0,14	0,39	0,26	0,18	0,17	0,11	0,12	0,13

7.3 Characterisation of the T_0 test specimen crack location

The vertical location of the brittle fracture initiation site with respect to the fatigue pre-crack tip was determined with a profilometer, Sensofar PLμ 2300 relying on a non-contact, dual-technology sensor, Table 23.

Table 23. Vertical location of the brittle fracture initiation site relative to the fatigue pre-crack plane.

Specimen ID	Vertical change in crack propagation plane µm	Specimen ID	Vertical change in crack propagation plane µm	Specimen ID	Vertical change in crack propagation plane µm
AS1	1	V1	16	K1	33
AS2	45	V2	81	K2	61
AS3	40	V3	67	K3	295
AS4	106	V4	1	K4	70
AS5	3	V5	301	K5	102
AS6	7	V6	14	K6	0
AS7	4	V7	138	K7	47
AS8	0	V8	75	K8	47
AS9	40	V9	58	K9	140
AS10	74	V10	207	K10	164
AS11	24	V11	56	K11	13
AS12	0	V12	15	K12	115
AS13	120	V13	30	K13	149
AS14	75	V14	166	K14	88
AS15	52	V15	19	K15	88

7.4 Characterization of LTCP test specimen fracture surfaces

A total of 12 successful LTCP tests were conducted, of which 11 resulted in applicable data (too much noise in one of the tests). Photographs of the fracture surfaces of the specimens tested with 30 and 100 cm^3 H_2/kg H_2O are presented in Figures 93-94, respectively. Crack growth direction is downwards in the photographs. The fracture surfaces are very uneven at most of the times, and the definition of the crack growth often required SEM examination. In the specimens tested with 30 cm^3 H_2/kg H_2O, the fatigue pre-crack typically only blunted during the J-R test. However, in one 5000 h aged and in both of the 10000 h aged specimens, small areas of possible intergranular crack growth were observed. Those areas are circled in the images. In specimens tested with a higher hydrogen content, 100 cm^3 H_2/kg H_2O, substantial IG crack propagation can be seen in some of the specimens, most notably in specimen A7, shown in Figure 94 b.

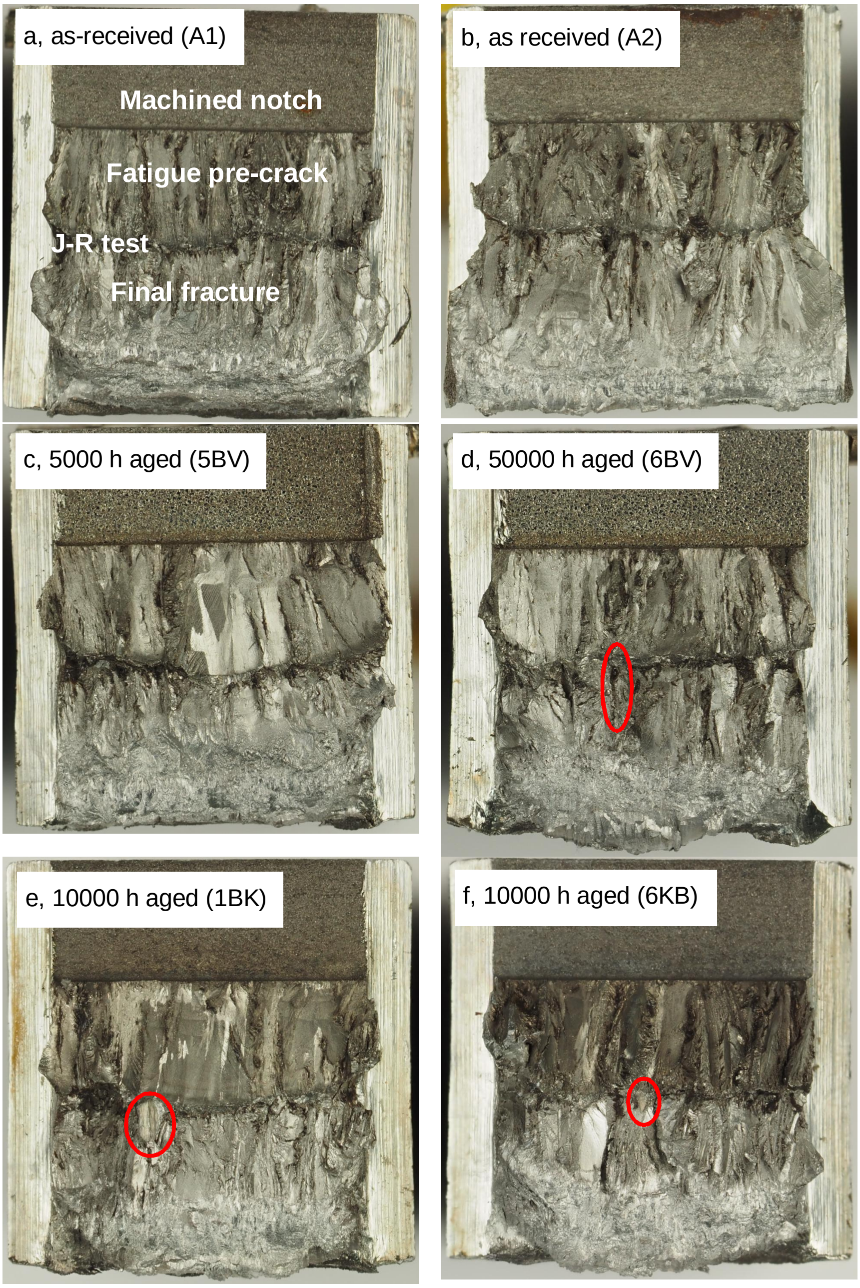

Figure 93. Photographs of the fracture surfaces of the LTCP test specimens tested in hydrogenated (30 cm^3 H_2/kg H_2O) low temperature water, a-f. Crack propagates downwards in the photographs. Areas of possible IG crack

propagation are circled in the images. No significant crack growth was observed in these specimens in addition to the local IG crack growth areas.

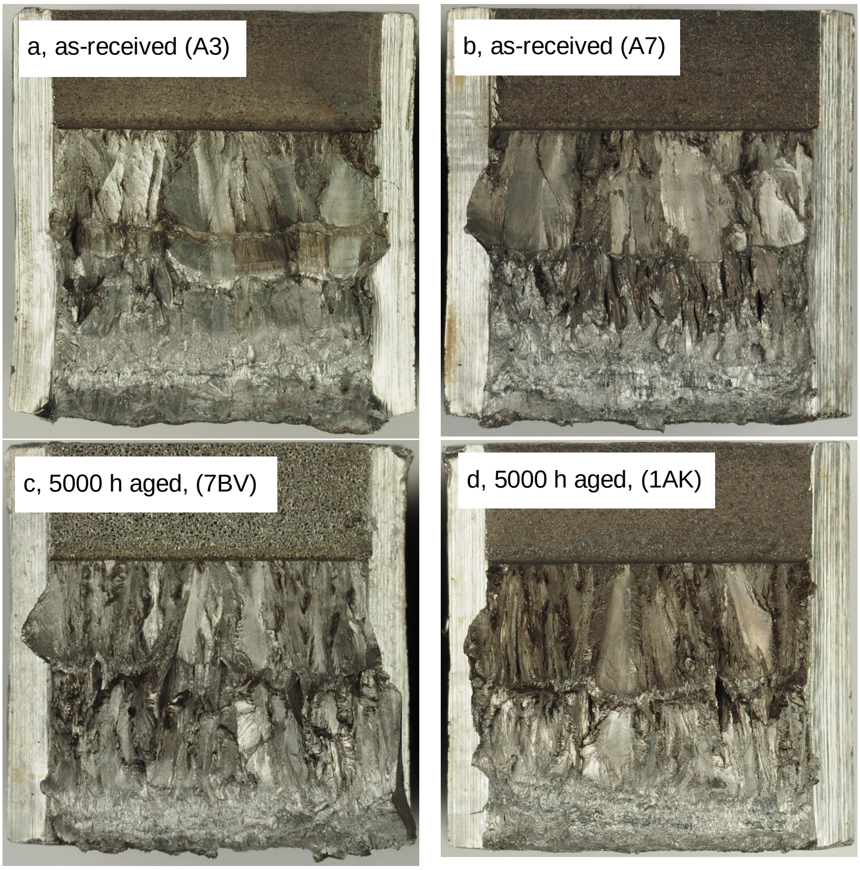

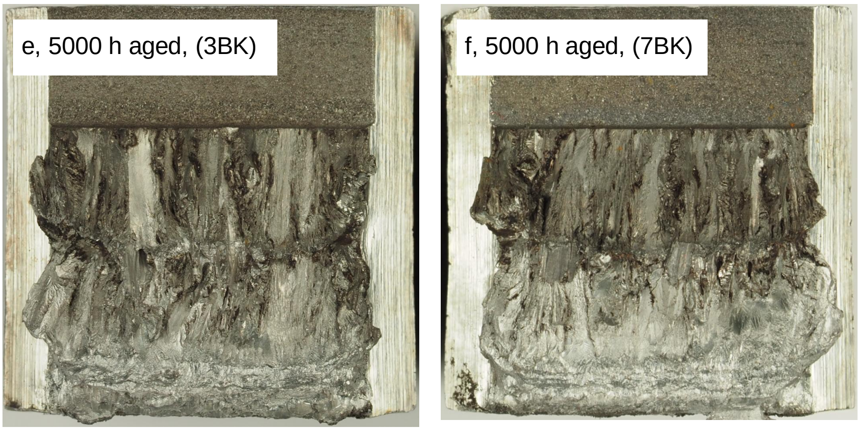

Figure 94. Photographs of the fracture surfaces of the LTCP test specimens tested in hydrogenated (100 cm^3 H_2/kg H_2O) low temperature water, a-f. Crack propagates downwards in the photographs. Substantial IG crack propagation can be seen in some of the specimens, most notably in specimen A7, shown in b.

It appears that the fatigue pre-crack has deviated from the specimen centreline in most of the specimens to some degree. An example of deviating cracks is seen in Figure 95, showing specimens A7, 7BV and 7BK.

Figure 95. SE(B) specimens after J-R testing, showing crack deviation from the centreline of the specimen.

J-R test specimens of the LTCP study were further characterized with SEM. The aim of the examination was to describe the overall appearance of the specimen fracture surfaces, to investigate how the crack initiates from the pre-crack when the J-R test is started, to evaluate if IG cracking occurs in the LTCP tests or not, and to characterize the features typical of hydrogen-induced cracking.

As illustrated in Figures 96-97, only pre-crack tip blunting occurs in J-R testing conducted for as-received material in 55 °C simulated PWR water with a PWR plant-relevant hydrogen content, 30 cm3 H2/kg H2O. This is consistent with the load-displacement data, which does not show signs of crack initiation and growth, either. However, some thermally aged specimens show local areas of crack propagation, of which examples are presented in Figures 98-99, where areas of fracture surfaces of two different 10000 h aged specimens are shown. A detailed view of the location showing crack propagation reveals that the crack propagation is basically intergranular, showing the carbide-rich fracture surface layer, repeatedly observed and reported in earlier LTCP studies of Alloy 52 (Ahonen et al. 2013, 2014, 2015, Ahonen 2016), but involves a significant amount of plastic deformation. As seen in Figure 100, the intergranular fracture surface is decorated by ductile ligaments.

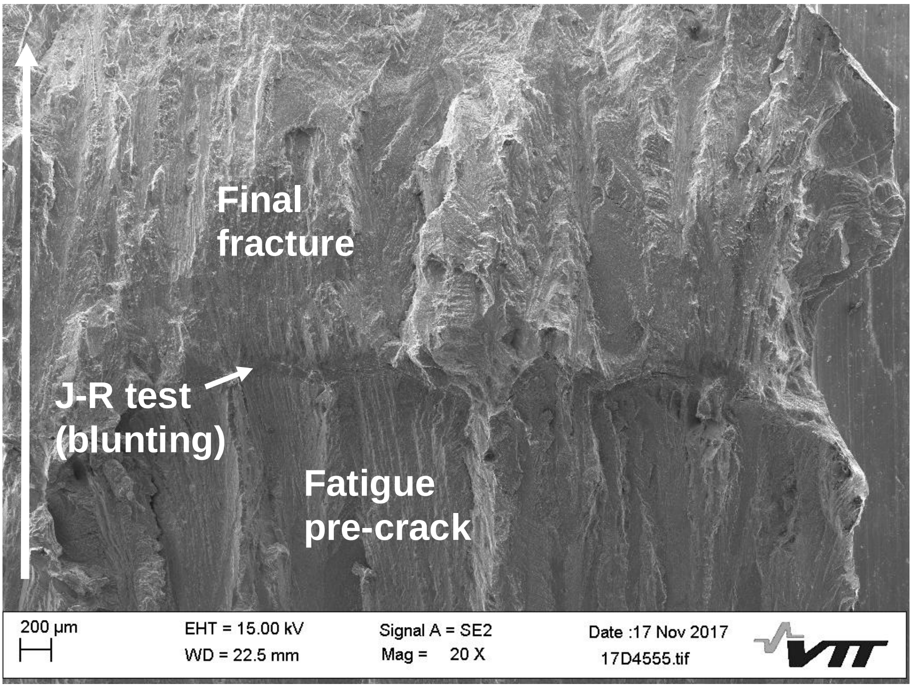

Figure 96. A SEM image of the fracture surface of an as-received state J-R test specimen tested with 30 cm^3 H_2/kg H_2O in low temperature (55 °C) simulated PWR water. Only pre-crack tip blunting is observed in the J-R testing in this specimen, and no actual crack growth.

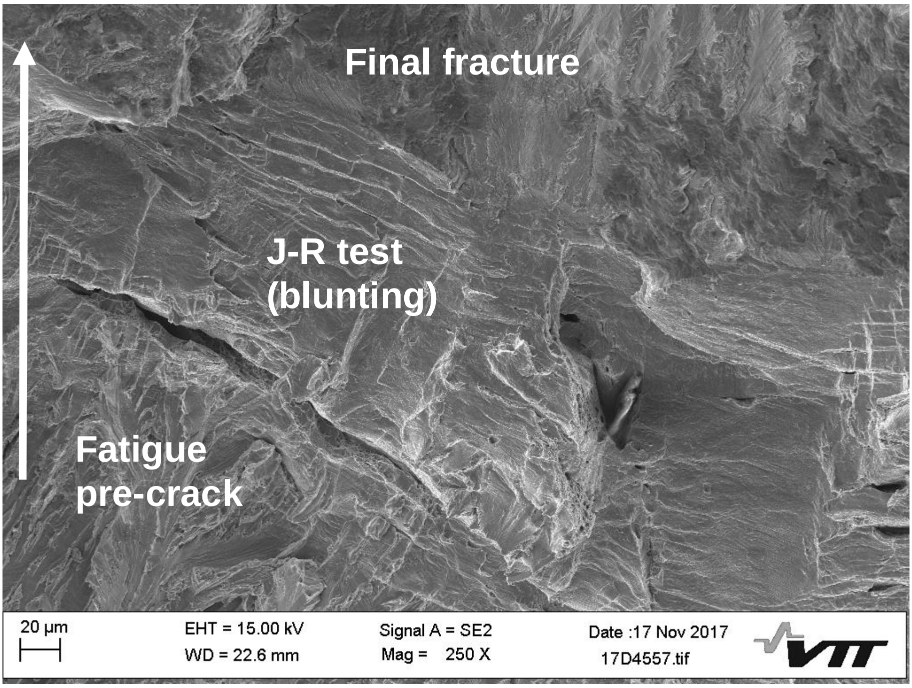

Figure 97. A SEM image of an as-received state J-R test specimen tested in 30 cm^3 H_2/kg H_2O low temperature (55 °C) simulated PWR water, showing the pre-crack tip blunting during J-R testing.

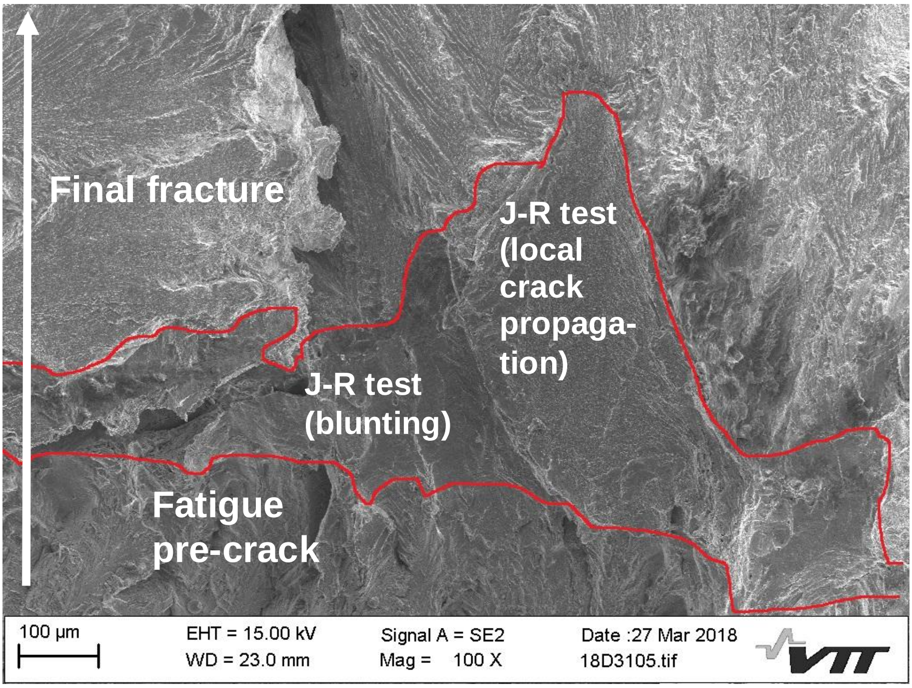

Figure 98. A SEM image of the fracture surface of a thermally aged (10000 h) J-R test specimen tested in 30 cm^3 H_2/kg H_2O low temperature (55 °C) simulated PWR water. Mostly pre-crack tip blunting is observed in the J-R testing in this specimen, but also local crack propagation. The fracture surface formed during the J-R testing is marked with a red line.

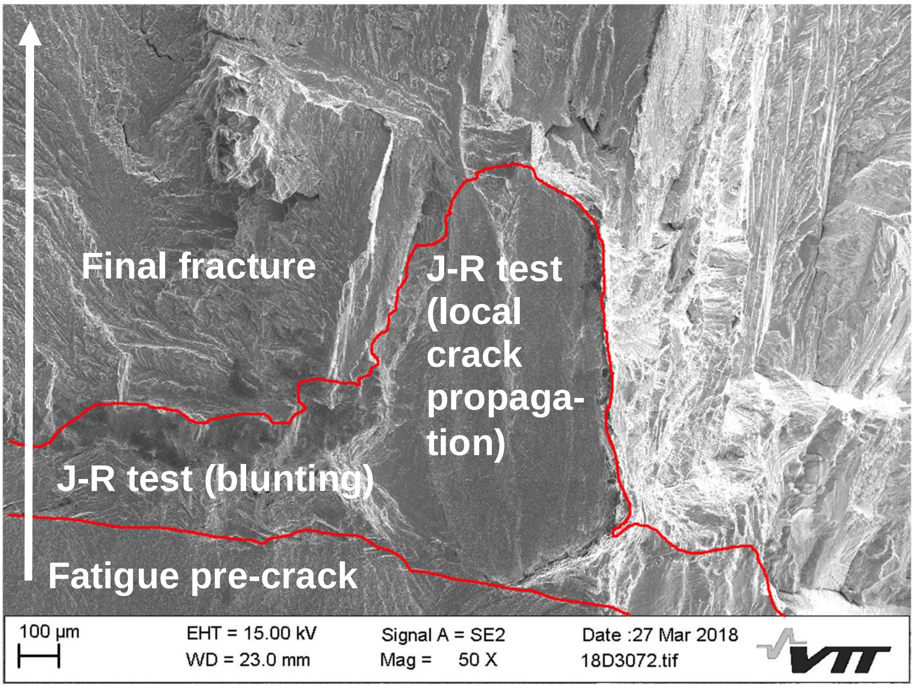

Figure 99. A SEM image of the fracture surface of a thermally aged (10000 h) J-R test specimen tested in 30 cm^3 H_2/kg H_2O low temperature (55 °C) simulated PWR water. Mostly pre-crack tip blunting is observed in the J-R testing in this specimen, but also local crack propagation. The fracture surface formed during the J-R testing is marked with a red line.

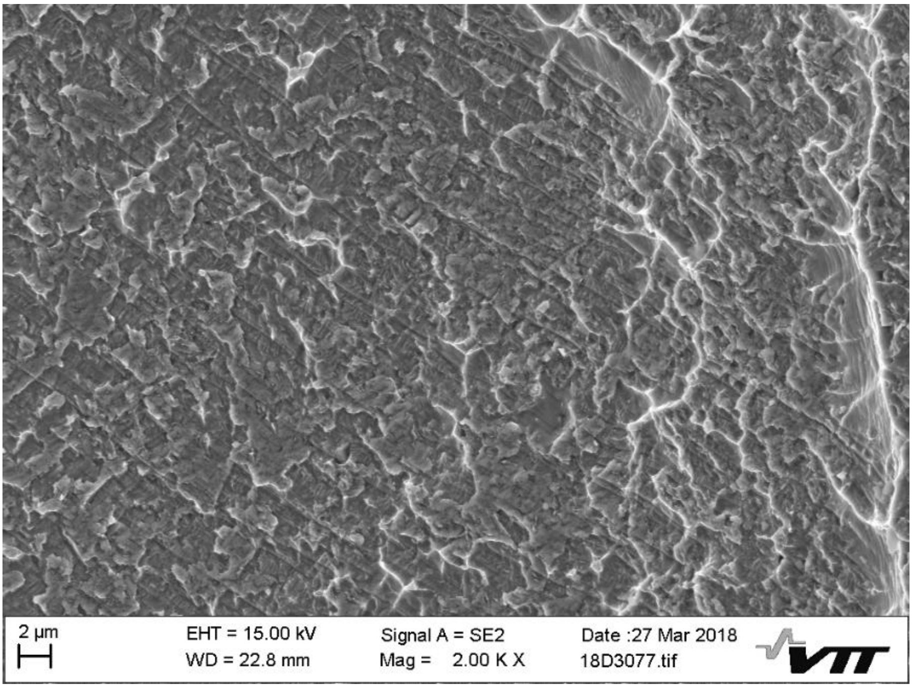

Figure 100. A SEM image of the local crack propagation on the fracture surface of a thermally aged (10000 h) J-R test specimen tested in 30 cm^3 H_2/kg H_2O low temperature (55 °C) simulated PWR water. The fracture surface at this area has mainly the appearance typical of intergranular hydrogen-induced cracking, but involves plastic deformation as well.

When tested with a higher hydrogen content, 100 cm^3 H_2/kg H_2O, some specimens show decreased fracture resistance. Significant areas of intergranular fracture can be seen on the fracture surfaces of the specimens showing the decreased fracture resistance due to the environment. As shown in Figure 101, large areas of intergranular cracking are seen in the specimen A3 (272 kJ/m^2), and even more so in the specimen A7 (Figure 102) showing the lowest J_Q value (107 kJ/m^2). A detailed view on the IG fracture surface of the specimen A3, Figure 103, shows much less ductility than in the case of local IG areas in specimens tested with 30 cm^3 H_2/kg H_2O.

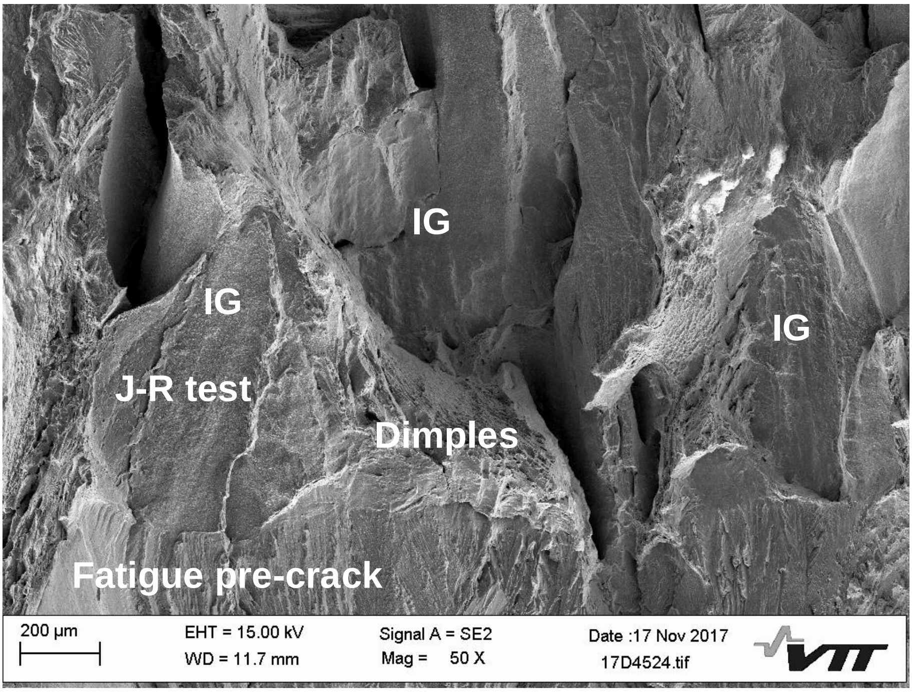

Figure 101. A SEM image of an as-received state J-R test specimen (A3) tested in 100 cm^3 H_2/kg H_2O low temperature (55 °C) simulated PWR water. Alternating areas of ductile dimple fracture and intergranular fracture are seen on this fracture surface.

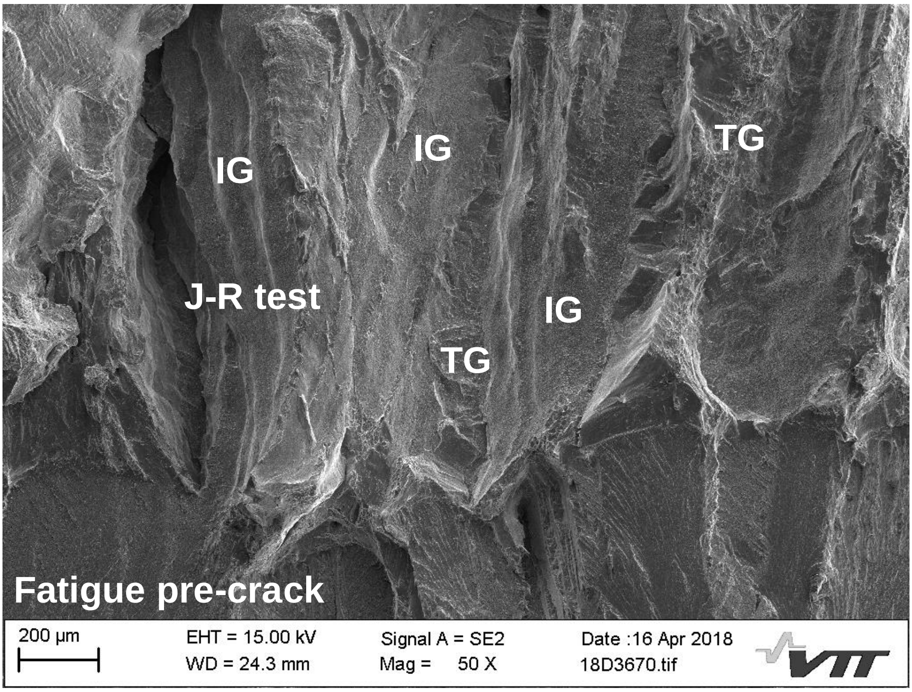

Figure 102. A SEM image of an as-received state J-R test specimen (A7) tested in 100 cm^3 H_2/kg H_2O low temperature (55 °C) simulated PWR water. The fracture type during testing is mainly intergranular. Small areas of transgranular fracture were observed between intergranular fracture.

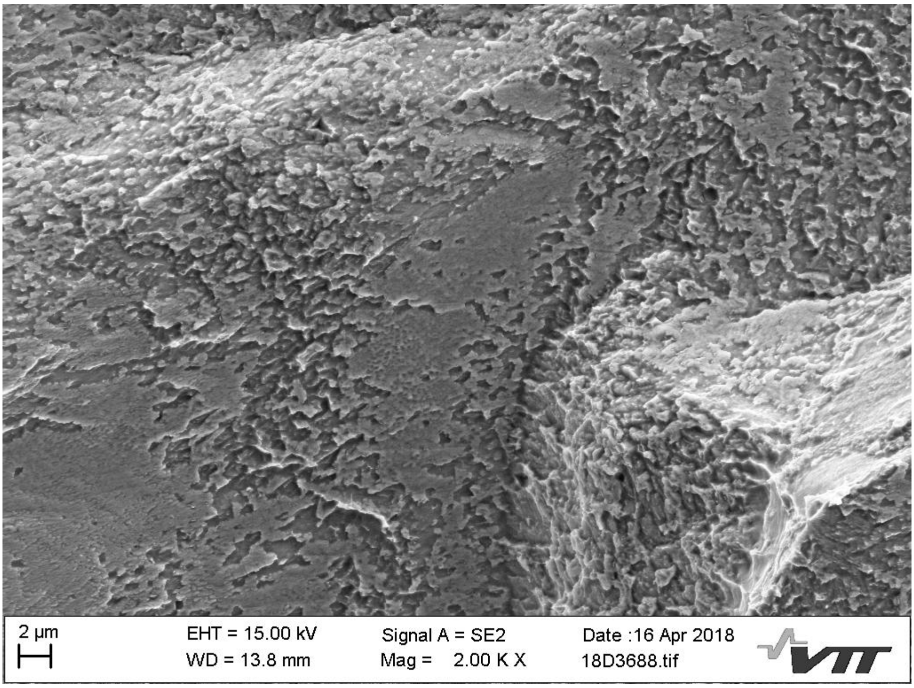

Figure 103. A SEM image of the local crack propagation on the fracture surface of an as-received J-R test specimen tested in 100 cm^3 H_2/kg H_2O low temperature (55 °C) simulated PWR water. The fracture surface at this area shows mainly the appearance typical of intergranular hydrogen-induced cracking, showing a layer-like carbide-rich fracture surface structure.

8. PARENT – Program to Assess the Reliability of Emerging Nondestructive Techniques

8.1 Introduction

The Program to Assess the Reliability of Emerging Nondestructive Techniques (PARENT) was established by the U.S. Nuclear Regulatory Commission (U.S. NRC). PARENT program was a follow-on to the Program for Inspection of Nickel Alloy Components (PINC). The NRC executed new agreements with VTT Technical Research Centre of Finland, Nuclear Regulatory Authority of Japan (NRA, former JNES), Korea Institute of Nuclear Safety (KINS), Swedish Radiation Safety Authority (SSM) and Swiss Federal Nuclear Safety Inspectorate (ENSI) in 2012 to establish PARENT. A series of round robin tests (RRTs) was conducted in PARENT based on the Bilateral International Agreements with participants and the in-kind contribution of resources from participating organisations.

PARENT was divided into blind and open RRT. The objective of blind testing was to evaluate the effectiveness of the established non-destructive examination (NDE) techniques for detection and sizing primary water stress corrosion cracking (PWSCC) in dissimilar metal welds (DMWs). Only qualified inspectors and procedures were applied in blind testing. The objective of open testing was to evaluate novel and emerging NDE techniques to find the most promising new techniques for the inspection of DMWs. Results of these RRTs are documented in reports (Meyer & Heasler 2017, Meyer et al. 2017a, Meyer et al. 2017b). At the last part of PARENT, a couple of Japanese and Korean Teams conducted a blind testing with novel techniques that were first applied in open testing. The results were reported by PNNL in 2018 (Meyer & Holmes 2018).

8.2 Test blocks

PARENT test blocks represented small bore (SBDMW) and large bore (LBDMW) test blocks together with bottom-mounted instrumentation nozzles (BMI). In addition, one weld overlay (WOL) was included in blind testing. Test blocks contained simulated flaws including laboratory-grown stress corrosion cracks (SCC), thermal fatigue cracks (TFC), mechanical fatigue cracks (MFC), tightened weld solidification cracks (SC), welding defects and electrical discharge machining (EDM) notches.

8.2.1 Blind test blocks

The test blocks used in blind testing are listed in Table 24 and the simulated flaw types in Table 25. VTT conducted blind testing for SBDMW test blocks P35 and P40.

Table 24. Summary of PARENT blind test blocks (Meyer & Heasler 2017).

Category	Typical weldment	Diameter/thickness	Test block IDs
SBDMW	DMW piping welds, BWR	OD: 289 mm, 815 mm Thickness: 35 mm, 39.5 mm	P35, P40
LBDMW	DMW piping welds, PWR	OD: 852–895 mm Thickness: 68–78 mm	P15–P17, P45, P13, P33
BMI	J-groove weld	Tube OD: 38–45 mm	P25, P26, P6, P8, P9
WOL		Pipe OD: 116 mm Overlay OD: 180 mm Pipe thickness: 14 mm	P27
OD = outer diameter			

Table 25. Summary of simulated flaws in PARENT blind test blocks (Meyer & Heasler 2017).

Flaw type	Total flaws
SCC	4
TFC	31
SC	44
Welding defects	10
MFC	5
EDM	3
Total	**97**

8.2.2 Open test blocks

The test blocks used in open testing are listed in Table 26 and the simulated flaw types in Table 27 (Meyer et al. 2017a). VTT conducted open testing for SBDMWs P1, P4, P41 and for flat bar (FB) test blocks P28–P32, P38, P42 and P46.

Table 26. Summary of PARENT open test blocks (Meyer et al. 2017a).

Category	Typical weldment	Diameter/thickness	Test block IDs
SBDMW full circumference	DMW piping welds, BWR	OD: 286–387 mm Thickness: 32–47 mm	P1, P4, P41
LBDMW full circumference	DMW piping welds, PWR	OD: 897 mm Thickness: 78.5 mm	P37
LBDMW partial circumference		OD: 852.5 mm Thickness: 77 mm	P12, P23, P24
Flat bar	DMW piping welds, BWR	OD: Flat Thickness: 30.3 mm	P28–P32, P38, P42, P46
BMI	J-groove weld	Tube OD: 38–45 mm	P21, P22, P5, P7

Table 27. Summary of simulated flaws in PARENT open test blocks (Meyer et al. 2017a).

Flaw type	**Test block ID (quantity)**	**Total flaws**
SCC	P12 (1), P28 (1), P29 (1), P31 (1), P32 (1), P38 (1)	6
TFC	P5 (3), P1 (4), P4 (2)	9
SC	P7 (4), P41 (12), P37 (9)	25
Welding defects	P37 (2)	2
MFC	P30 (1)	1
EDM	P4 (2), P42 (1), P12 (1), P21 (3), P22 (3), P23 (3), P24 (4)	17
Total		**60**

8.3 Inspection procedures

8.3.1 Blind testing procedures

Inspection procedure types in blind testing were based on phased array ultrasonic (PAUT), conventional ultrasonic (UT), eddy current (ECT) and time-of-flight diffraction (TOFD) techniques or combination of them. Procedure types and the number of inspection summary data sheets collected from each procedure type by test block type are listed in Table 28.

VTT's procedure provided by Zetec utilized PAUT technique with 1.5 MHz transmitter-receiver (TR) probes. Both longitudinal (LW) and shear wave (SW) modes were applied. Overview of the technique is shown in Table 29.

Table 28. Number of inspection procedure types and inspection summary data sheets by procedure and block types in PARENT blind testing (Meyer & Heasler 2017).

Procedure type	**Number of procedure types**	**Number of inspection summary data sheets**		
		DMW	**BMI**	**WOL**
PAUT	7	16	0	2
UT	5	17	0	0
ECT	3	1	8	0
UT.PAUT	3	13	0	0
UT.TOFD	1	2	0	0
UT.ECT	2	6	0	0
TOFD.ECT	1	0	2	0
UT.TOFD.ECT	1	2	0	0
Total	**25**	**57**	**10**	**2**

Table 29. Overview of PAUT technique used at VTT in blind testing.

Flaw orientation	Beam direction	Focal law type	Refracted angles	Skew angles
Circumferential	TR LW	Linear	45º, 60º, 70º	0º
	TR SW		45º, 60º	
Axial	TR LW	Azimuthal	22.5º, 30º, 37.5º, 45º (OD < 304.8 mm) 25º, 35º, 45º, 55º (OD ≥ 304.8 mm and < 1016 mm)	-25º to 25º, resolution 2.5º
	TR SW		35º, 40º,45º (OD < 304.8 mm) 35º, 45º,55º (OD ≥ 304.8 mm)	

8.3.2 Open testing procedures

The number of inspection summary records for block types and inspection procedure types in open testing are listed in Table 30.

VTT established two teams for open testing. Team 114 used the same procedure as VTT's blind testing team. As VTT performed open testing before blind, this test worked as an implementation of the procedure at VTT. Procedure of Team 122 utilized PAUT techniques shown in Table 31 with 1.5 MHz TR probe.

Table 30. Number of inspection summary records for procedure types and block types by access in PARENT open testing (Meyer et al. 2017a).

Procedure type	Number of inspection summary records						
	SBDMW ID	SBDMW OD	LBDMW ID	LBDMW OD	FB ID	FB OD	BMI
ADVPAUT	0	6	5	12	16	25	0
ADVPAUT, NLUT	0	3	0	1	0	10	0
ECT	6	0	4	0	15	3	9
GUW	0	1	0	0	0	0	1
LUV	0	4	0	0	0	0	6
MM	3	0	3	0	5	0	1
NLUT	0	2	0	0	3	11	0
PAUT	0	8	2	2	2	32	0
RT	0	1	0	0	0	9	0
UIR	0	0	0	0	0	6	0
UT	0	1	0	0	0	8	0
Total	**9**	**26**	**14**	**15**	**41**	**105**	**17**

ADVPAUT = advanced phased array ultrasonic testing, NLUT = nonlinear ultrasonic testing; GUW = guided ultrasonic waves; LUV = laser ultrasound visualization; MM = microwave near-field microscopy; RT = radiographic testing; UIR = ultrasound infrared tomography

Table 31. Overview of PAUT techniques used by VTT's Team 122 in open testing.

Flaw orientation	**Beam direction**	**Focal law type**	**Refracted angles**	**Beam skew angles**
Circumferential	TR LW	Linear	45º, 50º, 55º, 60º	0º
		Azimuthal	40º–70º, resolution 1º	

8.4 Data processing

8.4.1 Data reporting

The teams reported the results on technique datasheets and inspection summary datasheets. For example, if an ultrasonic inspection procedure consists of three refracted angles, which may be used separately for detection, length sizing and depth sizing, this information gives three individual technique datasheets. This information is combined in completion of inspection summary datasheet (Meyer & Heasler 2017).

8.4.2 Scoring procedure

PARENT utilized the same scoring criteria as in PINC. A tolerance box shown in Figure 104 where δX = δY = 10 mm was added to flaw true-state dimensions to avoid penalizing minor positioning errors (Meyer & Heasler 2017).

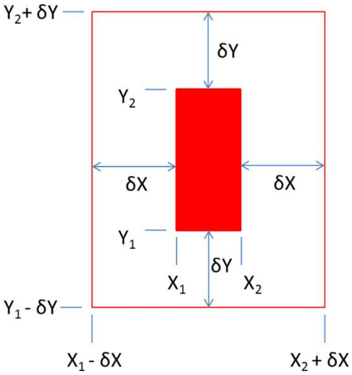

Figure 104. Tolerance (dX and dY) applied to flaw true state (in red) dimensions in PARENT (Meyer & Heasler 2017).

8.4.3 Detection performance analysis

Detection performance can be evaluated with probability of detection (POD) and false call probability (FCP). POD evaluation was done only for blind testing because in open testing, the teams were provided with true-state information of flaws. A logistic regression model was used to relate POD to flaw size *S*, which represents either depth or length. The following equations give the logistic regression model and the function logistic(x). (Meyer & Heasler 2017).

$$\mathrm{POD}(S) = \mathrm{logistic}(\beta 1 + \beta 2S) \tag{12}$$

$$\mathrm{logistic(x)} = \frac{1}{1 + \exp(-x)} \tag{13}$$

Where

$\beta 1$ and $\beta 2$ = unknown parameters to be determined by the regression algorithm.

8.4.4 Sizing analysis

Sizing analysis (depth and length) was done using linear regression. An error relation between the measured and true sizes of the flaws is defined by the following regression formula (Meyer & Heasler 2017).

$$M_i = B1 + B2(T_i + E_i) \tag{14}$$

Where

M_i = the measured size of flaw *i*
T_i = the true size of flaw *i*
E_i = the measurement error in sizing flaw *i*

The root mean square error (RMSE) aggregates the magnitude of the errors and is used in comparison of the results. RMSE is computed according to the formula shown below.

$$\mathrm{RMSE} = \sqrt{\frac{1}{n}\sum_{i=1}^{n}(M_i - T_i)^2} \tag{15}$$

The bias and standard deviation σ represent systematic and random components to the error and are calculated with the following formulas.

$$\mathrm{bias} = \frac{1}{n}\sum_{i=1}^{n}(M_i - T_i) \tag{16}$$

$$\sigma = \sqrt{\frac{1}{n}\sum_{i=1}^{n}[(M_i - T_i) - \mathrm{bias}]^2} \tag{17}$$

8.5 Blind testing results

This section presents a short overview of the blind testing results concentrating on ultrasonic testing results of SBDMWs, which was the only test block category that VTT tested.

8.5.1 Detection performance

Overall POD for all procedures applied to SBDMW blocks presented in Figure 105 and Figure 106 shows clearly better detection performance for PAUT than for UT. Table 32 presents the summary of POD versus depth for procedures where a rather good performance of VTT's procedure is observed. Figure 107 shows an example of indication plot for VTT's PAUT procedure with three detections, one false call and one missed flaw.

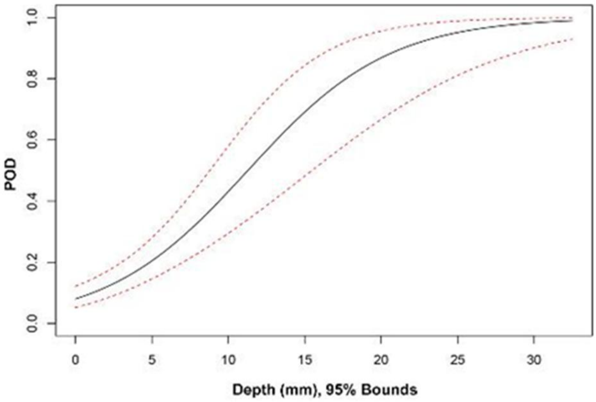

Figure 105. POD versus depth (mm) for UT procedures applied to SBDMW test blocks (Meyer & Heasler 2017).

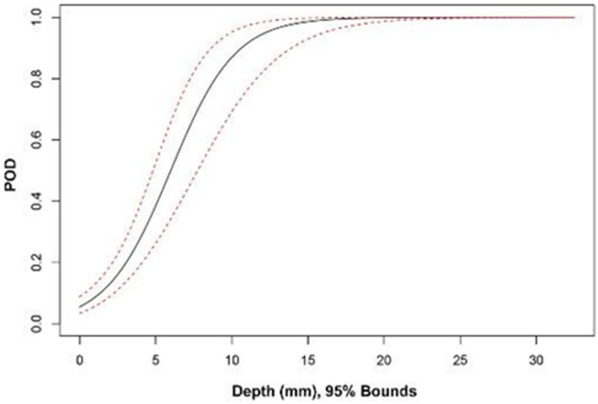

Figure 106. POD versus depth (mm) for PAUT procedures applied to SBDMW test blocks (Meyer & Heasler 2017).

Table 32. Summary of POD (%) versus depth for procedures applied to SBDMWs (OD access) (Meyer & Heasler 2017).

Procedure	**NOBS**	**0 mm**	**5 mm**	**10 mm**	**15 mm**	**30 mm**
PAUT.108.1	28	5	35	84	98	100
PAUT.115	28	6	58	97	100	100
PAUT.126.1	28	3	12	33	65	99
PAUT.128 (VTT)	28	11	51	89	99	100
UT.108	28	6	33	81	97	100
UT.126	28	8	14	23	35	76
UT.134.2	28	9	28	59	84	100
UT.25(a)	12	11	17	26	37	74
UT.TOFD.117	28	4	42	92	99	100
All	236	6	28	69	93	100

(a) UT.25 was not a qualified procedure.

NOBS = number of observations

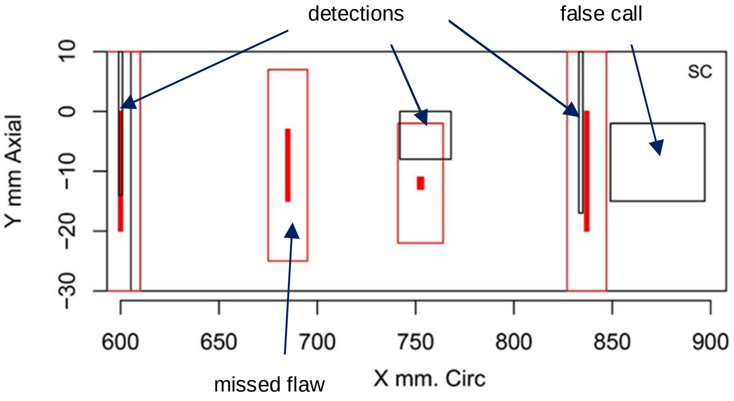

Figure 107. Example of indication plot for VTT's PAUT procedure applied to test block P35 (X-Y view) (Meyer & Heasler 2017).

Table 33 provides POD results as a function of depth, flaw orientation and access for LBDMW and SBDMW blocks. Better detection performance is observed for inside diameter (ID) access vs. OD access and better performance is observed for SBDMW test blocks than LBDMW test blocks for a given flaw size. The general trend indicates that circumferential flaws are easier to detect than axial flaws, although this appears to be dependent of flaw size for SBDMW test blocks with the effect diminishing with increasing flaw depth. This is likely an artifact caused by saturation of POD with flaw depth in SBDMW test blocks (Meyer & Heasler 2017).

Table 33. Summary of POD (%) by access, orientation and block type versus flaw depth (Meyer & Heasler 2017).

Access	**Orientation**	**Block type**	**0–5 mm**	**5–10 mm**	**10–20 mm**	**> 20 mm**
ID	Axial	LBDMW	25±23	75±13	83±17	75±13
OD	Axial	LBDMW	0±12	20±11	10±11	67±12
OD	Axial	SBDMW	22±14	44±12	78±14	100±7
ID	Circumferential	LBDMW	43±13	92±9	100±15	100±8
OD	Circumferential	LBDMW	30±10	27±12	40±22	80±13
OD	Circumferential	SBDMW	58±7	78±6	88±5	90±5

8.5.2 Depth sizing results

Summary of depth sizing errors for ultrasonic procedure types and each procedure are presented in Table 34 and Table 35, respectively. These tables indicate the best performance for PAUT. Only procedures PAUT.108.1 and PAUT.115 produced depth sizing RMSEs of less than the ASME Code requirement for depth sizing accuracy (3.2 mm). VTT's procedure is among the top five procedures when RMSE is used as criterion.

Depth sizing regression plots for all PAUT procedures and VTT's procedure applied to SBDMWs are presented in Figure 108 and Figure 109, respectively. These plots indicate slight oversizing of the shallow flaws and slight undersizing of deep flaws.

Table 34. Summary of depth sizing errors for ultrasonic procedure types on SBDMWs with OD access (Meyer & Heasler 2017).

Procedure type	**NOBS**	**Bias (mm)**	**RMSE (mm)**
PAUT	84	-0.9	3.6
UT	54	-3.5	7.9
UT.TOFD	19	0.6	4.1
All	157	-1.6	5.5

Table 35. Summary of depth sizing errors for procedures on SBDMWs (OD access) (Meyer & Heasler 2017).

Procedure	**NOBS**	**Bias (mm)**	**RMSE (mm)**
PAUT.108.1	21	-1.7	2.4
PAUT.115	25	-0.3	1.8
PAUT.126.1	14	-5.0	5.9
PAUT.128	24	1.4	4.2
UT.108	20	-1.0	4.2
UT.126	10	-4.1	7.1
UT.134.2	21	-4.9	9.5
UT.25[(a)]	3	-8.8	13.9
UT.TOFD.117	19	0.6	4.1
[(a)] UT.25 was not a qualified procedure.			

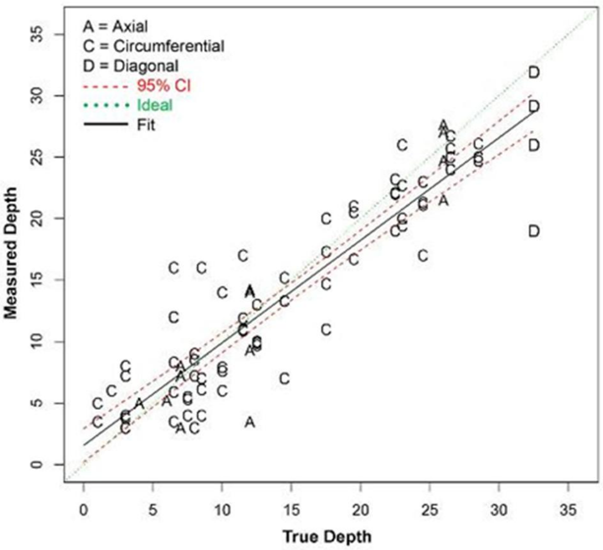

Figure 108. Depth sizing fit (mm) for PAUT procedures applied to SBDMWs (OD access) in PARENT blind testing (Meyer & Heasler 2017).

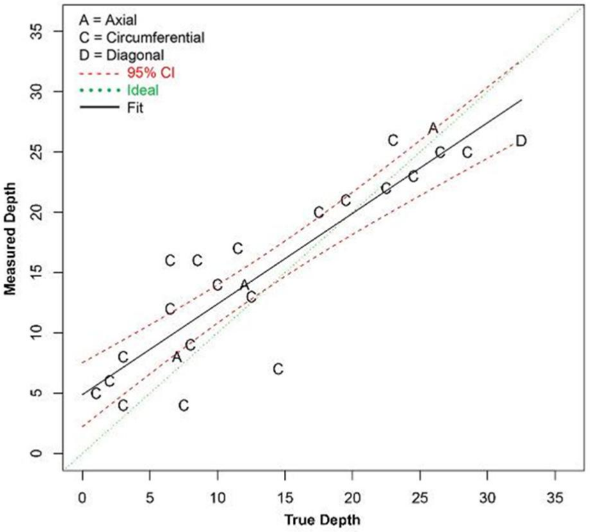

Figure 109. Depth sizing fit (mm) PAUT procedure PAUT.128 applied to SBDMWs (OD access) in PARENT blind testing (Meyer & Heasler 2017)

Depth sizing performance as measured by RMSE and bias is provided in Table 36 for each combination of access, block type, and flaw orientation variables. Better depth sizing performance is observed for ID versus OD access and on SBDMW versus LBDMW test blocks. Flaw orientation does not appear to have an influence on depth sizing performance (Meyer & Heasler 2017).

Table 36. Depth sizing results by access, orientation and block type (Meyer & Heasler 2017).

Access	Orientation	Block type	Bias (mm)	RMSE (mm)
ID	Axial	LBDMW	0.3	3.0
ID	Axial	SBDMW	-	-
ID	Circumferential	LBDMW	0.8	3.0
ID	Circumferential	SBDMW	-	-
OD	Axial	LBDMW	-6.1	10.0
OD	Axial	SBDMW	-1.3	5.0
OD	Circumferential	LBDMW	-0.1	9.7
OD	Circumferential	SBDMW	-1.2	4.7

8.5.3 Length sizing results

Summary of length sizing errors for ultrasonic procedure types and each procedure are presented in Table 34 and Table 35, respectively. These tables indicate no substantial difference between procedure types. All procedures except UT.126 produced depth sizing RMSEs of less than the ASME Code requirement for length sizing accuracy (19 mm). VTT's procedure is among the top five procedures when RMSE is used as criterion (Meyer & Heasler 2017).

Length sizing regression plots for all PAUT procedures and VTT's procedure applied to SBDMWs are presented in Figure 110 and Figure 111 respectively. These plots indicate slight oversizing of the shallow flaws for all procedures and regular slight oversizing of all flaws for VTT's procedure (Meyer & Heasler 2017).

Table 37. Summary of length sizing errors for ultrasonic procedure types on SBDMWs with OD access (Meyer & Heasler 2017).

Procedure type	NOBS	Bias (mm)	RMSE (mm)
PAUT	84	6.6	11.8
UT	54	6.0	12.8
UT.TOFD	23	4.3	11.7
All	161	6.1	12.1

Table 38. Summary of length sizing errors for procedures on SBDMWs (OD access) (Meyer & Heasler 2017).

Procedure	NOBS	Bias (mm)	RMSE (mm)
PAUT.108.1	21	1.0	9.2
PAUT.115	25	8.2	13.1
PAUT.126.1	14	5.7	12.4
PAUT.128	24	10.5	12.0
UT.108	20	3.9	8.0
UT.126	10	18.6	22.6
UT.134.2	21	1.4	9.9
UT.25[(a)]	3	10.0	12.7
UT.TOFD.117	23	4.3	11.7
[(a)] UT.25 was not a qualified procedure.			

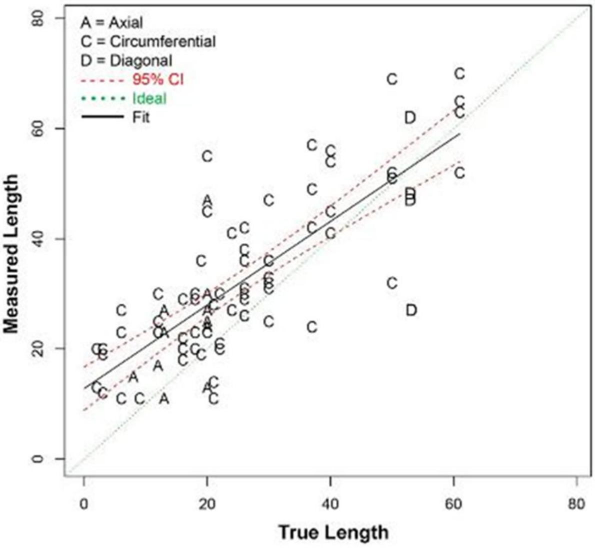

Figure 110. Length sizing fit (mm) for PAUT procedures applied to SBDMWs (OD access) in PARENT blind testing (Meyer & Heasler 2017).

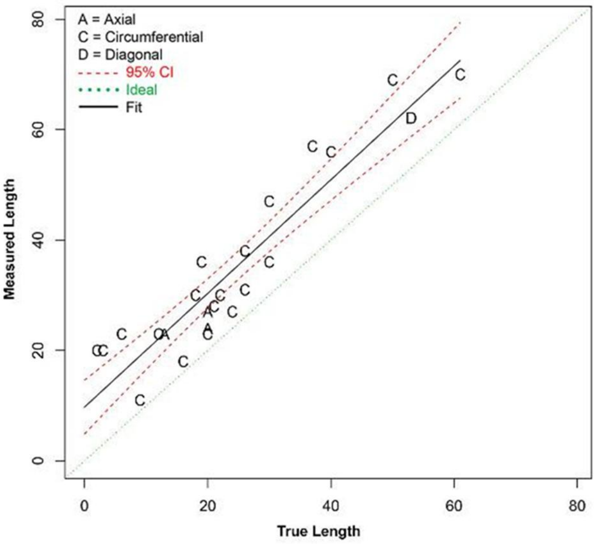

Figure 111. Length sizing fit (mm) for procedure PAUT.128 applied to SBDMWs (OD access) in PARENT blind testing (Meyer & Heasler 2017).

Length sizing performance as measured by RMSE and bias is provided in Table 39 for each combination of access, block type, and flaw orientation variables. Better length sizing performance is observed for ID versus OD access and better sizing performance is observed on axial SBDMW versus axial LBDMW test blocks. There does not appear to be an effect of block type or flaw orientation on length sizing performance.

Table 39. Length sizing results by access, orientation and block type (Meyer & Heasler 2017).

Access	Orientation	Block type	Bias (mm)	RMSE (mm)
ID	Axial	LBDMW	5.0	10.0
ID	Axial	SBDMW	-	-
ID	Circumferential	LBDMW	2.1	6.8
ID	Circumferential	SBDMW	-	-
OD	Axial	LBDMW	7.2	15.5
OD	Axial	SBDMW	3.9	8.7
OD	Circumferential	LBDMW	3.7	11.2
OD	Circumferential	SBDMW	7.3	12.6

8.6 Open testing results

This section provides a short overview of the open testing results concentrating on ultrasonic testing results of SBDMWs and FBs, which were the two test block categories that VTT tested.

8.6.1 Depth sizing results

Depth sizing results for procedure types and all procedures in PARENT open testing are shown in Table 40 and Table 41, respectively. These tables indicate the best performance for RT and UT procedures. 10 procedures including the three VTT's procedures produced depth sizing RMSEs of less than the ASME Code requirement for depth sizing accuracy (3.2 mm). (Meyer et al. 2017a).

Figure 112 presents the depth sizing regression for all PAUT procedures. Figure 113 through Figure 115 present the depth sizing regression for VTT's procedures on SBMW and FB test blocks, respectively. These plots indicate slight oversizing of the shallow flaws and slight undersizing of deep flaws. There is no difference in performance of linear and sectorial scan techniques (Figure 114 and Figure 115). An example of indication plot for VTT's procedure containing minor and major depth over- and undersizing results is seen in Figure 116 (Meyer et al. 2017a).

Table 40. Depth sizing results for procedure types applied to SBDMW and FB test blocks with OD access (Meyer et al. 2017a).

Procedure type	NOBS	Bias (mm)	RMSE (mm)
ADVPAUT	57	2.7	5.3
NLUT	38	0.7	6.7
PAUT	79	0.3	3.4
RT	14	-0.2	2.0
UIR	6	1.0	3.4
UT	11	-0.0	2.1
All	205	1.0	4.6

Table 41. Depth sizing results for procedures applied to SBDMW and FB test blocks with OD access (Meyer et al. 2017a).

Procedure	**NOBS**	**Bias (mm)**	**RMSE (mm)**
HHUT.27.1	9	3.2	11.1
HHUT.27.2	7	3.1	7.1
LASH.18	9	-1.7	3.3
PAATOFD.29.0	13	0.8	4.6
PAATOFD.29.1	7	3.6	5.5
PAATOFD.29.2	7	3.9	5.8
PATP.29	9	2.4	6.6
PAUT.114	26	0.2	2.8
PAUT.122.1	7	0.4	0.9
PAUT.122.2	7	-0.0	1.1
PAUT.131.1	5	4.1	8.8
PAUT.131.2	16	0.3	0.6
PAUT.131.4	8	-0.1	0.4
PAUT.20	10	-0.6	5.4
RT.109	5	-0.3	2.1
RT.112	9	-0.1	1.9
SAFT.17	21	3.3	4.8
SHPA.6.1	5	1.6	1.9
SHPA.6.2	4	-5.2	5.4
SHPA.6.3	4	1.0	1.4
UIR.20	6	1.0	3.4
UT.104	11	-0.0	2.1
All	205	1.0	4.6

HHUT = higher harmonic ultrasonic technique; LASH = large amplitude excitation subharmonic UT; PAATOFD = phased array asymmetrical beam time-of-flight diffraction; PATP = phased array twin probe; SAFT = synthetic aperture focusing technique; SHPA = subharmonic phased array

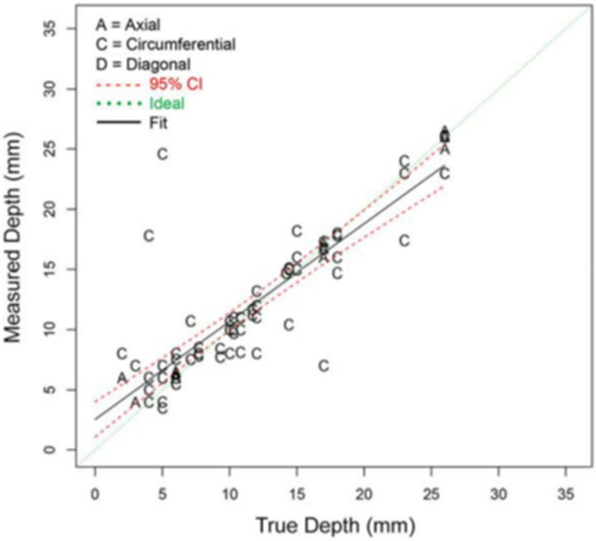

Figure 112. Depth sizing regression for PAUT procedures on SBDMW and FB test blocks in PARENT open testing with OD access (Meyer et al. 2017a).

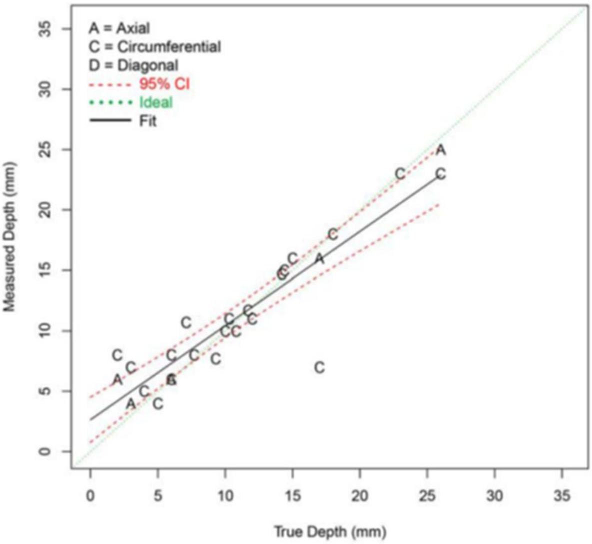

Figure 113. Depth sizing regression for procedure PAUT.114 on SBDMW and FB test blocks in PARENT open testing with OD access (Meyer et al. 2017a).

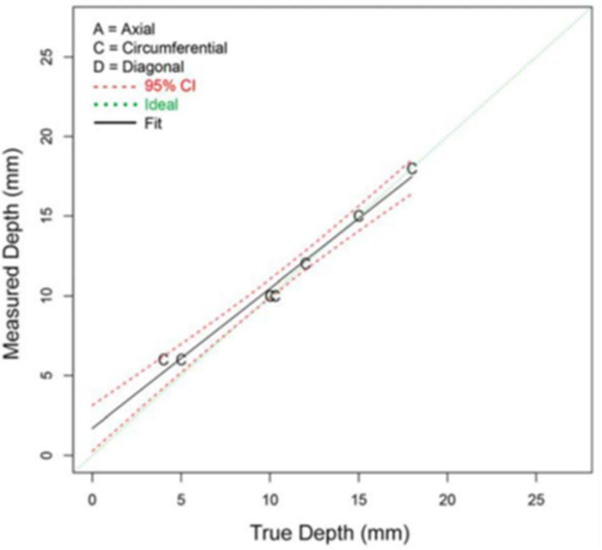

Figure 114. Depth sizing regression for procedure PAUT.122.1 (linear) on SBDMW and FB test blocks in PARENT open testing with OD access (Meyer et al. 2017a).

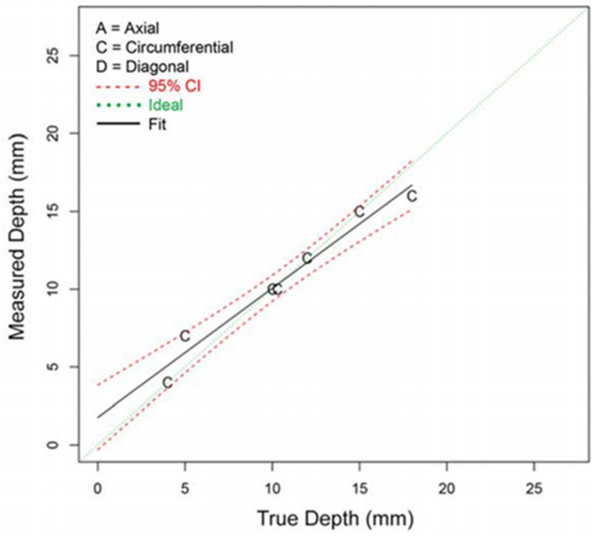

Figure 115. Depth sizing regression for procedure PAUT.122.2 (sectorial) on SBDMW and FB test blocks in PARENT open testing with OD access (Meyer et al. 2017a).

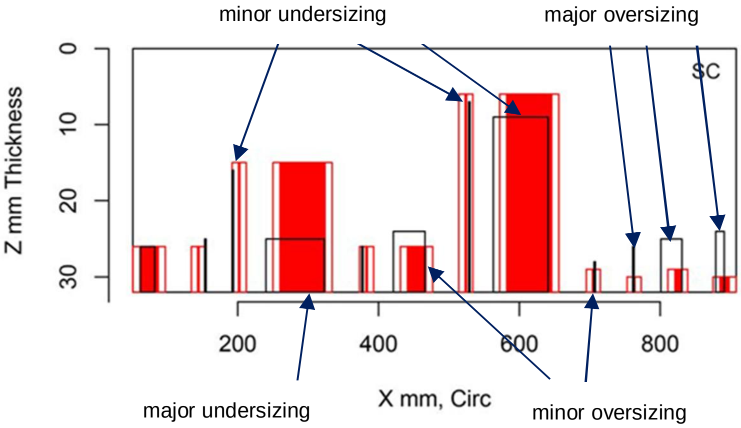

Figure 116. Indication plot for procedure PAUT.114 applied to test block P41 in PARENT open testing (X-Z view) (Meyer et al. 2017a).

Depth sizing RMSEs are summarized for ADVPAUT and PAUT applied to SBDMW and LBDMW test blocks with OD and ID access in Table 42. Generally better performance of PAUT techniques is observed. SBDMWs and FB test blocks were depth sized with better performance than LBDMW test blocks (Meyer et al. 2017a).

Figure 117 shows an example of two data image responses from VTT's inspection. The purpose of these images is to illustrate the difficulties to separate the crack tip response signal from the noise.

Table 42. Summary of depth sizing RMSEs for ADVPAUT and PAUT techniques applied to SBDMW and LBDMW test blocks with OD and ID access (Meyer et al. 2017a).

	ADVPAUT		**PAUT**	
	NOBS	**RMSE (mm)**	**NOBS**	**RMSE (mm)**
SBDMW and FB test blocks with OD access	57	5.3	79	3.4
SBDMW test blocks with OD access	36	5.5	47	2.4
FB test blocks with OD access	21	5.0	32	4.5
FB test blocks with ID access	14	3.1	2	1.2
LBDMW test blocks with OD access	36	9.1	3	5.1
LBDMW test blocks with ID access	8	6.7	8	5.2

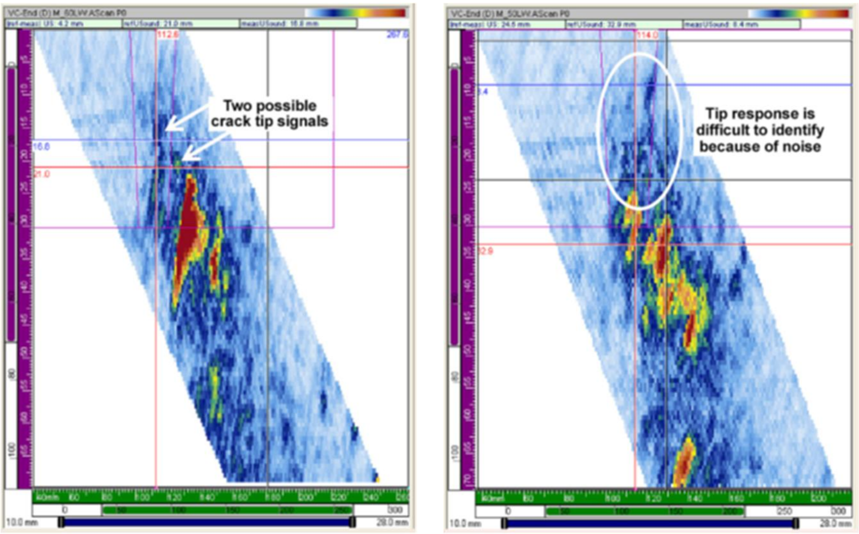

Figure 117. Data image response for PAUT.122.1 inspection of SCC flaws in P28 (left) and P32 (right) viewed from the right side of weld. The inspection was performed by linear scanning with TRL probe at 60° for P28 and 50° for P32. Arrows in the image on the left highlight two possible crack tip signals and the white circle in the image on the right indicates that it is difficult to separate the tip response from noise (Meyer et al. 2017a).

8.6.2 Length sizing results

Length sizing results for procedure types and all procedures in PARENT open testing are shown in Table 43 and Table 44, respectively. These tables indicate the best performance for PAUT and UT procedures. All but one procedures including VTT's procedure produced length sizing RMSEs of less than the ASME Code requirement for length sizing accuracy (19 mm) (Meyer et al. 2017a).

Figure 118 presents the length sizing regression for all PAUT procedures applied to SBDMW test blocks. Figure 119 shows the length sizing regression of VTT's procedure on SBMW test blocks. These plots indicate slight undersizing of the short flaws and slight oversizing of long flaws. (Meyer et al. 2017a).

Table 43. Length sizing results for procedure types applied to SBDMW test blocks with OD access (Meyer et al. 2017a).

Procedure type	**NOBS**	**Bias (mm)**	**RMSE (mm)**
ADVPAUT	14	3.9	14.0
NLUT	17	-10.9	17.0
PAUT	49	1.0	9.3
UT	4	1.2	2.4
All	84	-0.9	11.9

Table 44. Length sizing results for procedures applied to SBDMW test blocks with OD access (Meyer et al. 2017a).

Procedure	**NOBS**	**Bias (mm)**	**RMSE (mm)**
HHUT.27.1	9	-14.9	20.7
PAUT.114	19	2.1	13.0
PAUT.131.2	18	0.7	6.4
PAUT.131.4	8	2.2	3.4
PAUT.20	4	-5.0	7.6
SAFT.17	13	3.5	14.3
SHPA.6.1	4	1.8	4.9
SHPA.6.2	4	-14.8	15.6
UT.104	4	1.2	2.4
All	84	-0.9	11.9

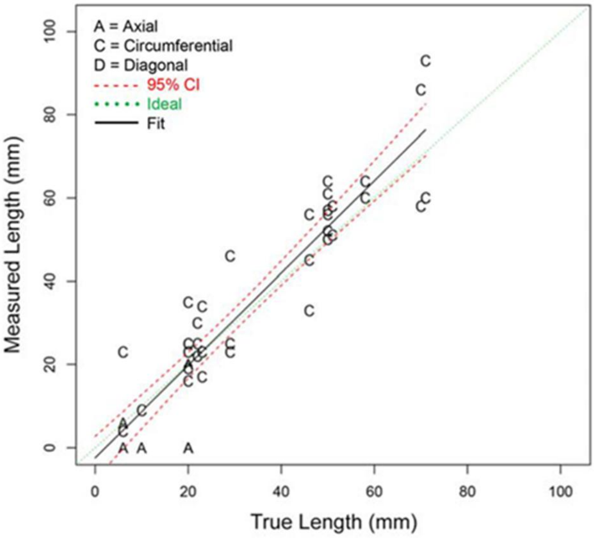

Figure 118. Length sizing regression for PAUT procedures on SBDMW test blocks in PARENT open testing with OD access (Meyer et al. 2017a).

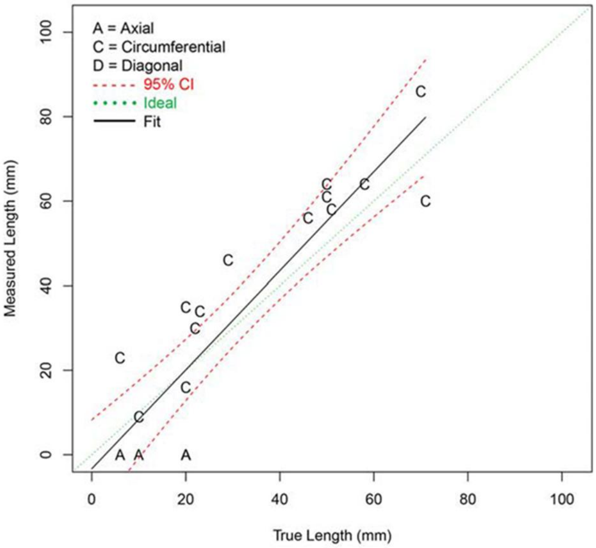

Figure 119. Length sizing regression for procedure PAUT.114 on SBDMW test blocks in PARENT open testing with OD access (Meyer et al. 2017a).

Length sizing RMSEs are summarized for ADVPAUT and PAUT applied to SBDMW and LBDMW test blocks with OD access in Table 45. Better performance of PAUT techniques on SBDMW test blocks and ADVPAUT techniques on LBDMWs is observed. SBDMWs were length sized with better performance than LBDMW test blocks (Meyer et al. 2017a).

Table 45. Summary of length sizing RMSEs for ADVPAUT and PAUT techniques applied to SBDMW and LBDMW test blocks with OD access (Meyer et al. 2017a).

	ADVPAUT		**PAUT**	
	NOBS	**RMSE (mm)**	**NOBS**	**RMSE (mm)**
SBDMW test blocks with OD access	14	14.0	49	9.3
LBDMW test blocks with OD access	9	15.2	4	20.8

8.7 PARENT Atlas information tool

The PARENT Atlas information tool was developed to document the open testing data and results together with flaw image responses. In addition, the PARENT Atlas includes relevant data from field experience and information of flaw relevance. A screenshot image of PARENT Atlas is shown in Figure 120 (Meyer et al. 2017a).

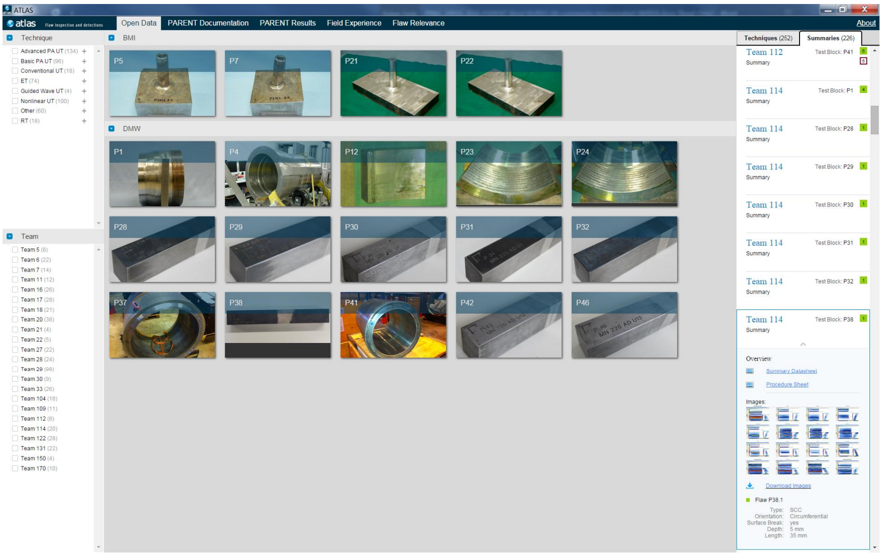

Flaw P38.1
Type: SCC
Orientation: Circumferential
Surface Break: yes
Depth: 5 mm
Length: 35 mm

Figure 120. Screenshot of PARENT Atlas information tool Open Data tab display (Meyer et al. 2017a).

8.8 Comparison of PARENT vs. PINC

Table 46 compares PINC results (Cumblidge et al. 2010) to the current PARENT blind RRT for SBDMW blocks with ultrasonic techniques. Table indicates that both PAUT and UT.TOFD procedures have performed better in PARENT than in PINC.

Table 47 shows a comparison of sizing results on SBDMW test blocks for both PINC and PARENT. Overall depth sizing RMSE is improved for PARENT, although the spread between best and worst sizing performers is larger for PARENT than PINC. Length sizing also appears to have improved in PARENT relative to PINC (25 mm RMSE for PINC and 12.1 mm for PARENT) and the spread between best and worst length sizing performers is narrower for PARENT relative to PINC. However, two gross outlier measurements were not included in the length sizing analysis for PARENT.

Table 46. Comparison of PINC and PARENT detection results (POD (%) versus depth for SBDMW test blocks (Meyer & Heasler 2017).

	0 mm	**5 mm**	**10 mm**	**15 mm**
PINC UT	6	36	51	67
PARENT UT	8	20	43	69
PINC PAUT	6	36	51	66
PARENT PAUT	6	39	87	99
PINC UT.TOFD	9	44	53	61
PARENT UT.TOFD	4	42	92	99

Table 47. Comparison of PINC and PARENT depth and length sizing error for SBDMW test blocks (Meyer & Heasler 2017).

	Depth sizing RMSE (mm)		
	All	**Best**	**Worst**
PINC	7.07	3.18	10.09
PARENT	5.5	1.8	13.9
	Length sizing RMSE (mm)		
	All	**Best**	**Worst**
PINC	25	3.56	91
PARENT(a)	12.1	8.0	22.6
(a) For PARENT evaluation, two outliers were excluded from length sizing.			

8.9 **Conclusions from PARENT**

Several conclusions can be obtained from PARENT blind testing (Meyer & Heasler 2017):

- Circumferential flaws exhibit a greater likelihood of detection than axial flaws, as a function of depth.
- Flaw orientation did not show an influence on depth sizing performance based on depth sizing RMSE results and regression plots.
- OD PAUT procedures exhibit better performance than OD conventional UT procedures for SBDMWs as measured by POD and depth sizing RMSE.
- PARENT results indicate substantial improvement in OD PAUT performance for SBDMWs, compared with PINC performance data.
- PARENT results indicate significant variability in performance for UT procedures employing similar techniques and for PAUT procedures employing similar techniques on SBDMWs.
- Two of nine procedures applied for depth sizing on SBDMW test blocks by OD surface access in the Blind test exhibited depth sizing performance that met the intent of the ASME Code, Section XI requirement of RSME within 3.2 mm. However, the flaw depth size distribution in these test blocks tended to be shallower than the requirements for flaw size distribution and it was not the intent of the PARENT test blocks to meet these requirements.
- One of nine procedures applied for length sizing on SBDMW test blocks by OD surface access in the Blind test exhibited length sizing performance that did not meet the intent of ASME Code, Section XI requirement of RMSE within 19 mm.

Some significant conclusions can be drawn from the open testing (Meyer et al. 2017a):

- A general trend is observed for oversizing shallow flaws and undersizing deep flaws with the exception of ADVPAUT procedure types and NLUT procedures based on sub-harmonic techniques, which exhibit a more consistent error over the range of flaw depths considered.
- ADVPAUT procedure types do not exhibit better overall depth sizing accuracy than PAUT procedure types in this study based on RMSE.
- Overall, NLUT procedure types do not exhibit better overall depth sizing accuracy in comparison to ADVPAUT and PAUT procedure types based on RMSE.
- Better depth sizing performance is observed on FB test blocks (most with laboratory-grown SCC flaws) for ADVPAUT, NLUT, and UT procedure types in comparison to SBDMW test blocks (with SC flaws).
- PAUT procedure types exhibit better depth sizing performance on SBDMW test blocks in comparison to FB test blocks.
- Data response images for PAUT technique PAUT.122.1 in Figure 117 illustrate that identifying crack tip signals with established PAUT can be difficult and that crack tip signal identification by image pattern analysis is, in part, a subjective determination. Tip diffraction signals with low SNR are easier to detect under open testing conditions with flaw information provided to test participants. Detecting tip diffraction signals with low SNR under blind test conditions will be more challenging.

- PAUT procedures exhibit a more consistent length sizing error over the range of flaw lengths considered for SBDMW test blocks in comparison to ADVPAUT, which tend to oversize short flaws and undersize long flaws in open testing.

8.10 Future NDE work

A new international agreement is under development by U.S. NRC to establish the Program for Investigation of NDE by International Collaboration (PIONIC). The objectives of PIONIC are

1. Share results of related NDE research.
2. Evaluate the capability of NDE modelling and simulation.
3. Perform analysis of flaw relevance on NDE responses.
4. Develop guidance for extending NDE performance during testing to actual field inspection.
5. Identify NDE techniques for monitoring material degradation.
6. Evaluate the reliability of NDE methods used to inspect nuclear power plant (NPP) systems and components.

9. Discussion

9.1 Microstructural characterization and hardness measurements

The microstructural characterization and the hardness measurement results do not show an effect of thermal ageing after PWHT on the LAS base material, the LAS HAZ or Alloy 52 weld metal when excluding the fusion boundary region. The hardness profile of the LAS HAZ is clearly linked to the grain size variations, with no influence of thermal ageing at 400 °C for 10000 h on either the grain size or carbide precipitation. The hardness increases from 200-220 HVIT in the LAS base material to 280 HVIT in the grain-refined zone about 400-600 µm away from the fusion boundary. The hardness in the grain-coarsening zone is similar to that of the LAS base material, corresponding to the grain size similar to that of the base material (2.5 µm). In Alloy 52 weld metal, no clear changes were observed in the nature or extent of precipitation, within grains or at GBs. Hardness levels remained similar before and after ageing, increasing from the crown to the root of the narrow-gap weld. The focus of the discussion is therefore on the changes occurring at the DMW interface, where the effects of PWHT and thermal ageing were notable.

Tables 48 and 49 summarize the key results of the nanoindentation hardness measurements in the SINI DMW before and after PWTH and in the NIWEL DMW before and after thermal ageing, respectively.

Table 48. Summary of the main hardness results and their locations at the LAS/Alloy 52 weld metal for SINI AW and SINI PWHT.

SINI	HV_{IT} (1.5 mN)	Location	Distance from fusion line (µm)
As-welded	667	PMZ	0
PWHT	840	Weld metal	0-5

Table 49. Summary of the main nanoindentation hardness results and their locations at the LAS/Alloy 52 weld metal for NIWEL AR, NIWEL 5000 h and NIWEL 10000 h.

NIWEL	HV_{IT} (1.5 mN)	Location	Distance from fusion line (µm)
As-received	858	Weld metal	0-2
5000 h	733	Weld metal	10
10000 h	637	Weld metal	20

As seen in Tables 48 and 49, the hardest zone of the LAS/Alloy 52 weld metal interface after welding is the martensite-like PMZ forming at the fusion boundary. Upon PWHT, however, a local strength mismatch is created with the widening of the CDZ of low hardness and the formation of a hardness peak in Alloy 52 weld metal starting from the fusion boundary. The same was observed in NIWEL AR. Thermal ageing clearly reduces the local strength mismatch, while it is visible that the position of the decreased hardness peak in Alloy 52 weld metal moves further away from the fusion boundary. Since the hardness peak in Alloy 52 weld metal is related to the formation of a CDZ in the LAS side and carbon diffusion and pile-up into the weld metal during PWHT, it is assumed that thermal ageing reduces the hardness peak in the weld metal side by allowing carbon to diffuse further away into the weld metal. This relation of hardness and carbon pile-up is clearly visible when comparing the hardness maps of the nanoindentation measurements to the EDS maps of the carbon content (see Figure 121).

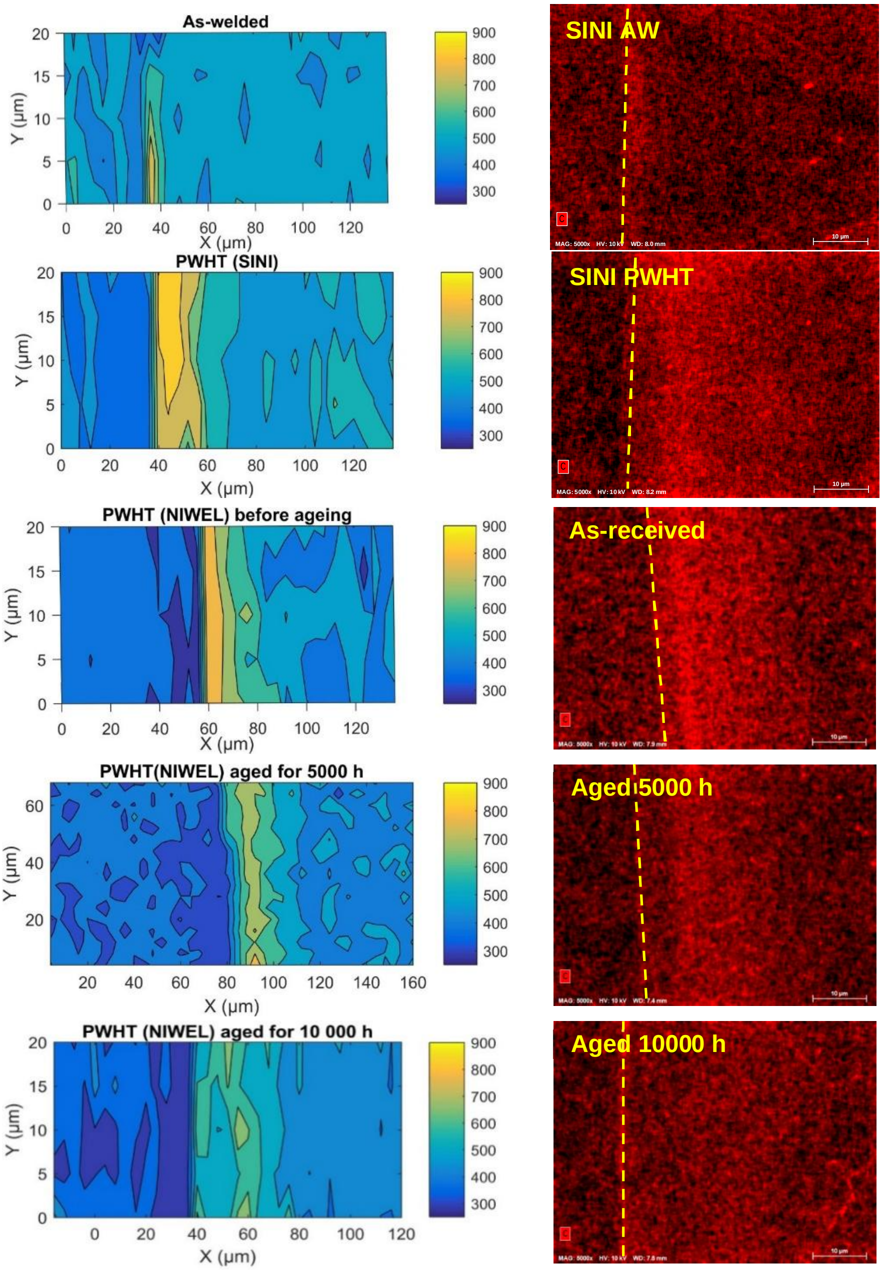

Figure 121. Nanoindentation hardness profiles (1.5 mN) across the LAS/Alloy 52 weld metal interface in all conditions (on the left), with the corresponding EDS maps showing the wt.% C. A clear correlation is seen between the hard layer in Alloy 52 weld metal near the FB and the carbon-rich layer in the EDS maps (on the right).

PWHT causing local strength mismatch in the RPV safe-end DMW may be a concern for PWRs. Previous studies on the fracture mechanical behavior of SINI mock-up showed that PWHT caused a significant decrease of fracture resistance for the J-R test specimens where the pre-crack location was close to the fusion boundary (Hänninen et al., 2014). In the case of SINI PWHT specimens, cracks in J-R testing initiated in LAS close to the FB and tended to propagate only along the soft LAS CDZ. On the contrary, in SINI AW J-R specimens, cracks were occasionally deflecting over the fusion boundary into the weld metal and back into the LAS, forming a serrated fracture surface (Sarikka et al., 2016a; Sarikka et al., 2017; Hänninen et al. 2014). A serrated type of fracture forms a larger surface area, which requires more energy than the formation of a planar fracture surface with a smaller surface area. The difference in formed fracture surface area may partly explain the higher measured fracture resistance (J_Q and J_{1mm}) of SINI AW.

Based on the observations made for NIWEL AR and NIWEL 10000 h, it can be assumed that the thermal ageing at 400 °C does not have significant detrimental effects on Alloy 52 weld metal or the LAS base material and HAZ. Instead, the LAS CDZ was found to remain microstructurally stable upon ageing, while the narrow hard layer in Alloy 52 weld metal was found to soften and move further away from the fusion boundary, in association with a progressive disappearance of the carbon build-up due to the thermal ageing in the weld metal near the fusion boundary. The thermal ageing at 400 °C for 5000 and 10000 h is therefore considered to be slightly beneficial in the case of the RPV safe-end Alloy 52 NG DMW, when considering the performance of the DMW in operation environment (high temperature PWR water), as it reduces the strength mismatch at the weld interface.

9.2 Effect of ageing on ductile-to-brittle transition temperature

9.2.1 Fracture toughness vs. impact toughness

For Charpy-V impact toughness test results, the effect of ageing is clear, when considering the change in ductile-to-brittle transition temperature T_{42J}. For the as-received material T_{42J} is -35 °C, and after ageing for 5000 and 10000 h the T_{42J} values increase to -2 and +12 °C, respectively. It is notable that the rate of ageing appears to decrease after 5000 h, since the difference in T_{42J} is smaller between the results for 5000 and 10000 h aged material than the difference between the as-received and 5000 h aged material (+33 vs. +14 °C), Figure 122.

The effect of ageing is not evident for the T_0 ductile-to-brittle transition temperature. The T_0 values show that the material maintains its high fracture toughness also after ageing. For the as-received material T_0 is -118 °C, and after ageing for 5000 and 10000 h the T_0 values are -112 and -129 °C, respectively. All of the obtained results for the three conditions are within the uncertainty limits (2 * standard deviation) of

T_0, thus showing that there is no clear effect of ageing on the brittle fracture initiation behaviour of the material (Figure 123).

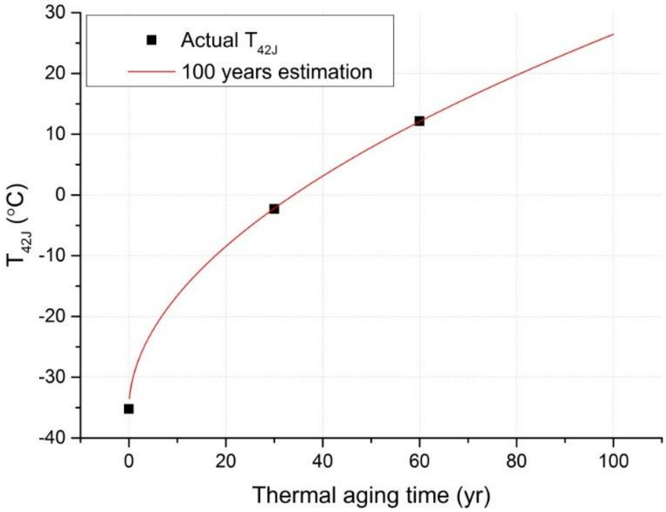

Figure 122. Estimation of the transition temperature, T_{42J}, for 100 years, 5000 h at 400 °C corresponds to 30 years and 10000 h at 400 °C corresponds to 60 years of normal operation. The estimation suggests that T_{42J} will be 27 °C.

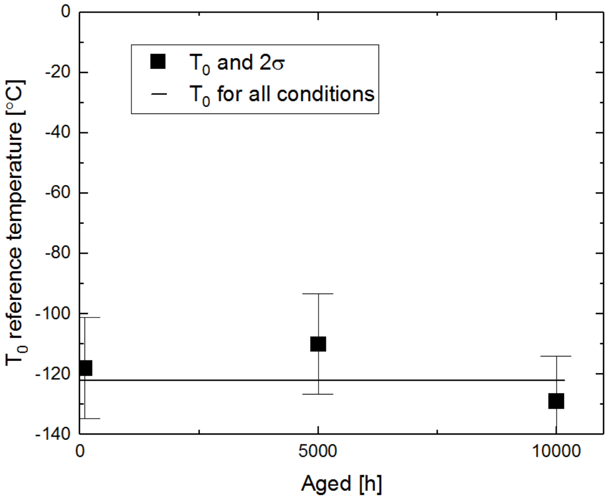

Figure 123. T_0 as a function of ageing time at 400 °C.

The different results from the impact toughness and fracture toughness testing may be explained by the nature of the test methods. T_0 describes the fracture toughness, i.e. material's tendency for cleavage initiation in front of a sharp pre-fatigued crack. It is a quasi-static test measuring the local properties of the material. Charpy-V test is a dynamic test and is affected by brittle fracture initiation, growth and arrest. During impact loading, the critical stress for cleavage fracture initiation is exceeded over a relatively large area, thus, the fracture event is more global. In Charpy-V specimens, the crack is a shallow and blunt notch. The differences are summarised in Table 50 (Wallin 2011).

Based on the mechanistic differences between impact toughness and fracture toughness, and the corresponding ductile-to-brittle temperature shifts, it is reasonable to assume, that thermal ageing affects the crack growth and crack arrest properties of the LAS HAZ of the DMW, while the tendency to cleavage crack initiation is not markedly affected. However, another factor that can affect the difference in the T_0 and T_{41J} behaviour is the crack location relative to the weakest location at the fusion boundary. The fracture toughness based T_0 values can be more sensitive to the location of the crack, since the critical stress is suppressed to a smaller region and the fracture event is thus more local than during impact toughness testing.

Table 50. Differences between impact and fracture toughness testing.

Difference	CVN	K_{IC}, K_{JC}
Loading rate	Dynamic	Quasi-static
Flaw geometry	Shallow blunt notch	Deep crack
Event described in the test	Fracture initiation + propagation + arrest	Fracture initiation
Critical stress field in front of the crack	Global	Local

Figure 124 shows that the fracture toughness, K_{Jc}, increases with the distance of the fatigue pre-crack tip to the fusion boundary. This comparison does not take into account the test temperature, thus a $T_{0(effective)}$ value was calculated for each test result following the equations in ASTM E1921 (2015). Figure 125 shows that higher $T_{0(effective)}$ values are obtained closer to the fusion boundary than further away.

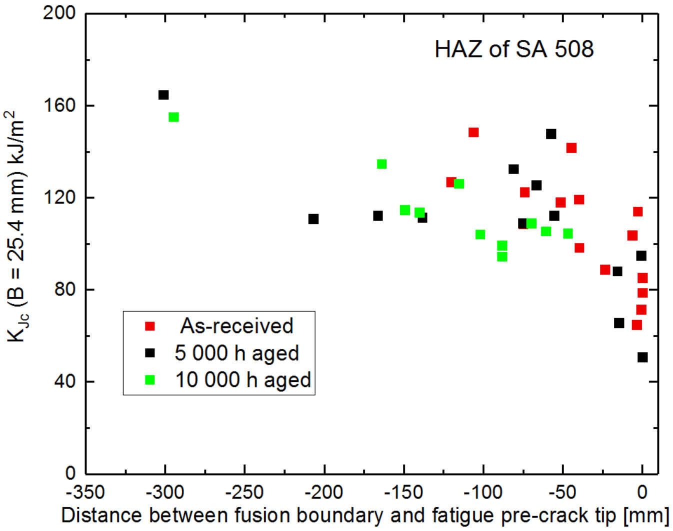

Figure 124. The K_{Jc} is lowest at the fusion boundary.

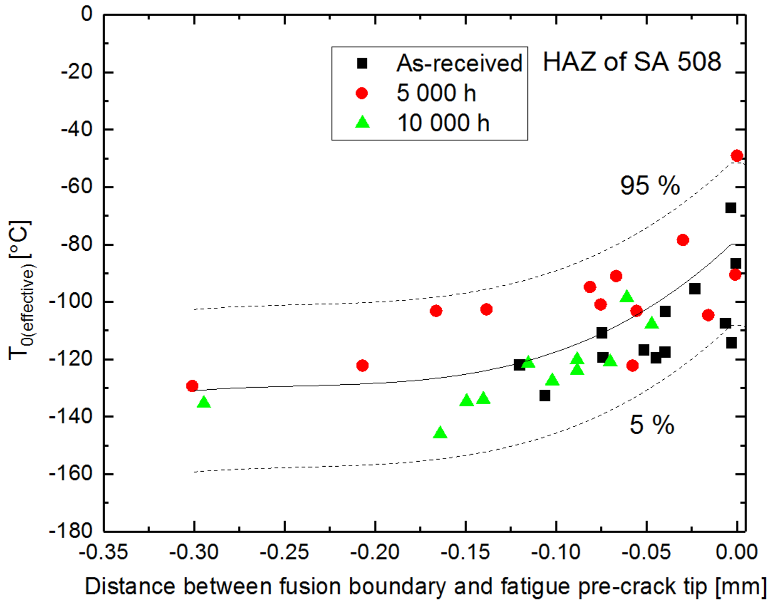

Figure 125. $T_{0(effective)}$ is highest at the fusion boundary.

The average value between fatigue pre-crack tip and fusion boundary of the qualified T_0 specimens is 0.02 mm for the as-received specimens, 0.03 mm for the 5000 h aged specimens, and 0.09 mm for the 10000 h aged specimens. The T_0 of the 10000 h aged condition is lower than that for the other conditions.

9.2.2 T_0 and T_{28J} dependence

Typically, T_0 and T_{28J} of ferritic steels follow the $T_0 = T_{28J}$ -18 °C dependence with a standard deviation of ~20 °C (Wallin 2011). The T_0 and T_{28J} values obtained from this study do not follow the typical dependence for ferritic steels, Figure 126. The T_{28J} value for as-received condition is in line with previous results for SA 508, but the T_0 values are slightly lower. However, the T_0 values are higher than observed for a similar DMW mock-up, MC4 mock-up, investigated by Joly et al. (2014), even if the T_{28J} is in the same range. A difference that can explain the difference in the T_0 results is the crack location. The cracks in the study by Joly et al. (2014) were located in average 0.2-0.3 mm from the fusion boundary, whereas in this study the cracks were located 0.02-0.09 mm from the fusion boundary. This issue will be investigated in detail in future.

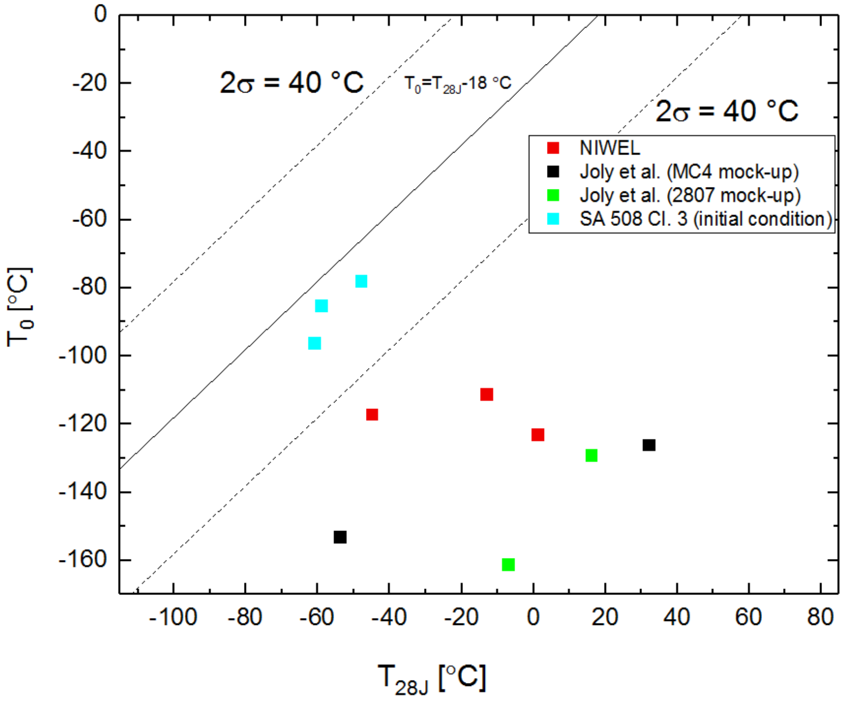

Figure 126. Dependence between impact toughness based T_{28J} and fracture toughness based T_0.

For MC4 mock-up (Joly et al., 2014), a 27 °C shift in T_0 was observed after ageing at 400 °C for 10000 h. The larger shift in T_0 after thermal ageing can be explained by the chemical content but also by the PWHT time. The PWHT of MC4 mock-up was 6+10 h in 600 °C, compared to 14.8 h in 550 °C and 7.7 h in 610 °C. The PWHT treatment of the MC4 mock-up was optimized to enhance the effect of thermal ageing on the transition temperature shift (Joly et al. 2014).

9.2.3 Initiation sites

Many of the crack fronts were curved, since the fatigue pre-crack was partially in the weld metal and had progressed less on that location. However, Figure 127 shows that the curvature of the crack front does not affect the location of the initiation site relative to the side surface.

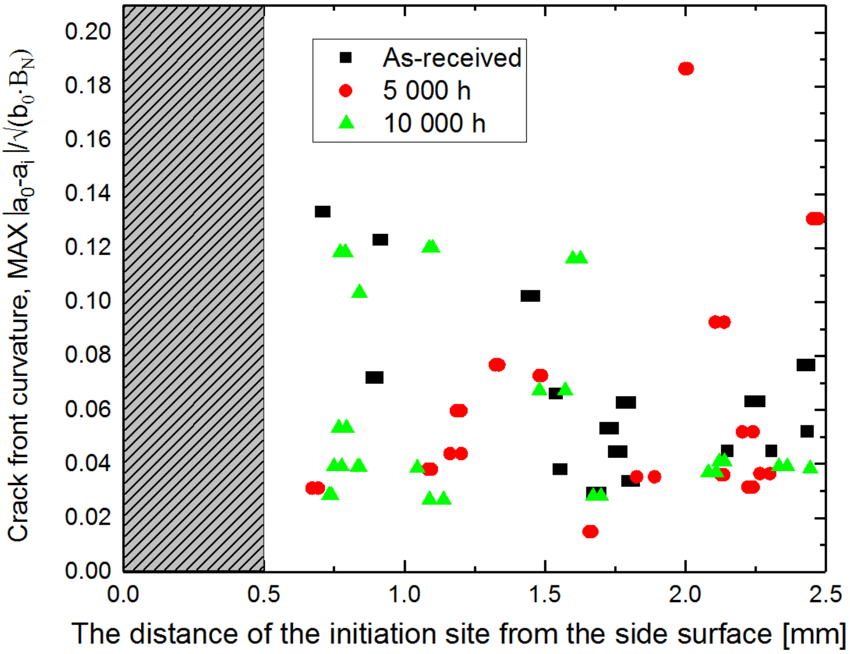

Figure 127. The crack front curvature does not affect the crack initiation site relative to the side surface.

The J-integral before brittle fracture, J_C, as a function of measured distance between initiation location and fatigue pre-crack tip follows the same trend as J_c as a function of the location of the maximum stress ahead of the fatigue pre-crack tip, Figure 128. In both cases, the distance of the initiation site to the crack tip increases with J_c. However, the difference between the location of maximum stress and location of measured brittle fracture initiation site increases with J_c. The location of maximum stress was estimated to be 2*CTOD (Anderson 2005).

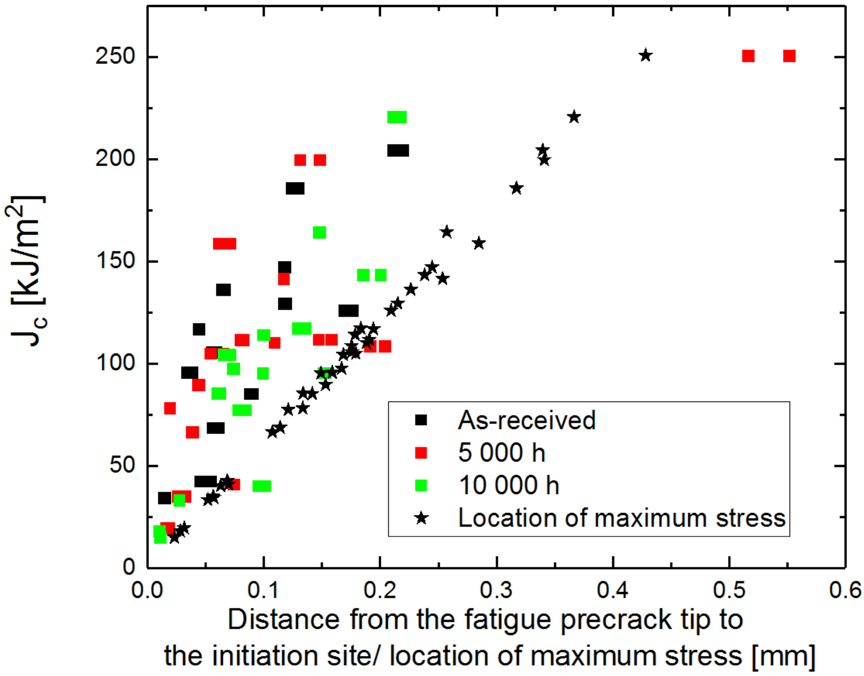

Figure 128. Relation between location of the brittle fracture initiation site and maximum stress relative to the fatigue pre-crack tip.

9.3 Effect of ageing on the ductile J-R curves

Figure 129 shows a decreasing trend in J_{1mm} values as a result of thermal ageing, although the effect is not large and the values after ageing are still at a high level (~400-500 kJ/m^2), and the J-R curves have still a rising trend. There is no significant difference between the results for T-L and T-S orientations, although, on average, the J_{1mm} values in T-L orientation are slightly higher than those in T-S orientation. For the 5000 h aged material, three J_{1mm} values are significantly higher, but in these cases the cracks are actually located further away from the fusion boundary. As illustrated in Figure 130, the closer the HAZ cracks are located to the fusion boundary, the lower J_{1mm} values are obtained.

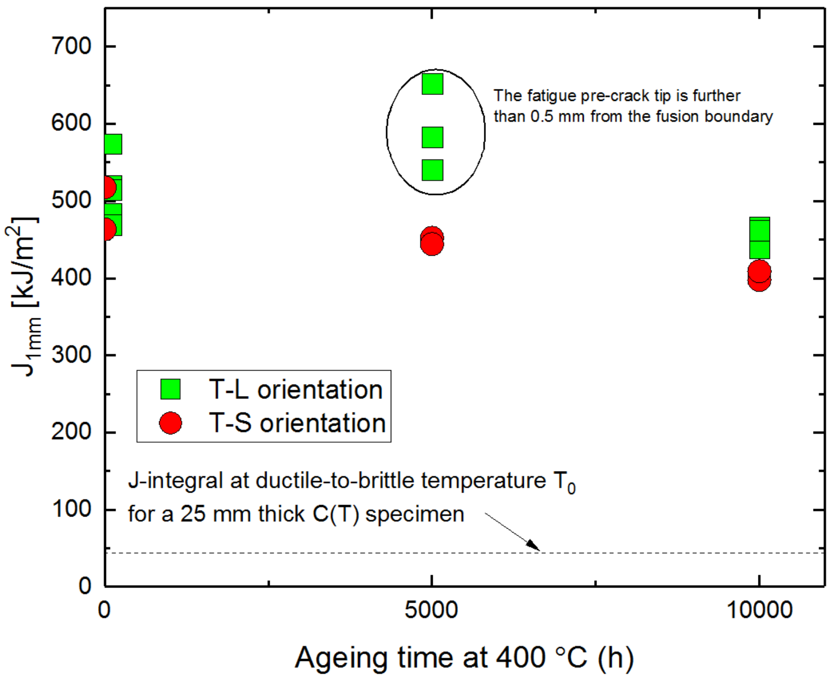

Figure 129. A graph of the J_{1mm} results for as-received and thermally aged material. J_{1mm} decreases slightly due to ageing at 400 °C.

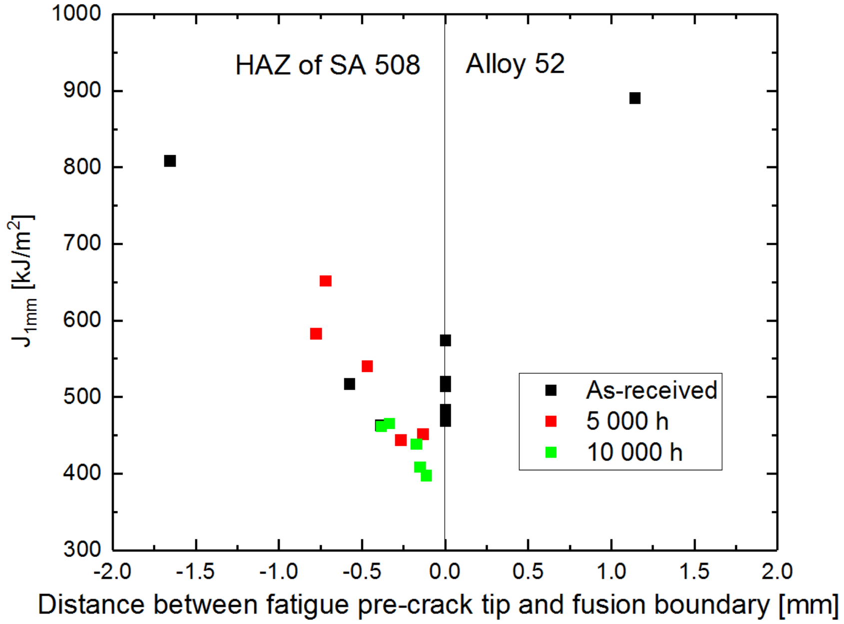

Figure 130. A graph of the J_{1mm} results for as-received and thermally aged material as a function of the distance between fatigue pre-crack tip and fusion boundary. The J_{1mm} is lowest at the fusion boundary.

Ageing can affect the preferable crack growth path, causing a decrease in the J_{1mm} values. Figures 131-133 show that the crack propagation path affects the shift in J_{1mm}. For the as-received condition, the crack tends to propagate in a larger extent on the weld metal side, and more weld metal is observed on the fracture surface. The cracks in the 10000 h aged material tend to grow mostly in the RPV steel. Figure 134 shows that the difference between the calculated and measured crack growth is largest for the as-received condition and smallest for the 10000 h aged condition.

Ageing affects the strength mismatch on the weld metal side adjacent to the fusion boundary. The hardness peak in the weld metal decreases and moves further away from the fusion boundary. This shift in strength mismatch can affect the preferable crack growth path. Another possible mechanism explaining the change in crack path is the combined effect of residual stresses and weld defects. Ageing can decrease the residual stresses, which may reduce the probability of crack deflections from HAZ to the weld metal. However, factors like the crack orientation relative to the fusion boundary can also affect the amount of RPV steel on the fracture surface, indicating that the shift in J_{1mm} is not necessary caused by ageing.

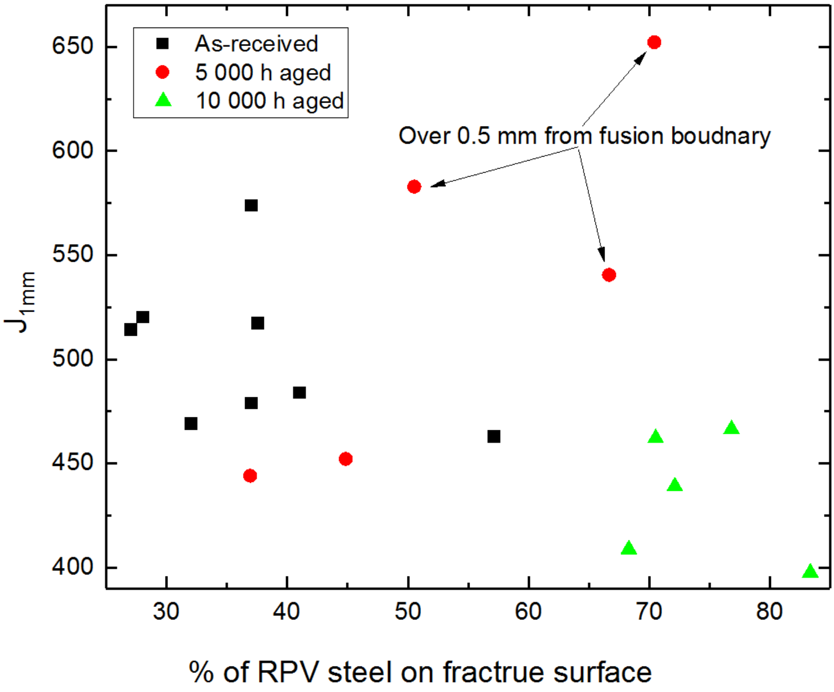

Figure 131. J_{1mm} as a function of % of RPV steel on fracture surface.

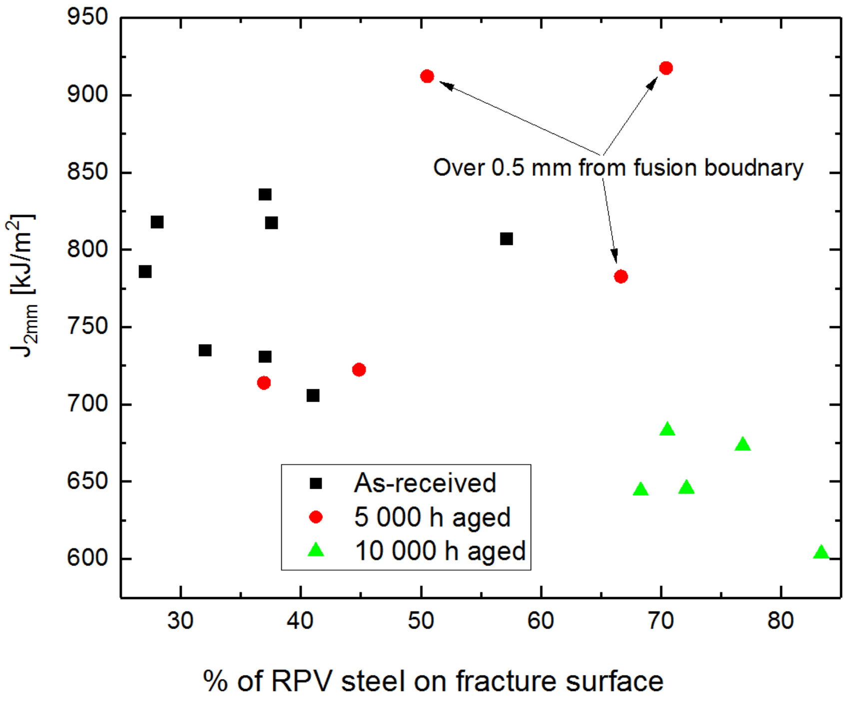

Figure 132. J_{2mm} as a function of % of RPV steel on fracture surface.

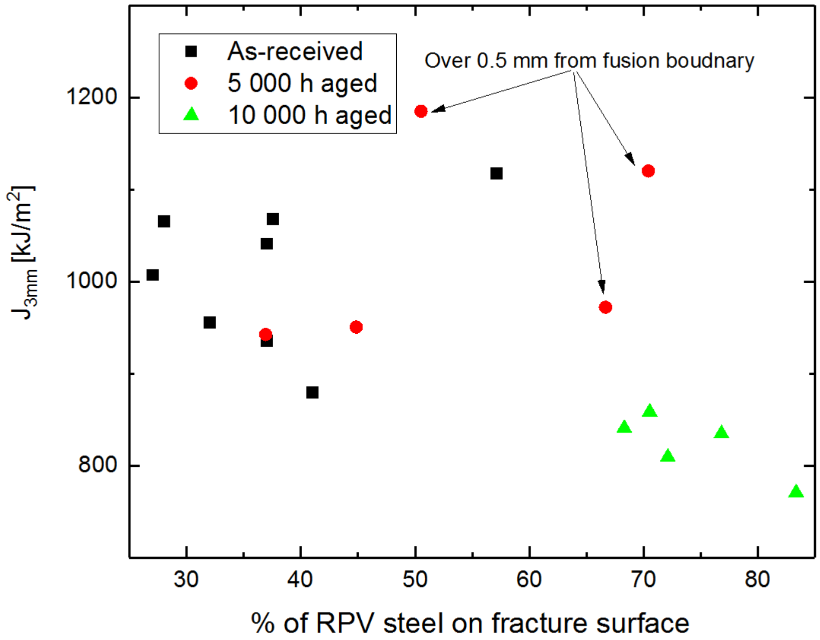

Figure 133. J_{3mm} as a function of % of RPV steel on fracture surface.

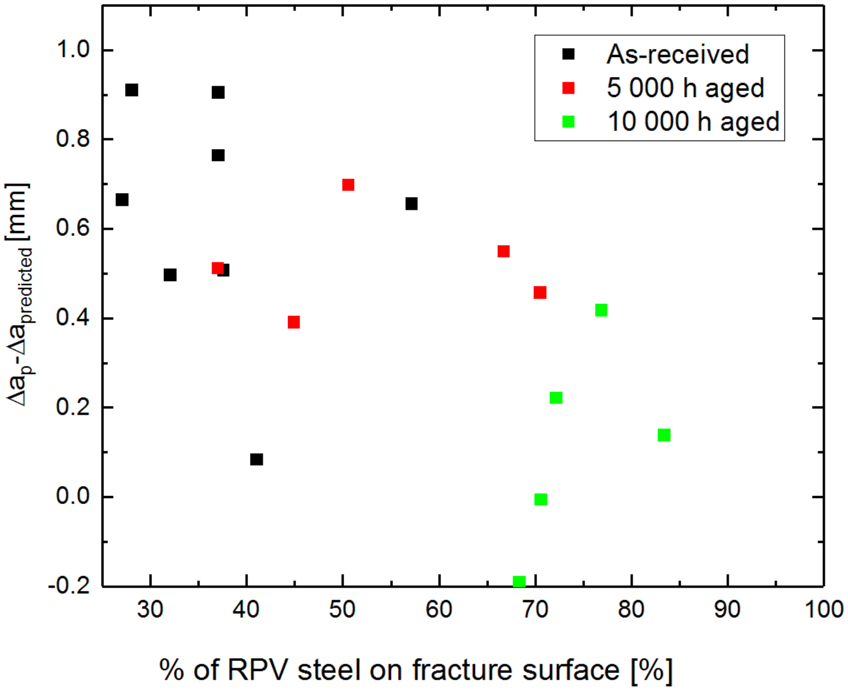

Figure 134. Difference between measured and calculated final crack length as a function of % of RPV steel on fracture surface.

9.4 Temperature dependence of J_{1mm} and ductile fracture properties in fusion boundary region

The decrease in J_{1mm} for fusion boundary cracks, due to temperature shift from 25 to 300 °C, appears to be more in line with the J_{1mm} temperature behaviour of nickel-base alloys than ferritic steels, Figure 135.

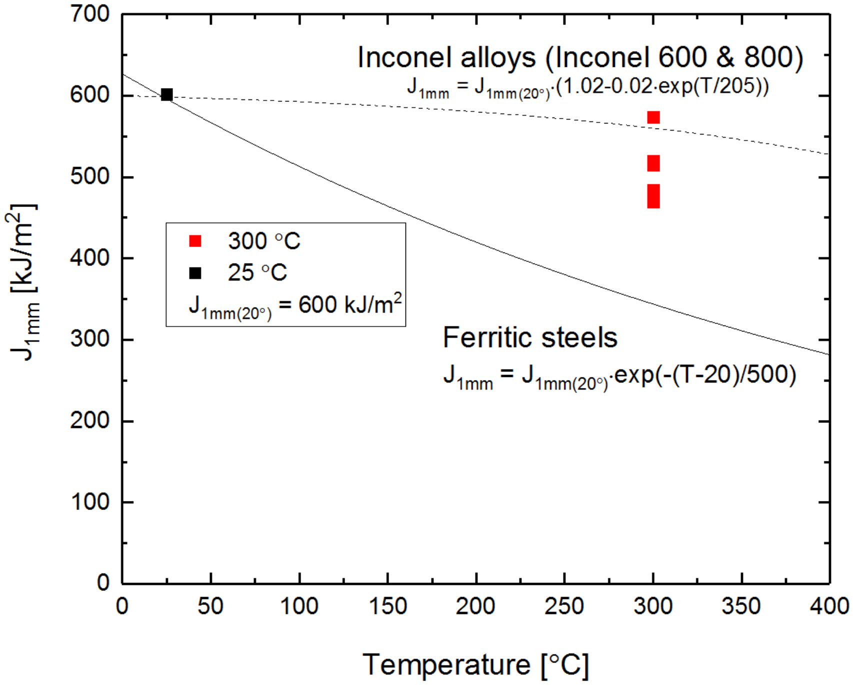

Figure 135. The J_{1mm} temperature behaviour at the fusion boundary compared to typical temperature behaviour of ferritic steels and nickel-base alloys (Wallin 2011).

Figure 136 shows that the J_{1mm} values, for cracks with fatigue pre-crack tip less than 0.25 mm from the fusion boundary, are in line with previous results obtained for Alloy 52 DMWs with SE(B) and C(T) specimens at room temperature (Lindqvist et al. 2018). This can be expected since the previous figure showed that the J_{1mm} temperature dependence at the fusion boundary follows that of nickel-base alloys, in other words, the shift in J_{1mm} is not large. However, as the distance of fatigue pre-crack tip to the fusion boundary grows, the J_{1mm} at 300 °C appears to start to behave as a typical ferritic steel, which can be observed as a growing difference to the room temperature J_{1mm} results obtained in the previous studies.

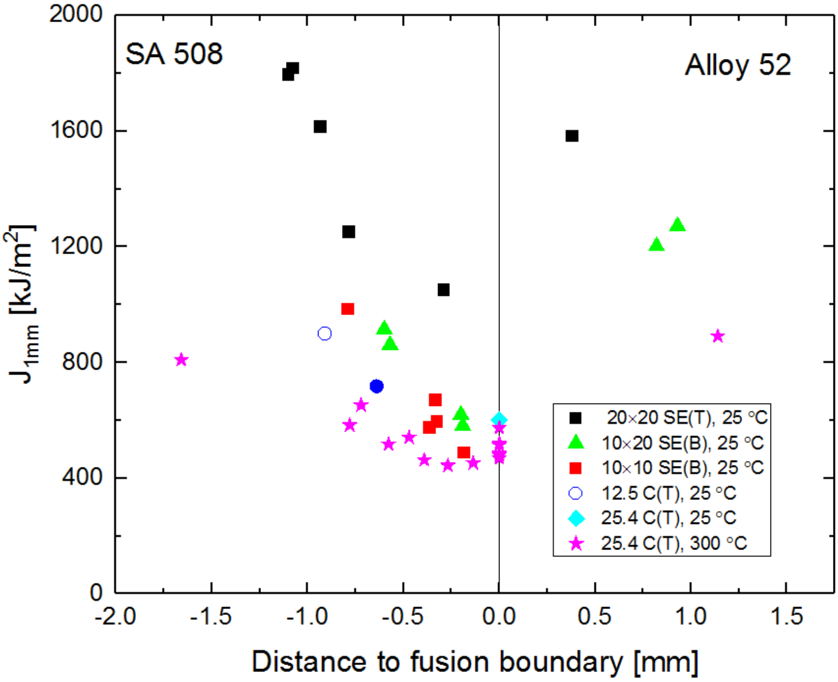

Figure 136. The effect of distance of the initial crack to the fusion boundary. The results are compared to previous investigations.

9.5 Weld mechanical mismatch and crack path

Crack path characterization and hardness measurement results showed that the local hardness mismatch determines where the crack propagates in ductile fracture when the pre-crack is located close to the fusion boundary. That observation is similar to that made by Sarikka et al. (2016a, 2016b, 2017a. 2017ba) in the previous studies in the SINI project. The behaviour is similar independent of which of the materials, i.e. base material or weld metal, is the softer one. In the study performed for the BWR Alloy 182 mock-up, the weld metal showed superior fracture toughness compared to the low-alloy steel, but the weld metal was the softer one of the two materials. Crack propagation occurred close to the fusion boundary in Alloy 182 when the pre-crack was located at the fusion boundary. Thus, it appears that the observed behaviour is not material dependant and follows the crack propagation occurs in the softer material even if it shows significantly higher fracture resistance.

Crack path deflections from SA 508 to Alloy 52 occurred due to the small weld defects observed in the Alloy 52 weld metal. Obviously, weld defects are not typically beneficial for the mechanical properties of the joint. I this case, however, deflections to the weld metal side of the fusion boundary have also a positive effect, because the crack growth in Alloy 52 requires more energy due to the higher fracture resistance of Alloy 52 compared to that of the CDZ of SA 508. This conclusion is supported by the evidence shown in the graph where the amount of weld metal with respect to measured fracture resistance is plotted (Figure 131).

Due to the hard zone close to the fusion boundary, crack did not typically deflect back to the LAS after deflecting into the weld metal, when tested in T-L orientation. In the case of T-S orientation, the wavy fusion boundary enables crack deflection at least partly back into the LAS, as can be seen on the fracture surfaces, e.g. in Figures 69-71.

9.6 LTCP testing

The obtained fracture resistance J_Q values are high, and thus, the LTCP susceptibility of the material is reasonably low overall. However, reduction from the air test results is significant in some specimens tested with 100 cm^3 H_2/kg H_2O. The lowest J_Q value, 107 kJ/m^2, was obtained for the as-received material. Furthermore, both specimens of the as-received material state showed intergranular cracking and decreased J_Q, whereas only one of three 10000 h aged specimens showed a measurable reduction of fracture resistance in J-R testing.

The results obtained in this study are compared to those obtained in the preceding SINI project in Figure 137. As the graph illustrates, there are some specimens of both SINI and NIWEL materials that show a clear reduction of fracture resistance, but most of the specimens do not show a measurable environmental effect. It must be pointed out, that since the specimen size is rather small, the J values can be reliably measured for Alloy 52 only until about 200 kJ/m^2, because beyond that the plastic zone typically grows as large as the remaining ligament. In addition to that, the load line displacement in the J-R testing performed with bellows loading device was restricted to 2 mm in SINI and 2.5 mm in NIWEL, which also limits the maximum measured J values for Alloy 52 (with a fatigue pre-crack length of about 5 to 5.5 mm) to about 300 and 450 kJ/m^2, respectively.

Scatter of the results is large, and the reason for that is material inhomogeneity and pre-crack location with respect to the microstructure. Weld metals are always inhomogeneous regarding local elemental variation, grain size, grain boundary orientation with respect to the fatigue pre-crack, grain boundary carbide distribution and weld pass boundaries. In addition, the small weld defects observed in the fracture surfaces of the J-R test specimens tested in air as well as in ductile Charpy-V test specimens may play a role in LTCP tests. However, the role of weld defects on LTCP susceptibility is not considered to be significant, since no weld defects were observed on the fracture surfaces of the specimens that showed LTCP susceptibility.

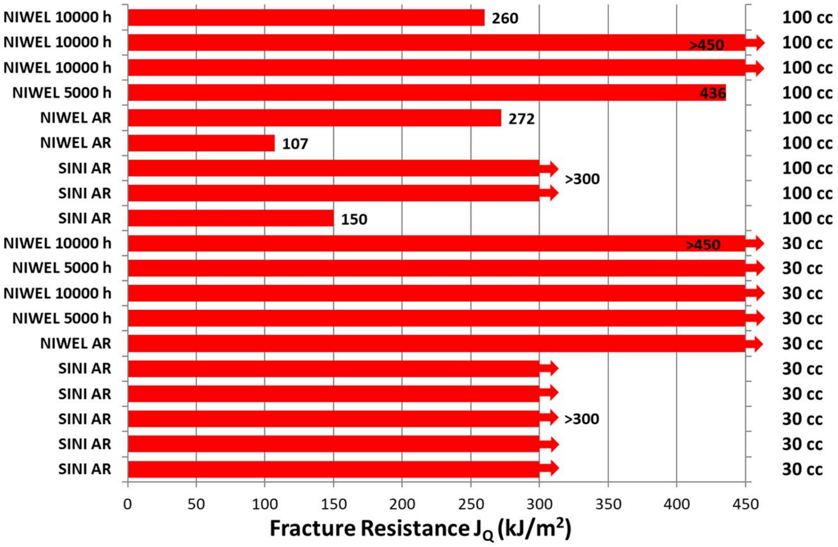

Figure 137. Comparison of the LTCP data obtained for Alloy 52 NG DMW mock-ups studied in SINI and NIWEL projects.

According to the results obtained in this LTCP study, the as-received material shows higher susceptibility to LTCP than thermally aged materials. It has been shown earlier (Ahonen 2016) that hydrogen outgassing from the weld metal increases the fracture resistance of Ni-base weld metals, when tested in low temperature (55 °C) hydrogenated water. In the case of the studied as-received (after PWHT) and thermally aged materials, the hydrogen content of the material prior to testing is considered to be negligible, because not much hydrogen is left in the bulk material after PWHT. During the J-R testing, hydrogen diffusion occurs from the water into the stressed zone near the crack tip. The hydrogen content in the crack tip region increases due to loading of the specimen and, the hydrogen trapping behaviour of the material is an important factor for the hydrogen-induced cracking. Thus, the increase in J_Q values due to ageing is possibly attributed to the decreased hydrogen trapping efficiency of the thermally aged materials.

Fractographic examinations of the LTCP specimens further confirm that the observed decrease in fracture resistance is attributed to intergranular hydrogen-induced fracture. When comparing Figures 100-103, showing detailed views on fracture surfaces of specimens tested with 30 and 100 cm^3 H_2/kg H_2O, respectively, the effect of hydrogen can be seen as decreased amount of plastic deformation during the fracture process.

10. Conclusions

Based on the obtained results the following conclusions are drawn:

- Narrow-gap Alloy 52 DMW sustains its high performance, regarding ductile and brittle fracture properties adjacent to the fusion boundary between SA508/Alloy 52 and for the weld metal, after thermal ageing (10000 h at 400 °C) representative of 60 years of plant operation.
- No significant changes were observed due to thermal ageing in J-R test results when testing in air at 300 °C. The fatigue pre-crack location was close to the fusion boundary in SA 508, which has the lowest fracture resistance based on the earlier studies. The J-R testing results for the material aged for 10000 h at 400 °C show J_{1mm} values in the range of about 400-500 kJ/m^2, which is about 10-20 % lower than the values obtained for the as-received material.
- All the J-R curves are rising and material fails by a ductile mechanism when tested at 300 °C.
- The lowest values in J-R testing were obtained for specimens where the fatigue pre-crack was located right next to the fusion boundary in the carbon-depleted zone of the HAZ.
- No significant effect of thermal ageing was observed in the yield strength of the HAZ, base material or the weld metal.
- Ductile-to-brittle transition temperature (T_{42J}) measured after 10000 h ageing is 12 °C, which gives a ΔT_{42J} of 47 °C as compared to the as-received material. The results obtained for the as-received, 5000 h aged and 10000 h aged materials show that the degrading effect of thermal ageing on Charpy-V impact toughness decreases as function of ageing time.
- Fracture toughness T_0 was not significantly affected by thermal ageing. Thus, it is assumed that thermal ageing may promote brittle crack propagation and degrade material’s capability to arrest the growing cracks at low temperatures, whereas the brittle crack initiation tendency of the material is not markedly affected. However, further investigations are needed to clarify the mechanisms explaining the differences.
- It appears that T_0 results are affected by the location of the pre-crack relative to the fusion boundary. The closer the pre-crack is to the fusion boundary, the lower fracture toughness values are obtained. More testing with varying pre-crack distances from the fusion boundary is needed in order to understand the T_0 behaviour as a function of pre-crack location.
- The studied material showed rather low susceptibility to low-temperature crack propagation in 55 °C hydrogenated water, although clear reduction of fracture resistance due to the environment was observed in some specimens. The as-received material appears to show lower fracture resistance than thermally aged materials.

- No microstructural changes were observed further away from the fusion boundary in the base material or in the weld metal due to thermal ageing.
- High local hardness mismatch at the fusion boundary is observed in the post-weld heat treated weld. A hardness peak was detected in the weld metal side of the fusion boundary. Thermal ageing slightly reduces the hardness of the peak and shifts it further into the weld metal for some tens of micrometers.
- The hardness peak in the weld metal side of the fusion boundary is caused by carbon diffusion from the low-alloy steel during post-weld heat treatment. The width of the carbon-depleted zone (CDZ) is not affected by thermal ageing.
- CDZ is the preferred crack path in all types of tests applied in this study. However, crack deflections to the weld metal side of the fusion boundary occur due to the small weld defects observed in the weld metal in tests, where the fracture mode is ductile. Crack deflections were typically associated to the weld pass boundary regions.
- The J-R testing specimens in which crack propagates mostly in the CDZ show lower J_{1mm} values than the specimens where crack deflections into the weld metal occur.

11. Future work

The work completed in the NIWEL project resulted in valuable data and observations on the behaviour of both the post-weld heat treated and thermally aged material. However, following topics remain of interest for further investigations:

- EAC testing of the narrow-gap mock-up has to be started. Although it has been assumed that the SCC resistance of the dilution zone, overlapping the hard zone, may be lower than that of the undiluted weld metal, SCC initiation in PWR conditions has widely been considered to take hundreds of years for Alloy 52. Recent literature (Chung et al. 2011, Dong et al. 2018) indicates, however, that SCC initiation may occur in the hard zone of the Alloy 52 weld metal in PWR conditions
- Additional fracture mechanical (T_0) testing on the fusion boundary region and J-R testing (including LTCP testing) of the hard zone in the weld metal is needed. The fracture mechanical behaviour of the hard zone in the weld metal side is not yet well known, and the scatter of the results for the fusion line specimens need further investigations. The reason for the different T_0 results obtained by Joly et al. (2014) are still unknown.
- Detailed microstructural characterization by TEM, WDS, Auger spectroscopy and atop probe tomography of both the carbon-depleted zone in the LAS and carbon-enriched zone in the weld metal has to be performed. Further characterization of the weld bead boundaries and various types of weld defects is needed. Also the distribution of the weld defects in the whole NG-DMW is necessary to know.
- Further investigations are needed to clarify the mechanisms explaining the difference in the transition temperature shift determined from impact toughness-based T_{42J} and fracture toughness-based T_0.
- The fusion boundary region of the NG-DMW of the austenitic stainless steel side has to be characterized for knowing the degree of sensitization, amount of residual plastic strain (and its distribution in the whole NG-DMW), and eventual sigma phase formation in the HAZ of the austenitic stainless steel piping as well as the extent of the dilution in the DMW weld metal including possible weld defects such as the ductility-dip cracking close to the fusion boundary. If the microstructural changes are considered marked, this side has to be included also to the EAC testing program.

References

Aaltonen, P. & Hänninen, H., 1997. Water Chemistry and Behavior of Materials in PWRs and BWRs. IAEA-TECDOC-965, pp. 205–222.

Ahonen, M. et al., 2013. Low Temperature Crack Propagation (LTCP) Susceptibility of Nickel-Based Alloy 182, 152 and 52 Weld Metals in PWR Primary Water. In: Proceedings of the 16th International Conference on Environmental Degradation of Materials in Nuclear Power Systems - Water Reactors. Asheville, North Carolina, August 11-15, 2013. USA: Omnipress (CD-ROM).

Ahonen M., 2015. Effect of Microstructure on Low Temperature Hydrogen-Induced Cracking Behaviour of Nickel-Based Alloy Weld Metals. Doctoral dissertation, VTT Science 105.

Alexandrov, B.T. et al., 2013. Fusion Boundary Microstructure Evolution Associated with Embrittlement of Ni-Base Alloy Overlays Applied to Carbon Steel. Welding in the World, 57(1), pp. 39–53.

Anderson, T.L., 2005. Fracture mechanics: Fundamentals and applications, 3rd edn. Taylor & Francis Group, LLC.

Andresen, P.L. et al., 2007. Effects of PWR Primary Water Chemistry on PWSCC of Ni Alloys. In Proceedings of the 13th International Conference on Environmental Degradation of Materials in Nuclear Power Systems - Water Reactors. CNS, pp. 1-21.

Andresen, P.L. et al., 2012. SCC of Alloy 690 and its Weld Metals. In Corrosion 2012, Paper C2012-0001187, NACE International.

ASTM E1820-15, 2015. Standard test method for measurement of fracture toughness. ASTM International, West Conshohocken, USA

ASTM E1921-15, 2015. Standard test method for determination of reference temperature, T0, for ferritic steels in the transition range. ASTM E1921-15. ASTM International.

Brown, C. M. & Mills, W. J., 2002. Fracture Toughness of Alloy 690 and EN52 Welds in Air and Water. Metallurgical and Materials Transactions A, 33A (6), pp. 1725-1735.

Cattant, F., 2014. Materials Ageing in Light Water Reactors - Handbook of Destructive Assays. Materials Ageing Institute, 1166 p.

Chung, W.-C. et al., 2011. Microstructure and Stress Corrosion Cracking Behavior of the Weld Metal in Alloy 52-A508 Dissimilar Welds. Materials Transactions, 52(1), pp. 12–19.

Corwin, W. R. et al., 1995. Thermal Embrittlement of Reactor Pressure Vessel Steels. United States, UNT Digital Library. http://digital.library.unt.edu/ark:/67531/metadc706620/. Accessed September 25, 2015.

Cumblidge, S.E. et al., 2010. Results of the program for the inspection of nickel alloy components, NUREG/CR-7019; PNNL-18713. U.S. Nuclear Regulatory Commission, Washington, D.C., USA. 180 p. + app. 396 p. https://www.nrc.gov/reading-rm/doc-collections/nuregs/contract/cr7019/r1/cr7019r1.pdf Accessed April 2, 2017.

DuPont, J.N. et al., 2009. Welding Metallurgy and Weldability of Nickel-Base Alloys. John Wiley and Sons, 440 p.

Ehrnstén, U., 2012. Corrosion and Stress Corrosion Cracking of Austenitic Stainless Steels. In T. R. Allen, R. E. Stoller, & S. Yamanaka, eds., Comprehensive Nuclear Materials, Vol. 5. Elsevier Ltd., pp. 93–104.

EPRI, 2009. Materials Reliability Program: Resistance to Primary Water Stress Corrosion Cracking of Alloy 690 in Pressurized Water Reactors (MRP-258).

Fan, K. et al., 2016. Local Failure Behavior of a Dissimilar Metal Interface Region with Mechanical Heterogeneity. Eng Fail Anal 59:419–433 . doi: 10.1016/j.engfailanal.2015.11.005.

Féron, D., 2012. Overview of Nuclear Materials and Nuclear Corrosion Science and Engineering. In Nuclear Corrosion Science and Engineering. Woodhead Publishing, pp. 31–56.

Fyfitch, S., 2012. Corrosion and Stress Corrosion Cracking of Ni-Base Alloys. In T. R. Allen, R. E. Stoller, & S. Yamanaka, eds., Comprehensive Nuclear Materials, Vol. 5. Elsevier Ltd., pp. 69–92.

Herms, E. et al., 2009. LTCP of Alloy 182/152 Test-ed in PWR Primary Water. In: Proceedings of the 14th International Symposium on Environmental Degradation of Materials in Nuclear Power Systems - Water Reac-tors. Virginia Beach, Virginia, August 23-27, 2009. USA: ANS (CD-ROM).

Hudson, J.A. et al., 1988. Thermal Ageing Effects in Structural Steels. Theoretical and Applied Fracture Mechanics 10 (1988), pp. 123-133.

Hänninen, H. et al., 2014. Structural Integrity of Ni-base Alloy Welds. VTT Technology 175, Espoo.

Joly, P. et al., 2014. Ageing Behavior of Decarburized Heat Affected Zone of Alloy 52. Pvp2014-29044, 52:1–13.

Kim, Y.J. et al., 2000. SINTAP Defect Assessment Procedure For Strength Mismatched Structures. Eng Fract Mech 67:529–546.

Laukkanen, A. et al., 2007. Charasteristics Relevant to Ductile Failure of Bimetallic Welds and Evaluation of Transferability of Fracture Properties. Nuclear Engineering and Design, 237(2007), pp. 1-15.

Lindqvist, S., 2014. Fracture Mechanical Characterisation of Multimetal Welds. MSc. Thesis, Aalto university.

Lindqvist, S., & Kuutti, J., 2018. Dependence between η -factor and crack location relative to a fusion boundary between hard and soft materials in a SE (B) specimen. Int J Fract 211:281–293 . doi: 10.1007/s10704-018-0288-5.

Lindqvist, S. et al., 2018. The effect of crack path on tearing resistance of a narrow-gap Alloy 52 dissimilar metal weld. Eng Fract Mech 0–1 . doi: 10.1016/j.engfracmech.2018.05.043.

Lippold, J.C., 2015. Welding Metallurgy Principles. In Welding Metallurgy and Weldability, John Wiley & Sons, 424 p.

Lu, Z. et al., 2015. Characterization of Microstructure, Local Deformation and Microchemistry in Alloy 690 Heat-Affected Zone and Stress Corrosion Cracking in High Temperature Water. Journal of Nuclear Materials, 465, pp. 471–481.

Lundin, C.D., 1982. Dissimilar Metal Welds — Transition Joints Literature Review. Welding Journal, 61(Supplement), pp. 58–63.

MacDonald, D.D. & Cragnolino, G.A., 1989. Corrosion of Steam Cycle Materials. In P. Cohen, ed., ASME Handbook on Water Technology for Thermal Power Systems. ASME, pp. 659–1031.

McIllree, A. et al., 2006. Effects of Hydrogen and Temperature on the Fracture Resistance of Weld Metals 182 and 152 in Simulated PWR Shutdown Environment. Proceedings of the 6th Fontevraud Conference, 18-22-September 2006, Fontevraud Royal Abby, France (CD-ROM).

Meyer, R.M. & Heasler, P.G., 2017. Results of Blind Testing for the Program to Assess the Reliability of Emerging Nondestructive Techniques. NUREG/CR-7235. U.S. Nuclear Regulatory Commission, Washington, D.C., USA. 174 p.

+ app. 351 p. https://www.nrc.gov/docs/ML1715/ML17159A466.pdf.

Meyer, R.M. et al., 2017. Analysis of PARENT Technique Data. PNNL-26399. Pacific Northwest National Laboratory, Richland, WA, USA. 252 p.

Meyer, R.M. & Holmes, A.E., 2018. Blind Testing of PARENT Open Techniques. Results. PNNL-26993. Pacific Northwest National Laboratory, Richland, WA, USA. 64 p. + app 100 p.

Meyer, R.M. et al., 2017. Results of Open Testing for the Program to Assess the Reliability of Emerging Nondestructive Techniques. NUREG/CR-7236, Vol. 1 and 2, U.S. Nuclear Regulatory Commission, Washington, D.C., USA. 218 p. + app 780 p.

Mills, W.J. & Brown, C.M., 2001. Fracture Toughness of Alloy 600 and EN82H Weld in Air and Water. Metallurgical and Materials Transactions A, 32A (5), pp. 1161-1174.

Mouginot, R ., 2017. Effect of Thermal Ageing on Alloys 690 and 52 in Pressurized Water Reactor Applications. Doctoral dissertation, Aalto University.

Nelson, T.W. et al., 1998. Investigation of Boundaries and Structures in Dissimilar Metal Welds. Science and Technology of Welding and Joining, 3(5), pp. 249–255.

Nevasmaa, P. et al., 2010. Fracture mechanical characterisation of ferrite-austenite dissimilar metal welds (DMWs) for elevated temperature service in view of metallurgical mis-match. p 17.

Payne, B.E., 1969. Nickel-base Welding Consumables for Dissimilar Metal Welding Applications. Metal Construction, 1(12), pp.79–87.

Peng, Q. et al., 2005. SCC Behavior in the Transition Region of an Alloy 182-SA 508 Cl.2 Dissimilar Weld Joint under Simulated BWR-NWC Conditions. In Proceedings of the 12th International Conference on Environmental Degradation of Materials in Nuclear Power Systems - Water Reactors. TMS, pp. 589–599.

Peng, Q. J. et al., 2012. Environmentally Assisted Crack Growth in One-Dimensionally Cold Worked Alloy 690TT in Primary Water. Corrosion Science, 57 (2012), pp. 81-88.

Rajeev, R. et al., 2001. Origin of Hard and Soft Zone Formation During Cladding of Austenitic/Duplex Stainless Steel on Plain Carbon Steel. Materials Science and Technology, 17(8), pp. 1005–1011.

Sarikka, T., 2016a. Effect of Strength Mismatch on Fracture Behavior of Ferrite-Austenite Interface in Ni-Base Alloy Dissimilar Metal Welds. Doctoral dissertation, Aalto University.

Sarikka, T. et al., 2016b. Microstructural, Mechanical, and Fracture Mechanical Characterization of SA 508-Alloy 182 Dissimilar Metal Weld in View of Mismatch State. International Journal of Pressure Vessels and Piping, 145, pp. 13–22.

Sarikka, T. et al., 2017a. Effect of Mechanical Mismatch on the Fracture Mechanical Behavior of SA 508-Alloy 52 Narrow Gap Dissimilar Metal Weld. International Journal of Pressure Vessels and Piping, 157, pp. 30-42.

Sarikka, T. et al., 2017b. Microstructural Characterization of Alloy 52 Narrow-Gap Dissimilar Metal Weld after Aging. In Proceedings of the 18th International Conference on Environmental Degradation of Materials in Nuclear Power Systems - Water Reactors. TMS, pp. 763-778.

Scenini, F. et al., 2005. Alloy Oxidation Studies Related to PWSCC. In Proceedings of the 12th International Conference on Environmental Degradation of Materials in Nuclear Power Systems -Water Reactors. TMS, pp. 891–902.

Scott, P.M., 1996. Environment Assisted Cracking in Austenitic Components.

International Journal of Pressure Vessels and Piping, 65(3), pp. 255–264.

Simonovski, I. et al., 2015. J-Integral Fracture Toughness Assessment of Specimens Containing Dissimilar Metal Welds. In: 23 nd Conference on Structural Mechanics in Reactor Technology (SMiRT). Manchester.

Sudha, C. et al., 2002. Systematic Study of Formation of Soft and Hard Zones in the Dissimilar Weldments of Cr–Mo Steels. Journal of Nuclear Materials, 302(2-3), pp. 193–205.

Sui, G. et al., 1997. Stress Corrosion Cracking of Alloy 600 and Alloy 690 in Hydrogen/Steam at 380 °C. Corrosion Science, 39(3), pp. 565–587.

Toloczko, M. et al., 2016. Alloy 152/52-LAS Dilution Zone and Interface/Fusion Line PWSCC Testing. In EPRI 690/152/52 PWSCC Research Collaboration Meeting, Nov. 29-Dec. 1, 2016,Tampa, FL.

Wallin, K., 2011. Fracture toughness of engineering materials - estimation and application. EMAS publishing.

Wallin, K. et al., 2004. Master Curve analysis of inhomogeneous ferritic steels. 71:2329–2346 . doi: 10.1016/j.engfracmech.2004.01.010.

Wang, H.T. et al., 2013a. Local mechanical properties of a dissimilar metal welded joint in nuclear power systems. Mater Sci Eng A 568:108–117.

Wang, H.T. et al., 2013b. An experimental investigation of local fracture resistance and crack growth paths in a dissimilar metal welded joint. Mater Des 44:179–189 . doi: 10.1016/j.matdes.2012.07.067.

Young, B. et al., 2005. Reduction of Toughness for Weld Metal in a PWR Primary Water Environment with Varying Dissolved Hydrogen, Lithium and Boric Acid Concentrations. In: Allen, T.R. (Ed.) Proceedings of the 12th International Symposium on Environmental Degradation of Materials in Nuclear Power Systems – Water Reactors. Salt Lake City, Utah, August 14-18, 2005. USA: TMS (CD-ROM).

Young, G.A. et al., 2013. The Kinetics of Long Range Ordering in Ni-Cr and Ni-Cr-Fe Alloys. In Proceedings of the 16th International Conference on the Environmental Degradation of Materials in Nuclear Power Systems - Water Reactors. CNS, pp. 1–22.

Series title and number

VTT Technology 333

Title

Thermal ageing and mechanical performance of narrow-gap dissimilar metal welds

Author(s)

Matias Ahonen, Sebastian Lindqvist, Teemu Sarikka, Roman Mouginot, Esa Leskelä, Jari Lydman, Ulla Ehrnstén, Pekka Nevasmaa, Tommi Seppänen, Pentti Arffman & Hannu Hänninen

Abstract

NIWEL (Nickel-Base Alloy Welding Forum) project was primarily addressed to the needs of the nuclear energy industry, and it was the fourth consecutive cooperative project on the dissimilar metal weld (DMW) topics. The main focus of the NIWEL project was to assess the effects of thermal aging on the performance of DMWs. Cooperation with PARENT (Program to Assess the Reliability of Emerging Nondestructive Techniques) program was also a part of the NIWEL project, and PARENT results are shortly presented in this report.

The long-term behaviour of the DMWs is of particular interest in Finland, because the nuclear power plants are at critical stages of their lifetime: either beginning their operation or reaching lifetime extensions. In both cases, understanding of the aging phenomena is of utmost importance in order to ensure safe operation for lifetimes that can reach 60 years or even beyond that.

With the exception of the fusion boundary region, the obtained microstructural characterization results on the weld metal and the base material did not show any clear indications of metallurgical changes. The fusion boundary region exhibits zones that are very narrow, some tens of micrometres or even less in width. The nanoindentation results show that the high local hardness mismatch between the soft carbon-depleted zone (CDZ) and very hard carbon-enriched zone in the Alloy 52 weld metal side of the fusion boundary, caused by PWHT, reduces due to thermal ageing. Narrow-gap Alloy 52 DMW sustains its high performance, regarding ductile and brittle fracture properties adjacent to the fusion boundary between SA 508/Alloy 52 after thermal aging (10000 h at 400 °C) representative of 60 years of plant operation. Ductile-to-brittle transition temperature (T_{42J}) measured after 10000 h aging is 12 °C, which gives a ΔT_{42J} of 47 °C as compared to the as-received material. Fracture toughness T_0 was not significantly affected by thermal aging. Thus, it is assumed that thermal aging may promote brittle crack propagation and degrade material's capability to arrest the growing cracks at low temperatures, whereas the brittle crack initiation tendency of the material is not markedly affected. However, further investigations are needed to clarify the mechanisms explaining the differences. CDZ is the preferred crack path in all types of fracture mechanical tests applied in this study. However, crack deflections to the Alloy 52 weld metal side of the fusion boundary occur due to the small weld defects observed in the weld metal in tests, where the fracture mode is ductile.

ISBN, ISSN, URN

ISBN 978-951-38-8656-1 (Soft back ed.)
ISBN 978-951-38-8655-4 (URL: http://www.vttresearch.com/impact/publications)
ISSN-L 2242-1211
ISSN 2242-1211 (Print)
ISSN 2242-122X (Online)
http://urn.fi/URN:ISBN:978-951-38-8655-4

Date

June 2018

Language

English, Finnish abstract

Pages

189 p.

Name of the project

NIWEL

Commissioned by

Keywords

Dissimilar metal weld, Ni-base alloy, ageing, microstructure, fracture

Publisher

VTT Technical Research Centre of Finland Ltd
P.O. Box 1000, FI-02044 VTT, Finland, Tel. 020 722 111

Julkaisun sarja ja numero

VTT Technology 333

Nimeke	**Kapearailo-eripariliitosten vanheneminen ja mekaaniset ominaisuudet**
Tekijä(t)	Matias Ahonen, Sebastian Lindqvist, Teemu Sarikka, Roman Mouginot, Esa Leskelä, Jari Lydman, Ulla Ehrnstén, Pekka Nevasmaa, Tommi Seppänen, Pentti Arffman & Hannu Hänninen
Tiivistelmä	NIWEL-projekti (Nickel-Base Alloy Welding Forum) kohdistui ensisijaisesti ydinvoimayhtiöiden tarpeisiin ja se oli neljäs peräkkäinen yhteistyöprojekti eriparihitsaukseen liittyen. NIWEL-projektin pääasiallinen tavoite oli arvioida termisen vanhenemisen vaikutusta eripariliitosten toimintakykyyn. Yhteistyö PARENT-ohjelman (Program to Assess the Reliability of Emerging Nondestructive Techniques) kanssa oli osa NIWEL-projektia, ja PARENT-ohjelman tulokset on esitetty lyhyesti tässä raportissa. Eripariliitosten käyttäytyminen pitkällä aikavälillä on erityisen mielenkiinnon kohteena Suomessa, koska ydinvoimalaitokset ovat elinkaarensa erityisissä vaiheissa: joko aloittamassa toimintaansa tai siirtymässä pidennetyn käyttöiän vaiheeseen. Molemmissa tapauksissa vanhenemisilmiöiden tuntemus on ensiarvoisen tärkeää ydinvoiman turvallisen käytön varmistamiseksi, kun laitoksia käytetään 60 vuotta tai jopa sitä pidempään. Sularajan alue pois lukien, mikrorakennetutkimuksissa ei löydetty selviä metallurgisia muutoksia perus- tai hitsiaineen puolella. Sularajan alueella on erittäin ohuita hienorakenteisia vyöhykkeitä, joiden leveys on joitain kymmeniä mikrometrejä tai jopa sitä vähemmän. Nanoindentaatiomittausten tulokset osoittavat, että hitsin jälkilämpökäsittelyn aikaansaama suuri paikallinen kovuuden epäsopu pehmeän hiiliköyhän vyöhykkeen ja erittäin kovan hitsin puolella sijaitsevan hiilirikkaan vyöhykkeen välillä pienenee termisen vanhenemisen seurauksena. Alloy 52 kapearailo-eripariliitos säilyttää hyvät ominaisuutensa sitkeän ja haurasmurtuman suhteen SA 508 painesäiliöteräksen ja Alloy 52 hitsiaineen välisen sularajan läheisyydessä 60 vuoden laitoskäyttöä vastaavan termisen vanhennuksen (10000 h 400 °C:ssa) jälkeenkin. Sitkeä-hauras transitiolämpötila (T_{42J}) 10000 h vanhennuskäsittelyn jälkeen on 12 °C, joka on 47 °C korkeampi kuin toimitustilaiselle materiaalille mitattu arvo. Murtumissitkeys T_0 ei muuttunut termisen vanhennuksen vaikutuksesta. Tämän vuoksi arvioidaan, että terminen vanheneminen saattaa edesauttaa haurasmurtuman etenemistä ja huonontaa materiaalin kykyä pysäyttää etenevä haurasmurtuma, mutta haurasmurtuman ydintymisalttius ei muutu. Jatkotutkimuksia kuitenkin tarvitaan, jotta erot selittävät mekanismit pystytään selvittämään. Säröntkasvu pyrkii etenemään ensisijaisesti SA 508 reaktoripainesäiliöteräksen hiiliköyhässä vyöhykkeessä kaikissa murtumismekaanisissa kokeissa, joita tässä tutkimuksessa suoritettiin. Säröt poikkeavat kuitenkin toisinaan Alloy 52 hitsiaineen puolelle pienten hitsausvikojen vuoksi, joita havaittiin murtopinnoilla murtumismekanismin ollessa sitkeä.
ISBN, ISSN, URN	ISBN 978-951-38-8656-1 (nid.) ISBN 978-951-38-8655-4 (URL: http://www.vtt.fi/julkaisut) ISSN-L 2242-1211 ISSN 2242-1211 (Painettu) ISSN 2242-122X (Verkkojulkaisu) http://urn.fi/URN:ISBN:978-951-38-8655-4
Julkaisuaika	Kesäkuu 2018
Kieli	Englanti, suomenkielinen tiivistelmä
Sivumäärä	189 s.
Projektin nimi	NIWEL
Rahoittajat	
Avainsanat	Eriparihitsi, nikkeliseos, mikrorakenne, murtuminen
Julkaisija	Teknologian tutkimuskeskus VTT Oy PL 1000, 02044 VTT, puh. 020 722 111

Thermal ageing and mechanical performance of narrow-gap dissimilar metal welds

NIWEL (Nickel-Base Alloy Welding Forum) project was primarily addressed to the needs of the nuclear power plant industry, and it was a fourth consecutive cooperative project on the dissimilar metal weld (DMW) topics. The main focus of the NIWEL project is to assess the effect of thermal aging on the performance of DMWs. The long-term behaviour of the DMWs is of particular interest in Finland, because there are nuclear power plants that are at critical stages of their lifetime: either beginning their operation or reaching lifetime extensions. In both cases, understanding of the aging phenomena is of utmost importance in order to ensure safe operation for lifetimes that can reach 60 years or even beyond that.

With the exception of the fusion boundary region, the obtained microstructural characterization results on the weld metal and the base material did not show any clear indications of metallurgical changes. The fusion boundary region exhibits zones that are very fine, some tens of micrometres or even less in width. The nanoindentation results show that the high local hardness mismatch between the soft CDZ and very hard carbon-enriched zone in the weld metal side of the fusion boundary, caused by PWHT, reduces due to thermal ageing. Narrow-gap Alloy 52 DMW sustains its high performance, regarding ductile and brittle fracture properties adjacent to the fusion boundary between SA508/Alloy 52 after thermal aging (10000 h at 400 °C) representative of 60 years of plant operation. Ductile-to-brittle transition temperature (T_{42J}) measured after 10000 h aging is 12 °C, which gives a ΔT_{42J} of 47 °C as compared to the as-received material.

ISBN 978-951-38-8656-1 (Soft back ed.)
ISBN 978-951-38-8655-4 (URL: http://www.vttresearch.com/impact/publications)
ISSN-L 2242-1211
ISSN 2242-1211 (Print)
ISSN 2242-122X (Online)
http://urn.fi/URN:ISBN:978-951-38-8655-4